Final Report NAGW-2151

RETRIEVAL OF SOIL MOISTURE AND ROUGHNESS FROM THE POLARIMETRIC RADAR RESPONSE

Submitted to :
NASA Headquarters
Terrestrial Ecology Program
Washington D.C. 20546
Attn: Dr. Diane Wickland

Submitted by:

Kamal Sarabandi
Fawwaz T. Ulaby

Radiation Laboratory
Department of Electrical Engineering and Computer Science
The University of Michigan
Ann Arbor, MI 48109-2122
Tel: (313) 936-1575
Fax: (313) 747-2106

27593-1-F = RL-2417

1 Introduction

The purpose of this final report is to summarize our accomplishments over the period May 93 to October 1996 for the investigation entitled "Retrieval of soil moisture and roughness from the polarimetric radar response" supported by the Terrestrial Ecology Program of NASA Headquarter. The main objective of this investigation was the characterization of soil moisture using imaging radars. In order to accomplish this task, a number of intermediate steps had to be undertaken. In this proposal, the theoretical, numerical, and experimental aspects of electromagnetic scattering from natural surfaces was considered with emphasis on remote sensing of soil moisture. In the general case, the microwave backscatter from natural surfaces is mainly influenced by three major factors: (1) the roughness statistics of the soil surface, (2) soil moisture content, and (3) soil surface cover. First the scattering problem from bare-soil surfaces was considered and a hybrid model that relates the radar backscattering coefficient to soil moisture and surface roughness was developed. This model is based on extensive experimental measurements of the radar polarimetric backscatter response of bare soil surfaces at microwave frequencies over a wide range of moisture conditions and roughness scales in conjunction with existing theoretical surface scattering models in limiting cases (small perturbation, physical optics, and geometrical optics models). Also a simple inversion algorithm capable of providing accurate estimates of soil moisture content and surface rms height from single-frequency multi-polarization radar observations was developed. The accuracy of the model and its inversion algorithm is demonstrated using independent data sets. Next the hybrid model for bare-soil surfaces is made fully polarimetric by incorporating the parameters of the co- and cross-polarized phase difference into the model. Experimental data in conjunction with numerical simulations are used to relate the soil moisture content and surface roughness to the phase difference statistics. For this purpose, a novel numerical scattering simulation for inhomogeneous dielectric random surfaces was developed. Finally the scattering problem of short vegetation cover above a rough soil surface was considered. A general scattering model for grass-blades of arbitrary cross section was developed and incorporated in a first order random media model. The vegetation model and the bare-soil model are combined and the accuracy of the combined model is evaluated against experimental observations from a wheat field over the entire growing season. A complete set of ground-truth data and polarimetric backscatter data at L-, C-, and X-band over a wide range of incidence angles were collected. Also an inversion algorithm for estimating soil moisture and surface roughness from multi-polarized multi-frequency observations of vegetation-covered ground is developed.

In what follows a summary of major accomplishments with pertinent references are provided.

2 Summary of Major Accomplishments

The following tasks were accomplished during the past year:

1. Development of a polarimetric calibration technique for distributed targets:
   Quantitative analysis of the measured backscatter from rough surfaces required the use of a very precise radar calibration procedure. Traditionally, calibration of distributed targets is performed using calibration methods developed for point targets and using the illumination integral to calculate the backscattering coefficients. Using this method, possible phase variations or antenna cross-talk variations (between orthogonal polarization channels) across the beam are totally ignored, which may compromise the calibration accuracy. To rectify this deficiency of existing calibration techniques, a new technique was developed with which the radar polarization distortion matrix is characterized completely by measuring the polarimetric response of a sphere over the entire mainlobe of the antenna, rather than along only the boresight direction [1].

2. Development of a Semi-Empirical Scattering Model:
   At microwave frequencies many natural surfaces do not fall into the validity regions of the theoretical models, and even when they do, the results based on these models fail to agree with the measurements. To circumvent this difficulty, we took a rather unique approach to the problem. Using our calibrated polarimetric radar system, extensive backscatter measurements covering a wide range of surface roughness and moisture conditions were conducted. The statistical parameters of the surfaces were determined by a laser profilometer and soil moisture was measured by taking samples and using dielectric probes. Using the polarimetric data and the expected asymptotic behavior of backscattering coefficients in limiting cases, a semi-empirical model (SEM) was developed and its accuracy was tested [2, 3, 18]. item Development of a fully polarimetric hybrid model for bare soil surfaces:
   The semi-empirical model for bare soil surfaces which was developed in the first phase of this investigation was improved. The improved model is made fully polarimetric by including the phase difference statistics [19, 20].

3. Development of a Level-1 SAR image classifier:
   A radar image classifier was developed for the purpose of identifying statistically homogeneous distributed targets in the imaged scene. This task was important it bears directly on to the soil-moisture estimation objective. Basically it is mandatory to identify the cover class of a given pixel before any algorithm is applied to it. This classifier operates on calibrated L- and C-band data and segments the image into four categories: (1) Bare surfaces, (2) Short vegetation, (3) Tall vegetation, and (4) Urban. The accuracy of the classifier was tested using independent images acquired in different seasons [4].

4. Development of a dielectric probe for measuring the soil moisture:
   Traditionally coaxial probes have been used for measuring soil moisture in fields. These probes are very sensitive to pressure and have a very small contact area. Accurate measurement using these probes require a large number of sample measurements which is very time consuming. To rectify this problem we designed and completed a prototype soil probe based on microstrip resonators that is not only very accurate, but also very convenient to use. With this new probe it is also possible to predict the soil type to some extent [5].

5. Development of in situ and in vivo vegetation dielectric measurement technique:
   A waveguide technique for measuring the dielectric constant of vegetation needles was developed. Basically the dielectric constant of the sample is calculated from the measured reflection coefficient using a novel inversion algorithm based on an eigen-analysis of the impedance matrix of the method of moments solution [6].

6. Development of bistatic scattering measurement facility:
   In order to characterize soil moisture and roughness parameters of a surface covered with randomly oriented particles (as in the vegetation case), the bistatic scattering characteristics of the surface are required. The specular direction is the most important bistatic direction in this type of problems because the mean-field (coherent scattering) is not zero. For this purpose a fully polarimetric bistatic scattering system was designed and tested. The Bistatic Facility is currently configured to perform bistatic measurements in the 8.5-10 GHz and 34-35 GHz frequency range [7, 8].

7. Development of scattering model for inhomogeneous rough surfaces:
   One major problem with existing theoretical models for rough surfaces as applied to soil surfaces is their inability to treat inhomogeneous dielectric profile. Recently we developed a theoretical model that can take into account the effect of vertical inhomogeneity. For the first time a complete second order fully polarimetric scattering model for stratified rough surfaces with relatively small rms height. The model was experimentally verified using careful controlled experiments [9, 21].

8. Development of a numerical technique for rough surfaces:
   Numerical simulations are necessary to indicate the trend of the scattering behavior, particularly where theoretical solutions and/or controlled experimental data do not exit. In specific three different approaches addressing different problems in numerical evaluation scattering behavior of rough surfaces were considered:

   - One problem in numerical computation of scattering from rough surfaces is related to the fact that the scattering is usually computed from finite samples of rough surfaces. In order to eliminate the edge effect of finite samples, the magnitude of the incident wave is tapered. In these methods, the dimension of surface samples must be chosen large enough so that the backscatter becomes independent of footprint size [22]. To rectify this problem, we developed a novel numerical method that can be illuminated by plane waves. To eliminate the effect of edges, tapered resistive sheets are used. It is shown that the new method is numerically more efficient than the traditional methods [12].
   - The numerical techniques available in the literature are limited to perfectly conducting surfaces. However, the dielectric properties of soil surfaces are very much different from those of perfect conductors. Due to moisture variations and inhomogeneity among the constituent particles, the soil medium usually behaves as an inhomogeneous dielectric. The numerical simulation developed here has the capability of handling inhomogeneous dielectric surfaces. This simulation was used to evaluate

the effect of moisture profile and correlation function on the backscatter data. It was found that both the correlation function and the dielectric inhomogeneities play a very important role [10, 11].

- One limitation of existing numerical methods is their lack of efficiency. To improve the computation time wavelet basis function are used to produce spars impedance matrices which are easily invertible [23, 24].

9. Retrieval of soil moisture form vegetation covered surfaces:
Under this task some basic studies were carried out. We developed forward scattering models for characterizing the dependence of radar backscatter to soil moisture in the presence of short vegetation. The following models were developed:

    - Conducting of field measurements for surfaces covered with short vegetation:
    A complete set of ground-truth data and polarimetric backscatter data were collected. A wheat field was chosen as the test field and radar measurement was conducted over the entire growing season. The backscatter data collected on the wheat field was calibrated and processed completely. This data was collected in summer 1993 during the whole growing season (mid-April to mid-September) at 6 incidence angles and 3 frequencies (L-, C-, and X-band). The experimental results show a significant backscatter sensitivity to soil moisture for all three frequencies and under different vegetation biomass conditions [15].
    - Development of scattering model for grass blades:
    A analytical scattering model for grass-blades of arbitrary cross section was developed. Closed form expressions for the polarizability tensor elements are derived. This model is valid when the all cross section dimensions are small compared to the wavelength [13].
    - Generalization of Rayleigh-Gans model:
    A theoretical scattering model for long, thin dielectric cylinders of arbitrary cross section and electrical length was developed. This is an extension of our previous model for electrically long cylinders. Using this solution we are able to model scattering from grass blades of arbitrary cross section and curvature very accurately [14].
    - Coherent Scattering Model for Short Vegetation :
    A coherent scattering model with high fidelity was developed. In this model, the effects of coherence among the scatterers as well as non-uniform illumination are taken into account. The scattering formulation for the grass components accounts for fine geometrical features of the grass blades such as curvature and cross section. [16, 17]

3 Students

3.1 Ph.D. Students

1. Yisok Oh
   Dissertation Title: Microwave Polarimetric Backscattering from Natural Rough Surfaces.
   Graduation date: December 1993 Position: Assistant Professor, Hong-IK University, Seoul, Korea

2. Roger Dean De Roo
   Dissertation Title: Theory and Measurement of Bistatic Scattering of X-band Microwaves from Rough Dielectric Surfaces.
   Graduation date: December 1996. Position: Post Doctoral Fellow, Radiation Laboratory, The University of Michigan.

3. James Norman Stiles
   Dissertation Title: A Coherent Microwave Scattering Model for Grassland Structures and Canopies.
   Graduation date: January 1996
   Position: Assistant Professor, University of Kansas

4. Tesn Chie Chiu
   Dissertation Title: Electromagnetic Scattering from Rough Surfaces Covered with Short Vegetation.
   Graduation date: December 1997.

3.2 M.S. Students

1. Neil Peplinski
2. Andrew Zambetti

4 Publications

1. Sarabandi, K., Y. Oh, and F.T. Ulaby, "Measurement and calibration of differential Mueller matrix of distributed targets," *IEEE Trans. Antennas Propagat.*, vol. 40, no. 12, 1524-1532, Dec. 1992.

2. Oh, Y., K. Sarabandi, and F.T. Ulaby,"An empirical model and an inversion technique for radar scattering from bare soil surfaces," *IEEE Trans. Geosci. Remote Sensing.*, vol. 30, no. 2, March 1992.

3. Oh, Y., "Microwave Polarimetric Backscattering from Natural Rough Surfaces," Ph.D. Dissertation, The University of Michigan, 1993.

4. Pierce, L.E., F.T. Ulaby, K. Sarabandi, and M.C. Dobson,"Knowledge-based classification of polarimetric SAR images," *IEEE Trans. Geosci. Remote Sensing.*, vol. 32, no. 5, pp. 1081-1086, Sept. 94.

5. Sarabandi, K., and E. S. Li, "A microstrip ring resonator for non-invasive dielectric measurements," *IEEE Trans. Geosci. Remote Sensing.*, accepted for publication (Dec. 96).

6. Sarabandi, K., "A technique for dielectric measurement of cylindrical objects in a rectangular waveguide," *IEEE Trans. Instrum. Meas.*, vol. 43, no. 6, 793-798, Dec. 1994.

7. De Roo, R.D., R. Hartikka, N. Peplinski, and A, Zambetti, "Bistatic Measurement Facility User's Manual", The University of Michigan, Ann Arbor, MI", 031163-F, Aug. 1994.

8. De Roo, R.D., and F.T. Ulaby, "Bistatic Specular Scattering from Rough Dielectric Surfaces", *IEEE Trans. Antennas and Propagat.*, vol. 42, no. 2, pp. 220–231, Feb. 1994.

9. Sarabandi,K., and T.C. Chiu "Electromagnetic scattering from slightly rough surfaces with inhomogeneous dielectric profile," *IEEE Trans. Antennas Propagat.,* accepted for publication (Nov. 1996).

10. Sarabandi, K., Y. Oh, and F.T. Ulaby, "A numerical simulation of scattering from inhomogeneous dielectric random surfaces," *IEEE Trans. Geosci. Remote Sensing,* vol. 34, no.2, 425-432, March 1996.

11. Sarabandi, K., "Scattering from dielectric structures above impedance surfaces and resistive sheets," *IEEE Trans. Antennas Propagat.*, vol. 40, no. 1, 67-78, Jan. 1992.

12. Oh, Y., and K. Sarabandi, "An improved numerical simulation of electromagnetic scattering from perfectly conducting random surfaces," *IEE Proceedings- Microwave, Antennas and Propagat.,* accepted for publication.

13. Stiles, J.M., K. Sarabandi, and F.T. Ulaby, "Microwave scattering model for grass blade structures," *IEEE Trans. Geosci. Remote Sensing,* vol. 31, no. 5, 1051-1059, Sept. 1993.

14. Stiles, J.M., and K. Sarabandi, "A scattering model for thin dielectric cylinders of arbitrary cross-section and electrical length," *IEEE Trans. Antennas Propagat.,* vol. 44, no.2,260-266, Feb. 1996.

15. Stiles, J.M., "A Coherent Microwave Scattering Model for Grassland Structures and Canopies" Ph.D. Dissertation, The University of Michigan, 1996.

16. Stiles, J.M., and K. Sarabandi, "Scattering from cultural grass canopies: a phase coherent model,"*IEEE Trans. Geosci. Remote Sensing,* submitted for publication, (March 97).

17. Stiles, J.M., K. Sarabandi, and F.T. Ulaby, "Scattering from cultural grass canopies: measured and modeled data," *IEEE Trans. Geosci. Remote Sensing*, submitted for publication, (March 97).

Conference Papers

18. Oh, Y., K. Sarabandi, and F.T. Ulaby, "An inversion algorithm for retrieving soil moisture and surface roughness from polarimetric radar observation," *Proc. IEEE Trans. Geosci. Remote Sensing Symp.*, Pasadena, California, Aug. 1994.
19. Oh, Y., K. Sarabandi, and F.T. Ulaby, "Development of a semi-empirical polarimetric scattering model for microwave radar observations from bare soil surfaces," *Proc. IEEE Trans. Geosci. Remote Sensing Symp.*, Firenze, Italy, July 1995.
20. Oh, Y., K. Sarabandi, and F.T. Ulaby, "An Empirical model for phase difference statistics of rough surfaces," presented at IGARSS'93, Tokyo, 1993.
21. Sarabandi, K., and T.C. Chiu, "A perturbation scattering solution for rough surfaces with nonuniform dielectric profile using volumetric integral equation," *Proc. IEEE Trans. Geosci. Remote Sensing Symp.*, Lincoln, Nebraska, May 1996.
22. Sarabandi, K., and Y. Oh, "Effect of antenna footprint on the statistics of radar backscattering ," *Proc. IEEE Trans. Geosci. Remote Sensing Symp.*, Firenze, Italy, July 1995.
23. Sabet, K.F., and K. Sarabandi, "Analysis of scattering from curvilinear surfaces using wavelet concepts," *IEEE Antennas Propagat.& URSI Symp.,* Baltimore, Maryland, July 1996.
24. Zahn, D., K.F. Sabet, and K. Sarabandi, "Numerical simulation of scattering from rough surfaces: A wavelet-based approach," *Proc. IEEE Antennas Propagat. Symp.,* Montreal Canada, July 1997.
25. Stiles, J.M., and K. Sarabandi, "A rigorous analysis of the generalized Rayleigh-Gans approximation," *Proc. IEEE Antennas Propagat. Symp.,* Newport Beach CA, June 1995.
26. Stiles, J.M., and K. Sarabandi, "Estimation of soil moisture under short vegetation canopies," *Remote Sensing Science Workshop,* NASA Goddard Space Flight Center, Whashington D.C., Feb. 27- March 1, 1995.
27. Stiles, J.M., K. Sarabandi, and F.T. Ulaby, "Microwave Scattering Model for Grassland and short vegetation canopies," *Proc. IEEE Trans. Geosci. Remote Sensing Symp.*, Pasadena, California, Aug. 1994.
28. Chiu, T.C., K. Sarabandi, and F.T. Ulaby, "Polarimetric Backscattering Measurements of Herbaceous Vegetation : A Sensitivity Study for Soil Moisture Retrieval," *Proc. IEEE Trans. Geosci. Remote Sensing Symp.*, Lincoln, Nebraska, May 1996.
29. arabandi, K., and E.S. Li, "Characterization of soil moisture using a microstrip resonator," *Proc. IEEE Trans. Geosci. Remote Sensing Symp.*, Pasadena, California, Aug. 1994.

30. Oh, Y., and K. Sarabandi, "An improved numerical simulation of electromagnetic scattering from perfectly conducting random surfaces," *Proc. IEEE Antennas Propagat. Symp.*, Seattle, June 1994.

31. Ulaby, F.T., L. Pierce, M.C. Dobson, S. Chacon, and K. Sarabandi, "Land cover calssification by SAR," Presented at IGARSS'94, Pasadena, California, Aug. 1994.

32. Oh, Y., K. Sarabandi, and F.T. Ulaby, "Scattering from a three-dimensional dielectric hump above an impedance surface," *Proc. IEEE Trans. Antennas Propagat. Symp.*, Ann Arbor, 1993.

33. Oh, Y., K. Sarabandi, F.T. Ulaby, "Re-examination of the Kirchhoff approximation for scattering from a rough surface," *Digest URSI Meeting,* Ann Arbor, 1993.

34. Sarabandi, K., Y. Oh, and F.T. Ulaby, "Scatterometer measurement of differential Mueller matrix of distributed targets," presented at IGARSS'92, Houston, May 1992.

35. Oh, Yisok, K. Sarabandi, and F.T. Ulaby, "Algorithm for measuring moisture and roughness of bare soil surfaces from multi-polarized radar observations," presented at IGARSS'92, Houston, May 1992.

36. Sarabandi, K., "Scattering from dielectric structures above impedance surfaces and resistive sheets," *Proc. of Progress in Electromag. Research Symp.*, Boston, July 1991.

37. Sarabandi, K., Y. Oh, and F.T. Ulaby, "Polarimetric radar measurements of bare soil surfaces at microwave frequencies", *Proc. IEEE Trans. Geosci. Remote Sensing Symp.*, Espoo, Finland, June 1991.

38. De Roo, R. D., F T. Ulaby, Y. Kuga, and M. C. Dobson, "Experimental Studies of the Microwave Backscattering by Well-Characterized Surfaces," *Digest Progress in Electromagnetic Research Symposium (PIERS '89)*, July 1989.

Appendix

Reprints of Journal Papers

1524 IEEE TRANSACTIONS ON ANTENNAS AND PROPAGATION, VOL. 40, NO. 12, DECEMBER 1992

Measurement and Calibration of Differential Mueller Matrix of Distributed Targets

Kamal Sarabandi, *Member, IEEE,* Yisok Oh, *Student Member, IEEE,* and
Fawwaz T. Ulaby, *Fellow, IEEE*

***Abstract*—The recent interest in radar polarimetry has led to the development of several calibration techniques to retrieve the Mueller matrix of a distributed target from the multipolarization backscatter measurements recorded by a radar system. Because a distributed target is regarded as a statistically uniform random medium, the measurements usually are conducted for a large number of independent samples (usually spatially independent locations), from which the appropriate statistics characterizing the elements of the Mueller matrix can be derived. Existing calibration methods rely on two major assumptions. The first is that the illuminated area of the distributed target is regarded as a single equivalent point target located along the antenna's boresight direction, and that the statistics of the scattering from all of the measured equivalent point targets (representing the spatially independent samples observed by the radar) are indeed the same as the actual scattering statistics of the distributed target. The second assumption pertains to the process by which the actual measurements made by the radar for a given illuminated area are transformed into the scattering matrix of that area. The process involves measuring the radar response of a point calibration target of known scattering matrix, located along the boresight direction of the antenna, and then modifying the measured response by a constant, known as the illumination integral, when observing the distributed target. The illumination integral accounts for only magnitude variations of the illuminating fields. Thus, possible phase variations or antenna crosstalk variations (between orthogonal polarization channels) across the beam are totally ignored, which may compromise the calibration accuracy. To rectify this deficiency of existing calibration techniques, a new technique is proposed with which the radar polarization distortion matrix is characterized completely by measuring the polarimetric response of a sphere over the entire main lobe of the antenna, rather than along only the boresight direction. Additionally, the concept of a "differential Mueller matrix" is introduced, and by defining and using a correlation-calibration matrix derived from the measured radar distortion matrices, the differential Mueller matrix is accurately calibrated. Comparison of data based on the previous and the new techniques shows significant improvement in the measurement accuracy of the copolarized and cross-polarized phase difference statistics.**

I. INTRODUCTION

THE literature contains a variety of different methods for measuring the backscattering cross section of point targets. In all cases, however, the calibration part of the measurement process involves a comparison of the measured radar response due to the unknown target with the measured response due to a calibration target of known radar cross section. Under ideal conditions, both the unknown and calibration targets are placed along the antenna boresight direction, thereby ensuring that both targets are subjected to the same illumination by the radar antenna. The situation is markedly different for distributed targets; the unknown distributed target is illuminated by the full antenna beam, whereas the calibration target—being of necessity a point target—is illuminated by only a narrow segment of the beam centered around the boresight direction. Consequently, both the magnitude and phase variations across the antenna pattern become part of the measurement process.

The magnitude variation usually is taken into account through a calculation of the illumination integral [1]–[4], but the phase variation has so far been ignored. The role of this phase variation across the beam with regard to polarimetric radar measurements and the means for taking it into account in the measurement process are the subject of this paper.

Terrain surfaces, including vegetation-covered and snow-covered ground, are treated as random media with statistically uniform properties. In radar measurements, the quantities of interest are the statistical properties of the scattered field per unit area. One such quantity is the scattering coefficient σ^o, which is defined in terms of the second moment of the scattered field:

$$\sigma^o = \lim_{r\to\infty} \lim_{A\to\infty} \frac{4\pi r^2}{A} \cdot \frac{\langle |E^s|^2\rangle}{|E^i|^2}$$

where E^i and E^s are the incident and scattered fields, A is the illuminated area, and r is the range between the target area and the observation point. The above definition of σ^o is based on the assumption that the target is illuminated by a plane wave. Although in practice such a condition cannot be absolutely satisfied, it can be approximately satisfied under certain circumstances. The correlation length l of a distributed target represents the distance over which two points are likely to be correlated, implying that the currents induced at the two points due to an incident wave will likely be correlated as well. Thus, the correlation length may serve as the effective dimension of individual scatterers comprising the distributed target. The plane-wave approximation may be considered

Manuscript received February 6, 1992. This work was conducted under ARO Contract DAAL 03-91-G0202 and JPL Contract JPL-C-958749.

The authors are with the Radiation Laboratory, Department of Electrical Engineering and Computer Science, University of Michigan, Ann Arbor, MI 48109.

IEEE Log Number 9204943.

0018-926X/92$03.00 © 1992 IEEE

valid as long as the magnitude and phase variations of the incident wave are very small across a distance of several correlation lengths. In most practical situations, this "local" plane-wave approximation is almost always satisfied. When this is not the case, the measured radar response will depend on both the illumination pattern and the statistics of the distributed target [5], [6].

An implied assumption in the preceding discussion is that the phase variation across the antenna beam is the same for both the transmit and receive antennas. When making polarimetric measurements with dual-polarized transmit and receive antennas, the phase variation of the transmit and receive patterns may be different, which may lead to errors in the measurement of the scattering matrix of the target, unless the variations are known for all of the polarization combinations used in the measurement process and they are properly accounted for in the calibration process.

In this paper, we introduce a calibration procedure that accounts for magnitude and phase imbalances and antenna crosstalk across the entire main beam of the antenna. By applying this procedure, we can make accurate measurements of the differential Mueller matrix of a distributed target using the local plane-wave approximation. The differential Mueller matrix can then be used to compute the scattering coefficient for any desired combination of receive and transmit antenna polarizations, and by employing a recently developed technique [7], the statistics of the polarization phase differences can also be obtained. By way of illustrating the utility of the proposed measurement technique, we will compare the results of backscatter measurements acquired by a polarimetric scatterometer system for bare soil surfaces using the new technique with those based on calibrating the system with the traditional approach, which relies on measuring the response due to a calibration target placed along only the boresight direction of the antenna beam.

II. THEORY

Consider a planar distributed target illuminated by a polarimetric radar system as shown in Fig. 1. Suppose the distributed target is statistically homogeneous and the antenna beam is narrow enough so that the backscattering statistics of the target can be assumed constant over the illuminated area. Let us subdivide the illumination area into a finite number of pixels, each including many scatterers (or many correlation lengths), and denote the scattering matrix of the ijth pixel by $\Delta\bar{\bar{S}}(x_i, y_j)$. The scattering matrix of each pixel can be considered as a complex random vector. If the radar system and its antenna are ideal, the scattered field associated with the ijth pixel is related to the incident field by

$$\begin{bmatrix} E_v^s \\ E_h^s \end{bmatrix} = K\frac{e^{2ik_0 r(x_i, y_j)}}{r(x_i, y_j)^2}\begin{bmatrix} \Delta S_{vv}(x_i, y_j) & \Delta S_{vh}(x_i, y_j) \\ \Delta S_{hv}(x_i, y_i) & \Delta S_{hh}(x_i, y_j) \end{bmatrix}\begin{bmatrix} E_v^i \\ E_h^i \end{bmatrix} \tag{1}$$

where E_v and E_h are the components of the electric field along two orthogonal directions in a plane perpendicular

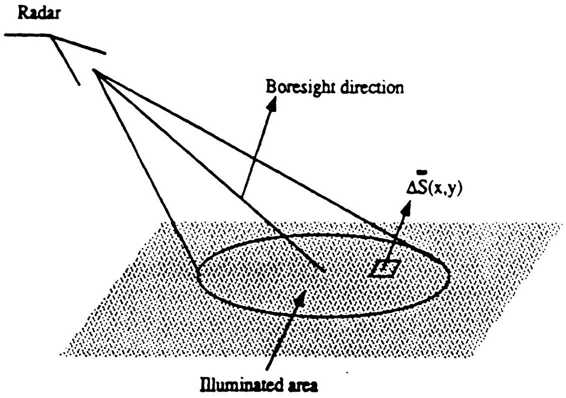

Fig. 1. Geometry of a radar system illuminating a homogeneous distributed target.

to the direction of propagation and K is a constant. In reality, radar systems are not ideal in the sense that the vertical and horizontal channels of the transmitter and receiver are not identical, and the radar antenna introduces some coupling between the vertical and horizontal signals at both transmission and reception. Consequently, the measured scattering matrix $\bar{\bar{U}}$ is related to the actual scattering matrix of a point target $\bar{\bar{S}}$ by [8]

$$\bar{\bar{U}} = \frac{e^{2ik_0 r}}{r^2}\bar{\bar{R}}\,\bar{\bar{S}}\,\bar{\bar{T}} \tag{2}$$

where $\bar{\bar{R}}$ and $\bar{\bar{T}}$ are known as the receive and transmit distortion matrices. For small point targets where the illumination pattern of the incident field can be approximated by a uniform plane wave, measurement of $\bar{\bar{S}}$ is rather straightforward, and in recent years, this problem has been investigated thoroughly by many investigators [9]–[11]. The distortion matrices are obtained by measuring one or more targets of known scattering matrices, and then by inverting (2), the scattering matrix of the unknown target is obtained. In the case of distributed targets, however, distributed calibration targets do not exist. Moreover, the distortion matrices and the distance to the scattering points are all functions of position. That is, for the ijth pixel, the measured differential scattering matrix $\Delta\bar{\bar{U}}$ can be expressed by

$$\Delta\bar{\bar{U}} = \frac{e^{2ik_0 r(x_i, y_j)}}{r^2(x_i, y_j)}\bar{\bar{R}}(x_i, y_j) \cdot \begin{bmatrix} \Delta S_{vv}(x_i, y_j) & \Delta S_{vh}(x_i, y_j) \\ \Delta S_{hv}(x_i, y_j) & \Delta S_{hh}(x_i, y_j) \end{bmatrix}\bar{\bar{T}}(x_i, y_j). \tag{3}$$

The radar measures the sum of fields backscattered from all pixels within the illuminated area coherently, i.e.,

$$\bar{\bar{U}} = \sum_i \sum_j \frac{e^{2ik_0 r(x_i, y_j)}}{r^2(x_i, y_j)}\bar{\bar{R}}(x_i, y_j)\Delta\bar{\bar{S}}(x_i, y_j)\bar{\bar{T}}(x_i, y_j). \tag{4}$$

Thus, the measured scattering matrix is a linear function of the random scattering matrices of the pixels. For uniform distributed targets, we are interested in deriving information about the statistics of the differential scattering matrix from statistics of the measured scattering matrix $\overline{\overline{\mathbf{U}}}$. One step in relating the desired quantities to the measured ones is to perform a calibration procedure to remove the distortions caused by the radar and the antenna systems. The traditional approach used for calibrating polarimetric measurements of extended-area targets relies on two approximations. First, it is assumed that for each measured sample, the differential scattering matrix of the illuminated area is equal to some equivalent scattering matrix at boresight. Using this approximation, it is hoped that the equivalent scattering matrix has the same statistics as the original differential scattering matrix. This approximation is purely heuristic and cannot be justified mathematically. Second, the measured data for each sample are calibrated as if they were a point target, and the result is modified by a constant known as the illumination integral to account for the nonuniform illumination [3], [4]; thus, the crosstalk variations away from the antenna's boresight direction over the illuminated area are ignored. The illumination integral accounts for only magnitude variations of the gain patterns of the transmitter and receiver antennas, and no provision is made for accounting for any possible phase variations in the radiation patterns.

In this paper, we attempt to derive the second moments of the differential scattering matrix from the statistics of the measured matrix without making any approximation in the radar distortion matrices or using the equivalent differential scattering matrix representation. In random polarimetry, the scattering characteristics of a distributed target usually are represented by its Mueller matrix, which is the averaged Stokes matrix [4]. The Mueller matrix contains the second moments of the scattering matrix elements. By the central limit theorem, if the scatterers in the illuminated area are numerous and are of the same type, then the statistics describing the scattering are Gaussian (Rayleigh statistics). In such cases, knowledge of the Mueller matrix is sufficient to describe the scattering statistics of the target [7].

In a manner analogous with the definition of the scattering coefficient as the scattering cross section per unit area, let us define the differential Mueller matrix $\overline{\overline{\mathbf{M}}}^o$ as the ratio of the Mueller matrix ($\Delta\overline{\overline{\mathbf{M}}}$) derived from the differential scattering matrix ($\Delta\overline{\overline{\mathbf{S}}}$) to the differential area, i.e.,

$$\overline{\overline{\mathbf{M}}}^o = \lim_{\Delta A \to 0} \frac{\Delta\overline{\overline{\mathbf{M}}}}{\Delta A}.$$

To compute the differential Mueller matrix, the ensemble average of the cross products of the differential matrix components is needed. Let us define

$$\overline{\overline{\mathbf{W}}}^o = \begin{bmatrix} \langle S_{vv}^{o*} S_{vv}^o \rangle & \langle S_{vh}^{o*} S_{vh}^o \rangle & \langle S_{vh}^{o*} S_{vv}^o \rangle & \langle S_{vv}^{o*} S_{vh}^o \rangle \\ \langle S_{hv}^{o*} S_{hv}^o \rangle & \langle S_{hh}^{o*} S_{hh}^o \rangle & \langle S_{hh}^{o*} S_{hv}^o \rangle & \langle S_{hv}^{o*} S_{hh}^o \rangle \\ \langle S_{hv}^{o*} S_{vv}^o \rangle & \langle S_{hh}^{o*} S_{vh}^o \rangle & \langle S_{hh}^{o*} S_{vv}^o \rangle & \langle S_{hv}^{o*} S_{vh}^o \rangle \\ \langle S_{vv}^{o*} S_{hv}^o \rangle & \langle S_{vh}^{o*} S_{hh}^o \rangle & \langle S_{vh}^{o*} S_{hv}^o \rangle & \langle S_{vv}^{o*} S_{hh}^o \rangle \end{bmatrix} \tag{5}$$

where

$$\langle S_{pq}^{o*} S_{st}^o \rangle = \lim_{\Delta A \to 0} \frac{\langle \Delta S_{pq}^* \, \Delta S_{st} \rangle}{\Delta A}.$$

In terms of the correlation matrix $\overline{\overline{\mathbf{W}}}^o$, the differential Mueller matrix can be computed from

$$\overline{\overline{\mathbf{M}}}^o = 4\pi\nu\overline{\overline{\mathbf{W}}}^o\nu^{-1} \tag{6}$$

where [4]

$$\nu = \begin{pmatrix} 1 & 0 & 0 & 0 \\ 0 & 1 & 0 & 0 \\ 0 & 0 & 1 & 1 \\ 0 & 0 & -i & i \end{pmatrix}.$$

In order to calibrate a radar system so as to measure the differential Mueller matrix, let us represent each 2 × 2 matrix in (4) by a corresponding four-component vector, in which case (4) simplifies to

$$\overline{\mathscr{U}} = \sum_i \sum_j \frac{e^{2ik_0 r(x_i, y_j)}}{r^2(x_i, y_j)} \overline{\overline{\mathbf{D}}}(x_i, y_j) \, \overline{\Delta\mathscr{S}}(x_i, y_j) \tag{7}$$

where

$$\overline{\mathscr{U}} = \begin{bmatrix} U_{vv} \\ U_{vh} \\ U_{hv} \\ U_{hh} \end{bmatrix}, \quad \overline{\Delta\mathscr{S}}(x_i, y_j) = \begin{bmatrix} \Delta S_{vv}(x_i, y_j) \\ \Delta S_{vh}(x_i, y_j) \\ \Delta S_{hv}(x_i, y_j) \\ \Delta S_{hh}(x_i, y_j) \end{bmatrix} \tag{8}$$

$$\overline{\mathscr{R}}(x_i, y_j) = \begin{bmatrix} R_{vv}(x_i, y_j) \\ R_{vh}(x_i, y_j) \\ R_{hv}(x_i, y_j) \\ R_{hh}(x_i, y_j) \end{bmatrix}, \quad \overline{\mathscr{T}}(x_i, y_j) = \begin{bmatrix} T_{vv}(x_i, y_j) \\ T_{vh}(x_i, y_j) \\ T_{hv}(x_i, y_j) \\ T_{hh}(x_i, y_j) \end{bmatrix}$$

and it can be easily shown that

$$\overline{\overline{\mathbf{D}}}(x_i, y_j) = \begin{bmatrix} R_{vv}T_{vv} & R_{vv}T_{vh} & R_{vh}T_{vv} & R_{vh}T_{vh} \\ R_{vv}T_{hv} & R_{vv}T_{hh} & R_{vh}T_{hv} & R_{vh}T_{hh} \\ R_{hv}T_{vv} & R_{hv}T_{vh} & R_{hh}T_{vv} & R_{hh}T_{vh} \\ R_{hv}T_{hv} & R_{hv}T_{hh} & R_{hh}T_{hv} & R_{hh}T_{hh} \end{bmatrix}. \tag{9}$$

The mth component of the measured target vector ($\overline{\mathscr{U}}_m$) defined by (8) can be obtained from (7), and is given by

$$\mathscr{U}_m = \sum_i \sum_j \frac{e^{2ik_0 r(x_i, y_j)}}{r^2(x_i, y_j)} \left[\sum_{l=1}^{4} D_{ml}(x_i, y_j) \Delta\mathscr{S}_l(x_i, y_j) \right].$$

Thus, the averaged cross products of these components are

$$\begin{aligned} \langle \mathscr{U}_m \mathscr{U}_n^* \rangle = {} & \sum_i \sum_j \sum_{i'} \sum_{j'} \frac{e^{2ik_0[r(x_i, y_j) - r(x_{i'}, y_{j'})]}}{r^2(x_i, y_j) r^2(x_{i'}, y_{j'})} \\ & \cdot \sum_{l=1}^{4} \sum_{p=1}^{4} D_{ml}(x_i, y_j) D_{np}^*(x_{i'}, y_{j'}) \\ & \left\langle \Delta\mathscr{S}_l(x_i, y_j) \Delta\mathscr{S}_p^*(x_{i'}, y_{j'}) \right\rangle. \end{aligned} \tag{10}$$

If the number of scatterers in each pixel is assumed to be large, or the correlation length of the surface is much smaller than the pixel dimensions, then

$$\langle \Delta\mathscr{S}_l(x_i, y_j)\Delta\mathscr{S}_p^*(x_{i'}, y_{j'})\rangle = \begin{cases} 0, & i \neq i' \text{ and } j \neq j' \\ \langle \mathscr{S}_l^o \mathscr{S}_p^{o*}\rangle \Delta A_{ij}, & i = i' \text{ and } j = j'. \end{cases}$$

It should be mentioned here again that the target is assumed to be statistically homogeneous, and the antenna beam is assumed to have a narrow beam. Hence, $\langle \mathscr{S}_l^o \mathscr{S}_p^{o*}\rangle$ is not a function of position within the illuminated area. In the limit as ΔA approaches zero, (10) takes the following form:

$$\langle \mathscr{U}_m \mathscr{U}_n^*\rangle = \sum_{l=1}^{4}\sum_{p=1}^{4}\left[\iint_A \frac{1}{r^4(x,y)} D_{ml}(x,y) \cdot D_{np}^*(x,y)\,dx\,dy\right]\langle \mathscr{S}_l^o \mathscr{S}_p^{o*}\rangle. \tag{11}$$

Equation (11) is valid for all combinations of m and n and, therefore, it constitutes 16 equations for the 16 correlation unknowns. Let us denote the measured correlations by a 16-component vector $\bar{\mathscr{Y}}$, and the actual correlations by another 16-component vector $\bar{\mathscr{X}}$ so that

$$\mathscr{X}_i = \langle \mathscr{S}_l^o \mathscr{S}_p^{o*}\rangle, \qquad i = 4(l-1) + p$$

$$\mathscr{Y}_j = \langle \mathscr{U}_m \mathscr{U}_n^*\rangle, \qquad j = 4(m-1) + n.$$

In this form, (11) reduces to the following matrix equation:

$$\bar{\mathscr{Y}} = \bar{\bar{\mathbf{B}}}\bar{\mathscr{X}} \tag{12}$$

where the ij element of $\bar{\bar{\mathbf{B}}}$ is given by

$$b_{ij} = \iint_A \frac{1}{r^4(x,y)} D_{ml}(x,y) D_{np}^*(x,y)\,dx\,dy \tag{13}$$

and, as before,

$$i = 4(l-1) + p, \qquad j = 4(m-1) + n.$$

Once the elements of the correlation calibration matrix $\bar{\bar{\mathbf{B}}}$ are found from (13), (12) can be inverted to obtain the correlation vector $\bar{\mathscr{X}}$. The elements of the correlation vector are not arbitrary complex numbers; for example, $\mathscr{X}_2$ and $\mathscr{X}_5$ are complex conjugate of each other and $\mathscr{X}_1$ is a real number; thus, these relationships can be used as a criterion for calibration accuracy. The differential Mueller matrix can be obtained from the correlation matrix $\bar{\bar{\mathbf{W}}}^o$ whose entries in terms of the vector $\bar{\mathscr{X}}$ are given by

$$\bar{\bar{\mathbf{W}}}^o = \begin{bmatrix} \mathscr{X}_1 & \mathscr{X}_6 & \mathscr{X}_2 & \mathscr{X}_5 \\ \mathscr{X}_{11} & \mathscr{X}_{16} & \mathscr{X}_{12} & \mathscr{X}_{15} \\ \mathscr{X}_3 & \mathscr{X}_8 & \mathscr{X}_4 & \mathscr{X}_7 \\ \mathscr{X}_9 & \mathscr{X}_{14} & \mathscr{X}_{10} & \mathscr{X}_{13} \end{bmatrix}.$$

Evaluation of the elements of $\bar{\bar{\mathbf{B}}}$ requires knowledge of the radar distortion matrices over the main lobe of the antenna system. The distortion matrices of the radar can be found by applying the calibration method presented in the next section.

III. CALIBRATION PROCEDURE

As was shown in the previous section, the correlation vector $\bar{\mathscr{X}}$ can be obtained if the calibration matrix $\bar{\bar{\mathbf{D}}}(x, y)$ given by (9) is known. A simplified block diagram of a radar system is shown in Fig. 2. The quantities $\bar{t}_v, \bar{t}_h, \bar{r}_v, \bar{r}_h$ represent fluctuating factors of the channel imbalances caused by the active devices in the radar system. Without loss of generality, it is assumed that the nominal value of these factors is one, and their rate of change determines how often the radar must be calibrated. The antenna system also causes some channel distortion due to variations in the antenna pattern and path length differences. The crosstalk contamination occurs in the antenna structure, which is also a function of the direction of radiation. It has been shown that the antenna system, together with two orthogonal directions in a plane perpendicular to the direction of propagation, can be represented as a four-port passive network [8]. Using the reciprocity properties of passive networks, the distortion matrices of the antenna system were shown to be [8]

$$\bar{\bar{\mathscr{R}}}_a(\psi, \xi) = \begin{bmatrix} r_v(\psi,\xi) & 0 \\ 0 & r_h(\psi,\xi) \end{bmatrix}\begin{bmatrix} 1 & C(\psi,\xi) \\ C(\psi,\xi) & 1 \end{bmatrix} \tag{14}$$

$$\bar{\bar{\mathscr{T}}}_a(\psi, \xi) = \begin{bmatrix} 1 & C(\psi,\xi) \\ C(\psi,\xi) & 1 \end{bmatrix}\begin{bmatrix} t_v(\psi,\xi) & 0 \\ 0 & t_h(\psi,\xi) \end{bmatrix} \tag{15}$$

where ψ, ξ are some coordinate angles defined with respect to the boresight direction of propagation. The quantity $C(\psi, \xi)$ is the antenna crosstalk factor and $r_v(\psi, \xi), r_h(\psi, \xi), t_v(\psi, \xi), t_h(\psi, \xi)$ are the channel imbalances caused by the antenna system. These quantities are not subject to change due to variations in active devices, and once they are determined, they can be used repeatedly.

In order to find the radar distortion parameters at a given point (x, y) on the surface, we first need to specify a convenient coordinate system with respect to the antenna's boresight direction so that the distortions become independent of incidence angle and range to the target. The azimuth-over-elevation coordinate angles (ψ, ξ) provide a coordinate system that is appropriate for antenna pattern measurements. The angle ξ specifies the elevation angle and ψ specifies the azimuth angle in a plane with elevation ξ, as shown in Fig. 3. The mapping from (ψ, ξ) coordinates to (x, y) coordinates can be obtained by considering a radar at height h with incidence angle θ_0 and the boresight direction in the y–z plane, as shown in Fig. 4. It is easy to show that constant-ξ curves on the surface of a sphere map to constant-y lines and constant-ψ curves map to hyperbolic curves. The mapping functions are

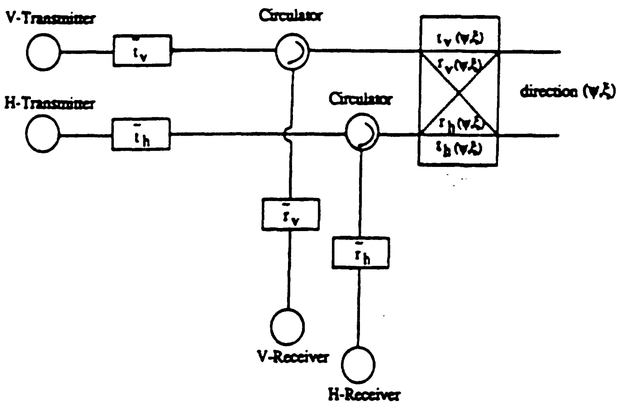

Fig. 2. Simplified block diagram of a polarimetric radar system.

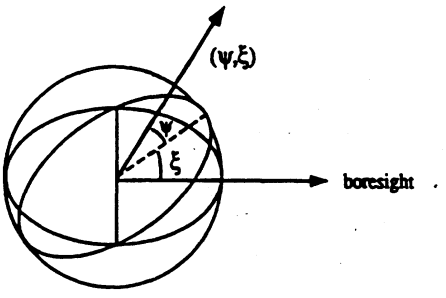

Fig. 3. Azimuth-over-elevation coordinate system (ψ, ξ) specifying a point on the surface of a sphere.

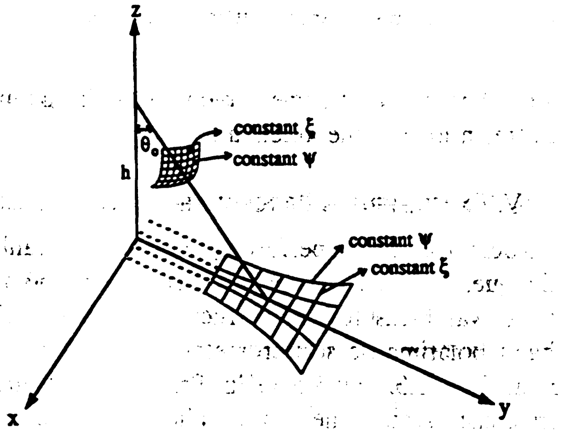

Fig. 4. Geometry of a radar above x–y plane and transformation of azimuth-over-elevation coordinate to Cartesian coordinate.

given by

$$x = \frac{h \tan \psi}{\cos(\theta_0 + \xi)}$$

$$y = h \tan(\theta_0 + \xi)$$

where $\psi = \xi = 0$ represents the boresight direction.

The entries of the calibration matrix $\bar{\bar{D}}(\psi, \xi)$ as defined by (9) should be obtained through a calibration procedure. Following the single-target calibration technique given in [8], a single sphere is sufficient to determine the channel imbalances as well as the antenna crosstalk factor for a given direction. Hence, by placing a sphere with radar cross section σ^s at a distance r_0 and a direction (ψ, ξ) with respect to the radar, the receive and transmit distortion parameters can be obtained as follows:

$$R_{vv}T_{vv} = r_0^2 e^{-2ik_0r_0} \frac{U^s_{vv}}{(1 + C^2)\sqrt{\sigma^s/4\pi}}$$

$$\beta \triangleq \frac{R_{hh}}{R_{vv}} = \frac{2C}{(1 + C^2)} \frac{U^s_{hh}}{U^s_{vh}}$$

$$\alpha \triangleq \frac{T_{hh}}{T_{vv}} = \frac{1 + C^2}{2C} \frac{U^s_{vh}}{U^s_{vv}}$$

$$C = \pm\frac{1}{\sqrt{a}}(1 - \sqrt{1 - a}) \tag{16}$$

where

$$a \triangleq \frac{U^s_{vh}U^s_{hv}}{U^s_{vv}U^s_{hh}}$$

and $\bar{\bar{U}}^s$ is the measured (uncalibrated) response of the sphere at a specific direction (ψ, ξ). In terms of the known quantities given by (16), the calibration matrix $\bar{\bar{D}}$ can be written as

$$\bar{\bar{D}}(\psi, \xi) = R_{vv}T_{vv} \begin{bmatrix} 1 & C\alpha & C & C^2\alpha \\ C & \alpha & C^2 & C\alpha \\ C\beta & C^2\alpha\beta & \beta & C\alpha\beta \\ C^2\beta & C\alpha\beta & C\beta & \alpha\beta \end{bmatrix} \tag{17}$$

where the dependences on ψ and ξ of all parameters i understood.

In practice, it is impossible to measure the sphere fo all values of ψ and ξ within the desired domain; however by discretizing the domain of ψ and ξ (main lobe) int sufficiently small subdomains over which the antenn characteristics are almost constant, the integral given b (13) can be evaluated with good accuracy.

Polarimetric measurement of a sphere over the entir range of ψ and ξ is very time consuming, and under fiel conditions, performing these measurements seems impossible. However, this measurement can be performed in a anechoic chamber with the desired resolution $\Delta\psi$ and Δ only once, and then under field conditions, we need t measure the sphere response only at boresight to kee track of variations in the active devices. Without loss o generality, let us assume that $\bar{r}_v = \bar{r}_h = \bar{t}_v = \bar{t}_h = 1$ for th sphere measurements when performed in the anechoi chamber, and that these quantities can assume othe values for the measurements made under field condition If the measured distortion parameters at boresight (fiel condition) are denoted by prime and calculated from (16 then the channel imbalances corresponding to the fiel

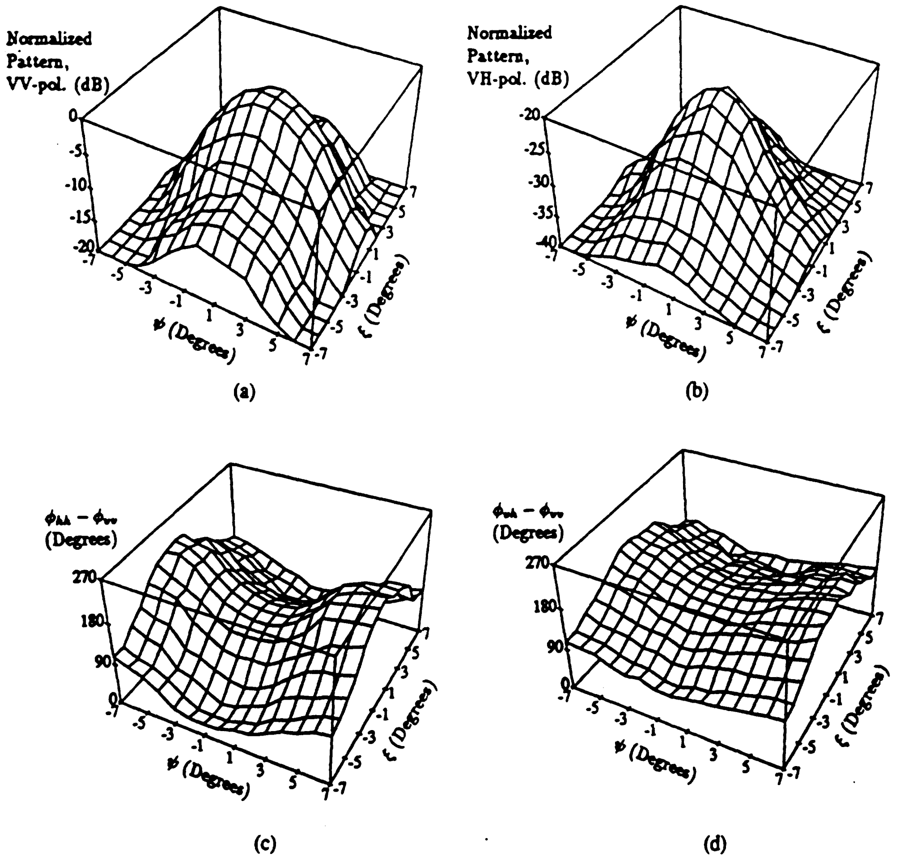

(a) (b)

(c) (d)

Fig. 5. Polarimetric response of a metallic sphere over the entire mainlobe of X-band scatterometer; normalized σ_{vv} (a) corresponds to G_v^2 and normalized σ_{vh} (b) corresponds to G_vG_h; phase difference between copolarized (c) and cross-polarized (d) components of the sphere response correspond to phase variation of the co- and cross-polarized patterns of the antenna.

measurements are

$$\bar{r}_v\bar{t}_v = \left(\frac{r_0'}{r_0}\right)^2 e^{-2ik_0(r_0'-r_0)}\frac{R'_{vv}(0,0)T'_{vv}(0,0)}{R_{vv}(0,0),T_{vv}(0,0)}$$

$$\frac{\bar{t}_h}{\bar{t}_v} = \frac{T'_{hh}(0,0)}{T'_{vv}(0,0)}\cdot\frac{T_{vv}(0,0)}{T_{hh}(0,0)}$$

$$\frac{\bar{r}_h}{\bar{r}_v} = \frac{R'_{hh}(0,0)}{R'_{vv}(0,0)}\cdot\frac{R_{vv}(0,0)}{R_{hh}(0,0)}. \tag{18}$$

Now, the calibration matrix at any direction ($\bar{\bar{\mathbf{D}}}'(\psi, \xi)$) can be obtained from (17) by replacing $R_{vv}T_{vv}$, α, and β by $R'_{vv}T'_{vv}$, α', and β' where

$$R'_{vv}T'_{vv} = \bar{r}_v\bar{t}_vR_{vv}T_{vv}$$

$$\alpha' = \frac{\bar{t}_h}{\bar{t}_v}\alpha$$

$$\beta' = \frac{\bar{r}_h}{\bar{r}_v}\beta. \tag{19}$$

Having found the calibration matrices for all subdomains, the element ij of the correlation–calibration matrix ($\bar{\bar{\mathbf{B}}}$), as given by (13), in the azimuth-over-elevation coordinate system takes the following form:

$$b_{ij} = \int\int_{\Omega} D_{ml}(\psi, \xi)D^*_{np}(\psi, \xi) \cdot\frac{\cos^2\psi\cos(\theta_0+\xi)}{h^2}\,d\psi\,d\xi \tag{20}$$

where Ω is the solid angle subtented by the illuminated area (main lobe of the antenna).

IV. Experimental Procedure and Comparison

To demonstrate the performance of the new calibration technique, the polarimetric response of a random rough surface was measured by a truck-mounted L-, C-, and X-band polarimetric scatterometer with center frequencies at 1.25, 5.3, and 9.5 GHz. Prior to these measurements, each scatterometer was calibrated in an anechoic chamber. The scatterometer was mounted on an azimuth-over-elevation positioner at one end of the chamber, and a 36 cm metallic sphere was positioned at the antenna boresight at a distance of 12 m. Then the polarimetric response of the sphere was measured over the mainlobe of the antenna. The sphere measurements at L-band, which has the widest beam of the three systems, was performed over $(\psi, \xi) \in [-21°, +21°]$ in steps of 3°, and the ranges of (ψ, ξ) for C- and X-band were $\pm 10.5°$ and $\pm 7°$ with steps of 1.5° and 1°, respectively. To improve the signal-to-noise ratio by removing the background contribution, the chamber in the absence of the sphere was also measured for all values of ψ and ξ.

Fig. 5(a) and (b) shows the co- and cross-polarized responses of the sphere at X-band, and Fig. 5(c) and (d) shows the co- and cross-polarized phase differences ($\phi_{hh} - \phi_{vv}$, $\phi_{hv} - \phi_{vv}$). Similar patterns were obtained for the L- and C-band. Using the sphere responses, the

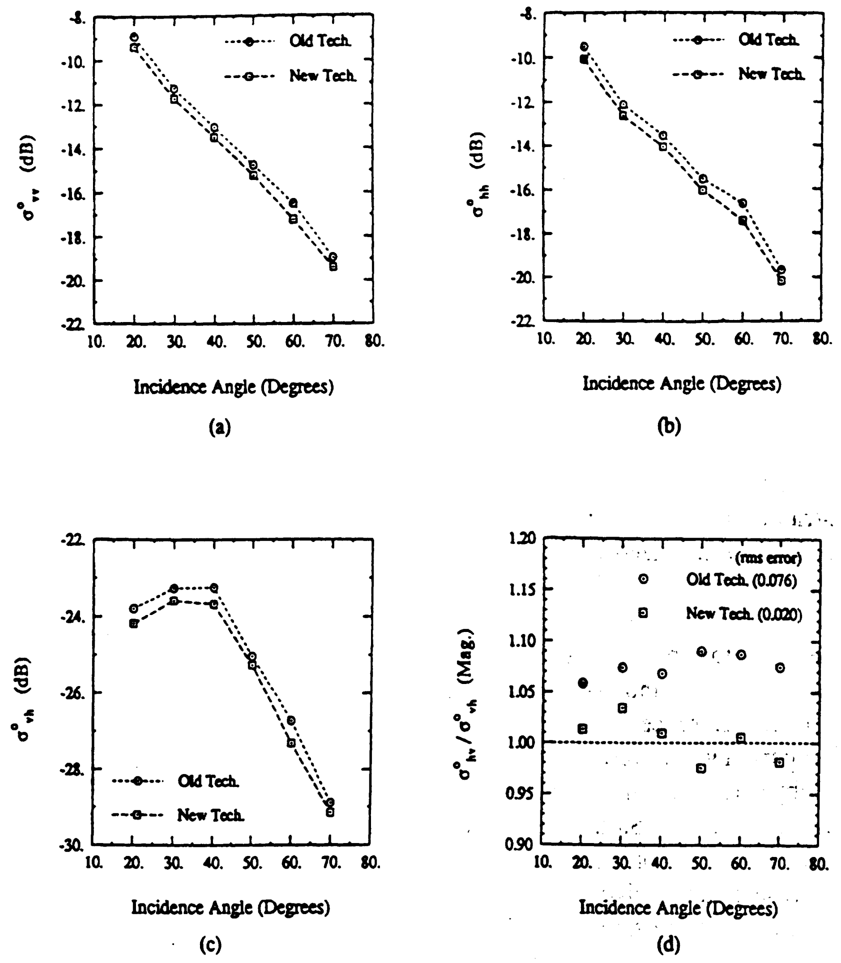

(a) (b) (c) (d)

Fig. 6. Comparison between the new and old calibration techniques applied to the X-band measured backscatter from a bare soil surface. (a), (b), and (c) show the difference in the co- and cross-polarized backscattering coefficients, and (d) demonstrates the enhancement in the ratio of the cross-polarized backscattering coefficients obtained by the new method.

correlation-calibration matrices were determined as outlined in the previous section.

To evaluate the improvement provided by the new calibration technique, we shall compare results of polarimetric observations of a bare soil surface processed using the new technique with those obtained previously on the basis of the boresight-only calibration technique. The data were acquired from a truck-mounted 17-m-high platform for a rough surface with a measured rms height of 0.56 cm and a correlation length of 8 cm. The polarimetric backscatter response was measured as a function of incidence angle over the range 20°–70°. To reduce the effect of speckle on the measured data, 100 spatially independent samples were measured at each frequency and incidence angle. Also, the response of the sphere at the boresight was measured to account for any possible changes in the active devices. The collected backscatter data were calibrated by the new and old methods. The first test of accuracy of the new calibration algorithm was to make sure that the components of the correlation vector $\mathscr{X}$ satisfy their mutual relationships, as explained in Section II. For all cases, these relationships were found to be valid within ±0.05%.

The second step in the evaluation process is the relative comparison of the backscattering coefficients and phase statistics derived from the two techniques. Fig. 6(a)–(c) shows the co- and cross-polarized backscattering coefficients as a function of incidence angle, calibrated by the old and the new methods. The differences in backscattering coefficients, as shown in these figures, are less than 0.75 dB. It was found that the difference in backscattering coefficients is less than 1 dB for all frequencies anc incidence angles. Although 1 dB error in σ° may seem negligible, in some cases, such as the variation with soi moisture content for which the total dynamic range of σ° is about 5 dB, the 1 dB error becomes significant. Fig. 6(d shows the ratio of two cross-polarized scattering coefficients after calibration by each of the two methods. Theoretically, this ratio must be one and independent of incidence angle. In this figure, it is shown that the new calibration method more closely agrees with theoretica expectations than the old method.

The third step involves a comparison of the phase difference statistics of the distributed target. It has been shown that when the dimensions of the antenna footprin are much larger than the correlation length, the probability density function (pdf) of the phase differences can b expressed in terms of two parameters: the degree c correlation (α) and the polarized phase difference (ζ) [7 The degree of correlation is a measure of the width of th pdf, and the polarized phase difference represents the phase difference at which the pdf is maximum. These parameters can be computed directly from the components of the Mueller matrix and are given by [7]

$$\alpha = \frac{1}{2}\sqrt{\frac{(\mathcal{M}_{33}+\mathcal{M}_{44})^2+(\mathcal{M}_{34}-\mathcal{M}_{43})^2}{\mathcal{M}_{11}\mathcal{M}_{22}}}$$

$$\zeta = \tan^{-1}\left(\frac{\mathcal{M}_{34}-\mathcal{M}_{43}}{\mathcal{M}_{33}+\mathcal{M}_{44}}\right).$$

Parameter α varies from zero to one, where zero corresponds to a uniform distribution and one corresponds to a delta-function distribution (fully polarized wave). Parameter ζ varies between $-180°$ and $180°$.

Fig. 7(a)–(c) shows the degree of correlation calculated by the new and old methods for the copolarized phase difference ($\phi_{hh}-\phi_{vv}$) at the L-, C-, and X-band, respectively. There is a significant difference between the two methods in all cases. The partially polarized backscattered Stokes vector obtained by the old calibration method appears more unpolarized than the Stokes vector obtained by the new method. The virtue of this result can be checked in the limiting case if an analytical solution is available. A first-order solution of the small perturbation method for slightly rough surfaces shows that the backscatter signal is fully polarized, and therefore, the pdf of the copolarized phase difference is a delta function, corresponding to $\alpha = 1$. The roughness parameters of the surface under investigation falls within the validity region of the small perturbation method at L-band. The value of α at L-band derived from the new calibration method is in much closer agreement with theoretical expectations than the value obtained by the old method. Fig. 8(a)–(c) shows plots of the copolarized phase difference at the L-, C-, and X-band, respectively. At the L- and X-bands, the value of ζ obtained by the two methods are positive and not very different from each other. Also, it noted that ζ has a positive slope with incidence angle. However, this is not the case for the C-band; the value of ζ obtained by the old method is negative, has a negative slope, while the behavior of ζ obtained by the new method is very similar to that at the other two frequencies. This deviation is due to the large variation of phase difference between the V- and H-channels of the C-band radar over the illumination area, and since the old method does not account for phase variations, it is incapable of correcting the resulting errors. Similar results were observed for the statistics of the cross-polarized phase difference ($\phi_{hv}-\phi_{vv}$).

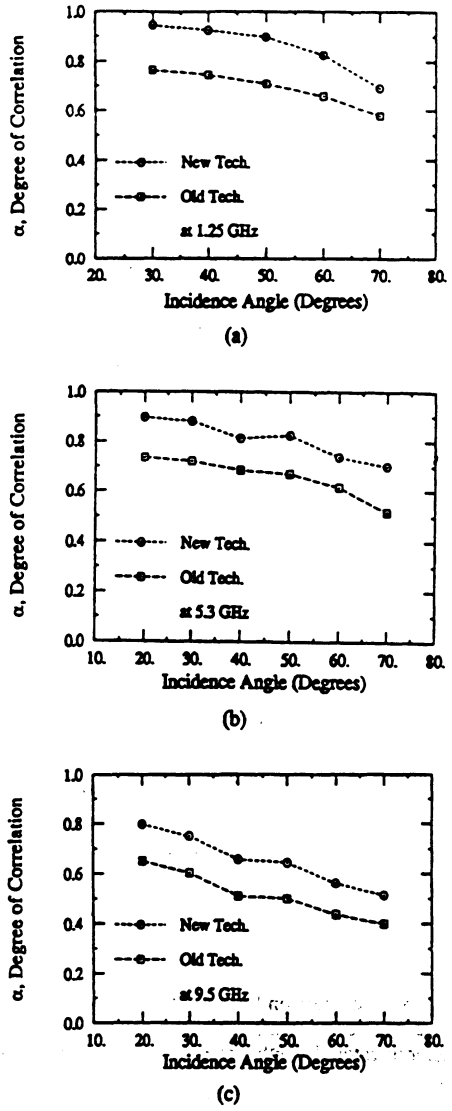

Fig. 7. Degree of correlation for copolarized components of the scattering matrix for the L-band (a), C-band (b), and X-band (c).

V. CONCLUSIONS

A rigorous method is presented for calibrating polarimetric backscatter measurements of distributed targets. By characterizing the radar distortions over the entire mainlobe of the antenna, the differential Mueller matrix is derived from the measured scattering matrices with a high degree of accuracy. It is shown that the radar distortions can be determined by measuring the polarimetric response of a metallic sphere over the main lobe of the antenna. The radar distortions are categorized into two groups, namely, distortions caused by the active devices, and distortions caused by the antenna structure (passive). Since passive distortions are immune to changes once they are determined, they can be used repeatedly. The active distortions can be obtained by measuring the sphere response only at boresight, thereby reducing the time required for calibration under field conditions. The calibration algorithm was applied to backscatter data collected from a rough surface by L-, C-, and X-band scatterometers. Comparison of results obtained with the new algorithm with the results derived from the old calibration method show that the discrepancy between the two methods is less 1 dB for the backscattering coefficients. The discrepancy, however, is more drastic for the phase-difference statistics, indicating that removal of the radar distortions from the cross products of the scattering matrix elements (differential Mueller matrix elements)

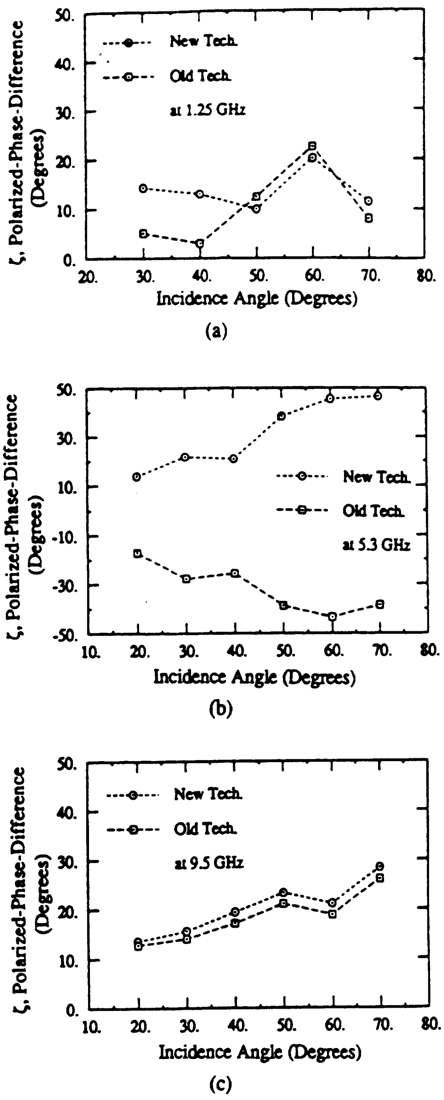

Fig. 8. Polarized phase difference for copolarized components of the scattering matrix for the L-band (a), C-band (b), and X-band (c).

cannot be accomplished with the traditional calibration methods.

REFERENCES

[1] F. T. Ulaby, R. K. Moore, and A. K. Fung, *Microwave Remote Sensing: Active and Passive, Vol. II—Radar Remote Sensing and Scattering Emission Theory.* Dedham, MA: Artech House, 1986.

[2] K. Sarabandi, Y. Oh, and F. T. Ulaby, "Polarimetric radar measurements of bare soil surfaces at microwave frequencies," in *Proc. IEEE Geosci. Remote Sensing Symp.*, Espoo, Finland, June 1991.

[3] M. A. Tassoudji, K. Sarabandi, and F. T. Ulaby, "Design consideration and implementation of the LCX polarimetric scatterometer (POLARSCAT)," Radiation Lab. Rep. 022486-T-2, Univ. Michigan, Ann Arbor, June 1989.

[4] F. T. Ulaby and C. Elachi, *Radar Polarimetry for Geoscience Applications.* Dedham, MA: Artech House, 1990.

[5] H. J. Eom and W. M. Boerner, "Rough surface incoherent backscattering of spherical wave," *IEICE Trans.*, vol. E 74, Jan. 1991.

[6] A. K. Fung and H. J. Eom, "Coherent scattering of spherical wave from an irregular surface," *IEEE Trans. Antennas Propagat.*, vol. AP-31, Jan. 1983.

[7] K. Sarabandi, "Derivation of phase statistics from the Mueller matrix," *Radio Sci.*, vol. 27, Sept.–Oct. 1992.

[8] K. Sarabandi and F. T. Ulaby, "A convenient technique for polarimetric calibration of radar systems," *IEEE Trans. Geosci. Remote Sensing*, vol. 28, Nov. 1990.

[9] R. M. Barnes, "Polarimetric calibration using in-scene reflectors," Rep. TT.65, M.I.T. Lincoln Lab., Lexington, MA, Sept. 1986.

[10] M. W. Whitt, F. T. Ulaby, P. Polatin, and V .V. Liepa, "A general polarimetric radar calibration technique," *IEEE Trans. Antennas Propagat.*, vol. 39, Jan. 1991.

[11] K. Sarabandi, F. T. Ulaby, and M. A. Tassoudji, "Calibration of polarimetric radar systems with good polarization isolation," *IEEE Trans. Geosci. Remote Sensing*, vol. 28, Jan. 1990.

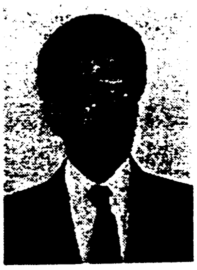

Kamal Sarabandi (S'87–M'90) was born in Tehran, Iran, on November 4, 1956. He received the B.S. degree in electrical engineering from Sharif University of Technology, Tehran, Iran, in 1980. He entered the graduate program at the University of Michigan in 1984, and received the M.S.E. degree in electrical engineering in 1986, and the M.S. degree in mathematics and the Ph.D. degree in electrical engineering in 1989.

From 1980 to 1984 he worked as a Microwave Engineer in the Telecommunication Research Center in Iran. He is presently an Assistant Professor in the Department of Electrical Engineering and Computer Science, University of Michigan. His research interests include electromagnetic scattering, microwave remote sensing, and calibration of polarimetric SAR systems.

Dr. Sarabandi is a member of the Electromagnetics Academy and USNC/URSI Commission F.

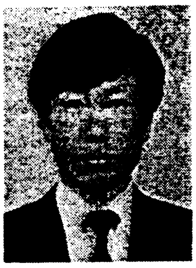

Yisok Oh (S'88) received the B.S. degree in electrical engineering from Yonsei University, Seoul, Korea, in 1982, and the M.S. degree in electrical engineering from the University of Missouri, Rolla, in 1988.

He is currently working towards the Ph.D. degree in electrical engineering at the University of Michigan, Ann Arbor, where he is a Research Assistant with the Radiation Laboratory. His research interests include microwave remote sensing, with an emphasis on the interface between experimental measurements and theoretical models for electromagnetic wave scattering from earth terrain.

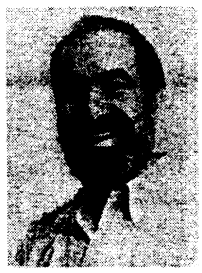

Fawwaz T. Ulaby (M'68–SM'74–F'80) received the B.S. degree in physics from the American University of Beirut, Lebanon, in 1964 and the M.S.E.E. and Ph.D. degrees in electrical engineering from the University of Texas, Austin, in 1966 and 1968, respectively.

He is currently a Professor of Electrical Engineering and Computer Science at the University of Michigan, Ann Arbor, and Director of the NASA Center for Space Terahertz Technology. His current interests include microwave and millimeter-wave remote sensing, radar systems, and radio wave propagation. He has authored several books and published over 400 papers and reports on these subjects.

Dr. Ulaby is the recipient of numerous awards, including the IEEE Geoscience and Remote Sensing Distinguished Achievement award in 1983, the IEEE Centennial Medal in 1984, the Kuwait Prize in Applied Science in 1986, and the NASA Achievement Award in 1990.

An Empirical Model and an Inversion Technique for Radar Scattering from Bare Soil Surfaces

Yisok Oh, Kamal Sarabandi, *Member, IEEE*, and Fawwaz T. Ulaby, *Fellow, IEEE*

Abstract— **Polarimetric radar measurements were conducted for bare soil surfaces under a variety of roughness and moisture conditions at L-, C-, and X-band frequencies at incidence angles ranging from 10° to 70°. Using a laser profiler and dielectric probes, a complete and accurate set of ground truth data were collected for each surface condition, from which accurate measurements were made of the rms height, correlation length, and dielectric constant. Based on knowledge of the scattering behavior in limiting cases and the experimental observations, an empirical model was developed for σ°_{hh}, σ°_{vv}, and σ°_{hv} in terms of ks (where $k = 2\pi/\lambda$ is the wave number and s is the rms height) and the relative dielectric constant of the soil surface. The model, which was found to yield very good agreement with the backscattering measurements of this study as well as with measurements reported in other investigations, was used to develop an inversion technique for predicting the rms height of the surface and its moisture content from multipolarized radar observations.**

I. INTRODUCTION

Investigation of the radar backscattering response of natural surfaces is an important problem in remote sensing because of its potential in retrieving the desired physical parameters of the surface, namely, its soil moisture content and surface roughness. Although the problem of electromagnetic wave scattering from random surfaces has been investigated for many years, because of its complexity theoretical solutions exist only for limiting cases. When the surface profile deviates only slightly from that of a smooth surface, perturbation solutions can be used. In the classic treatment of the small perturbation method (SPM) [1], [2] it is required that the rms height be much smaller than the wavelength and the rms slope be on the same order of magnitude as the wavenumber times the rms height. Recently, a perturbation method based on perturbation expansion of the phase of the surface field (PPM) was developed which extends the region of validity of SPM to higher values of the rms height s, provided the slope remains relatively small [3]. The other limiting case is when surface irregularities are large compared to the wavelength, which is equivalent to having a large radius of curvature at each point on the surface. In this limit, the Kirchhoff approximation (KA) is applicable [4], [5]. Various types of modifications and improvements to this model can be found in the literature. In these papers, the effects of shadowing and multiple scattering are discussed, which basically extend the region of validity of the KA solution, but by only a limited extent [6]. Combined solutions of KA and SPM, which are applicable for composite surfaces, have basically the same regions of validity as the individual models [7].

At microwave frequencies many natural surfaces do not fall into the validity regions of the theoretical models, and even when they do, the available models fail to provide results in good agreement with experimental observations. This assertion will be demonstrated by the results of the present study. The major goal of this investigation is to determine the dependence of the radar backscatter on the roughness parameters and soil moisture content of natural surfaces through extensive backscatter measurements for a variety of moisture and roughness conditions, over a wide range of incidence angles and frequencies. Once the dependence of the radar backscatter on these parameters has been established, an empirical model can be used to retrieve the surface roughness and soil moisture content from measured radar data.

The radar measurements reported in this study were obtained by a truck-mounted network-analyzer-based scatterometer (LCX POLARSCAT) [8]. The data were recorded in a fully polarimetric format at L-, C-, and X-band frequencies at incidence angles ranging from 10° to 70°. An empirical model was formulated using the magnitudes of the measured data, and another data set was used to verify the model performance. Excellent qualitative and reasonable quantitative agreements were obtained. The polarimetric measurements included recordings of the phase statistics of the backscattered signal, but these will not be discussed in this paper as they are the subject of a separate report.

II. EXPERIMENTAL PROCEDURE

Fig. 1 shows a diagram of the scatterometer system and drawings of the laser profiler and dielectric probe. A brief description of each follows.

A. Scatterometer

The University of Michigan's LCX POLASCAT [8] was designed with the capability to measure the scattering matrix of point or distributed targets at L-, C- and X-band (with center frequencies at 1.25, 4.75, and 9.5 GHz, respectively). The scatterometer consists of an automatic vector network analyzer (HP 8753A), a computer unit, a disk drive for data storage, an amplifying and pulsing circuitry for hardware range gating, a relay actuator, and L-, C-, and X-band RF

Manuscript received June 1, 1991; revised September 26, 1991. This work was supported by NASA under grant NAGW-2151.

The authors are with the Radiation Laboratory, Department of Electrical Engineering and Computer Science, the University of Michigan, Ann Arbor, MI 48109-2122.

IEEE Log Number 9105684.

TABLE I
POLARIMETRIC SCATTEROMETER (POLARSCAT) CHARACTERISTICS

	L	*C*	*X*
Center Frequency	1.50 GHz	4.75 GHz	9.50 GHz
Frequency Bandwidth	0.3 GHz	0.5 GHz	0.5 GHz
Antenna Type	Dual Polarized Pyramidal Horn		
Antenna Gain	22.1 dB	25.3 dB	29.5 dB
Antenna Beamwidth	12.0°	8.0°	5.4°
Far Field ($2d^2/\lambda$)	8.5 m	5.8 m	10.5 m
Platform Height	18 m	18 m	18 m
Cross-pol Isolation†	45 dB	45 dB	45 dB
Calibration Accuracy	±0.3 dB	±0.3 dB	±0.3 dB
Measurement Precision ($N > 100$)	±0.4 dB	±0.4 dB	±0.4 dB
Phase Accuracy†	±3°	±3°	±3°

†After polarimetric calibration using STCT [9].

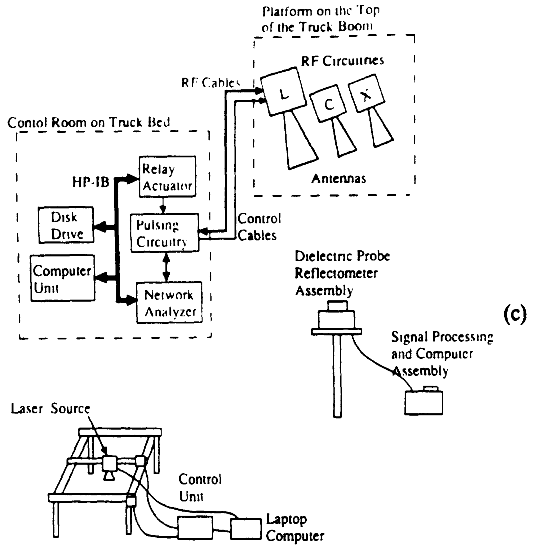

Fig. 1. Experimental system: (a) Scatterometer block diagram. (b) Laser profile meter. (c) Dielectric probe.

circuits and antennas, as shown in Fig. 1. The antennas are dual-polarized with orthogonal mode transducers (OMT) used for simultaneous transmission of a V-polarized signal and reception of both the V- and H- components of the backscattered signal. The process is then repeated for an H-polarized transmitted signal.

A computer is used to control the network analyzer (through an HP-IB interface bus) to acquire the desired data automatically. The computer also controls a relay actuator which energizes the desired frequency and polarization switches. Table I contains a list of the basic characteristics of the scatterometers, including specifications of the center frequencies, bandwidths, antenna characteristics, and overall performance.

To achieve good statistical representation of the measured backscatter for distributed targets, a large number of spatially independent samples are required. In this experiment 90 and 60 independent samples were taken at incidence angles of 10°, 20°, 30° and 40°, 50°, 60°, 70°, respectively. To achieve good range resolution, and also to increase the number of independent samples, the measurements were performed over bandwidths of 0.3 GHz for *L*-band and 0.5 GHz for *C*- and *X*-band. By treating the backscattering coefficient as constant over the mentioned bandwidths, the total number of independent samples represented by each measurement of the scattering coefficient σ°, including those achieved through frequency averaging, exceeds 1000 at most incidence angles.

In addition to the soil backscatter data, the noise background level was measured by pointing the antennas toward the sky. The noise background level was subtracted from the soil backscatter data coherently to improve the signal to noise ratio. The polarimetric response of a conducting sphere was measured to achieve absolute calibration of the radar system [9]. To minimize the time elapsed between the four polarization measurements comprising a single polarimetric data set, the soil backscatter data were collected in a raw-data format. The radar data was then postprocessed to separate the unwanted short-range returns from the target return using the time domain gating capability. The gated target response was then calibrated using the sphere data.

B. Laser Profile Meter

The height profiles of the soil surfaces were measured by a laser profile meter mounted on an *XY*-table, as shown in Fig. 1. The laser profiler, which is driven by a stepper motor, can measure a surface profile with 1 mm horizontal resolution and 2 mm vertical accuracy. A laptop computer is connected to the stepper-motor controllers to position the laser distance meter with the desired steps in the *X* and *Y* directions. The heights measured by the laser profiler are also collected and stored by the same computer. A minimum of ten 1-m profiles were collected for each surface with steps of 0.25 cm in the horizontal direction. In addition to the surface profiles acquired by the laser profiler, two 3-m profiles were collected using chart paper and spray paint to monitor large scale roughness variations. The radar measurements were conducted for four surface-roughness conditions, covering the range from 0.32 cm to 3.02 cm in rms height (Table II).

C. Dielectric Probe

The dielectric constant of the soil surface was measured by a *C*-band field-portable dielectric probe [10]. The probe consists of a reflectometer assembly with a coaxial probe tip and a signal processing assembly with a calculator. The dielectric

TABLE II
SUMMARY OF ROUGHNESS PARAMETERS

Surface	s (cm)	l (cm)	m	Freq(GHz)	ks	kl	
				1.50	0.13	2.6	L1
S-1	0.40	8.4	0.048†	4.75	0.40	8.4	C1
				9.50	0.80	16.7	X1
				1.50	0.10	3.1	L2
S-2	0.32	9.9	0.032†	4.75	0.32	9.8	C2
				9.50	0.64	19.7	X2
				1.50	0.35	2.6	L3
S-3	1.12	8.4	0.133†	4.75	1.11	8.4	C3
				9.50	2.23	16.7	X3
				1.50	0.95	2.8	L4
S-4	3.02	8.8	0.485‡	4.75	3.00	8.8	C4
				9.50	6.01	17.5	X4

s = rms height
l = correlation length
m = rms slope
$k = 2\pi/\lambda$
†$m = s/l$ assuming exponential autocorrelation function
‡$m = \sqrt{2}s/l$ assuming Gaussian autocorrelation function

TABLE III
SUMMARY OF SOIL MOISTURE AND DIELECTRIC DATA

Surface Number	Measured ϵ_r (4.8 GHz)		Estimated m_v		calculated $(\epsilon_r', \epsilon_r'')$ for (0-4 cm) layer		
	Top Soil	4 cm depth	Top	4 cm	1.5 GHz	4.75 GHz	9.5 GHz
1 -wet	14.15	16.74	0.29	0.33	15.57, 3.71	15.42, 2.15	12.31, 3.55
1 -dry	6.58	11.05	0.14	0.24	7.99, 2.02	8.77, 1.04	5.70, 1.32
2 -wet	14.66	14.30	0.30	0.29	14.43, 3.47	14.47, 1.99	12.64, 3.69
2 -dry	4.87	8.50	0.09	0.19	5.85, 1.46	6.66, 0.68	4.26, 0.76
3 -wet	15.20	15.10	0.31	0.31	15.34, 3.66	15.23, 2.12	13.14, 3.85
3 -dry	7.04	10.02	0.15	0.22	7.70, 1.95	8.50, 1.00	6.07, 1.46
4 -wet	8.80	10.57	0.19	0.23	8.92, 2.24	9.64, 1.19	7.57, 1.99
4 -dry	7.28	8.84	0.16	0.19	7.23, 1.83	8.04, 0.92	6.28, 1.53

constant was measured at the soil surface and at a depth of 4 cm at each of more than 50 locations randomly chosen over each surface. The relative dielectric constant (ϵ_r) was used to estimate the moisture contents (m_v) by inverting a semiempirical model [11] which gives ϵ_r in terms of m_v. The real part of ϵ_r was used in the dielectric-to-moisture inversion because the error in measuring the imaginary part of ϵ_r by the dielectric probe is relatively higher [12]. The mean value of m_v was then used in the same semiempirical model to obtain an estimate for ϵ_r at L-, C-, and X-band. Table III gives the measured values of ϵ_r' at 4.8 GHz and the estimated values of m_v for the top surface and 4-cm deep layers, from which the 0–4 cm average dielectric constant was calculated at L-, C-, and X-band. Soil density was determined from soil samples with known volume.

III. EXPERIMENTAL OBSERVATIONS AND COMPARISON WITH CLASSICAL SOLUTIONS

In this section we present samples of the measured radar data to illustrate the spectral, angular, and polarization behavior of rough surface scattering. Next, for surfaces whose statistical roughness parameters fall within the region of validity of theoretical models, we will compare the experimental observations with theoretical predictions.

A. Experimental Observations

Four different fields (S1, S2, S3, and S4) were examined in this study. Each was measured under two different moisture conditions, relatively wet and relatively dry. The roughness parameters of the surfaces, such as the rms height s, autocorrelation function $\rho(\xi)$, correlation length l, and rms slope m, were calculated from the measured surface height profiles and are given in Table II.

Based on an analysis of the surface-height distributions, we concluded that the surface-height deviation is approximately Gaussian for all four surfaces, with a probability density function given by

$$p(z) = \frac{1}{\sqrt{2\pi}s} \exp\left[-\frac{z^2}{2s^2}\right]. \tag{1}$$

For the first three surfaces, the measured autocorrelation function $\rho(\xi)$ was found to be closer in shape to an exponential function of the form

$$\rho(\xi) = \exp[-\mid \xi \mid / \ell] \tag{2}$$

than to the Gaussian function

$$\rho(\xi) = \exp[-\xi^2/\ell^2]. \tag{3}$$

The Gaussian form provided a better fit for the roughest field, S4. This is illustrated in Fig. 2 for fields S1 and S4. The

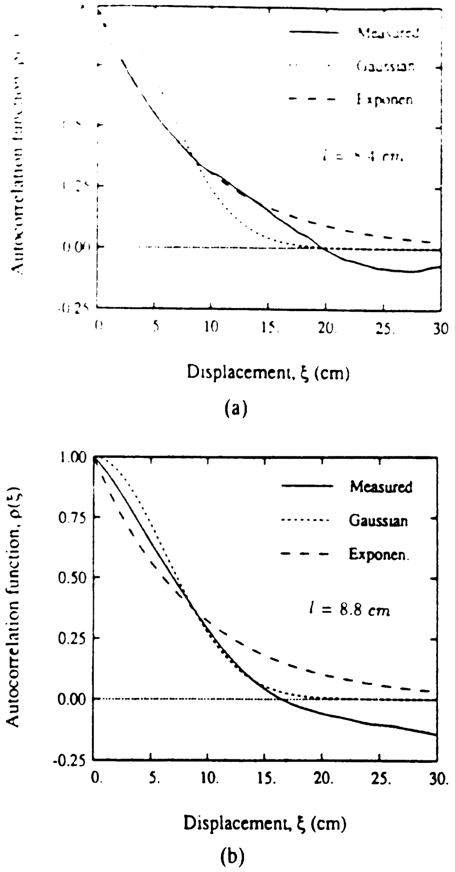

Fig. 2. Comparison of the measured autocorrelation functions with the Gaussian and exponential functions for surfaces (a) S1 and (b) S4.

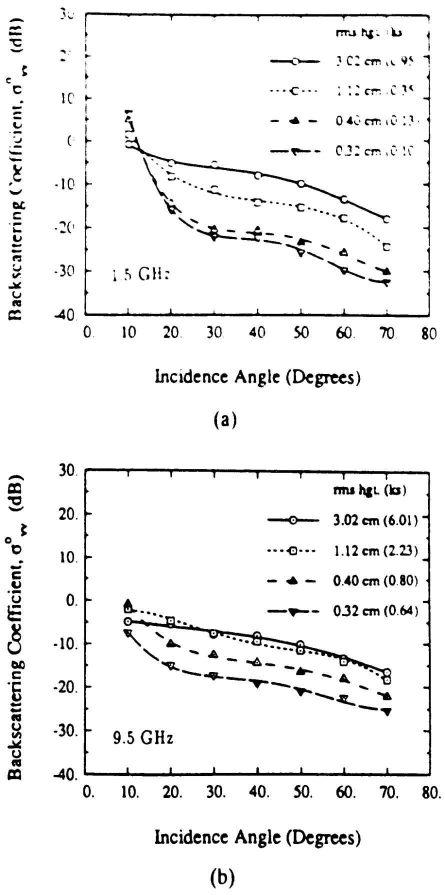

Fig. 3. Angular response of σ^o_{vv} for four different surface roughnesses at moderately dry moisture condition ($m_v \simeq 0.15$) at (a) 1.5 GHz and (b) 9.5 GHz.

surface rms slope can be calculated from $m = s\sqrt{|\rho''(0)|}$, where $\rho''(0)$ is the second derivative of $\rho(\xi)$ evaluated at $\xi = 0$, which yields $m = s/l$ for the exponential function and $m = \sqrt{2}s/l$ for the Gaussian function.

Among the four surfaces, surface S2 is the smoothest ($s = 0.32$ cm), surface S1 ($s = 0.4$ cm) is slightly rougher, surface S3 ($s = 1.12$ cm) represents an intermediate-roughness condition, and surface S4 ($s = 3.02$ cm) is a very rough surface that was generated by ploughing the top 15-cm surface layer. Electromagnetically, these surfaces cover a wide range of roughness conditions (Table II), extending from $ks = 0.1$ to $ks = 6.01$ (where $k = 2\pi/\lambda$ is the wave number) and from $k\ell = 2.6$ to $k\ell = 19.7$. The 12 roughness conditions corresponding to the four surfaces and three wavelengths are identified in $ks - k\ell$ space in Fig. 7, together with the boundaries for the regions of validity of the small perturbation model (SPM) and the physical optics (PO) and geometric optics (GO) solutions of the Kirchhoff approximation.

Fig. 3 shows angular responses of the vv-polarized backscattering coefficient (σ^o_{vv}) for four different bare soil surfaces with rms heights ranging from 0.3 cm to 3.0 cm, all at a moderately dry moisture condition ($m_v \simeq 0.15$). The sensitivity of σ^o_{vv} to surface roughness is clearly evident at both 1.5 GHz (Fig. 3(a)) and 9.5 GHz (Fig. 3(b)); over the 30° – 70° angular range, σ^o_{vv} exhibits a dynamic range of 16 dB at 1.5 GHz and 10 dB at 9.5 GHz, corresponding to the surface roughness (s) range from 0.3 cm to 3 cm. We also observe that at 9.5 GHz, the surfaces with $ks = 2.23$ and 6.01 exhibit approximately the same radar response, suggesting that σ^o_{vv} becomes approximately insensitive to surface roughness for $ks \geq 2.0$.

Further illustration of the effect of surface roughness on the angular response of σ^o is shown in Fig. 4, which contains plots of the three principal polarization components for the smoothest case (Fig. 4(a)), corresponding to surface S2 at 1.5 GHz, and for the roughest-surface condition (Fig. 4(b)), corresponding to surface S4 at 9.5 GHz. Based on these and on the data measured for the other surfaces, we note that the ratio of σ^o_{hh} to σ^o_{vv}, which will be referred to as the copolarized ratio, is always smaller than or equal to 1, and it approaches 1 as ks becomes large. Very rough surfaces, such as C4 (surface 4 at C-band) and X4, do not show any noticeable differences between σ^o_{vv} and σ^o_{hh}, while smooth surfaces show values of $\sigma^o_{hh}/\sigma^o_{vv}$ smaller than 1. It is also observed that the copolarized ratio is a function of incidence angle for smooth surfaces and decrease as the incidence angle increases. The sensitivity of the copolarized ratio ($\sigma^o_{hh}/\sigma^o_{vv}$) to surface roughness and incidence angle is shown in Fig. 5. For very rough surfaces ($ks \geq 3$), $\sigma^o_{hh}/\sigma^o_{vv} \simeq 1$ and is independent of incidence angle. Another point worth noting is that the shape of the angular pattern of the cross-polarized backscattering coefficient σ^o_{hv}, is similar to that of σ^o_{vv}, but the ratio $\sigma^o_{hv}/\sigma^o_{vv}$, which will be referred to as the cross-polarized ratio, increases with ks as shown in Figs. 4(a) and (b) (and more explicitly in Fig. 11).

The backscattering coefficient of a surface is also a function of its moisture content. Fig. 6(a) shows the backscattering

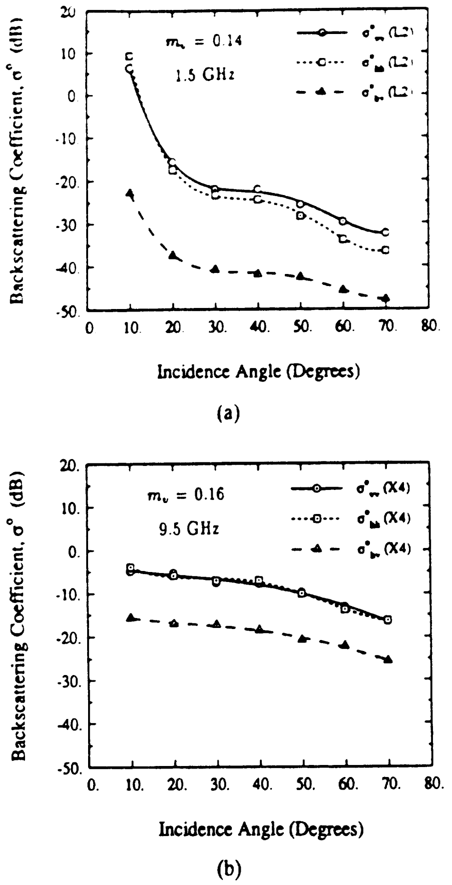

Fig. 4. Angular responses of σ°_{vv}, σ°_{hh} and σ°_{hv} for (a) a smooth surface at 1.5 GHz (L2) and (b) a very rough surface at 9.5 GHz (X4).

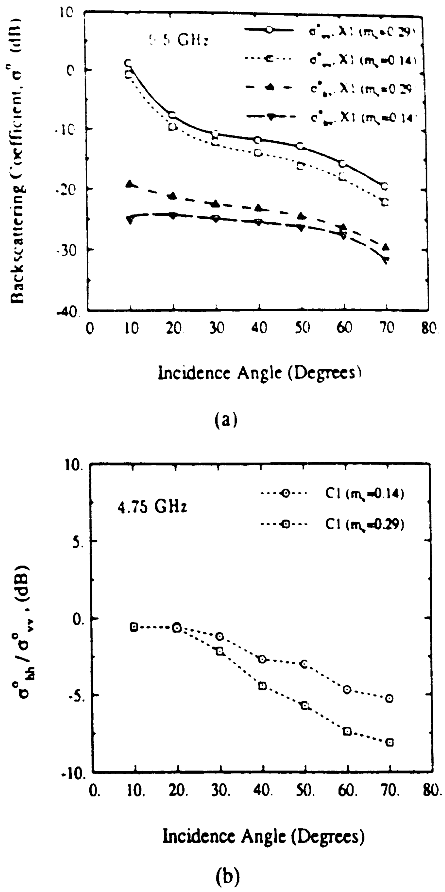

Fig. 6. Angular plots of (a) σ°_{vv} and σ°_{hv} of surface S1 at X-band for two different moisture conditions and (b) the copolarized ratio, $\sigma^\circ_{hh}/\sigma^\circ_{vv}$, for the same surface at C-band.

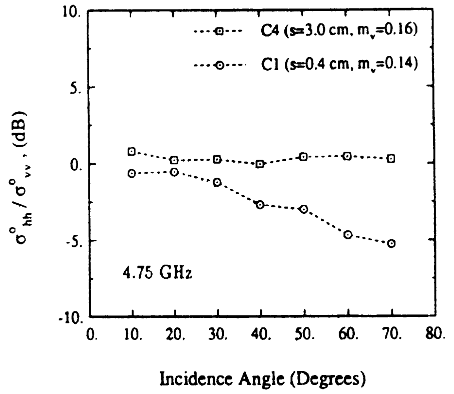

Fig. 5. Angular dependence of the copolarized ratio, $\sigma^\circ_{hh}/\sigma^\circ_{vv}$, at 4.75 GHz for a smooth surface and a very rough surface.

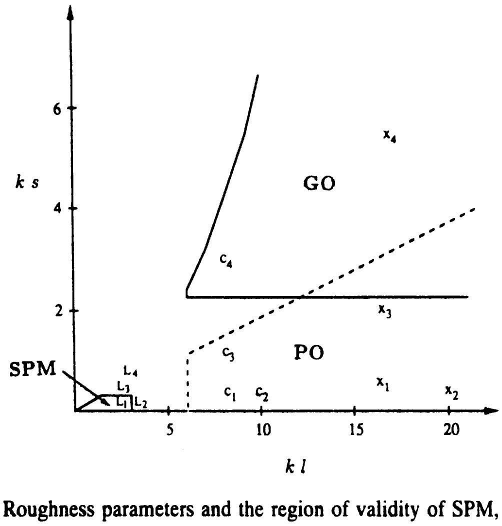

Fig. 7. Roughness parameters and the region of validity of SPM, PO, and GO models.

coefficient of surface 1 for two moisture conditions, $m_v = 0.29$ and $m_v = 0.14$. The ratio of σ°_{vv} (or σ°_{hv}) of wet soil to σ°_{vv} (or σ°_{hv}) of dry soil is about 3 dB at incidence angles in the 20° to 70° range. Fig. 6(b) shows the angular response of the copolarized ratio $\sigma^\circ_{hh}/\sigma^\circ_{vv}$ for a fixed roughness at two different moisture contents. The magnitude of the copolarized ratio is larger for the wet surface (6 dB at 50°) than for the dry surface (3 dB at 50°).

B. Comparison with Classical Solution

This section evaluates the applicability of the small perturbation method (SPM), the physical optics (PO) model, and the geometric optics (GO) model to the measured radar data. Expressions for the backscattering coefficient σ° and the regions of validity of these models are given in [5]. The locations of the 12 surface roughness conditions are identified in $ks - kl$ space in Fig. 7. Also shown are the regions of validity of the SPM, PO, and GO models for random surfaces characterized by a Gaussian autocorrelation function. The lower limit of the ks value of the validity region of the GO model is given by $ks > \sqrt{2.5}/\cos\theta$, which varies from 1.62 at 10° to 6.32 at 60°. The limit shown in Fig. 7 corresponds to $\theta = 40°$.

TABLE IV
AUTOCORRELATION FUNCTIONS AND THE CORRESPONDING ROUGHNESS SPECTRA

Normalized $\rho(\xi)$	$W(2k \sin\theta)$
Gaussian: $\exp[-\xi^2/l^2]$	$(l^2/2)\cdot\exp[-(kl \sin\theta)^2]$
Exponential: $\exp[-\lvert\xi\rvert/l]$	$(l^2/2)\cdot[1+(2kl \sin\theta)^2]^{-1}$
Measured: Numerical data	Fourier Transform of $\rho(\xi)$

According to Fig. 7, some of the surface roughness conditions fall outside the regions of validity of all three models, while several satisfy the model conditions. In order to compare the measured data with model predictions, we have selected surface 1 at 1.5 GHz (L1) to compare with the SPM, surface 1 at 9.5 GHz (X1) to compare with the PO model, and surface 4 at 9.5 GHz (X4) to compare with the GO model.

1) Small Perturbation Model: The measured angular responses of σ°_{vv} and σ°_{hh} are shown in Figs. 8(a) and (b) for data set L1 (surface 1 at 1.5 GHz), together with plots calculated using the SPM for each of three autocorrelation functions: a Gaussian function of the form given by (3), an exponential function of the form given by (2), and the measured autocorrelation function obtained from the measured surface profile, which is approximately exponential in form (Fig. 2(a)). The calculated curves include a coherent component to account for the strong backscatter response near normal incidence (see Table IV).

Overall, SPM provides a reasonable fit for σ°_{hh} when used in conjunction with the exponential correlation function, but not as well for σ°_{vv}. Fig. 8(c) provides a comparison of the measured data for $\sigma^\circ_{vv}, \sigma^\circ_{hh}$, and σ°_{hv} with SPM calculated using the exponential correlation function. The cross-polarized backscattering coefficient σ°_{hv}, which was computed using the second-order SPM [2], is in close agreement with data and exhibits an angular response similar to that of σ°_{vv} (at angles greater than 20°).

2) Physical Optics Model: Several of the surface roughness conditions examined in this study fall within the region of validity of the PO model. We have chosen X1 for detailed examination in this section. The plots shown in Fig. 9 indicate that the PO model provides good agreement with measured data for σ°_{hh} when an exponential correlation function is used, but the model underestimates σ°_{vv} at angles beyond 40° . Since the PO approximation does not account for cross-polarization in the backscattering direction, comparison with the measured σ°_{hv} data is not warranted.

Similar comparisons between theory and measured data were performed for the other five surface conditions that, according to Fig. 7, satisfy the validity conditions of the PO model. In all cases, the deviation between theory and measurements was greater than what was noted above for X1 (Fig. 9), with some of the deviations being as large as 20 dB. Furthermore, the level of the measured angular response of σ°_{vv} was observed to be always greater or equal to that of σ°_{hh} for all surfaces, moisture contents, and incidence angles, which is contrary to the behavior of the PO model.

3) Geometrical Optics Model: For angles below 50°, the GO model was found to differ from the measured angular responses of σ°_{hh} and σ°_{vv} by 3 dB or less for surface condition X4 (Fig. 10) and by 4 dB or less for C4. The coherent component of the backscattering coefficient is negligibly small for a very rough surface, and the noncoherent component dominates at all angles including normal incidence.

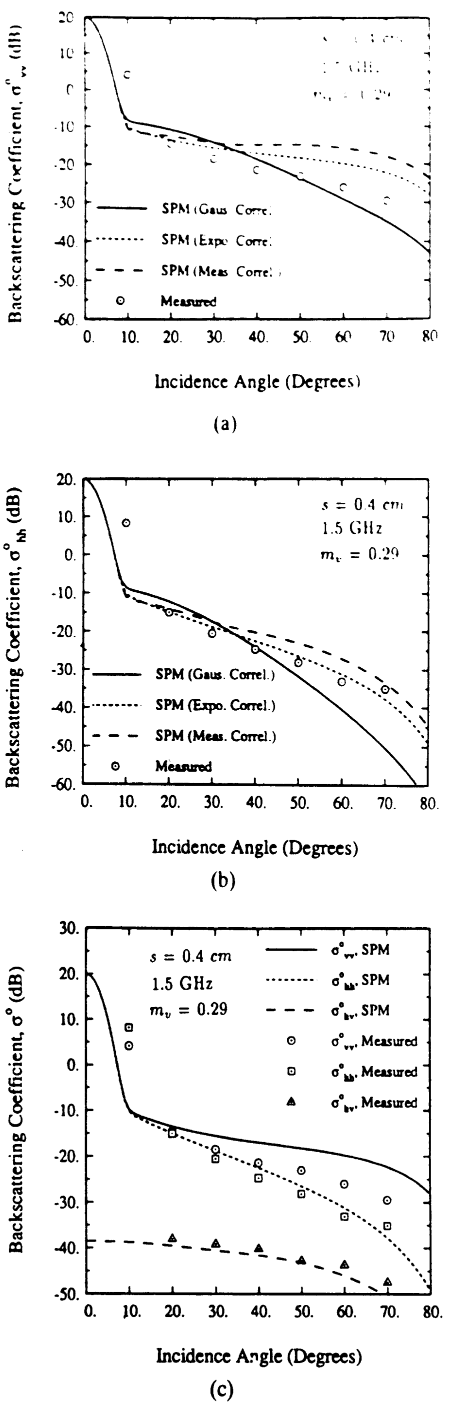

(a)

(b)

(c)

Fig. 8. SPM model with different autocorrelation functions compared to the measured data of L1 (surface 1 at 1.5 GHz, ks=0.13) for (a) VV-polarization, (b) HH-polarization, and for (c) VV-, HH-, and HV-polarizations using an exponential autocorrelation function.

The major conclusions we drew from our analysis of the measured radar data when compared with the predictions of the SPM, PO, and GO models are:

1) Some natural surface conditions fall outside the regions of validity of all three models.
2) None of the models provides consistently good agreement with the measured data, particularly at incidence angles greater than 40°.

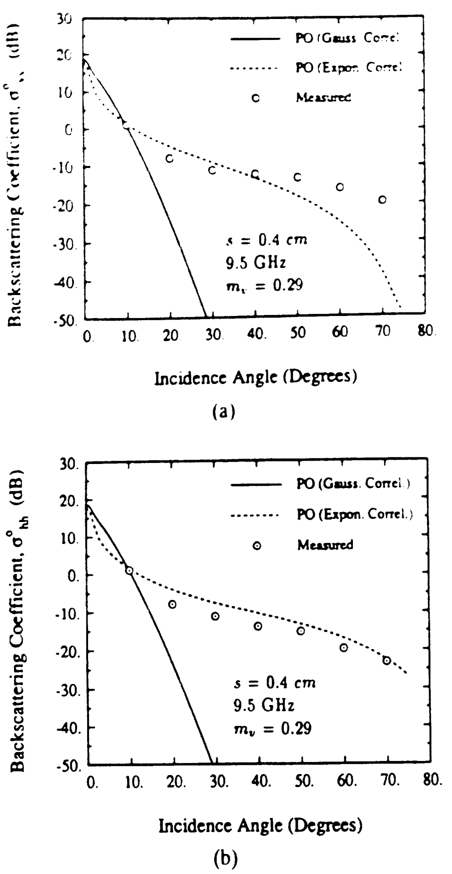

(a)

(b)

Fig. 9. PO model with different autocorrelation functions compared to the measured data of X1 (surface 1 at 9.5 GHz, ks=0.80) for (a) VV-polarization, and (b) HH-polarization.

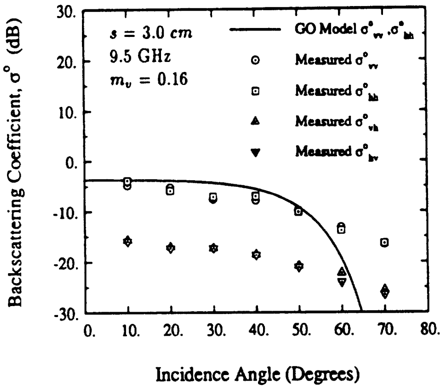

Fig. 10. GO model compared to the measured data of X4 (surface 4 at 9.5 GHz, ks=6.0).

3) The PO model predicts that $\sigma^\circ_{vv} < \sigma^\circ_{hh}$, contrary to all observations.

In addition, since they are first-order solutions, both the PO and GO models cannot be used for σ°_{hv}. Faced with these inadequacies of the available theoretical scattering models, we decided to develop an empirical model that relates $\sigma^\circ_{vv}, \sigma^\circ_{hh}$, and σ°_{hv} to the roughness (ks) and dielectric constant (ϵ_r) of the surface. This is the subject of the next section.

IV. EMPIRICAL MODEL

The empirical model developed in this section is based on the radar backscatter data measured in this investigation and on knowledge of the scattering behavior in the limiting

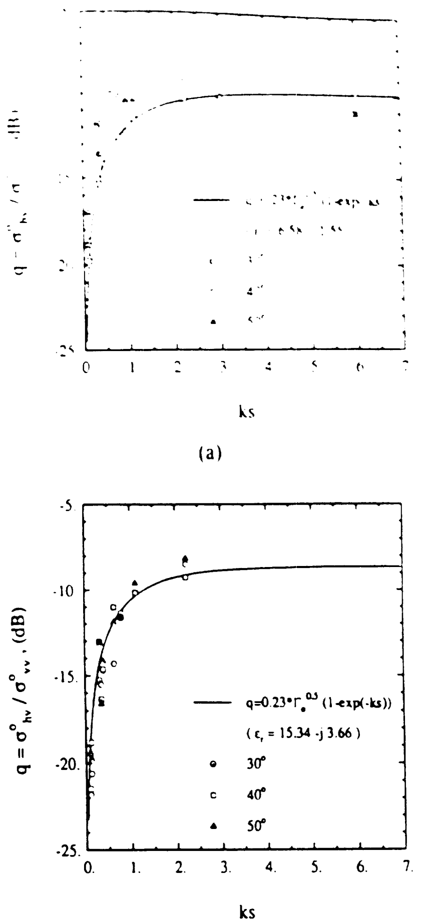

(a)

(b)

Fig. 11. The sensitivity of the cross-polarized ratio, $\sigma^\circ_{hv}/\sigma^\circ_{vv}$, to surface roughness for (a) dry soil and (b) wet soil.

cases (such as when ks is very large). For this data set, the surface roughness and moisture content cover the ranges: $0.1 < ks < 6.0, 2.6 < k\ell < 19.7$, and $0.09 < m_v < 0.31$.

We begin with an examination of the cross-polarized ratio $q = \sigma^\circ_{hv}/\sigma^\circ_{vv}$. We observed from the measured angular responses that σ°_{hv} and σ°_{vv} exhibit similar variations with incidence angle, particularly over the 30° – 50° range, for all surface roughnesses, moisture contents, and frequencies. Figs. 11(a) and (b) show the measured values of q as a function of ks for dry and wet soils, respectively. They include the values measured at $30°, 40°$, and $50°$ for all surface-frequency combinations. We observe that for the dry soils q increases rapidly from about -20 dB at $ks = 0.1$ to about -10 dB at $ks = 3$, and then maintains that level for $ks > 3$. For the wet soils, q exhibits a similar behavior as that noted for the dry soils, except that its saturation level is closer to -8.5 dB for $ks > 3$.

The curves shown in Fig. 11, which provide a good fit to the data, are given by the empirically determined function

$$q \triangleq \frac{\sigma^\circ_{hv}}{\sigma^\circ_{vv}} = 0.23\sqrt{\Gamma_\circ}[1 - \exp(-ks)] \tag{4}$$

where $\Gamma_\circ$ is the Fresnel reflectivity of the surface at nadir,

$$\Gamma_\circ = \left|\frac{1-\sqrt{\epsilon_r}}{1+\sqrt{\epsilon_r}}\right|^2. \tag{5}$$

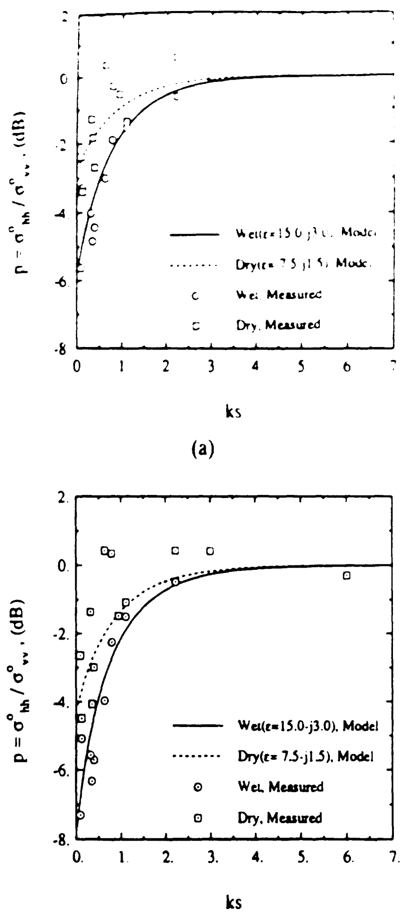

(a)

(b)

Fig. 12. The sensitivity of the copolarized ratio, $\sigma^\circ_{hh}/\sigma^\circ_{vv}$, to surface roughness and soil moisture, at (a) 40°, and (b) 50°.

Next, we shall examine the copolarized ratio $p = \sigma^\circ_{hh}/\sigma^\circ_{vv}$. The measured values of this ratio are shown in Fig. 12 for wet and dry moisture conditions at 40° and 50°. For very smooth surfaces, this ratio is about −6 dB, and for very rough surfaces it is equal to 0 dB. Similar results were obtained at 30°. The curves shown in Fig. 12 are based on the empirical expression

$$\sqrt{p} \triangleq \sqrt{\frac{\sigma^\circ_{hh}}{\sigma^\circ_{vv}}} = 1 - \left(\frac{2\theta}{\pi}\right)^{[1/3\Gamma_\circ]} \cdot \exp(-ks) \qquad (6)$$

where θ is the incidence angle in radians.

Having established empirical formulas for $q = \sigma^\circ_{hv}/\sigma^\circ_{vv}$ and $p = \sigma^\circ_{hh}/\sigma^\circ_{vv}$ that provide reasonable agreement with the measured data, the remaining task is to relate the absolute level of any one of the three linearly polarized backscattering coefficients to the surface parameters. Upon examining the measured data, we developed the following empirical expression for the magnitude of σ°_{vv}:

$$\sigma^\circ_{vv}(\theta, \epsilon_r, ks) = \frac{g\cos^3\theta}{\sqrt{p}} \cdot [\Gamma_v(\theta) + \Gamma_h(\theta)] \qquad (7)$$

where

$$g = 0.7\left[1 - \exp\left(-0.65(ks)^{1.8}\right)\right] \qquad (8)$$

and p is as given by (6).

With the ratios p and q being given explicitly in terms of ks and ϵ_r (through $\Gamma_\circ$) and the function g being governed by only ks, the three linearly polarized backscattering coefficients are given by (7) for σ°_{vv} and by

$$\sigma^\circ_{hh}(\theta, \epsilon_r, ks) = g\sqrt{p}\cos^3\theta[\Gamma_v(\theta) + \Gamma_h(\theta)] \qquad (9)$$

and

$$\sigma^\circ_{hv}(\theta, \epsilon_r, ks) = q\sigma^\circ_{vv}(\theta, \epsilon_r, ks). \qquad (10)$$

for the other two components. We note that both σ°_{vv} and σ°_{hh} are proportional to the average of the vertically and horizontally polarized Fresnel reflectivities of the surface at the incidence angle θ. The HH component is smaller than the VV component by a multiplying factor $p (p \leq 1)$. For $ks > 3, p \simeq 1$ and $\sigma^\circ_{vv} \simeq \sigma^\circ_{hh}$. For smaller values of ks, the factor p accounts for the difference in level between σ°_{vv} and σ°_{hh} and includes a dependence on ϵ_r.

Aside from the dependence on θ inherent in the quantity $[\Gamma_v(\theta) + \Gamma_h(\theta)]$ and in the function p, both σ°_{vv} and σ°_{hh} vary as $\cos^3\theta$. A more elaborate functional dependence for the power of $\cos\theta$ can be devised in terms of ϵ_r and ks, but this was found to be unnecessary. As we will see next, the empirical model was found to provide a good representation of the measured data at all frequencies and over a wide angular range. The model was evaluated against three data sets: (a) the data measured in this study, (b) another independently measured data set that was not used in the development of the model, which shall be refered to as Independent Data Set II, and (c) a data set that was recently reported by Yamasaki *et al.* [13] at 60 GHz.

A. Comparison With Measured Data

Because of space limitations, we will present only two typical examples illustrating the behavior of the empirical model, in comparison with the data measured in this study. This is shown in Figs. 13 and 14 for surface S1 (representing a very smooth surface with $s = 0.40$) and surface S4 (representing a very rough surface with $s = 3.02$). In both cases, very good agreement is observed between the model and the measured data at all three frequencies and across the entire angular range between 20° and 70°. The levels of the measured values of σ°_{vv} and σ°_{hh} at $\theta = 10°$ for surface S1 include a strong contribution due to the coherent backscattering component that exists at angles close to normal incidence. No attempt has been made at this stage to add a coherent component to the empirical model, and, therefore, its range of applicability does not include the angular range below 20° for smooth surfaces. If the surface is rough, as is the case for surface S4 (Fig. 14), the coherent backscattering coefficient is negligibly small, in which case the empirical model may be used at all angles between 0° and 70°.

B. Comparison With Independent Data Set II

Prior to conducting the measurements reported in this study, another data set was acquired by the same radar system for three surface roughnesses. The surface profiles were measured by inserting a plate into the surface and spraying it with paint. Such a technique provides an approximate representation of the surface, but it is not as accurate as that obtained using

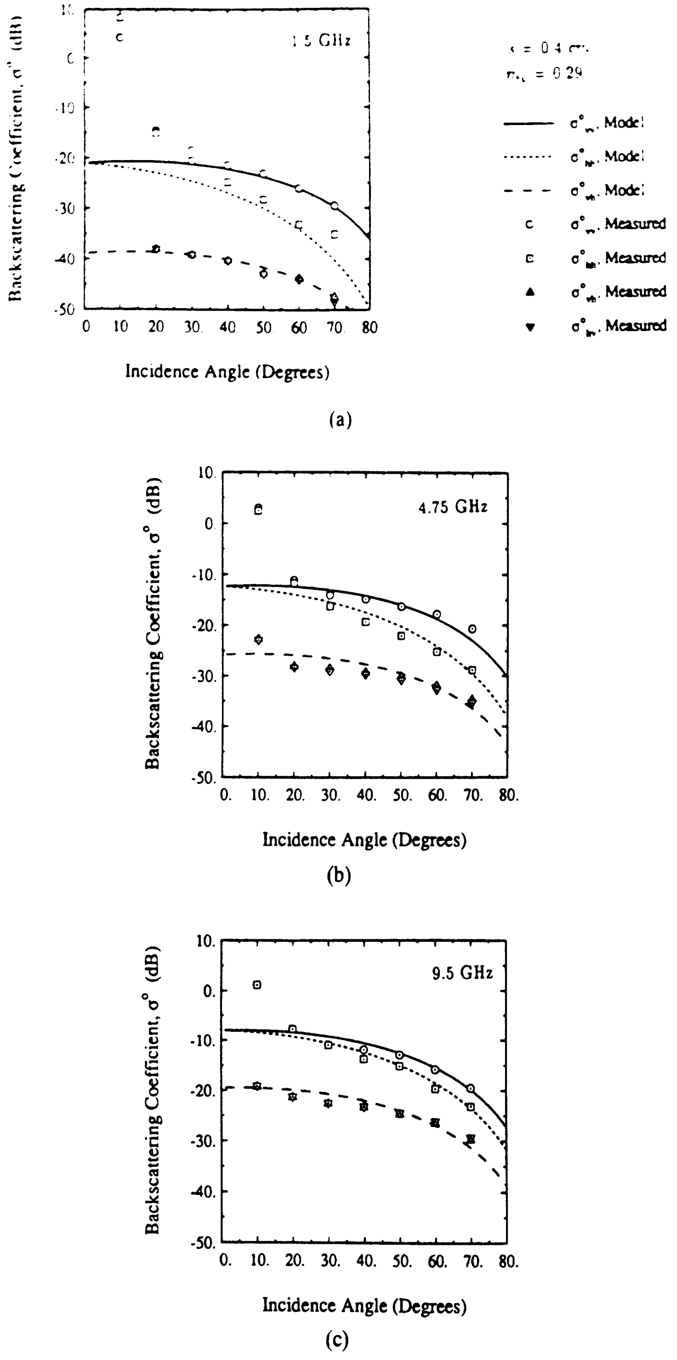

Fig. 13. Empirical model compared to the measured data of surface 1 for wet soil at (a) 1.5 GHz, (b) 4.75 GHz, and (c) 9.5 GHz.

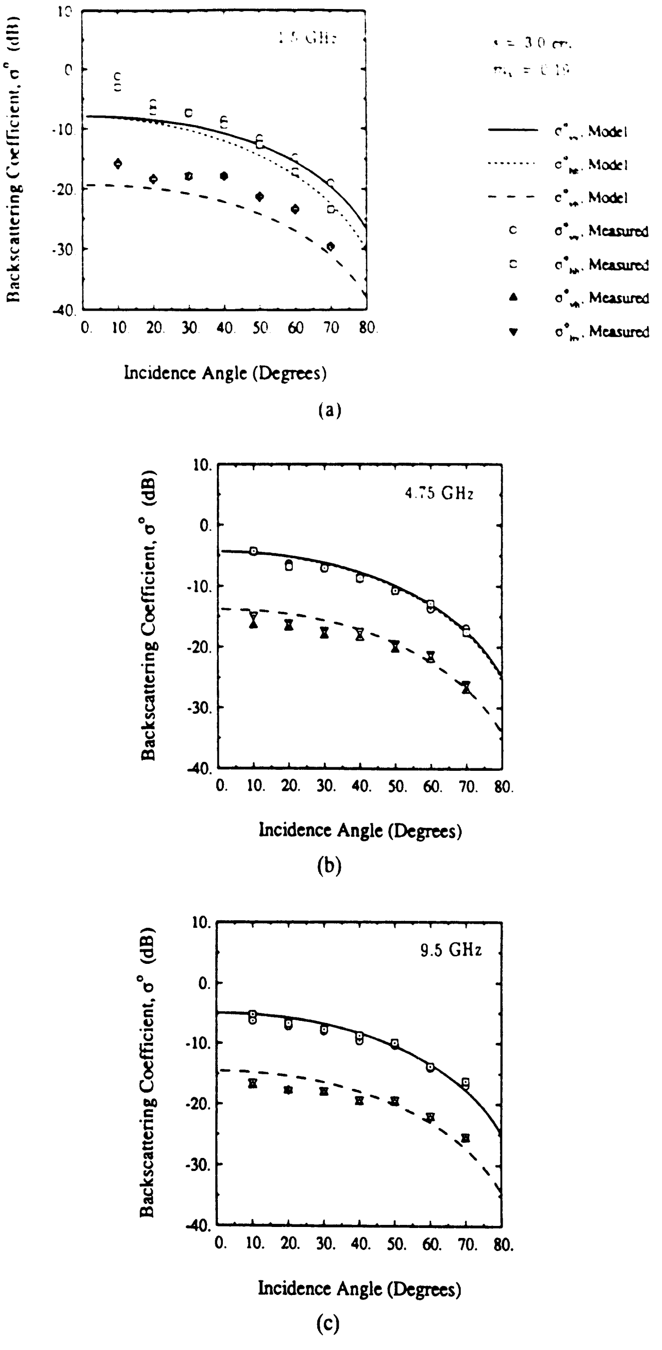

Fig. 14. Empirical model compared to the measured data of surface 4 for wet soil at (a) 1.5 GHz, (b) 4.75 GHz, and (c) 9.5 GHz.

the laser profiler. Hence, our estimate of the values of ks and kl for Independent Data Set II are not as accurate as those we obtained with the laser profiler for the surfaces discussed in the preceding sections of this paper. Nevertheless, we conducted an evaluation of the empirial model by comparing its prediction with the backscatter data of Independent Data Set II and found the agreement to be very good at all three frequencies, provided we are allowed to modify the value of s measured with the metal plate technique. An example is given in Fig. 15 in which the curves were calculated using the empirical model with $s = 0.7$ cm; the value of s estimated from the metal-plate record was 0.46 cm.

C. Comparison With 60 GHz Data

Our final comparison is with a 60 GHz data set that was recently reported by Yamasaki *et al.* [13]. Even though $k = 2\pi/\lambda = 1260$ at 60 GHz, the three surfaces examined in this study were extremely smooth, with rms heights of 0.055, 0.12, and 0.20 cm. The corresponding values of ks are 0.16, 0.64, and 1.75. Good overall agreement is observed (Fig. 16) between this data and the empirical model, despite the fact that the correlation lengths for all three surfaces are smaller than the smallest correlation length of the surfaces on the basis of which the empirical model was developed.

V. INVERSION MODEL

Having established in the preceding section that the empirical model is a good estimator of $\sigma^o_{vv}, \sigma^o_{hh}$, and σ^o_{hv} over a wide range of ks (0.1 to 6), we shall now invert the model to obtain estimates of s and the moisture content m_v from

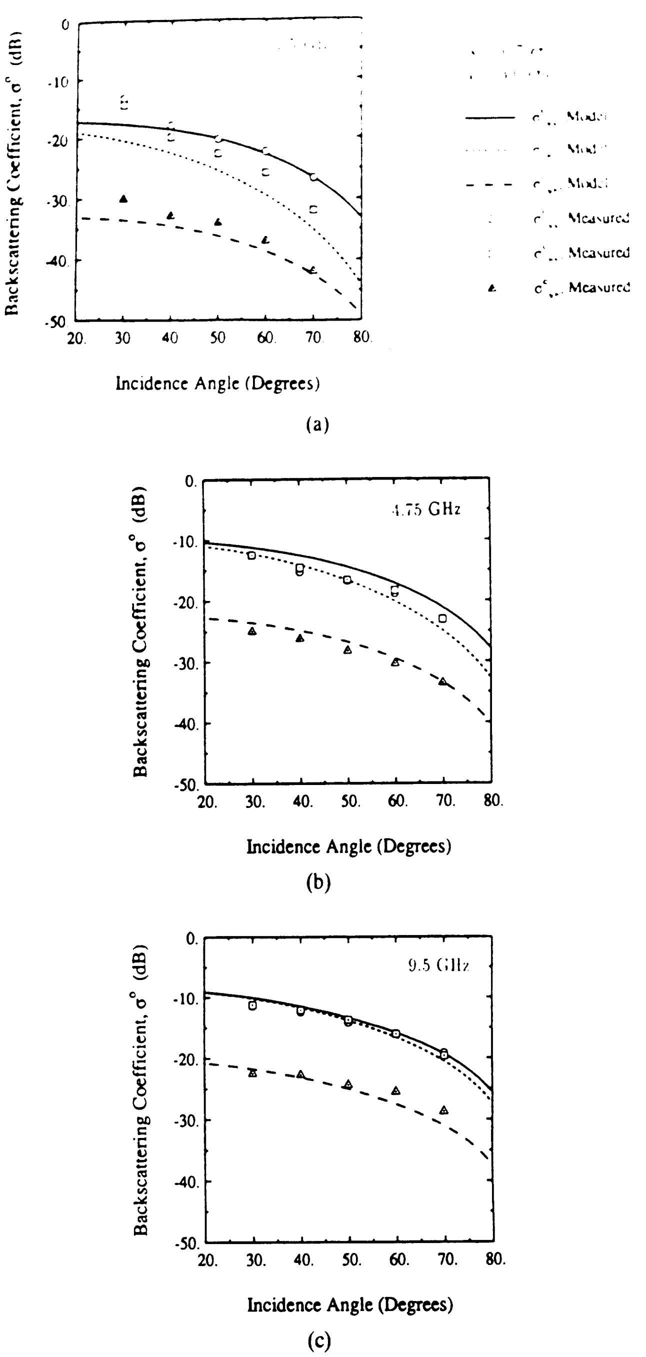

Fig. 15. Empirical model compared with the data from independent data set II for a surface with $s = 0.7$ cm and $l = 3.0$ cm, measured at (a) 1.5 GHz, (b) 4.75 GHz, and (c) 9.5 GHz.

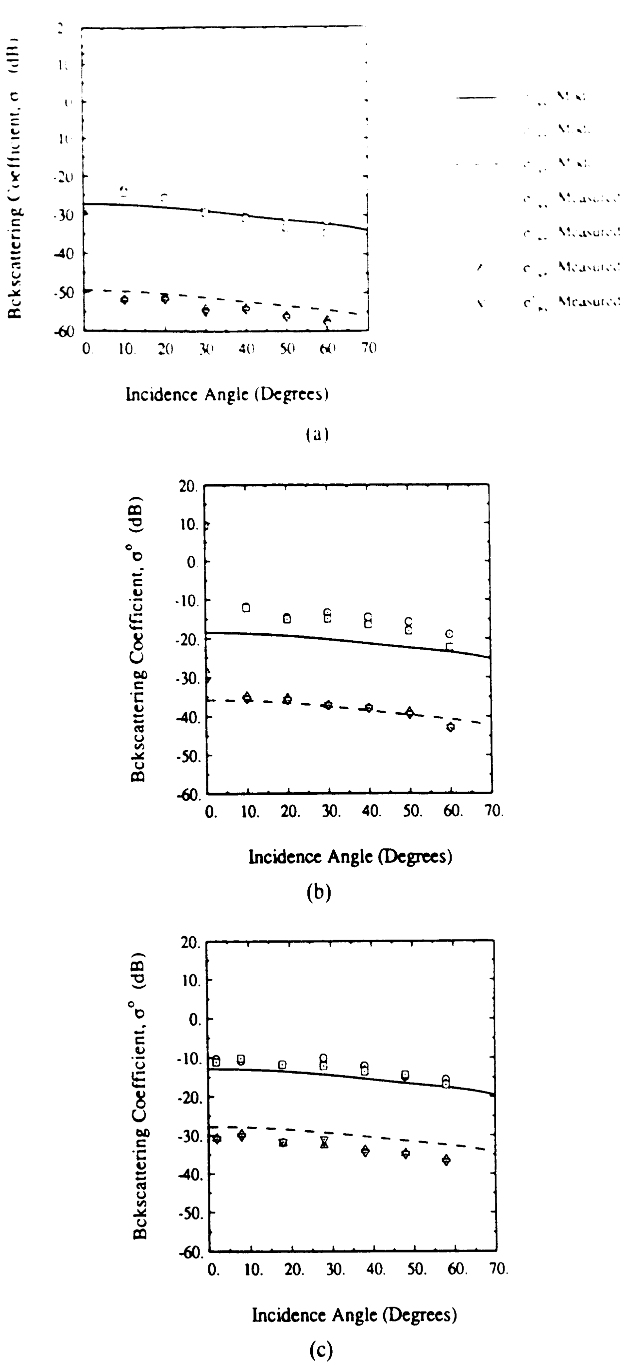

Fig. 16. Empirical model compared with the data reported by Yamasaki *et al.* [13] at 60 GHz for (a) soil-1 ($s = 0.013$ cm, $\ell = 0.055$ cm), (b) soil-2 ($s = 0.051$ cm, $\ell = 0.12$ cm), and (c) for soil-3 (s=2.88 cm, l=0.20 cm).

observation of $\sigma^\circ_{vv}, \sigma^\circ_{hh}$, and σ°_{hv}. Because the empirical model was developed on the basis of data for surfaces with kl in the range $2.6 < kl < 19.7$, we cannot ascertain its applicability or the applicability of the inversion model for surfaces with kl outside this range.

Suppose we have measurements of $\sigma^\circ_{vv}, \sigma^\circ_{hh}$, and σ°_{hv} for a given surface at a given incidence angle θ and wavelength λ. From these measurements, we compute the copolarized and cross-polarized ratios $p = \sigma^\circ_{hh}/\sigma^\circ_{vv}$ and $q = \sigma^\circ_{hv}/\sigma^\circ_{vv}$. By eliminating ks from (4) and (6), we obtain the following nonlinear equation for $\Gamma_\circ$:

$$\left(\frac{2\theta}{\pi}\right)^{1/3\Gamma_\circ} \cdot \left[1 - \frac{q}{0.23\sqrt{\Gamma_\circ}}\right] + \sqrt{p} - 1 = 0 \qquad (11)$$

where θ is in radians. After solving for $\Gamma_\circ$ using an iterative technique, we can calculate the real part of the dielectric constant ϵ'_r from (5) by ignoring the imaginary part ϵ''_r, which is a valid approximation for a soil material. Next, the moisture content m_v and the imaginary part of the dielectric content ϵ''_r can be determined from the model given in [11]. Finally, with $\Gamma_\circ$ known, the roughness parameter ks can be determined from (6).

Because the copolarized and cross-polarized ratios p and q are not sensitive to surface roughness for very rough surfaces ($ks > 3$), this technique cannot estimate ks for such surfaces. Hence, it is preferable to use radar observations at the lowest available frequency for estimating the moisture content and rms height of a bare soil surface. By way of illustrating the

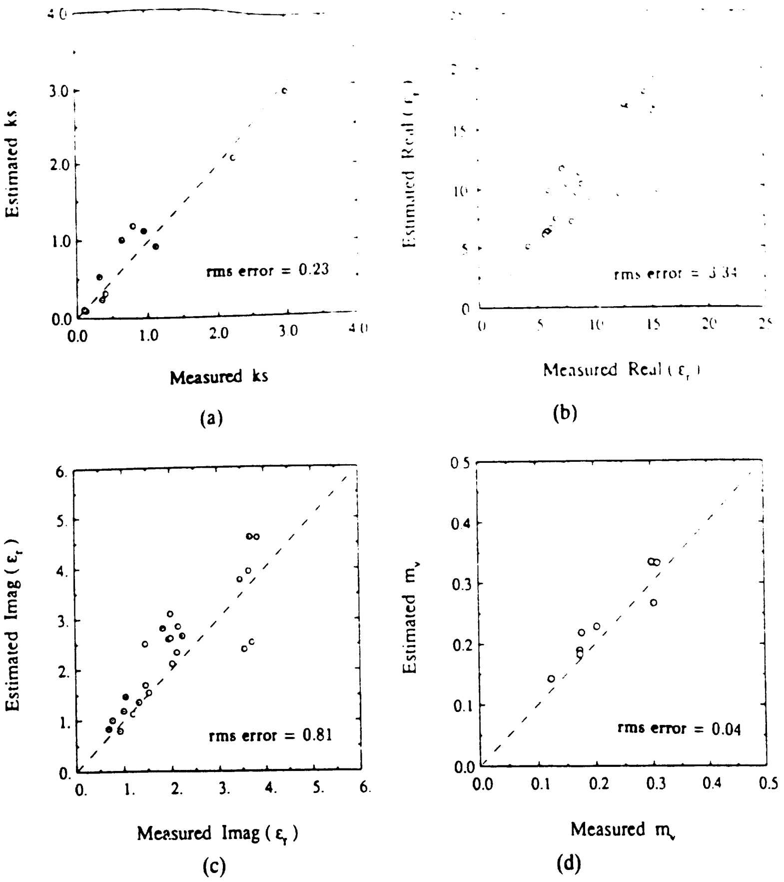

Fig. 17. Comparison between the values of surface parameters estimated by the inversion technique and those measured *in situ* for (a) ks, (b) the real part of ϵ_r, (c) the imaginary part of ϵ_r, and (d) the volumetric moisture content m_v.

capability of the inversion technique, we present in Fig. 17(a) the values of *ks* estimated by the inversion technique plotted against the values measured *in situ*. The data points include the data measured in support of this study for all surface conditions, but exclude surfaces for which $ks > 3$. of Figs. 17(b) and (c) show the results for ϵ_r' and ϵ_r'', respectively, for all surfaces measured in this study (the inversion technique is capable of estimating $\epsilon_r', \epsilon_r''$, and m_v for any ks, but it is incapable of estimating ks if $ks > 3$), and Fig. 17(d) presents the results for m_v. Note that for each value of m_v, we have three sets of values for $\epsilon_r', \epsilon_r''$, and ks, corresponding to the three frequencies used in this study.

The results displayed in Fig. 17 represent the first demonstration ever reported of a practical algorithm for estimating the roughness, dielectric constant, and moisture content of a bare soil surface from multipolarized radar observations. Before this technique can be widely applied, however, it is prudent to conduct additional experiments over a wide range of roughness and moisture conditions.

VI. CONCLUDING REMARKS

The major results of this study are summarized as follows:

1) At microwave frequencies, the available rough-surface scattering models are incapable of predicting the scattering behavior observed for bare-soil surface.
2) The copolarized ratio $p = \sigma_{hh}^{\circ}/\sigma_{vv}^{\circ} \leq 1$ for all angles, roughness conditions, and moisture contents; p increases rapidly with increasing ks up to $ks \simeq 1$, then it increases at a slower rate, reaching the value 1 for $ks > 3$. For $ks < 3$, p decreases with increasing incidence angle and with increasing moisture content.
3) The cross-polarized ratios $q = \sigma_{hv}^{\circ}/\sigma_{vv}^{\circ}$ exhibits a strong dependence on ks and a relatively weak dependence on moisture content. The ratio q increases rapidly with increasing ks up to $ks \simeq 1$, then it increases at a slower rate, reaching a constant value (that depends on the moisture content) for $ks > 3$.
4) The proposed scattering model provides very good agreement with experimental observations made over the ranges $0.1 \leq ks \leq 6, 2.5 \leq kl \leq 20$, and $0.09 \leq m_v \leq 0.31$. The model was found to be equally applicable when tested against radar data measured for surfaces with parameters outside the above ranges.
5) Soil moisture content (m_v) and surface roughness (ks) can be retrieved from multipolarized radar observations by applying the inversion technique developed in this paper.

REFERENCES

[1] S. O. Rice, "Reflection of electromagnetic waves by slightly rough surfaces," *Commun. Pure Appl Math.*, vol. 4, pp. 351–378, 1951.
[2] L. Tsang, J. A. Kong, and R. T. Shin, *Theory of Microwave Remote Sensing*. New York: John Wiley and Sons, 1985.
[3] D. Wineberner and A. Ishimaru, "Investigation of a surface field phase perturbation technique for scattering from rough surfaces," *Radio Sci.*, vol. 20, pp. 161–170, Mar. 1985.
[4] P. Beckmann and A. Spizzichino, *The Scattering of Electromagnetic Waves from Rough Surfaces*. Norwood, MA: Artech House, 1987.

[5] F. T. Ulaby, M. K. Moore, and A. K. Fung, *Microwave Remote Sensing, Active and Passive*, vols. 2 and 3. Norwood, MA: Artech House, 1986.

[6] A. K. Fung and H. J. Eom, "Multiple scattering and depolarization by a randomly rough Kirchhoff surface," *IEEE Trans. Antennas Propagat.*, vol. AP-26, pp. 463–471, May 1981.

[7] G. S. Brown, "Backscattering from a Gaussian distributed perfectly conducting rough surface," *IEEE Trans. Antennas Propagat.*, vol. AP-26, pp. 472–482, May 1978.

[8] M. A. Tassoudji, K. Sarabandi, and F. T. Ulaby, "Design consideration and implementation of the LCX polarimetric scatterometer (POLARSCAT)," Rep. 022486-T-2, Radiation Laboratory, the University of Michigan, June 1989.

[9] K. Sarabandi and F. T. Ulaby, "A convenient technique for polarimetric calibration of radar systems," *IEEE Trans. Geosci. Remote Sensing*, vol. 28, pp. 1022–1033, 1990.

[10] D. R. Brunfeldt, "Theory and design of a field-portable dielectric measurement system," *IEEE Int. Geosci. Remote Sensing Symp. (IGARSS) Digest* vol. 1, pp. 559–563, 1987.

[11] M. T. Hallikainen, F. T. Ulaby, M. C. Dobson, M. A. El-Rayes, and L. Wu, "Microwave dielectric behavior of wet soil -Part I: Empirical models and experimental observations," *IEEE Trans. Geosci. Remote Sensing*, vol. GE-23, pp. 25–34, 1985.

[12] T. J. Jackson, "Laboratory evaluation of a field-portable dielectric soil-moisture probe," *IEEE Trans. Geosci. Remote Sensing*, vol. 28, pp. 241–245, Mar. 1990.

[13] H. Yamasaki, J. Awaka, A. Takahashi, K. Okamoto, and T. Ihara, "Measurements of soil backscatter with a 60 GHz scatterometer," *IEEE Int. Geosci. Remote Sensing Symp. (IGARSS '91) Digest*, vol. 2, pp 403–406, 1991.

Yisok Oh (S'88) received the B.S. degree in electrical engineering from Yonsei University, Seoul, Korea, in 1982 and the M.S. degree in electrical engineering from the University of Missouri, Rolla, MO, in 1988.

He is currently working toward the Ph.D. degree at the University of Michigan, Ann Arbor, MI. His research interests include electromagnetic wave scattering from random surfaces and microwave remote sensing.

Kamal Sarabandi (S'87–M'90), for a photograph and biography, please see page 211 of this issue of the TRANSACTIONS.

Fawwaz T. Ulaby (M'68–SM'74–F'80), for a photograph and biography, please see page 211 of this issue of the TRANSACTIONS.

Knowledge-Based Classification of Polarimetric SAR Images

Leland E. Pierce, Fawwaz T. Ulaby, Kamal Sarabandi, and M. Craig Dobson

Abstract—**In preparation for the flight of the Shuttle Imaging Radar-C (SIR-C) on board the Space Shuttle in the spring of 1994, a Level-1 automatic classifier was developed on the basis of polarimetric SAR images acquired by the JPL AirSAR system. The classifier uses L- and C-Band polarimetric SAR measurements of the imaged scene to classify individual pixels into one of four categories: tall vegetation (trees), short vegetation, urban, or bare surface, with the last category encompassing water surfaces, bare soil surfaces, and concrete or asphalt-covered surfaces. The classifier design uses knowledge of the nature of radar backscattering from surfaces and volumes to construct appropriate discriminators in a sequential format. The classifier, which was developed using training areas in a test site in Northern Michigan, was tested against independent test areas in the same test site and in another site imaged three months earlier. Among all cases and all categories, the classification accuracy ranged between 91% and 100%.**

I. INTRODUCTION

SYNTHETIC aperture radar (SAR) is capable of generating high-resolution images of terrain, and, when operated in a polarimetric mode, it records the scattering matrix of each pixel in the imaged scene [1]. To reduce the effects of speckle, which is characteristic of fully focused SAR images, multiple pixels are averaged together prior to using the image for the extraction of quantitative information. The images used in the present study were generated by the JPL AirSAR system, which operated at P-, L-, and C-Bands [2]. Each image consisted of 1024 × 750 pixels, each representing nominally an area 12 m in azimuth × 6.6 m in slant range, or 12 m × 10 m average on the ground surface (Table I), with each such pixel being an average of four looks (or, equivalently, four fully focused pixels). The incidence angle ranged from approximately 30° at the near range (top) of the image to 60° at the far range (bottom).

The motivation of the present study is to develop a Level-1 classifier capable of accurately classifying the pixels in the imaged scene into four terrain categories (classes): tall vegetation (trees), short vegetation, urban, and bare surfaces (which includes water surfaces, bare soil surfaces, and road surfaces). In an earlier SAR classifier [3] all vegetation was lumped into one class: insufficient for our future needs.

TABLE I
SAR IMAGE ATTRIBUTES

JPL AirSAR	L-Band: 1.25 GHz, C-Band: 5.3 GHz
Test Sites	Pellston, MI; Raco, MI
Pixel spacing	12 m azimuth, x × 6.6 m slant range, y
Image sizes	1024 pixels az. × 750 pixels range
	12.4 Km az. × 7.5 Km range
	Each is nominally a 4-look pixel

Simulated annealing was used by Rignot and Chellappa in an attempt to post-process the results of an MLE classifier [4] and performed quite well, yielding better than 95% classification accuracy for up to 13 classes. However, simulated annealing is a complex and time-consuming procedure to apply over an entire image. Wong and Posner [5] developed a clustering technique that can automatically devise the best number of classes and their means in feature space using a simulated annealing procedure. The classifier was based on the Mahalonobis distance [6] from each of these class means. While classification accuracies were not given, the procedure performed quite well, visually.

Another classifier, similar in methodology to the present work was presented by Moghaddam and Freeman [7]. A set of hierarchical decision rules was used to distinguish between basic land cover types. No published accuracies were given, and our own experience with their code has been disappointing.

The classifier developed here is to use only L- and C-Band data as input because the classifier is part of a broader program at the University of Michigan aimed at the development of an automatic information extraction processor that can be applied to the image data expected from the Shuttle Imaging Radar-C/X-SAR system, that is scheduled for flight on the Space Shuttle in April 1994. The SIR-C/X-SAR system has been designed to produce polarimetric radar images at L- and C-bands, and VV-polarized images at X-Band.

Fig. 1 depicts the eventual structure of the information processor. Following full calibration of the SAR images, a Level-1 classifier is used to classify the scene into the four aforementioned classes. For the bare surfaces, contextual information is to be used when separating water surfaces from bare ground surfaces. For the latter, an inversion algorithm [8] is applied to determine the soil moisture content and surface roughness. In practice, bare

---

Manuscript received October 29, 1993; revised March 14, 1994.

The authors are with the Radiation Laboratory, Department of Electrical Engineering and Computer Science, University of Michigan, Ann Arbor, MI 48109.

IEEE Log Number 9403652.

0196-2892/94$04.00 © 1994 IEEE

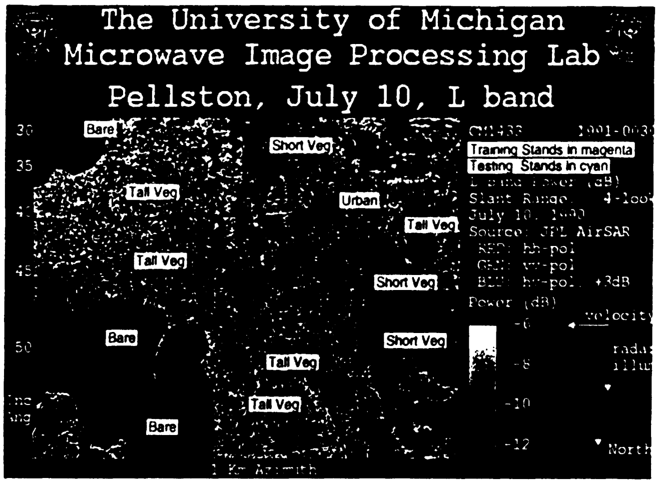

Fig. 2. Pellston test site showing training and test stands used during classification.

tested with other stands of the same type but different incidence angles. The short vegetation class was based solely on grasslands, cultivated and fallow (airport). Water was the only large bare feature in this image, and so the bare class was trained and tested with water alone. However, an apron and the runways at the airport were successfully classified as bare.

III. Classifier Design

The input data space consists of 14 channels, corresponding to the image attributes described in the previous section. All of these channels, however, are partially correlated with one another. Our initial attempt at developing a classifier was based on the application of traditional pattern recognition techniques such as the Bayesian estimator and the principal components approach [12], [13]. Although mathematically rigorous, these techniques did not lead to classifiers with good classification accuracy. As an alternative, we pursued a different approach that relied very heavily on our understanding of the physics of the scattering process and the experience gained from extensive experimental measurements and theoretical analyses conducted for various types of terrain media. We call the result of this approach a "knowledge-based classifier."

Fig. 3 provides an outline of the classifier design procedure. The first step attempts to separate "urban" pixels from everything else where an urban pixel refers to a ground area containing man-made physical structures such as buildings. Scattering by such structures is characterized by a double-bounce reflection mechanism resulting in a co-polarized phase difference ζ close to ±180°. Additionally, urban scenes exhibit higher values of image texture than do other distributed targets. Fig. 4(a) shows the boundaries of the urban/nonurban discriminator based on ζ_L and $T_{hh}(C)$. Urban pixels are classified as urban with an accuracy of 100%, while a few percent of the nonurban pixels are incorrectly classified as urban. This was purposely done to make sure that all the urban pixels were correctly classified to ensure that urban features were not incorrectly identified as trees. The majority of the misclassified pixels are in areas close to the city of Pellston and along roads and highways (Fig. 5), suggesting that in reality these are "mixed" pixels including buildings along roads and lakefronts.

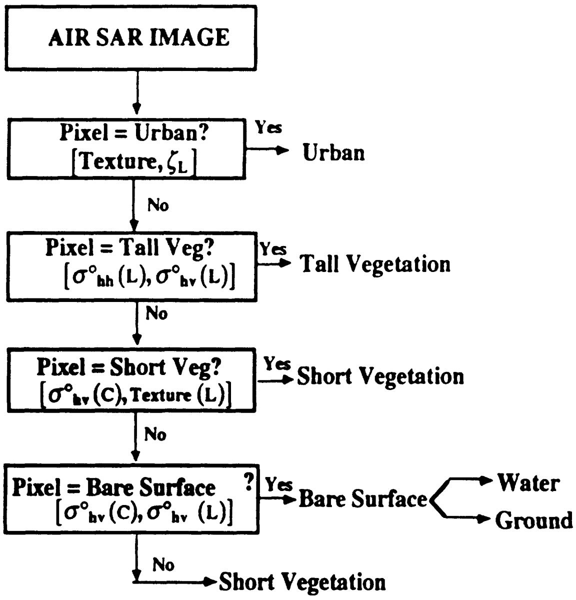

Fig. 3. Classifier design.

After removing all pixels classified as urban from further consideration, the next step is to identify those that are tall vegetation. The single most useful channel in this regard is $\sigma^0_{hv}(L)$, the cross-polarized L-Band backscattering coefficient. This is evident in Fig. 4(b) which shows that tall vegetation can be easily discriminated against the other two remaining categories (bare surface and short vegetation) using this channel. Physically, this is due to large branches in the crown, which generate a much larger cross-polarized return that do smaller leaves and grass. The discrimination can be improved slightly with the additional use of $\sigma^0_{hh}(L)$ (the final classification results are summarized later in Section IV).

After removal of the tall vegetation pixels from further consideration, classifying the remaining pixels among the last two classes (bare surface and short vegetation) involves a two-step process. In the first step, short vegetation pixels are identified on the basis of $\sigma^0_{hv}(C)$ and $T^0_{vv}(L)$, as seen in Fig. 4(c). The remaining pixels are classified as bare if both cross-polarized returns are very low [Fig. 4(d)], while the remaining pixels with a higher cross-polarized return are classified as short vegetation. Physically, water and other bare surfaces are expected to give very low cross-polarized returns due to a lack of large angled features. Very rough water, however, has an increased cross-polarized return, but also increased texture, especially in $\sigma^0_{vv}(L)$.

Pixels that are not classified initially as short vegetation, nor later as bare, are reclassified as short vegetation. This final assignment rule was used because most of the "unclaimed" pixels did indeed belong to the short-vegetation class.

In order for other investigators to try out this classifier on their own images, the equations used for each rule are explain both large texture and a high double-bounce content in the backscattered signal. In a future version of this algorithm a context-sensitive post-processing step will be used to remove anomalous classifications such as these.

IV. Results

The classifier was developed on the basis of SAR data for the training areas shown in Fig. 2. The classification results for pixels in the training areas are given in Table II, and the results for independent test areas are given in Table III. For both training and test areas, the classification accuracy exceeds 98% for three of the four classes, and for the fourth (short vegetation) the classification accuracy is better than 90%.

Note that classification accuracies are not given for the urban class. This has been done for two reasons: 1) since there is only one urban area, testing with the training area is unfair and misleading; and 2) since the urban area is not uniformly filled with urban features, but also contains trees, short vegetation, and surfaces, the classification accuracy calculated over the rectangular urban training stand will be inaccurate. The other three classes have accurate and uniform testing areas and so classification accuracies can be evaluated accurately. The urban class has been optimized so that it appears wherever buildings are known to occur, and does not appear within forested areas.

The classified image, shown in Fig. 5, contains a certain amount of "speckle," which presumably is a result of misclassification. These areas may also be correctly classified areas that are just areas of sparse vegetation surrounded by denser areas. In either case, one may want to apply an "aggregator" to the classified image. In comparing this image to a map produced through air photos, a certain amount of aggregating has already been performed on that data. In order to perform a fair comparison, the SAR classifier should apply a similar aggregation step. The aggregation algorithm used here is very simple: examine a 3 × 3 pixel region surrounding the pixel of interest and if over 70% of these pixels are a particular class, then the center pixel is assigned that class. Application of this aggregator improves the classification accuracy somewhat, but the image has dramatically less "speckle" (Fig. 6).

To allow a visual comparison of classification accuracy, a classification map from 15 years ago [14] is shown in Fig. 7. This map was manually interpreted from air photos. We have reclassified it so that only the four classes that our classifier uses are visible. Note that the airport was classed as an airport (land use) and that we have colored it as short vegetation since that is the majority of the land cover there. The city of Pellston is also a solid polygon because it is a land use rather than land cover map. The remainder of the map shows remarkable similarity to our classified image, except for the few new clear cuts.

The classification algorithm was also applied to a completely different site, Raco, imaged three months earlier, April 1. There are no large urban areas at this site, but

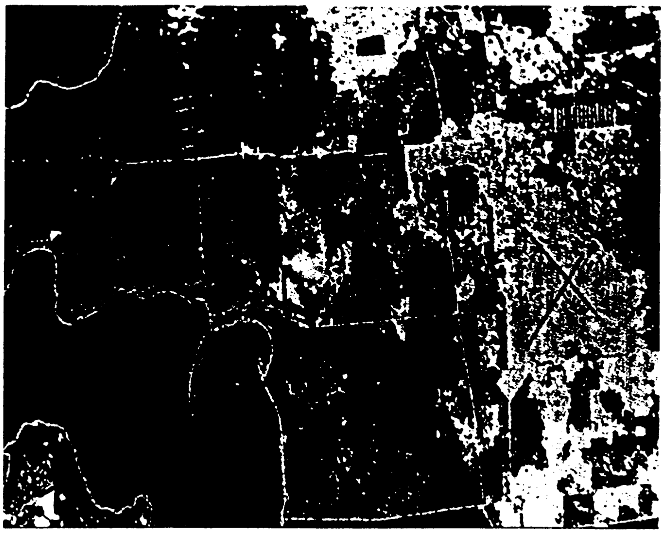

Fig. 6. Fully classified Pellston test site with aggregation. Urban is in white, tall vegetation is green, short vegetation is light brown, bare is blue.

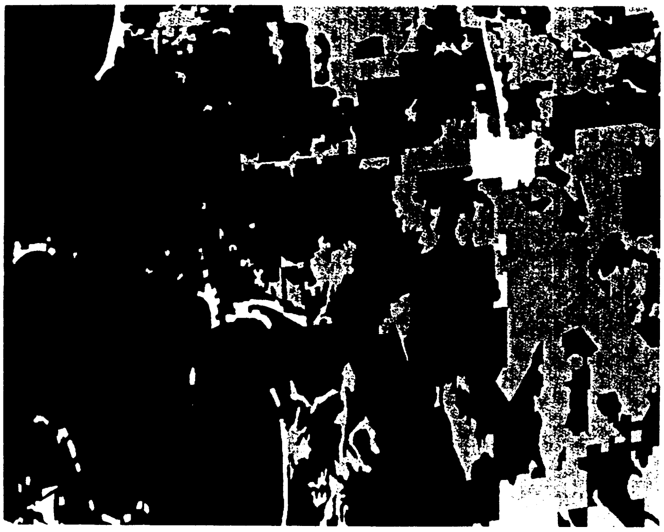

Fig. 7. Manually classified Pellston test site. Abstracted from Michigan DNR MIRIS data [14]. Urban is in white, tell vegetation is green, short vegetation is light brown, bare is blue.

TABLE II
Classification Accuracy, No Aggregation, Pellston Site, Training Areas, July

	True Class		
Classified As	Tall Veg	Short Veg	Bare
Tall Veg	98.32	0.00	0.00
Short Veg	1.46	94.74	0.87
Bare	0.00	5.26	99.07

TABLE III
Classification Accuracy, No Aggregation, Pellston Site, Testing Areas, July

	True Class		
Classified As	Tall Veg	Short Veg	Bare
Tall Veg	98.04	2.84	0.01
Short Veg	1.96	90.77	0.18
Bare	0.00	5.54	99.80

A Microstrip Ring Resonator for Soil Moisture Measurements

Kamal Sarabandi and Eric S. Li

Radiation Laboratory
Department of Electrical Engineering and Computer Science
The University of Michigan
Ann Arbor, MI 48109-2122

ABSTRACT

Accurate determination of spatial soil moisture distribution and monitoring its temporal variation have a significant impact on the outcomes of hydrologic, ecologic and climatic models. Development of a successful remote sensing instrument for soil moisture relies on the accurate knowledge of the soil dielectric constant (ϵ_{soil}) to its moisture content. Two existing methods for measurement of dielectric constant of soil at low and high frequencies are, respectively, the time domain reflectometry and the reflection coefficient measurement using an open-ended coaxial probe. The major shortcoming of these methods is the lack of accurate determination of the imaginary part of ϵ_{soil}. In this paper a microstrip ring resonator is proposed for the accurate measurement of soil dielectric constant. In this technique the microstrip ring resonator is placed in contact with soil medium and the real and imaginary parts of ϵ_{soil} are determined from the changes in the resonant frequency and the quality factor of the resonator respectively. The solution of the electromagnetic problem is obtained using a hybrid approach based on the method of moments solution of the quasi-static formulation in conjunction with experimental data obtained from reference dielectric samples. Also a simple inversion algorithm for $\epsilon_{soil} = \epsilon_r' + j\epsilon_r''$ based on regression analysis is obtained. It is shown that the wide dynamic range of the measured quantities provides excellent accuracy in the dielectric constant measurement. A prototype microstrip ring resonator at L-band is designed and measurements of soil with different moisture contents are presented and compared with other approaches.

1 Introduction

Successful modeling and understanding of global change are dependent upon an improved understanding of climatic and hydrologic processes. Soil moisture and its spatial and temporal variations play an important role in both climatic and hydrologic models. Radar remote sensing of soil moisture has been an ongoing area of research over the past two decades. Characterization of dependence of dielectric constant of soil to its moisture content is an important step in this endeavor. In this paper the theoretical and experimental aspects of a field-portable device for accurate measurement of both the real and imaginary parts of soil dielectric constant are discussed.

Two commonly used methods for field measurement of dielectric constant of soil are the time domain reflectometry (TDR) and the reflection coefficient measurement using an open-ended coaxial probe. In the TDR method the dielectric constant of the soil medium is determined from the delay time of the reflected wave from the open ends of a two-wire transmission line buried inside a soil medium [1]. The time delay can only provide the information about the real part of dielectric constant ϵ_r'. The accuracy of the TDR method is limited by the resolution of the TDR system. In the coaxial probe method [2], the complex dielectric constant is estimated from the measured complex reflection coefficient of the open-ended coaxial line pressed against the unknown material. The accuracy of this technique is limited by the small dynamic range of reflection coefficient as a function of ϵ_r'. Another problem with this technique when applied to soil medium is the small contact area of the coaxial tip which may be comparable to the soil particles. It should also be noted that soil dielectric measurement using coaxial probe is very sensitive to the applied pressure which degrades the accuracy of this measurement technique.

In this paper a microstrip ring resonator as a device for the dielectric measurement of soil is proposed to overcome the aforementioned problems with the existing devices. Application of ring resonators in characterizing the dielectric properties of materials is not a new idea [3, 4, 5]. However, these techniques are specialized for dielectric measurements of thin materials in a stripline configuration and/or only characterization of real part of low dielectric materials is considered. Since both the real and imaginary parts of the dielectric constant of soil have a wide dynamic range with respect to the soil moisture content and the measurement configuration is different from those reported in the literature, a careful theoretical and experimental study of the proposed problem is required. The dielectric measurement technique is very similar to the standard cavity measurement technique [6] with a subtle difference. Basically, the real and imaginary parts of the dielectric constant are to be inferred from the shift in the resonant frequency and the change in the quality factor of the resonator after placing the resonator in contact with the soil medium. The subtlety stems from the fact that the microstrip resonator can be regarded as a partially-filled resonant cavity and therefore the simple relationship between the dielectric constant and the measured changes in the resonant frequency and the quality factor can no longer be applied. Although the partially-filled nature of the microstrip resonators complicates the retrieval of dielectric constant from the measured quantities, it is a desirable feature in the soil dielectric constant measurements. In the standard cavity measurement, if the loss tangent of the dielectric material exceeds 0.05, it becomes practically impossible to accurately measure the resonant frequency (f_0) and the quality factor (Q) of the loaded cavity. However, for the partially-filled resonators the changes in f_0 and Q are substantially less affected by the loading dielectric material. It is shown that with appropriate microstrip resonator design, dielectric constant of soil with moisture content as high as 40% can easily be measured.

In Section 2 the theoretical analysis of the problem is given. In this analysis which will be referred to as the forward problem a numerical solution for calculating the resonant frequency and the quality factor of the resonator in terms of ϵ_r' and ϵ_r'' is provided. The numerical solution is constructed based on a quasi-static formulation. Since the practical microstrip resonators are constructed on finite substrate, the effect of finite substrate width is also investigated. In Section 3 the inverse problem is considered. There, a simple algorithm for retrieval of ϵ_r' and ϵ_r'' from the measured changes in f_0 and Q based on regressional analysis is developed. Finally in Section 4 experimental results are presented. It is shown that the accuracy of the quasi-static solution degrades as the dielectric constant of the unknown material increases. This phenomenon has also been observed in stripline resonators [3]. In this section the theoretical results based on the quasi-static analysis are slightly modified to agree with experimental data obtained from reference dielectric samples. To verify the accuracy of this hybrid model, dielectric constant of a sandy soil with different moisture contents were measured using a prototype microstrip ring resonator and the results are compared with those measured by three other independent methods.

2 Theory

A microstrip ring resonator is a simple transmission line resonator whose geometry is shown in Fig. 1. The resonator is excited by a transmission line through a capacitive coupling and at certain frequencies, depending on the electrical length (perimeter) of the resonator, a standing wave pattern forms around the circular path of the resonator. The maximum voltage of the standing wave occurs at the exciting point. The resonant frequencies correspond to a condition where the perimeter of the ring is an integer multiple of the guided wavelength, that is,

$$\lambda_g = \frac{\pi d}{n} \quad n = 1, 2, 3, \cdots$$

where d is the diameter of the ring and λ_g is a function of the microstrip parameters w_s, h, ϵ_s and ϵ_2 as shown in Fig. 2.

At resonant frequencies there exists a voltage maximum at $\frac{\pi d}{2}$ away from the excitation point. By placing a capacitively coupled transmission line at this voltage maximum point, the field in the resonator can be probed to detect the resonant frequencies. Basically the transmission coefficient S_{21} of the two-port resonator is measured as a function of frequency and the resonant frequencies are identified as frequencies for which $|S_{21}|$ is maximized. It should be noted that the coupling capacitors tend to lower the resonant frequency and these must be as small as possible for accurate measurement of the resonant frequency. Spectral measurement of $|S_{21}|$ can also reveal the quality factor of the resonator which is a measure of power loss in the resonator. The dissipated power in the resonator includes the dielectric loss, the conductor loss and the radiation loss. For a given microstrip resonator with known substrate dielectric constant ϵ_s, strip width w_s, and substrate height h we are seeking an algorithm that would enable us to compute the complex dielectric constant of the half-space medium in contact with the ring resonator from the spectral measurement of $|S_{21}|$. To establish the relationship between the complex dielectric constant of the unknown medium and the measured guided wavelength and the Q of the resonator, the quasi-static approximation for microstrip transmission lines is used. Strictly speaking microstrip structures cannot support TEM waves, however, at low frequency where the substrate height and strip width are small compared to the wavelength, it is expected that the quasi-static approximation provides accurate results [7]. The quasi-static approximations found in the literature are usually concerned with lossless dielectrics. In what follows a brief derivation of Poisson's equation for lossy dielectrics is given from which an integral equation for the charge distribution on the microstrip will be obtained. Starting from Maxwell's equations for time harmonic fields

$$\nabla \times H = j\omega\epsilon' E + \sigma E, \tag{1}$$

$$\nabla \cdot D = \rho_c + \rho_{imp} \quad ; D = \epsilon' E \tag{2}$$

where ρ_c is the conduction charge density, ρ_{imp} is the impressed charge density and ϵ' and σ are the permittivity and conductivity of the medium respectively. The conduction current $J = \sigma E$ can be related to the conduction charge density ρ_c through the continuity relationship $\nabla \cdot J = -j\omega\rho_c$ and therefore

$$\frac{j\sigma}{\omega}\nabla \cdot E = \rho_c. \tag{3}$$

Combining (3) and (2) and defining the complex permittivity as $\epsilon = \epsilon' - \frac{j\sigma}{\omega}$, it can easily be shown that

$$\epsilon \nabla \cdot E = \rho_{imp}. \tag{4}$$

For TEM waves the electric and magnetic fields are irrotational and therefore the electric field can be obtained from a complex potential function ϕ through

$$E = -\nabla\phi$$

which together with (4) results

$$\nabla^2\phi = -\frac{\rho_{imp}}{\epsilon}. \tag{5}$$

Assuming the ground plane and the strip of the microstrip are at potentials zero and V_0, (5) can be solved subject to the boundary conditions. In this case $\rho_{imp} = \rho(x)$ is the induced charge distribution on the strip. If $G(x, y, x', y')$ represents the Green's function of the problem, then the complex potential function can be obtained from

$$\phi(x, y) = \int_{\frac{-w}{2}}^{\frac{w}{2}} \rho(x') G(x, y, x', y') dx'.$$

Using the Fourier transform technique the Green's function for the microstrip problem is found to be

$$G(x-x',y,h)=\frac{1}{\pi}\int_0^\infty \frac{e^{-\alpha(y-h)}\cos(\alpha(x-x'))}{(\epsilon_s\coth(\alpha h)+\epsilon_2)\alpha}d\alpha, \tag{6}$$

where ϵ_s is the dielectric constant of the substrate and ϵ_2 is the dielectric constant of the upper half-space. Since the potential function is known over the metalic strip, the integral equation for the induced charge density can be derived by evaluating the potential over the strip and is given by

$$V_0=\int_{\frac{-w}{2}}^{\frac{w}{2}} \rho(x')G(x-x',h,h)dx'. \tag{7}$$

The integral equation can be solved numerically using the method of moments and point matching technique. Subdividing the strip into N sufficiently small cells, (7) can be cast into a matrix equation

$$\bar{\bar{Z}}\bar{R}=\bar{V}$$

where $\bar{R}$ is the vector of unknown charge density and $\bar{V}$ is the excitation vector whose entries are constant V_0 potentials. To evaluate entries of $\bar{\bar{Z}}$, the Green's function given by (6) must be computed for different values of observation (x_m) and source (x_n) points. The decay rate of the integrand of (6) (when $y=h$) as a function of α is rather poor (the asymptotic behavior of the integrand for large values of α is $\frac{1}{\alpha(\epsilon_s+\epsilon_2)}$). To improve the convergence rate the order of integrations in (7) can be changed and the entries of the matrix are found to be

$$Z_{mn}=\frac{2}{\pi}\int_0^\infty \frac{\sin(\alpha\frac{\Delta x}{2})\cos(\alpha(x_m-x_n))}{\alpha^2[\epsilon_s\coth(\alpha h)+\epsilon_2]}d\alpha \tag{8}$$

where $\Delta x=\frac{w}{N}$. It is noted that the impedance matrix is Toeplitz and symmetric, that is, $Z_{mn}=Z_{pq}$ when $m-n=p-q$ and $Z_{mn}=Z_{nm}$. Thus integral in (8) must be evaluated only N times to fully characterize the impedance matrix. Once the impedance matrix is characterized the charge density can be obtained from

$$\bar{R}=\bar{\bar{Z}}^{-1}\bar{V}\ .$$

The quantities of interest in the microstrip resonator are the electrical length and the quality factor of the resonator which are directly related to the line capacitance and conductance. The line capacitance is proportional to the total charge in phase with the voltage and the line conductance is proportional to the conduction current. The total complex charge on the strip represented by $Q=Q_r+jQ_i$ can be obtained from

$$Q=\int_{\frac{-w}{2}}^{\frac{w}{2}} \rho(x)dx \simeq V_0\sum_i\sum_j Z_{ij}^{-1}$$

from which the line admittance can be calculated and is given by

$$Y=\frac{I}{V_0}=j\omega\frac{Q}{V_0}=j\omega\sum_i\sum_j Z_{ij}^{-1}.$$

It can be shown that over a narrow range of frequency the microstrip line behaves like a capacitor in parallel with a resistor. The line capacitance and conductance thus are given by

$$C = \sum_i \sum_j Re[Z_{ij}^{-1}] \quad F/m \tag{9}$$

$$G = -\omega \sum_i \sum_j Im[Z_{ij}^{-1}] \quad S/m. \tag{10}$$

For wideband applications a more complicated equivalent circuit must be considered. Assuming that the substrate material and the upper half-space medium are nonmagnetic, the line inductance becomes only a function of geometrical feature of the line and can be obtained from magnetostatic analysis. An alternative approach is to find the line capacitance of the air-filled microstrip line (C_0) and find the line inductance from

$$L = \frac{1}{C_0 V_p^2}$$

where V_p=3×10^8 m/s is the phase velocity of the air-filled line [7]. To check the validity and accuracy of the numerical method, the line capacitance computed by the method of moments with $\epsilon_2 = 1.0$ and $\epsilon_s = 6.15$ is compared with the line capacitance computed using the conformal mapping technique and is shown in Fig. 3.

The quality factor of the resonator is defined as the ratio of the total average energy stored in the resonator to the power dissipated in a cycle. At resonance $W_e = W_m = \frac{1}{4}CV^2$, thus the quality factor due to the dielectric loss can be obtained from [6]

$$Q_d = \omega \frac{W_e + W_m}{P} = \omega \frac{\frac{1}{2}CV^2}{\frac{1}{2}GV^2} = \frac{\omega C}{G}. \tag{11}$$

Another issue of practical importance is the finiteness of the substrate. The theoretical analysis given above is valid when the microstrip ground plane is of infinite extent. In practice the resonator substrate is finite and its effect on the line capacitance and conductance per unit length derived for microstrip with infinite ground plane must be investigated. Fig. 2 shows a microstrip with finite substrate and ground plane in contact with a half-space homogeneous medium. Our objective here is to characterize the smallest substrate width w_g so that the difference between the line capacitance per unit length in this case and that of the infinite substrate is negligible. In this case a simple integral equation for the surface charge density on the strip and ground plane is obtained. The substrate dielectric is replaced with the induced polarization charge

$$\rho_p = \epsilon_0(\epsilon_s - 1)\,[\delta(\vec{r} - \vec{r_c})\hat{n} \cdot E - \nabla \cdot E] \tag{12}$$

where $\vec{r_c}$ is a position vector that specifies the contour of the substrate (C) and $\hat{n}$ is an outward unit vector normal to the substrate boundary. After applying the Green's theorem the integral equation for the surface charge density and the complex potential function is found to be

$$(\frac{\epsilon_s+1}{2})\phi(x,y) = -\epsilon_0(\epsilon_s-1)\int_C \phi(x',y')\frac{\delta G(x,y;x',y')}{\delta n'}dc + \int_{-w_s/2}^{w_s/2}\rho_s(x')G(x,y;x',0)dx' + \int_{-w_g/2}^{w_g/2}\rho_g(x')G(x,y;x',-h)dx' \quad (13)$$

where $G(x,y;x',y')$ is the Green's function of the half-space dielectric problems and is given by

$$G(x,y;x',y') = -\frac{1}{2\pi\epsilon_0}\left[\ln\sqrt{(x-x')^2+(y-y')^2} - \frac{\epsilon_2-1}{\epsilon_2+1}\ln\sqrt{(x-x')^2+(y+y')^2}\right]. \quad (14)$$

Once the integral equation is solved numerically the line capacitance and conductance per unit length can be obtained as shown before. Fig. 4 shows the line capacitance of a finite substrate microstrip line with $\epsilon_s = 6.15$, $h = 0.245cm$, and $w_s = 0.37cm$ as a function of w_g/w_s for $\epsilon_2 = 1$. It is shown that when $w_g/w_s > 5$ the formulation based on infinite substrate is accurate for computation of the line capacitance.

3 Inversion Algorithm

In this section a retrieval algorithm for the complex dielectric constant of a half-space dielectric medium in contact with a microstrip ring resonator is sought. Following the standard cavity dielectric measurement approach the real and imaginary parts of the effective dielectric constant of the loaded resonator can be obtained from which the complex dielectric constant of the half-space medium must be inferred. Basically, first the resonant frequencies of the loaded (resonator in contact with the dielectric medium) and unloaded (resonator in free space) resonators are found from the measured frequency spectrum of $|S_{21}|$. Then noting that at resonance the electrical length of the resonator is equal to the guided wavelength, it can easily be shown that:

$$\frac{f^u}{f^l} = \frac{Re[\sqrt{\epsilon^l_{eff}}]}{\sqrt{\epsilon^u_{eff}}} \quad (15)$$

where f^l and f^u are, respectively, the resonant frequencies of the loaded and unloaded resonators. Since the ring resonator is a transmission line resonator, the relationship between the effective dielectric constant and the line parameters can be obtained from:

$$k_0\sqrt{\epsilon_{eff}} = \omega\sqrt{LC(1-j\frac{G}{\omega C})}.$$

Assuming the substrate is lossless ($G^u = 0$) and noting that the line inductance is not a function of dielectric loading, it can be shown that

$$C^l = C^u\frac{\epsilon'^l_{eff}}{\epsilon^u_{eff}} \quad (16)$$

$$\frac{G^l}{\omega^l C^u} = \frac{\epsilon''^l_{eff}}{\epsilon^u_{eff}}. \tag{17}$$

Comparing (17) to (11) and using (16), the imaginary part of the effective dielectric constant of the loaded resonator can be obtained from

$$\epsilon''^l_{eff} = \frac{\epsilon'^l_{eff}}{Q_d}. \tag{18}$$

Using (15) and (18) the real part of the effective dielectric constant of the loaded resonator ϵ'^l_{eff} in terms of measured $\frac{f^u}{f^l}$ and Q_d and ϵ^u_{eff} can be obtained. Once ϵ'^l_{eff} and ϵ''^l_{eff} are obtained the line capacitance and conductance can be derived from (16) and (17).

Besides the dielectric loss, other factors such as radiation and conduction losses determine the quality factor of the resonator. If Q_u represents the quality factor of the unloaded resonator and Q_d is the quality factor due to the dielectric loss, the measured quality factor of the resonator (Q_m) can be obtained from [6]

$$\frac{1}{Q_m} = \frac{1}{Q_u} + \frac{1}{Q_d}. \tag{19}$$

Equation (19) can be used to measure Q_d when the radiation losses of the loaded resonator and unloaded resonator are the same or the radiation loss is negligible compared to the conductor and substrate losses. This can be verified by measuring the quality factor of the resonator when loaded with different lossless dielectrics. However, if the radiation loss is significant and varies with dielectric loading, (19) can be modified to

$$\frac{1}{Q_m} = \frac{1}{Q_u} + \frac{1}{Q_r} + \frac{1}{Q_d} \tag{20}$$

where Q_r the quality factor due to radiation loss and its dependency to ϵ'_2 must be determined empirically. As will be shown later, for most soil conditions $Q_d << Q_u$ and therefore characterization of Q_r with respect to ϵ'_2 is not necessary.

The last step in the inversion algorithm is the computation of ϵ'_2 and σ_2 from the measured C^l and G^l. In the previous section a numerical forward model for computation of the line capacitance and conductance in terms of ϵ'_2 and σ_2 was developed. Computation of the forward model for various ϵ'_2 and σ_2 reveals that C^l and G^l are smooth functions of ϵ'_2 and σ_2. Over the region of interest for ϵ'_2 and σ_2 these functions are one-to-one and onto which implies that the inverse functions exist. Since $C(\epsilon'_2, \sigma_2)$ and $G(\epsilon'_2, \sigma_2)$ are gentle functions of ϵ'_2 and σ_2, the inverse functions are also gentle functions of C and G. To demonstrate this fact, ϵ'_2 and σ_2 versus the line capacitance and conductance of a microstrip with $\epsilon_s = 6.15$, $h = 0.245cm$, and $w_s = 0.37cm$ are calculated numerically and are shown in Figs. 5 and 6. It is shown that the line capacitance is strongly dependent on ϵ'_2 and less influenced by σ_2 as expected. Also the line conductance is most sensitive to σ_2 and to a lesser extent to ϵ'_2 . Therefore the inverse functions can simply be approximated by their Taylor series expansions, that is

$$\begin{aligned}\epsilon_2 \approx\, & a_0 + a_1 C + a_2 G + a_3 CG + a_4 C^2 + a_5 G^2 + a_6 CG^2 + a_7 C^2 G + a_8 C^3 + a_9 G^3 \\ & + a_{10} C^2 G^2 + a_{11} CG^3 + a_{12} C^3 G + a_{13} C^4 + a_{14} G^4\end{aligned} \tag{21}$$

$$\begin{aligned}\sigma_2 \approx\, & b_0 + b_1C + b_2G + b_3CG + b_4C^2 + b_5G^2 + b_6CG^2 + b_7C^2G + b_8C^3 + b_9G^3 \\ & + b_{10}C^2G^2 + b_{11}CG^3 + b_{12}C^3G + b_{13}C^4 + b_{14}G^4. \end{aligned} \tag{22}$$

The coefficients of the polynomials can be obtained from the forward model using at least fifteen pairs of (C, G). However, in order to find better estimate of the coefficients much more data points over the region of interest should be used in a least-mean-square estimator. Once the coefficients are determined the measured C and G can directly be used in (21) and (22) to find the unknowns ϵ_2' and σ_2.

4 Experimental Results

In this section the design considerations for the development of a prototype microstrip ring resonator and some experimental results are given. Prompted by the need for a high quality factor transmission line resonator, the ring resonator as opposed to other types of transmission line resonators, such as a half-wavelength straight line resonator, was chosen. Another attractive feature of this resonator in measuring the dielectric constant of soil is its relatively large contact area with the soil medium. The coupling of energy to the resonator is accomplished using an unconventional method. Ring resonators are usually excited by a microstrip line through a capacitive air gap as shown in Fig. 7. However, for dielectric measurement applications it is better to excite the resonator with an open-ended coaxial line placed right underneath of the conducting strip as shown in Fig. 1. In this method the coupling capacitance of the resonator is not affected by the dielectric constant of the unknown material and therefore the quality factor due to the resonator coupling (Q_u) remains unchanged. Another important design parameter is the resonator filling factor. This parameter signifies the percentage of the stored electric energy in the substrate to the overall stored energy. For example to measure very lossy dielectrics a large filling factor is required to keep most of the field lines inside the substrate. The filling factor is directly proportional to the line capacitance of the unloaded microstrip (inversely proportional to the unloaded characteristic impedance).

A microstrip ring resonator with a moderate filling factor that would allow accurate dielectric measurement of soil with volumetric moisture contents varying from 0% to 30% was designed using trial and error. It was found that a line with characteristic impedance of 50Ω would satisfy the filling factor requirements. For the prototype design, a Duroid 6006 substrate with $\epsilon_s = 6.15$ and $h = 0.254cm$ was used. The strip width and the ring perimeter for the required unloaded characteristic impedance of 50Ω and resonant frequency of 1.25 GHz were calculated to be $w_s = 0.37cm$ and $\ell = 11.35cm$ respectively. The dimension of the finite substrate was chosen so that the constraint $w_g/w_s > 5$ is satisfied for every point on the circular ring of the resonator. To examine the accuracy of the measurement technique and the aforementioned inversion algorithm, lossless reference dielectric samples were measured. An HP 8720 Network Analyzer with synthesized source was used to measure the quality factors and resonant frequencies reported in this paper. Six thick reference dielectric slabs (Stycast) with nominal dielectric constants of 2.2, 3, 6, 10, 13, and 16 were measured using the prototype resonator. It was found that the measurement accuracy degrades as the dielectric constant of the medium increases.

The experiments indicate that the quasi-static approximation overestimates the line capacitance when the dielectric constant of the half-space medium is increased. To investigate this phenomenon, two methods were pursued: (1) experimental, and (2) numerical. In the experimental investigation the effect of surface waves and the quasi-TEM nature of the approximate solution were examined. It is known that when the substrate height h is large the structure becomes capable of supporting surface waves in the substrate. Three thinner substrates were used to construct ring resonators (all with characteristic impedance of 50Ω) and the measurements with reference samples were repeated. Same amount of discrepancies were obtained independent of substrate thickness. Next we examined the effect of quasi-TEM approximation in our formulation. For this purpose, a resonator was made from Duroid 6010 substrate with $\epsilon_s = 10$ and used to measure the permittivity of the Stycast sample with dielectric constant 10. In this case the medium surrounding the microstrip is homogeneous and the fundamental mode of propagation is TEM. However, a discrepancy in the measured dielectric on same order as before was observed. Having obtained inconclusive results from our experimental investigation, we resorted to numerical techniques. First a full-wave analysis for calculation of the effective propagation constant in microstrip lines based on the method of moments was used [8]. It was found that for the frequencies and microstrip dimensions used in this investigation the quasi-static solution provided very accurate results. Next the problem was analyzed completely using a three-dimensional FDTD numerical code [9]. After 20,000 iteration corresponding to 7 hours CPU time on a Cray super-computer, it was found that the resonant frequency obtained by the FDTD method had more discrepancy with the measured one than that obtained from the quasi-static method. One possible reason for the larger error is that the time domain methods may not be very suitable for resonant structures.

As a final resort we decided to rectify the problem by including an empirical correction factor in the quasi-static solution. Let us denote the line capacitances derived from the quasi-static solution and those measured from the inversion algorithm by C_q and C_m respectively. Fig. 8 shows the discrepancy in the line capacitance ($\Delta C = C_q - C_m$) as a function of the six measured dielectric constants. Since the measured discrepancy is a smooth function of ϵ_2 and no discrepancy exist when $\epsilon_2 = 1$ the following expression for the corrected line capacitance is obtained:

$$C_c = C_q - k(\epsilon_2' - 1), \tag{23}$$

where $k = 2.46 \times 10^{-12}$ is calculated using a least-mean-square linear estimator. This corrected line capacitance is then used in (21) and (22) to derive the coefficients $a_1 \cdots a_{14}$ and $b_1 \cdots b_{14}$. These coefficients are listed in Table 1 for a microstrip with $\epsilon_s = 6.15$, $h = 0.254cm$, and $w_s = 0.37cm$.

Next the behavior of the dielectric constant of a sandy soil as a function of moisture content is studied. The prototype ring resonator is used to measure soil samples with volumetric moisture contents ranging from 0% to 30%. Fig. 9 shows typical responses of the ring resonator in contact with soil samples having moisture contents ranging from 0% to 30%. Three other independent techniques were also used to measure the soil samples. These include the open-ended coaxial probe, cavity resonator, and air-filled coaxial line. The dielectric measurement using air-filled coaxial line is based on reflection coefficient measurement of a short-circuited coaxial line filled with soil samples. In this method the middle section of a long hollow coaxial line is used as the sample holder as shown in Fig. 10. Measuring the reflection coefficient over a wide bandwidth (B) and using the time domain capability of the network analyzer, the reflected signal after traveling twice through the sample can be measured. The hollow section of the coaxial line must be longer than the spatial resolution ($3 \times 10^8/2B$) of the system. Fig. 11 shows the steps involved in measuring the reflection coefficient of the short circuit for a 50Ω air-line of length $l = 50cm$ filled with $d = 20cm$ of dry sand. The measured complex reflection coefficient is related to the dielectric constant of the sample through

$$S_{11} = -(1 - R^2)^2 e^{-j2k_0 l} e^{-j2k_0(\sqrt{\epsilon_r}-1)d}, \tag{24}$$

where $R = \frac{1-\sqrt{\epsilon_r}}{1+\sqrt{\epsilon_r}}$ is the reflection coefficient at the interface of air and soil. By inverting (24) the real and imaginary parts of the soil dielectric are obtained. The accuracy of this method decreases as the imaginary part of the dielectric constant increases unless the sample length is decreased.

Figs. 12 and 13 show the measured real and imaginary parts of the dielectric constants of the sandy soil with seven different moisture contents using the four independent measurement techniques. The cavity method could only be used for the 0% and 5% moisture conditions and shows an excellent agreement with the ring resonator measurement. For the real part of the dielectric constant the agreement among all four techniques is very good. However, it is shown that the coaxial probe overestimates the imaginary part of the dielectric constant as the moisture content increases.

5 Conclusions

Theoretical, numerical, and experimental aspects of a microstrip ring resonator based dielectric measurement device are discussed in this paper. The real and imaginary parts of dielectric constant of a homogeneous medium in contact with the ring resonator is calculated from the shift in the resonant frequency and the change in the quality factor of the resonator. The solution to the forward problem is obtained from a numerical analysis of the quasi-static solution. For the inverse problem simple algebraic expressions based on regression analysis of the forward problem are also obtained. Measurements of reference dielectric samples showed that the accuracy of the quasi-static solution decreases as the dielectric constant of the half-space medium increases. To identify the source of error, full-wave numerical analysis and extensive experiments were conducted. Our efforts in identifying the source of errors were inconclusive. The errors in the quasi-static solution are corrected empirically from which the inversion expressions are obtained. The validity of the ring resonator measurement technique is demonstrated by comparing the measured dielectric constants of a sandy soil with different moisture contents with those obtained from three other measurement methods. It is shown that the measurement technique is both accurate and versatile. The ring resonator, because of its large contact area, is very suitable for dielectric measurement of soil and can easily be constructed into a field portable device.

Acknowledgement: This project was supported by NASA under contact NAGW-2151.

References

[1] Topp, G.C. and J.L. Davis,"Measurement of Soil Water Content Using Time-domain Reflectrometry (TDR): A Field Evaluation", *Soil Sci. Soc. Am. J.*, vol. 49, pp. 19–24, 1985.

[2] Ulaby, F.T., T.H. Bengal, M.C. Dobson, J.R. East, J.B. Garvin and D.L. Evans, "Microwave Dielectric Properties of Dry Rocks", *IEEE Trans. on Geoscience and Remote Sensing,* vol. 28, no.3, pp. 325–336, May. 1990.

[3] Bernard, P.A. and J. M. Gautray, "Measurement of Dielectric Constant Using a Microstrip Ring Resonator", *IEEE Trans. on Microwave Theory and Techniques,* vol. 39, no. 3, pp. 592–595, March 1991.

[4] Hoffman, R.K., Handbook of Microwave Integrated Circuits, Norwood, MA: Artech House, 1987.

[5] Vainikainen, P.V., E.G. Nyfors, and M.T. Fischer, "Radiowave Sensor for Measuring the Properties of Dielectric Sheets: Application to Veneer Moisture Content and Mass per Unit Area Measurement", *IEEE Trans. Inst. Measurement,* vol. 36, no. 4, Dec. 1987.

[6] Collin, R.E., Foundations for Microwave Engineering, New York: McGraw-Hill, pp 317–329, 1966.

[7] Elliott, R.S., An Introduction to Guided Waves and Microwave Circuits, Englewood Cliffs, New Jersey: Prentice Hall, pp 61–67, 1993.

[8] Jackson, R.W. and D. M. Pozar, "Full Wave Analysis of Microstrip Open-end and Gap Discontinuities", *IEEE Trans. on Microwave Theory and Techniques,* vol. MTT-33, no. 10, pp. 1036–1042, Oct. 1985.

[9] Dib, N., Personal Communication.

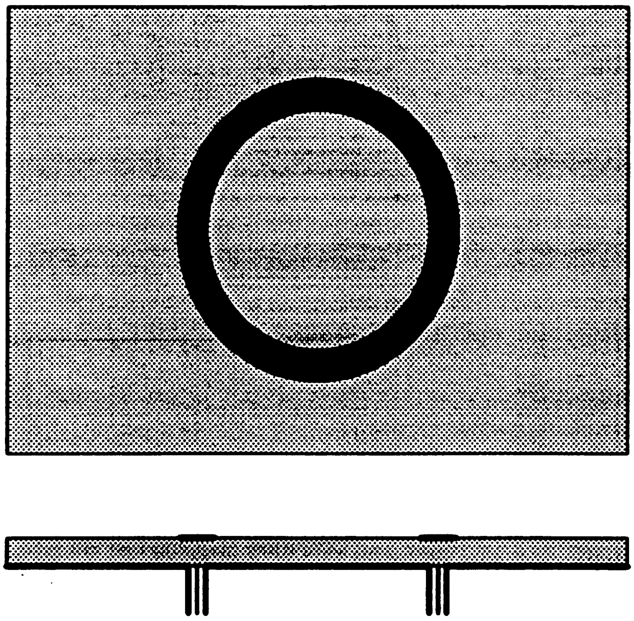

Figure 1: Top view and side view of a ring resonator used in this investigation.

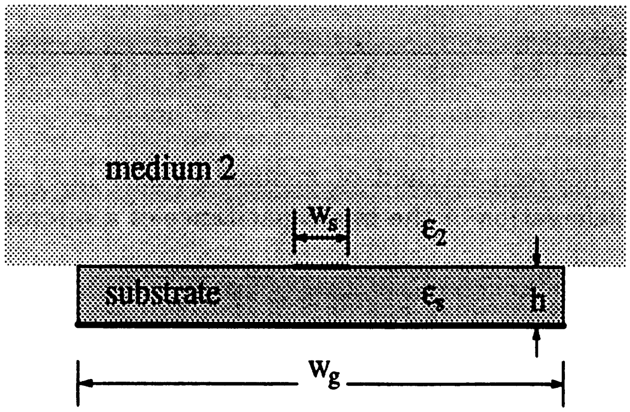

Figure 2: Geometry of a microstrip line in contact with a half-space homogeneous dielectric medium.

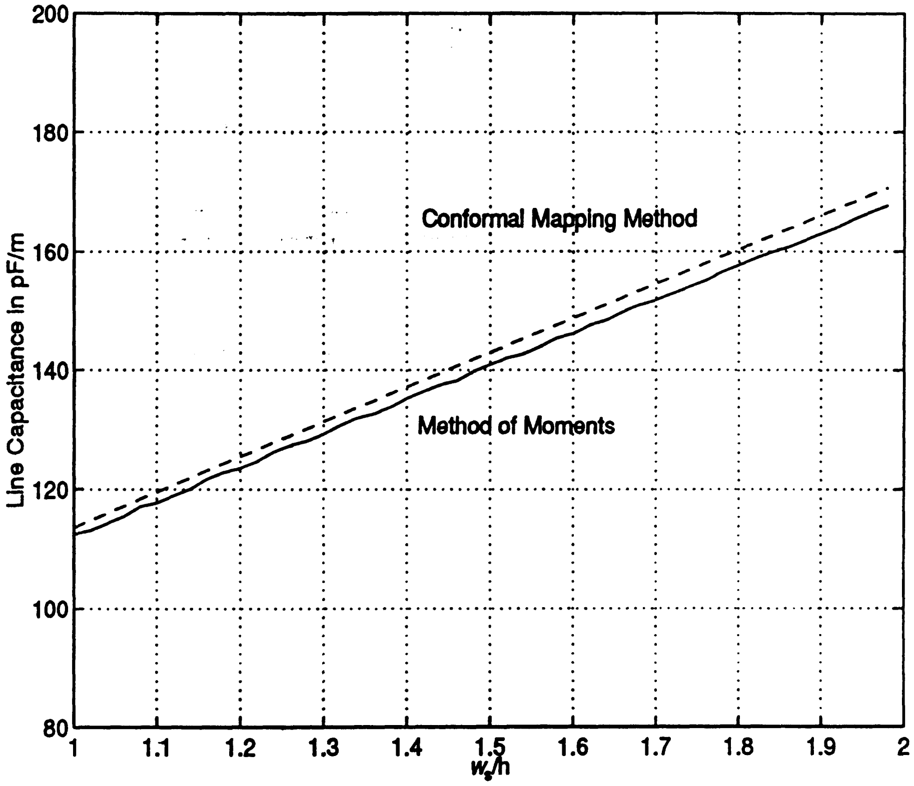

Figure 3: Comparison between method of mements (solid line) and conformal mapping method (dash line) in calculation of the line capacitance of a microstrip line with ϵ_s=6.15.

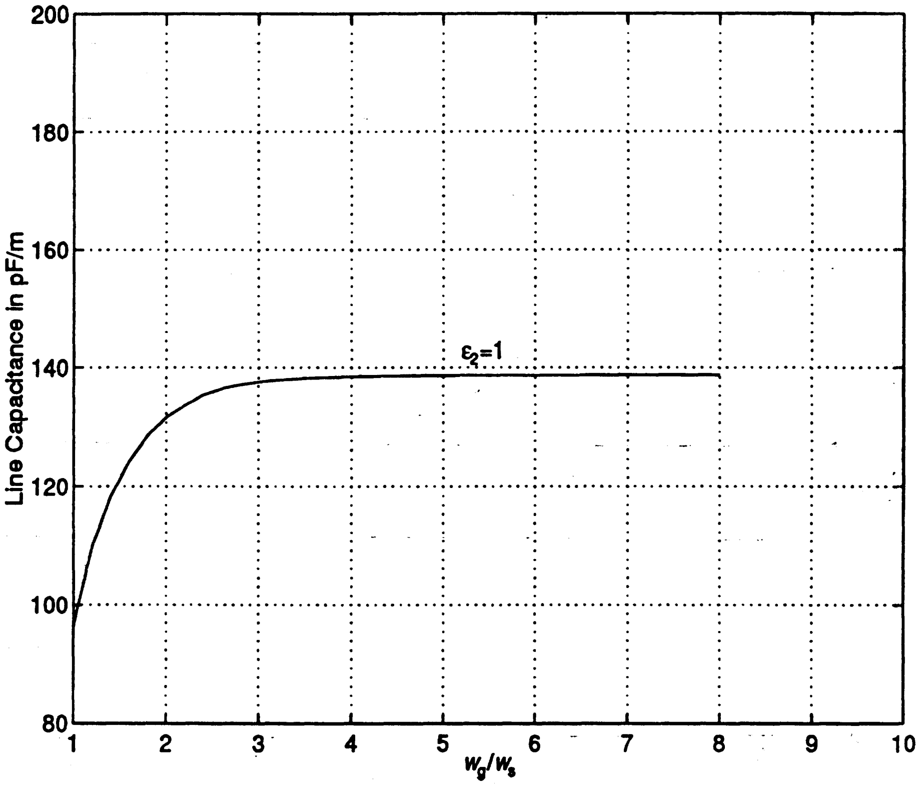

Figure 4: Line capacitance of a finite substrate microstrip line with ϵ_s=6.15 and w_s/h=1.46 as a function of w_g/w_s.

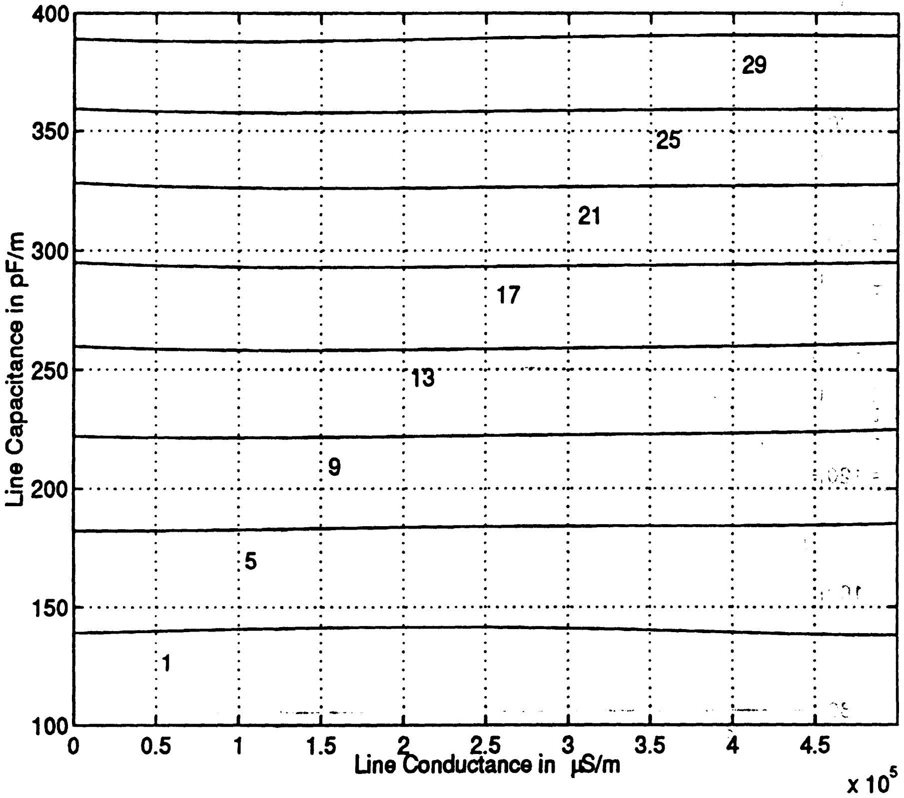

Figure 5: Contour map of the real part of dielectric constant as a function of line conductance and capacitance for a microstrip line with ϵ_s=6.15 and w_s/h=1.46.

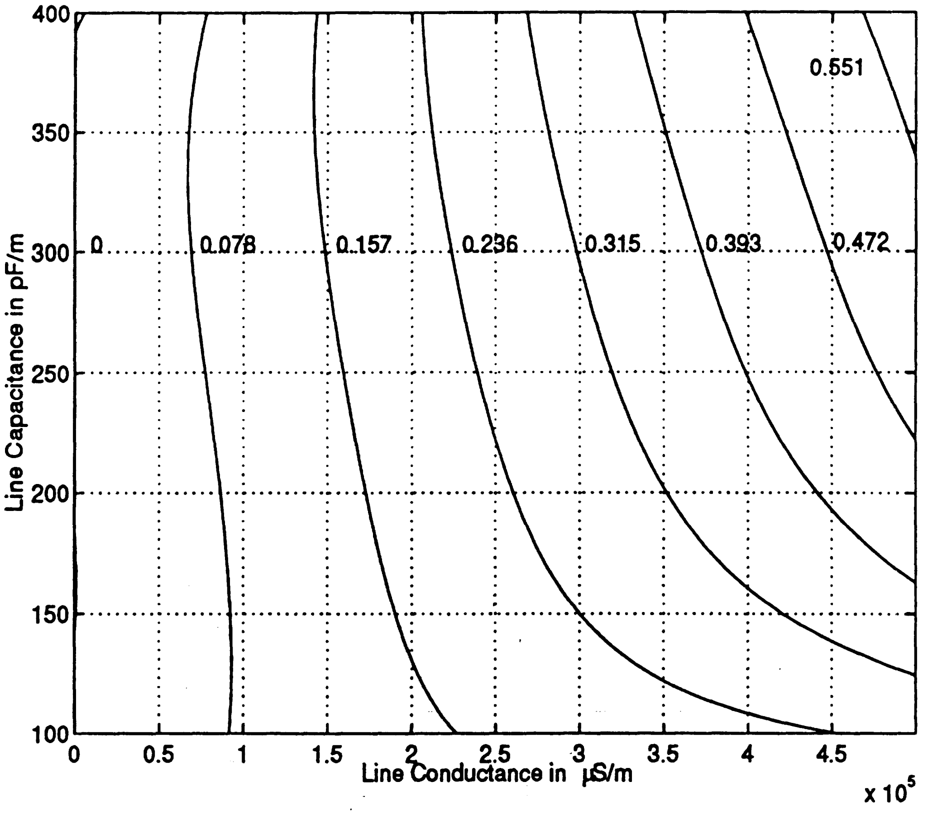

Figure 6: Contour map of conductivity as a function of line conductance and capacitance for a microstrip line with ϵ_s=6.15 and w_s/h=1.46.

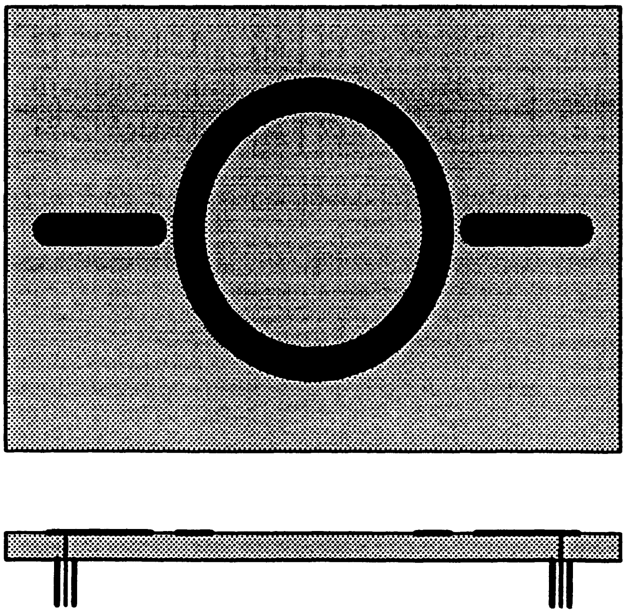

Figure 7: Top view and side view of a conventional ring resonator.

ϵ_2'		σ_2	
a_0	-0.787696E+01	b_0	0.333251E-01
a_1	0.113820E-01	b_1	-0.419435E-03
a_2	-0.625590E-06	b_2	0.619400E-07
a_3	-0.170414E-07	b_3	0.907383E-08
a_4	-0.437116E-03	b_4	0.755818E-06
a_5	0.518208E-11	b_5	-0.924463E-12
a_6	-0.858796E-13	b_6	0.863279E-14
a_7	0.193313E-09	b_7	-0.346372E-10
a_8	-0.465772E-06	b_8	0.610040E-08
a_9	0.628353E-17	b_9	-0.300749E-18
a_{10}	0.130853E-15	b_{10}	-0.121781E-16
a_{11}	0.344406E-19	b_{11}	-0.313788E-20
a_{12}	-0.386692E-12	b_{12}	0.504362E-13
a_{13}	0.359810E-09	b_{13}	-0.167593E-10
a_{14}	-0.123399E-22	b_{14}	0.903452E-24

Table 1: Taylor polynomial coefficients for ϵ_2' and σ_2 respectively.

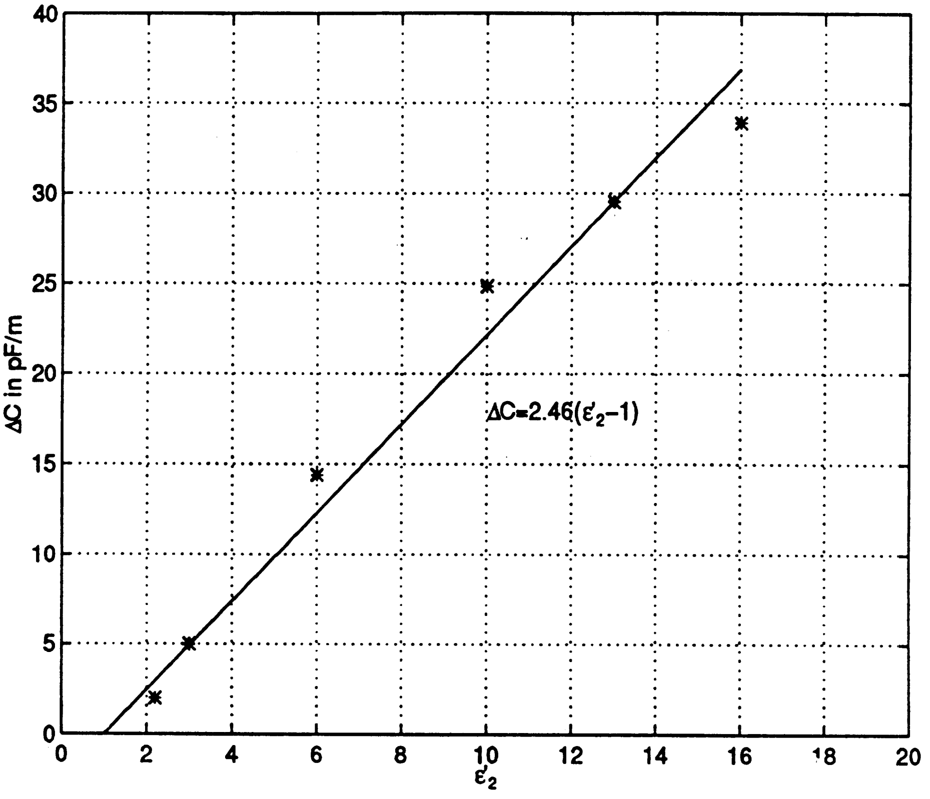

Figure 8: ΔC as a function of ϵ'_2.

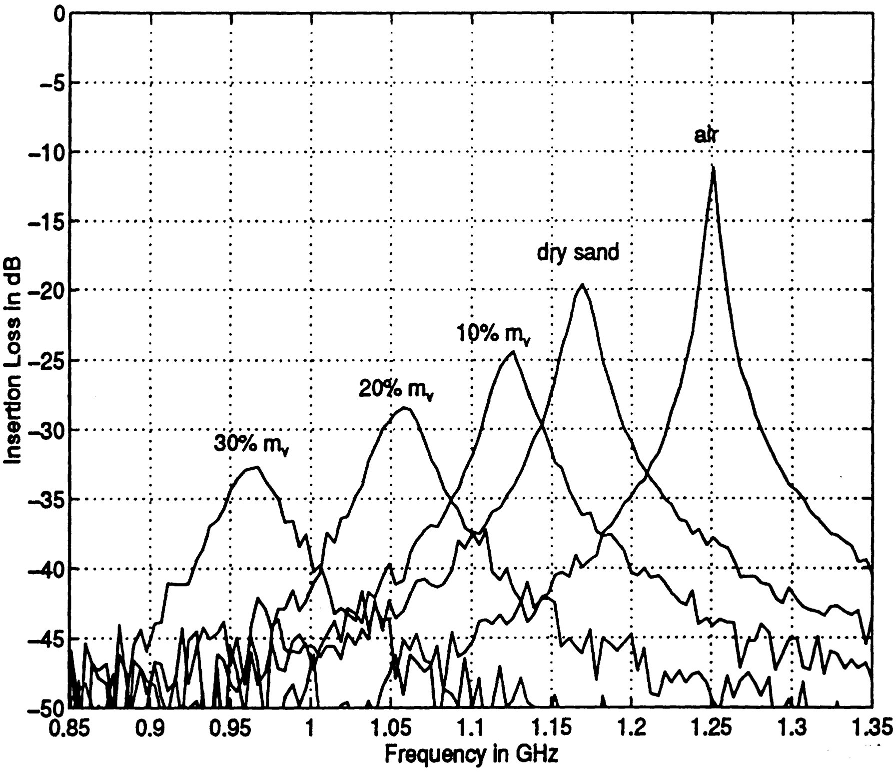

Figure 9: Sand moisture spectral response.

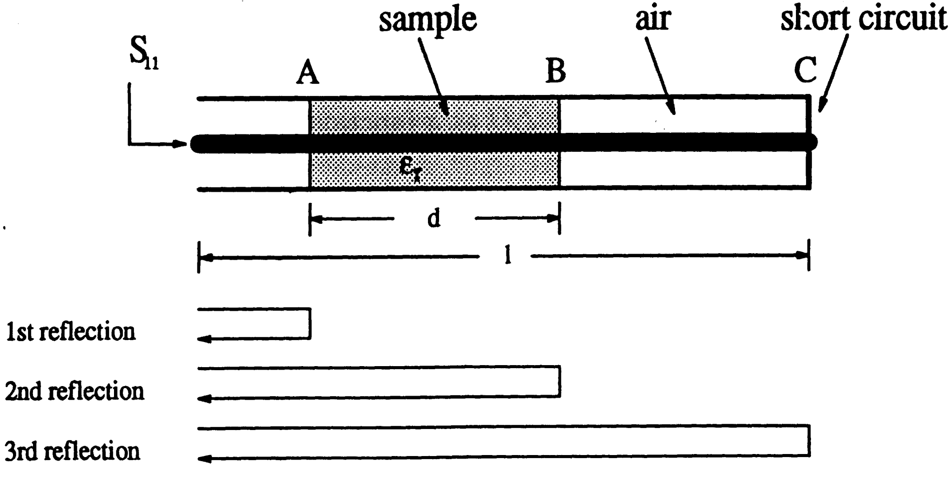

Figure 10: The air-filled coaxial line sample holder.

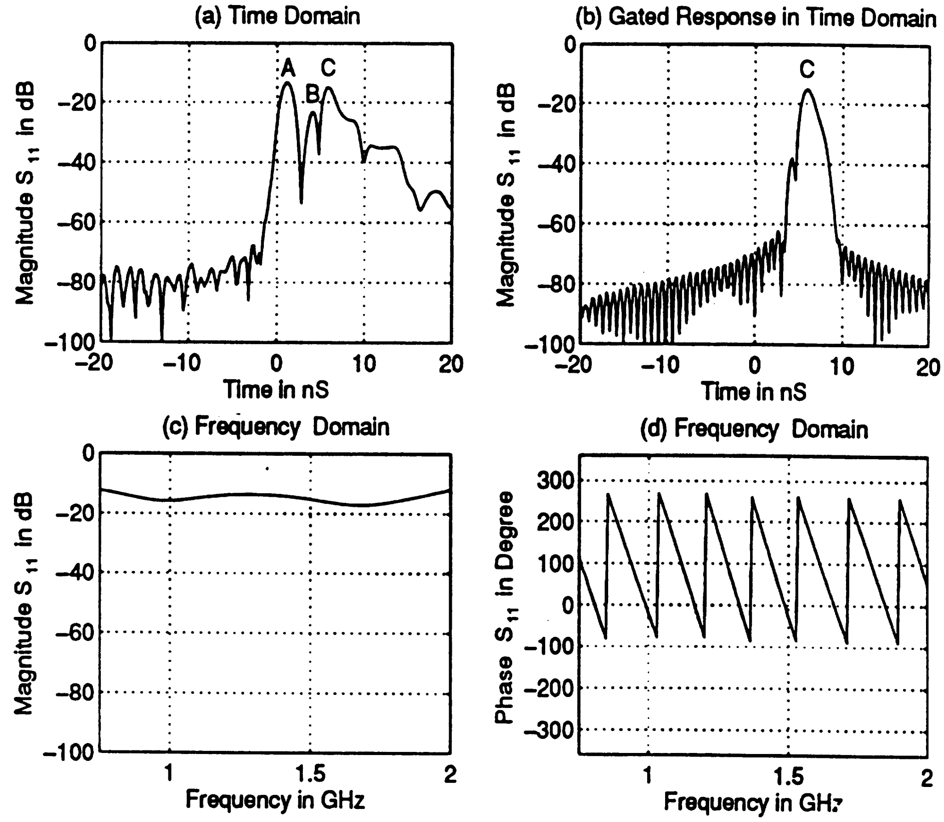

Figure 11: Steps in the measurement of the short circuit reflection coefficient: (a) time domain response of the total reflection coefficient, (b) time domain gated response of the short circuit, (c) magnitude and (d) phase of the short circuit reflecton coefficient.

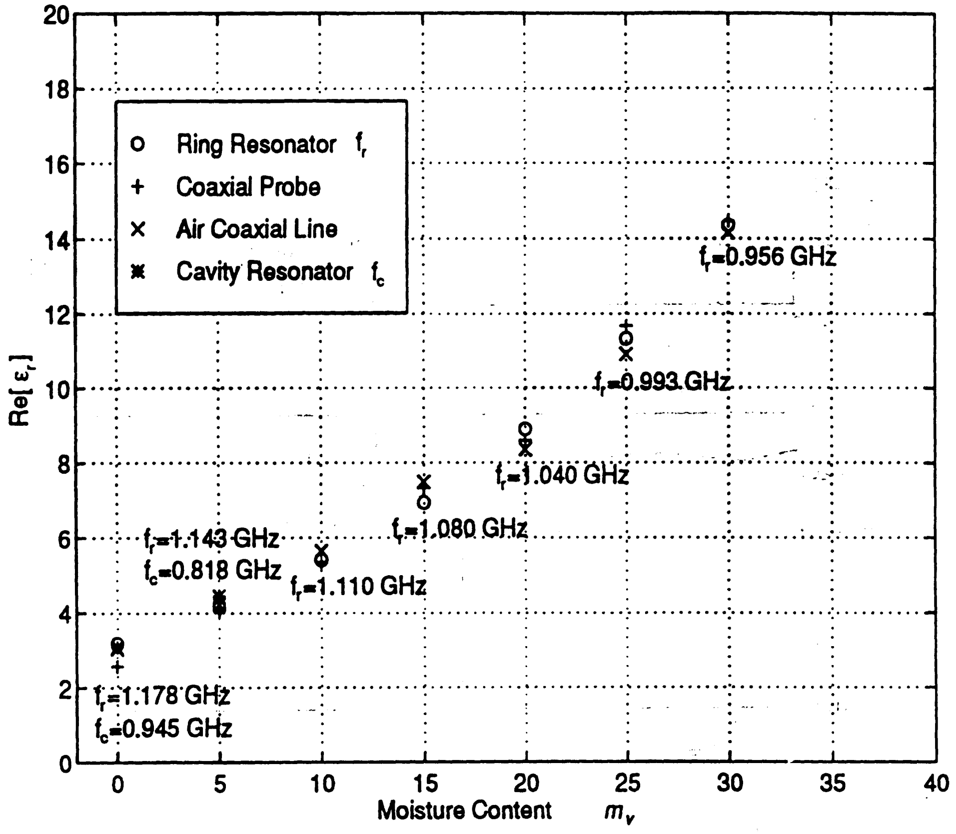

Figure 12: Different methods for measuring ϵ_r' of a sandy soil with various moisture contents.

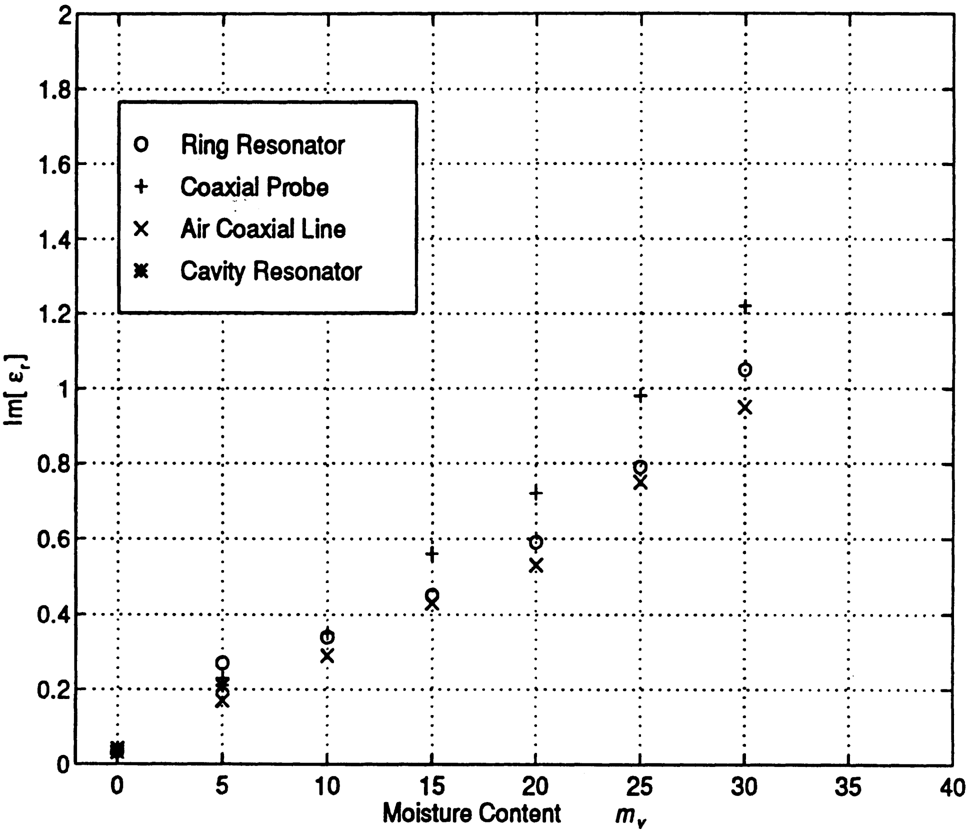

Figure 13: Different methods for measuring ϵ_r'' of a sandy soil with various moisture contents.

A Technique for Dielectric Measurement of Cylindrical Objects in a Rectangular Waveguide

Kamal Sarabandi, *Senior Member, IEEE*

***Abstract*— In this paper, the inverse scattering problem of a homogeneous dielectric post in a rectangular waveguide is considered. A novel inversion algorithm, based on the method of moments and eigen analysis, for computation of the dielectric constant of the post (ϵ) from the measured voltage reflection coefficient is introduced. In this method the integral equation for the polarization current induced in the dielectric post is cast into a matrix equation, and then the contribution of ϵ to the resulting reflection coefficient is expressed explicitly using the eigen analysis. It is shown that the dielectric constant can be obtained from the solution of a complex polynomial function which in turn can be obtained numerically using the conjugate gradient method. Practical aspects of dielectric measurement using this technique are discussed. The HP-8510 network analyzer is used to measure the reflection coefficient of dielectric posts in an X-band waveguide sample holder. Metallic and known dielectric posts are used to determine the accuracy of the dielectric measurement technique.**

I. INTRODUCTION

With advances in technology, synthetic aperture radars have become the most promising remote sensing tool in retrieving the biophysical parameters of a vegetation stand [1], [2]. For this reason in the past two decades considerable effort has been devoted to measurement and characterization of the dielectric constant of vegetation [3]–[8]. All existing methods for dielectric constant measurement of vegetation are destructive: that is, the samples must be cut to shape to fit in the sample holder. Therefore natural variation of the dielectric constant as a function of temperature and water content cannot be measured. Moreover, the existing methods of dielectric measurement are suitable for broad leaves, and a reliable dielectric measurement technique for pine needles does not exist. Motivated by the need for an accurate method to measure the complex dielectric constant of pine needles at microwave frequencies both *in situ* and *in vivo* conditions, the problem of scattering from a dielectric post in a rectangular waveguide is considered.

The dielectric measurement technique proposed in this paper is based on the reflection coefficient measurement from cylindrical obstacles in a rectangular waveguide. A slot or a small hole in a waveguide wall that does not interrupt the flow of currents on the walls does not couple energy to the outside: hence the internal fields remain undisturbed. For example, a hole whose diameter is much smaller than both the cutoff and guide wavelengths made on the broad walls parallel to the narrow walls and perpendicular to the axis of a waveguide does not disturb the surface currents of a TE_{10} mode. If a pine needle (or any dielectric object) is inserted through the hole, part of the incident wave will be scattered back towards the generator. The reflected wave is a function of both the dielectric constant and the geometry of the cylinder cross section. The idea is to measure the reflection coefficient of a cylinder with known cross section and then calculate its dielectric constant.

Analytical scattering solutions for cylindrical posts in a rectangular waveguide are limited to metallic circular posts of small diameters [9], [10]. A more complicated solution based on a grating formulation for a metallic circular cylinder can also be found [11]; however, the solution seems to be excessively complex and has limited potential for combination with other structures. For larger metallic cylinders or, in general, dielectric cylinders of arbitrary cross section one must resort to numerical techniques. In [12] a numerical solution for metallic circular cylinders of arbitrary diameter in a rectangular waveguide is given. In this paper a numerical solution for the scattering problem of a homogeneous dielectric cylinder in a rectangular waveguide supporting a TE_{10} mode is sought with the emphasis on the inverse scattering solution. Using a vector network analyzer and dielectric posts with known cross section and dielectric constant both the forward and inverse scattering formulations are verified.

II. FORWARD SCATTERING FORMULATION

Suppose a homogeneous dielectric cylinder with a known geometrical cross section is placed vertically in a rectangular waveguide. The post has a uniform cross section, and its position in the waveguide is also known. The width of the rectangular waveguide is a and its height is b. The geometry of the problem and the coordinate system used are shown in Fig. 1. It is assumed that the waveguide can only support the dominant TE_{10} mode which is propagating in the positive z-direction. The incident wave induces a polarization current in the dielectric cylinder which becomes the source of the scattered field in the waveguide. The scattered field can be expanded in terms of waveguide modes where the reflected and transmitted waves (away from the cylinder) can be evaluated by retaining only the first mode. Since the reflection and transmission coefficients in a rectangular waveguide can be measured with a high degree of accuracy [8], a numerical solution for the induced polarization current is sought in order to establish the relationship between ϵ and Γ.

Manuscript received December 15, 1993; revised March 29, 1994.

The author is with the Radiation Laboratory, Department of Electrical Engineering and Computer Science, The University of Michigan, Ann Arbor, MI 48109-2122 USA.

IEEE Log Number 9406569.

0018-9456/94$04.00 © 1994 IEEE

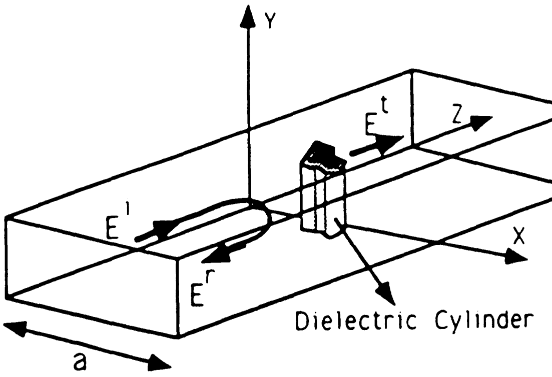

Fig. 1. Geometry of the scattering problem of a dielectric post in a rectangular waveguide.

The incident field and the cross section of the scatterer in this problem are independent of y which implies that the induced polarization current is also independent of y. Moreover, the incident field is along $\hat{y}$ and as mentioned $\delta/\delta y = 0$ for all field components; therefore the induced polarization current is along $\hat{y}$ as well. This simplifies the problem drastically because using the image theory, the top and lower waveguide walls can be removed provided that the dielectric rod is replaced by an infinite cylinder of the same dielectric constant and cross section placed in the resulting parallel-plate waveguide. To set the integral equation Green's function for the problem is required. Suppose an infinite current filament of magnitude I_0 is located at (x', z') parallel to the walls of the parallel-plate waveguide. Again by applying the image theory, the waveguide plates can be removed by replacing the filament current with two periodic arrays of filament currents of the same magnitude and 180° phase difference. Summing the contribution from all filaments:

$$G = -\frac{k_0 Z_0}{4} I_0 \sum_{n=-\infty}^{+\infty} H_0^1(k_0\rho_n^-) - H_0^1(k_0\rho_n^+)$$

where $\rho_n^- = \sqrt{(x - x' - 2na)^2 + (z - z')^2}$, $\rho_n^+ = \sqrt{(x + x' - 2na)^2 + (z - z')^2}$ and k_0 and Z_0 are, respectively, the propagation constant and the characteristic impedance of the free space. H_0^1 is the Hankel function of zeroth order and first kind. The convergence rate of this series is very poor; thus its numerical evaluation is very inefficient. A better representation for Green's function can be obtained using the Poisson summation formula [11] and is given by

$$G = -\frac{k_0 Z_0}{a} \sum_{n=1}^{\infty} \frac{\sin(\frac{n\pi}{a}x') \sin(\frac{n\pi}{a}x) e^{ik_{zn}|z-z'|}}{k_{zn}} \tag{1}$$

where k_{zn} is defined by

$$k_{zn} = \sqrt{k_0^2 - \left(\frac{n\pi}{a}\right)^2}.$$

Suppose a TE$_{10}$ mode with field distribution

$$E^i = \hat{y} \sin\left(\frac{\pi}{a}x\right) e^{ik_{1z}z}$$

is illuminating the cylinder, inducing a volumetric polarization current $J(x, z)$ in the cylinder. The induced current is proportional to the total electric field inside the cylinder and is given by

$$J(x, z) = -ik_0 Y_0(\epsilon - 1)(E^s + E^i)$$

where E^s is the scattered field given by

$$E^s(x, z) = \hat{y} \int_s J(x', z') G(x, z; x', z') dx' dz'.$$

Therefore the integral equation for the induced current is of the following form:

$$J(x, z) = -ik_0 Y_0(\epsilon - 1) \left[\sin\left(\frac{\pi}{a}x\right) e^{ik_{1z}z} + \int_s J(x', z') G(x, z; x', z') dx' dz' \right]. \tag{2}$$

An analytical solution for this integral equation is not known; however, an approximate numerical solution can be obtained using the method of moments. By subdividing the cross section of the cylinder into sufficiently small rectangular cells over which the induced current can be assumed constant, the integral equation can be cast into a matrix equation. If the discretized polarization current is denoted by a column vector $\mathcal{J}$, then

$$Z\mathcal{J} = V \tag{3}$$

where V is the excitation vector given by

$$v_i = \sin\left(\frac{\pi}{a}x_i\right) e^{ik_{1z}z_i}$$

and (x_i, z_i) is the Cartesian coordinate of the ith cell. In (3) Z is the impedance matrix whose elements can be computed from

$$z_{ij} = \begin{cases} \dfrac{k_0 Z_0}{a} \displaystyle\sum_{n=1}^{\infty} \dfrac{4 \sin\left(\frac{n\pi x_i}{a}\right) \sin\left(\frac{n\pi x_j}{a}\right) \sin\left(\frac{n\pi \Delta x}{2a}\right) \sin\left(\frac{k_{nz}\Delta z}{2}\right)}{ik_{nz}^2 \left(\frac{n\pi}{a}\right)} \times e^{ik_{nz}|z_i - z_j|} & z_j \neq z_i \\ \dfrac{k_0 Z_0}{a} \displaystyle\sum_{n=1}^{\infty} \dfrac{4 \sin\left(\frac{n\pi x_i}{a}\right) \sin\left(\frac{n\pi x_j}{a}\right) \sin\left(\frac{n\pi \Delta x}{2a}\right)}{ik_{nz}^2 \left(\frac{n\pi}{a}\right)} \times \left(e^{ik_{nz}\Delta z/2} - 1\right) & z_j = z_i \end{cases}$$

$$z_{ii} = \frac{i}{k_0 Y_0(\epsilon - 1)} + \frac{k_0 Z_0}{a} \sum_{n=1}^{\infty} \frac{4 \sin^2\left(\frac{n\pi x_i}{a}\right) \sin\left(\frac{n\pi \Delta x}{2a}\right)}{ik_{nz}^2 \left(\frac{n\pi}{a}\right)} \left(e^{ik_{nz}\Delta z/2} - 1\right)$$

where Δx and Δz are the pixel dimensions. Once the polarization current is obtained, by inverting (3), the scattered field can be calculated easily. Since the waveguide can only support the TE$_{10}$ mode, only the first term of Green's function is needed to compute the reflected or transmitted wave. For example, away from the dielectric cylinder the reflected wave is given by

$$E^r = -\frac{k_0 Z_0}{a k_{1z}} \sin\left(\frac{\pi x}{a}\right) e^{-ik_{1z}z} \int_s J(x', z') \sin\left(\frac{\pi x'}{a}\right) dx' dz'.$$

Therefore, the reflection coefficient, defined as the ratio of the reflected wave to the incident wave at $z = 0$, in vector notation is given by

$$\Gamma = -\frac{k_0 Z_0}{a k_{1z}} \Delta x \Delta z V^t \mathcal{J} \tag{4}$$

where V^t is the transpose of the excitation vector. In a similar manner the transmission coefficient can be obtained from

$$\tau = 1 - \frac{k_0 Z_0}{a k_{1z}} \Delta x \Delta z \tilde{V} \mathcal{J}$$

where $\tilde{V}$ is the conjugate transpose of V.

III. Retrieval of Dielectric Constant from Reflection Coefficient

The main goal of this analysis is the calculation of the dielectric constant of the dielectric cylinder from its measured reflection coefficient. As the analysis of the previous section shows there is no simple relationship between the dielectric constant ϵ and the reflection coefficient Γ. The only case where an analytical solution for ϵ can be obtained is when the cylinder is electrically thin, i.e., $k_0 d \ll 1$ with d being a typical dimension of the cylinder cross section. In this case the polarization current can be assumed constant, and it can be shown that

$$\epsilon = 1 + \frac{ia}{k_0^2 \left[\frac{\Delta S \sin^2 \frac{\pi x_0}{a} e^{2ik_{1z}z_0}}{k_{1z}\Gamma} \right] - A} \tag{5}$$

where ΔS is the area of the cross section of the thin cylinder, (x_0, z_0) is the coordinate of the cylinder center, and A is given by

$$A = \sum_{n=1}^{\infty} \frac{1}{k_{zn}} \sin\left(\frac{n\pi x_0}{a}\right) \int_{\Delta S} \sin\left(\frac{n\pi x'}{a}\right) e^{ik_{zn}|z_0 - z'|} dx' dz'.$$

Since the summation is slowly converging, the contribution of higher order terms, which are varying over the cylinder cross section, to the integral is significant; therefore the integral for each term must be evaluated carefully.

Direct retrieval of ϵ from $\Gamma(\epsilon)$ for thick cylinders is not possible. However, brute force numerical search methods such as Newton–Ralphson or conjugate gradient can be used to find the dielectric constant that satisfies

$$\Gamma(\epsilon) - \Gamma_m = 0$$

where Γ_m is the measured reflection coefficient, and $\Gamma(\epsilon)$ is the calculated reflection coefficient for a given dielectric constant and cross section geometry. Search routines, depending on the initial guess, usually require the calculation of Z^{-1} many times. The calculation of $\Gamma(\epsilon)$ using (4) is very slow which makes the search routine inefficient.

In what follows a procedure for the calculation of $\Gamma(\epsilon)$ is presented which does not require evaluation of Z^{-1} for different values of ϵ. The search routines can be made efficient by noticing that the dielectric constant appears only in the diagonal elements of the impedance matrix. The effect of ϵ in Z^{-1} can be made explicit by splitting the impedance matrix into two matrices:

$$Z = W + \beta I$$

where I is the identity matrix, $\beta = i/(k_0 Y_0(\epsilon - 1))$, and W is a matrix whose elements are defined as

$$w_{ij} = z_{ij} \quad i \neq j$$

$$w_{ij} = \frac{k_0 Z_0}{a} \sum_{n=1}^{\infty} \frac{4 \sin^2(n\pi x_i/a) \sin(n\pi \Delta x/2a)}{i k_{nz}^2 (n\pi/a)} \times \left(e^{ik_{nz}\Delta z/2} - 1\right) \quad i = j.$$

Computing the eigenvalues and eigenvectors of W it can be shown that

$$W = Q \Lambda Q^{-1} \tag{6}$$

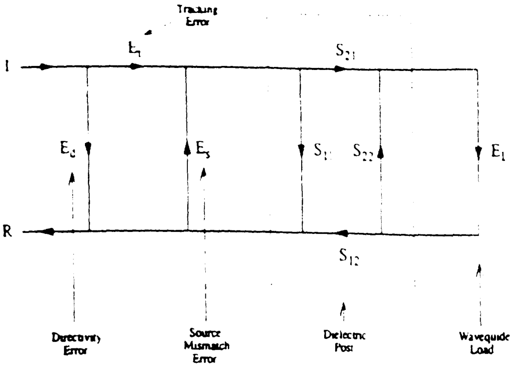

Fig. 2. The signal flow diagram of the measurement setup and the sample holder.

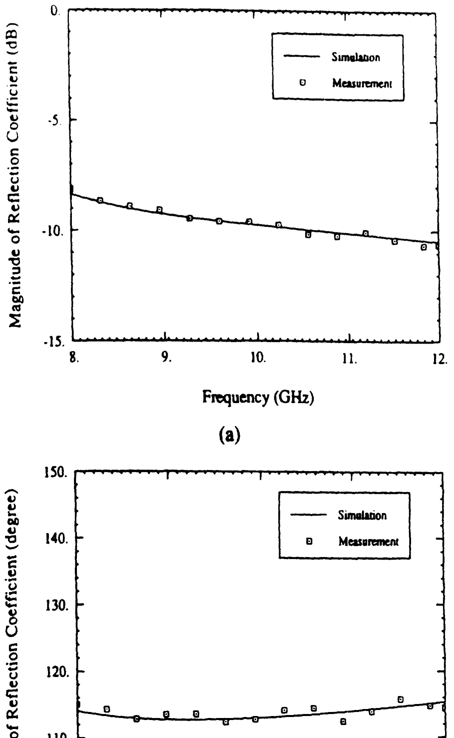

Fig. 3. Magnitude (a) and phase (b) of the reflection coefficient of a circular Teflon post with diameter $d = 0.7$ cm and $\epsilon = 2 + i0.005$ in a WR90 waveguide.

where Λ is the diagonal matrix containing the eigenvalues of $\boldsymbol{W}$, and $\boldsymbol{Q}$ is the matrix of eigenvectors; that is, the jth column of $\boldsymbol{Q}$ is the eigenvector of $\boldsymbol{W}$ corresponding to the jth eigenvalue λ_j. Noting that the identity matrix can be written as

$$I = QIQ^{-1} \tag{7}$$

and using (3), (6), and (7) the polarization current can be computed from

$$\mathcal{J} = \boldsymbol{Q}[\Lambda + \beta I]^{-1}\boldsymbol{Q}^{-1}\boldsymbol{V}.$$

The expression for the reflection coefficient can now be written as

$$\Gamma(\epsilon) = -\frac{k_0 Z_0}{a k_{1z}} \Delta x \Delta z [\boldsymbol{Q}^t \boldsymbol{V}]^t [\Lambda + \beta I] \boldsymbol{Q}^{-1} \boldsymbol{V}. \tag{8}$$

Defining $\boldsymbol{U} = \boldsymbol{Q}^t \boldsymbol{V}$ and $\boldsymbol{U}' = \boldsymbol{Q}^{-1}\boldsymbol{V}$, (8) can be expanded to get

$$\Gamma(\epsilon) = -\frac{k_0 Z_0}{a k_{1z}} \sum_{n=1}^{M} \frac{U_n U_n'(\epsilon - 1)}{\lambda_n(\epsilon - 1) + i k_0 Y_0} \tag{9}$$

where M is the dimension of $\boldsymbol{Z}$. From this expression it is obvious that once the eigenvalues and eigenvectors of $\boldsymbol{Z}$ are obtained, the reflection coefficient can easily be evaluated for any values for ϵ from (9). By setting the right-hand side of (9) equal to the measured reflection coefficient Γ_m, a polynomial of degree M is obtained whose roots are the possibe values of ϵ. The admissible solutions for ϵ must satisfy $\epsilon' \geq 1$ and $\epsilon'' \geq 0$ which can be imposed as a constraint in the search routine. In this paper the conjugate gradient method is used to search for the global minimum of the function

$$f(\epsilon) = |\Gamma(\epsilon) - \Gamma_m|^2$$

subject to the mentioned constraint. For relatively thin cylinders expression (5) can be used as the initial guess.

IV. Numerical and Experimental Results

In this section the applicability and accuracy of the dielectric measurement algorithm described in the previous section are examined. An automatic measurement setup comprised of an HP-8510B vector network analyzer, an HP-8511 test set, and an HP-9000 computer is used to measure the complex reflection coefficient Γ_m of a dielectric cylinder in an X-band waveguide sample holder. The waveguide sample holder consists of a waveguide matched load and a piece of waveguide with a coax-to-waveguide adapter which is connected to the HP-8511. The samples are placed at the junction of the two waveguide pieces ($z = 0$) and centered in the middle of the waveguide cross section ($x = a/2$). Centering the dielectric cylinder in the middle of the waveguide cross section increases the reflected wave, thus improving the signal-to-noise ratio for thin cylinders with low permittivity.

One difficulty in reflection coefficient measurement is the errors caused by the measurement setup. These errors are known as systematic errors which can be removed by an external calibration procedure. The signal flow diagram of the measurement setup is shown in Fig. 2 where E_d, E_s, E_t, E_l are, respectively, the directivity, source mismatch, frequency tracking, and load errors. The reflection coefficient measured by the network analyzer (Γ_a) before calibration is related to the actual scattering matrix of the cylinder ($\Gamma_m = s_{11}$) by

$$\Gamma_a = E_d + \frac{s_{11} + \frac{s_{12}s_{21}E_l}{1-s_{22}E_l}}{1 - E_s\left(s_{11} + \frac{s_{12}s_{21}E_l}{1-s_{22}E_l}\right)} E_t.$$

Calculation of s_{11} from this error model requires the two-port calibration procedure. However, E_l for waveguide loads can be as small as -50 dB and if cylinders with $s_{11} > -20$ dB are concerned, the error in s_{11} measurement would be less than 0.2 dB when E_l is set to zero. In this case the error model reduces to that of a single-port device. To correct for the system errors, the measurement system can be calibrated using three independent loads with known reflection coefficients. For the waveguide sample holder a short, an offset short, and a matched load were chosen to calibrate the system. Since the calibration is done over a frequency range $F^{\min} - F^{\max}$ the length of the offset short (l) must be chosen such that $k_z^{\max} l < \pi$ to assure the independence of the calibration loads.

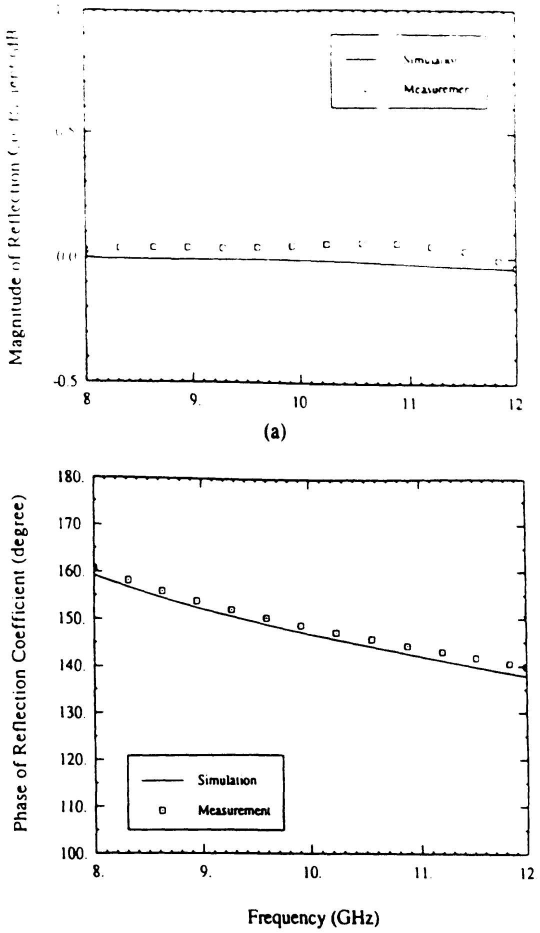

(a)

(b)

Fig. 4. Magnitude (a) and phase (b) of the reflection coefficient of a circular metallic post with diameter $d = 0.63$ cm in a WR90 waveguide.

To check the accuracy of the measurement setup and the forward algorithm, the reflection coefficients of a circular Teflon post with diameter $d = 0.7$ cm and dielectric constant $\epsilon = 2 + i0.005$ and a metallic post with radius $d = 0.63$ cm were measured and compared with the method of moments results. Figs. 3 and 4 show the measured and calculated

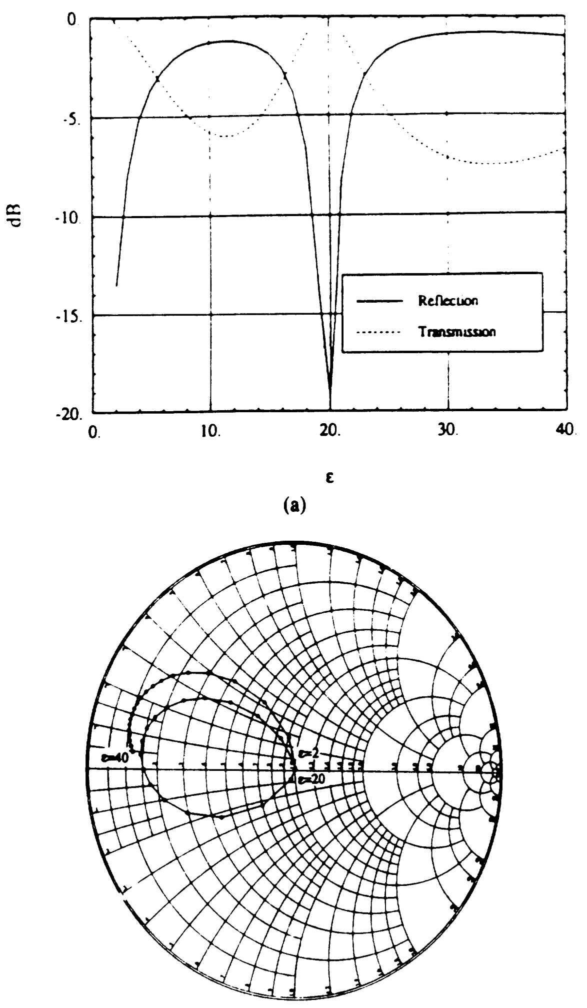

(a)

(b)

Fig. 5. Magnitude of the reflection and transmission coefficients (a) and complex reflection coefficient versus dielectric constant (b) for a circular cylinder with $d = 0.5$ cm at 10 GHz in a WR90 waveguide.

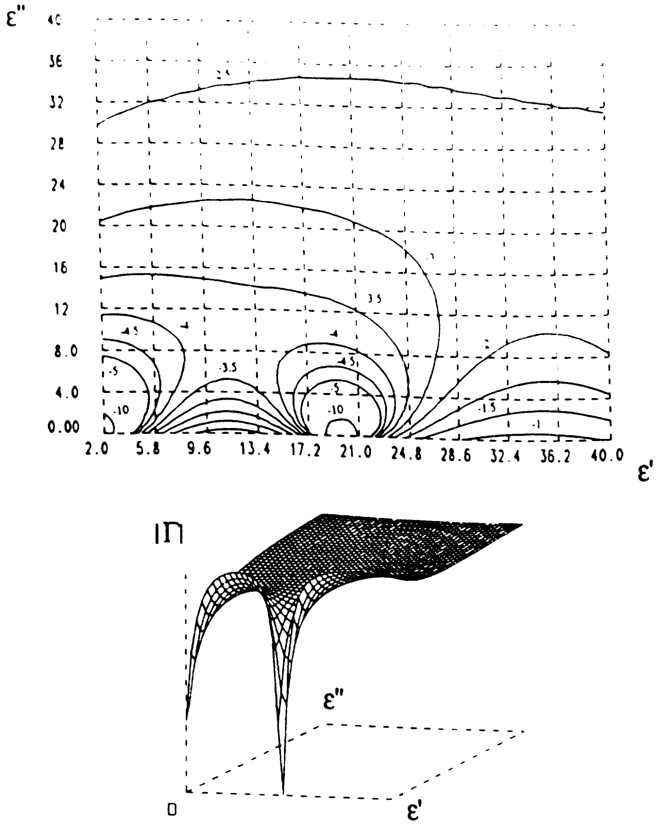

Fig. 6. Sensitivity of magnitude of the reflection coefficient to the real and imaginary parts of the dielectric constant for a circular cylinder with $d = 0.5$ cm at 10 GHz in a WR90 waveguide.

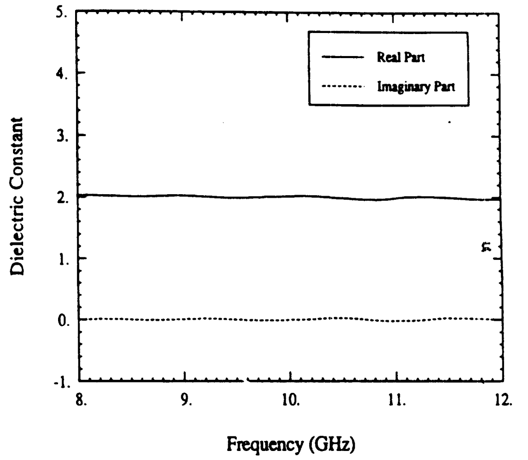

Fig. 7. Calculated real and imaginary parts of the dielectric constant from the measured reflection coefficient of a circularTeflon post with $d = 0.5$ cm.

reflection coefficients of the Teflon and metallic posts over the frequency range 8–12 GHz, respectively. The measured magnitude is within ±0.2 dB of the calculated magnitude, and the measured phase is within ±3° of the calculated phase of the reflection coefficient. With the confidence in the measurement technique, the inversion algorithm is attempted next. First let us examine the sensitivity of the reflection coefficient function to the dielectric constant. Fig. 5(a) shows the magnitude of the reflection and transmission coefficients as a function ϵ for a circular post with $d = 0.5$ cm at 10 GHz. It is noted that for $\epsilon = 20$ a resonance occurs where $s_{11} = 0$ and $s_{21} = 1$, satisfying the conservation of energy. Fig. 5(b) shows the complex reflection coefficient of the same cylinder as a function of the dielectric constant. It is also noted that the dielectric constant can be a multivalued function of the complex reflection coefficient. Due to the complex dependence of the reflection coefficient on the dielectric constant and the geometry of the post, criteria for the uniqueness of the solution cannot be established analytically. However, using the numerical analysis it was found that the dielectric constant becomes a single-valued function of the dielectric constant when the electrical thickness of the post $(d\sqrt{|\epsilon|})$ is small relative to the wavelength (away from the resonance). Fig. 6 shows the three-dimensional and the contour map of the magnitude of the reflection coefficient as a function of both ϵ' and ϵ'' for the circular dielectric post at 10 GHz. The sensitivity of the reflection coefficient function to changes in ϵ when both ϵ' and ϵ'' are large is very low and inversion may not be very accurate. Again using the forward numerical model it was found that Γ is very sensitive to ϵ when the electrical thickness of the post is small compared to the wavelength.

To examine the accuracy of the inversion algorithm a circular Teflon post with d =0.5 cm was placed in the sample holder, and its dielectric constant was calculated from the measured reflection coefficient. Fig. 7 shows the calculated dielectric constant of the Teflon post as a function of frequency

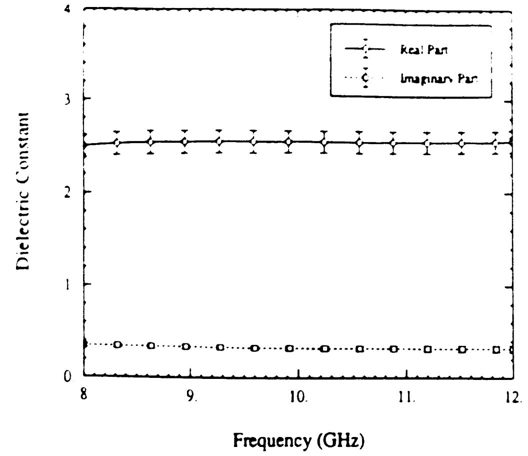

Fig. 8. Calculated real and imaginary parts of the dielectric constant from the measured reflection coefficient of circular dry wooden posts with $d = 0.32$ cm and moisture content $m_g < 0.01$.

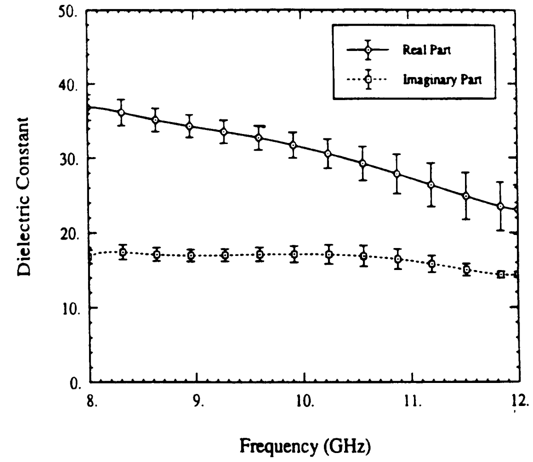

Fig. 9. Calculated real and imaginary parts of the dielectric constant from the measured reflection coefficient of circular wet wooden posts with $d = 0.32$ cm and moisture content $m_g < 0.5$.

which agrees well with the expected values of ϵ for Teflon. To show another example, the dielectric inversion algorithm was applied to wooden cylinders with different moisture contents (m_g). Ten samples of cylindrical wooden posts with $d = 0.32$ cm were prepared, and their reflection coefficients were measured. The experiment was repeated after the wooden posts were soaked in water for a day. The calculated average dielectric constants of the dry wood with $m_g < 0.01$ and wet wood with $m_g = 0.5$ are shown in Figs. 8 and 9, respectively. The bars on the measured real and imaginary parts of the dielectric constant indicate the standard deviation of the measured quantity derived from ten samples.

V. CONCLUSION

An accurate method for measurement of the dielectric constant of cylindrical objects with arbitrary cross section is presented. In this technique the dielectric constant of the cylinder with known cross section is calculated from the measured complex reflection coefficient of a matched rectangular waveguide containing the dielectric object. A novel and efficient inversion algorithm based on the method of moments and eigen analysis is introduced. The validity and accuracy of the method are examined from the measurement of dielectric posts with known dielectric constant. It is found that the accuracy in dielectric measurement decreases as the electrical thickness of the cylindrical post is increased. The choice of sample holder in this technique is suited for *in situ* and *in vivo* dielectric measurement of pine needles.

ACKNOWLEDGMENT

The author would like to thank Mr. T.-C. Chiu for his help in collecting the experimental data.

REFERENCES

[1] S. T. Wu, "Potential application of multipolarization SAR for pine-plantation biomass estimation," *IEEE Trans. Geosci. Remote Sensing*, vol. GRS-25, no. 3, May 1987.

[2] T. Le Toan, A. Beaudoin, J. Riom, and D. Guyon, "Relating forest biomass to SAR data," *IEEE Trans. Geosci. Remote Sensing*, vol. 30, no. 2, Mar. 1992.

[3] N. L. Carlson, "Dielectric constant of vegetation at 8.5 GHz," Tech. Rep. 1930–5, ElectroScience Laboratory, The Ohio State University, Mar. 1967.

[4] M. G. Broadhurst, "Complex dielectric constant and dielectric constant dissipation factor of foliage," National Bureau of Standards Rep. 9592, Oct. 1970.

[5] F. T. Ulaby and R. P. Jedlicka, "Microwave dielectric properties of plant materials," *IEEE Trans. Geosci. Remote Sensing*, vol. GRS-22, no. 4, July 1984.

[6] E. C. Burdette, F. L. Cain, and J. Seals, "*In vivo* measurement technique for determining dielectric properties at VHF through microwave frequencies," *IEEE Trans. Microwave Theory Tech.*, vol. MTT-28, no. 4, Apr. 1980.

[7] M. A. El-Rayes and F. T. Ulaby, "Microwave dielectric spectrum of vegetation—Part I: Experimental observations," *IEEE Trans. Geosci. Remote Sensing*, vol. GRS-25, pp. 541–549, 1987.

[8] K. Sarabandi and F. T. Ulaby, "Technique for measuring the dielectric constant of thin materials," *IEEE Trans. Instrum. Meas.*, vol. 37, no. 4, 1988.

[9] N. Marcuvitz, *Waveguide Handbook*. Lexington, MA: Boston Technical Publishers, 1964.

[10] H. Auda and R. F. Harrington, "Inductive posts and diaphragms of arbitrary shape and number in a rectangular waveguide," *IEEE Trans. Microwave Theory Tech.*, vol. MTT-32, no. 6, June 1984.

[11] B. Davis, *Integral Transforms and Their Applications*. New York: Springer-Verlag, 1985.

[12] Y. Leviatan, P. G. Li, A. T. Adams, and J. Perini, "Single-post inductive obstacle in rectangular waveguide," *IEEE Trans. Microwave Theory Tech.*, vol. MTT-31, no. 10, Oct. 1983.

Kamal Sarabandi (S'87–M'90–SM'93) received the B.S. degree in electrical engineering from Sharif University of Technology, Tehran, Iran, in 1980. From 1980 to 1984 he worked as a microwave engineer at the Telecommunication Research Center, Iran. He entered the graduate program at the University of Michigan in 1984 and received the M.S.E. degree in electrical engineering in 1986, and the M.S. degree in mathematics and the Ph.D. degree in electrical engineering in 1989.

He is presently an assistant professor in the Department of Electrical Engineering and Computer Science at the University of Michigan. His research interests include electromagnetic scattering, microwave and millimeter wave remote sensing, computational electromagnetics, and calibration of polarimetric SAR systems.

Dr. Sarabandi is the elected chairman of Geoscience and Remote Sensing Michigan chapter and a member of the Electromagnetics Academy and USNC/URSI Commission F.

220 IEEE TRANSACTIONS ON ANTENNAS AND PROPAGATION, VOL. 42, NO. 2, FEBRUARY 1994

Bistatic Specular Scattering from Rough Dielectric Surfaces

Roger D. De Roo, *Student Member, IEEE,* and Fawwaz T. Ulaby, *Fellow, IEEE*

***Abstract*— An experimental investigation was conducted to determine the nature of bistatic scattering from rough dielectric surfaces at 10 GHz. This paper focusses specifically on the dependence of coherent and incoherent scattered fields on surface roughness for the specular direction. The measurements, which were conducted for a smooth surface with $ks < 0.2$ (where $k = 2\pi/\lambda$ and s is the rms surface height) and for three rough surfaces with $ks = 0.5$, 1.39, and 1.94, included observations over the range of incidence angles from 20° to 65° for both horizontal and vertical polarizations. For the coherent component, the reflectivity was found to behave in accordance with the prediction of the Physical Optics model, although it was observed that the Brewster angle exhibited a small negative shift with increasing roughness. The first-order solution of Physical Optics also provided good agreement with observations for *hh*-polarized incoherent scattering coefficient, but it failed to predict the behavior of the *vv*-polarized scattering coefficient in the angular range around the Brewster angle. A second-order solution is proposed which appears to partially address the deficiency of the Physical Optics model.**

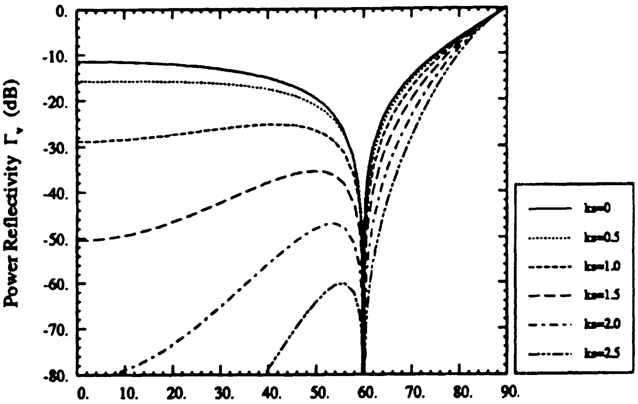

Fig. 1. Calculated coherent reflectivity for v polarization using the Physical Optics model for a Gaussian surface with ks vaired from 0 to 2.5, and $\epsilon = 3$.

I. INTRODUCTION

SCATTERING of electromagnetic fields by random rough surfaces in the backscatter direction has many uses and has been investigated extensively over the past few decades. By comparison, very few experimental investigations have been attempted to evaluate forward scattering in the specular direction. This is in part because the applications for specular scattering are not as straightforward as for backscattering. The many theoretical developments for scattering from random rough surfaces, while developed for the general bistatic case, have only been extensively used and tested for backscattering. Therefore, the usefulness and validity of these theories for specular scattering is largely unknown.

Recent developments in the modeling of terrain for radar backscattering indicate that specular scattering from a rough ground surface combined with scattering by an overstructure (such as trees or crops) can contribute significantly to the backscattering from the terrain as a whole [1]–[5]. Therefore an understanding of the nature of specular radar scattering and knowledge of the behavior of specular scattering theories are needed. Several experimental investigations were conducted at centimeter wavelengths in the 1946–1960 period to evaluate the variation of the coherent and incoherent components of the specularly reflected energy as a function of surface roughness. The results for the coherent component, which is represented by the reflection coefficient, are summarized in Beckmann and Spizzichino [6]. According to these results, the overall variation of the reflection coefficient with ks, where $k = 2\pi/\lambda$, and s is the rms height, may be explained by the coherent scattering term of the Physical Optics surface scattering model [6], [7]. The data, however, are rather lacking in several respects: (1) marginal accuracy with regard to both the measured reflected signal and the surface rms height, (2) limited dynamic range (10 dB relative to the level of the signal reflected from a perfectly smooth surface), and (3) no examination of the behavior in the angular region around the Brewster angle. Additional bistatic measurements were reported by Cosgriff *et al* [8] in 1960, but the data were not calibrated, nor were the surfaces characterized.

More recently, Ulaby *et al.* [9] measured bistatic scattering from sand and gravel surfaces at 35 GHz, and while the data were calibrated and the surfaces were characterized, no comparison to a theoretical prediction was given. In the optical regime, Saillard and Maystre [10] have measured the bistatic scattering of light from dielectric surfaces, and have observed a change in the Brewster angle as the roughness of the surface increased. Greffet [11] explained their observations using the Small Perturbation Method [12]. However, the Small Perturbation Method does not explain the observations reported in our present study: the first-order Small Perturbation Method predicts that the Brewster angle will move toward grazing as the roughness increases, while our observations indicate the opposite.

Manuscript received April 30, 1993; revised September 17, 1993. This work was supported by the Army Research Office, contract DAALO3-92-G-0269.

The authors are with The Radiation Laboratory, Department of Electrical Engineering and Computer Science, University of Michigan, Ann Arbor, MI, 48109-2122.

IEEE Log Number 9215659.

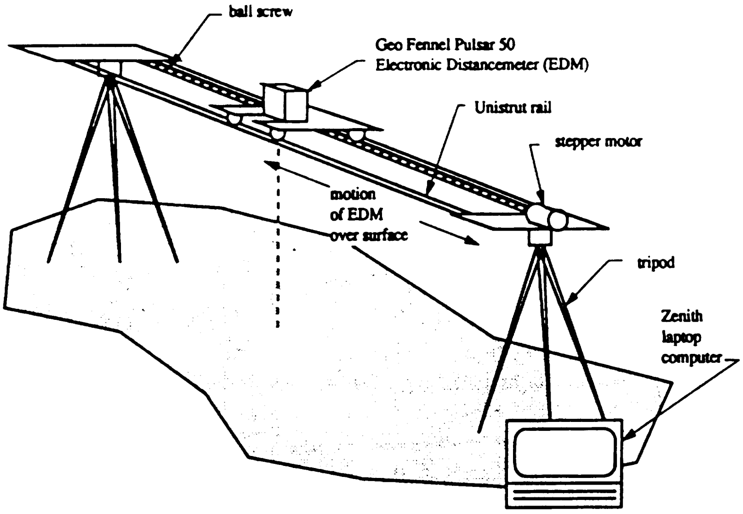

Fig. 2. Diagram of Laser Profiler.

There are three major rough surface scattering approaches which have long held the acceptance of the scientific community as valid for some ranges of surface roughness. The Geometric Optics (GO) model, the Physical Optics (PO) model, and the Small Perturbation Method (SPM) are the three theoretical approaches most commonly used at microwave frequencies for characterizing scattering from random rough surfaces [7]. While both GO and PO models rely on the Kirchhoff approach of using the tangent-plane approximation, they yield very different predictions for the scattering of waves from a rough surface. In particular, the GO model does not predict any coherent reflectivity from rough surfaces. This may appear to be an inadequacy of the GO approach; however, the GO approach is valid only for surfaces so rough that any coherent scattering would be very small anyway. The PO model, on the other hand, has a simple expression for the coherent scattering component, but the complete expression for incoherent scattering, even for single scattering, has not yet been formulated. SPM is a different approach, but its range of validity is restricted to surfaces with small rms heights and slopes. Because the ranges of validity for the GO and SPM theories are outside the range of rms heights described in this paper, comparisons to GO and SPM will not be discussed.

In this paper we will examine experimental measurements of the coherent and incoherent scattering components in the specular directions at 10 GHz for several dry sand surfaces covering a wide range of rms heights (0.5 mm to 1.4 cm). The measurements were conducted over an incidence angle range extending from 20° to 65° for both horizontal and vertical polarizations. The sand, with a relative dielectric constant of 3.0 and negligible loss factor, exhibits a null for vertical polarization at the Brewster angle of 60°. The experimental data are compared with predictions based on a revision of the Physical Optics solution that is slightly different from and more accurate than the standard form available in the literature [7].

II. PHYSICAL OPTICS MODEL—A VECTOR SOLUTION

The Physical Optics approach involves integration of the Kirchhoff scattered field over the rough surface. The coherent field reflection coefficient from a surface with a Gaussian height distribution is given by [7]:

$$R_q(\theta) = R_{q0} e^{-2k^2 s^2 \cos^2\theta} \delta_{pq} \tag{1}$$

where the polarization subscripts p, q are either h or v, and $\cos\theta = -\hat{z} \cdot \hat{k}_i$. The angle θ is both the angle of incidence and reflection; coherent scattering occurs only in the specular direction from the mean surface. The reflection coefficient R_{q0} for a plane surface is given by (15) and (16) below. Fig. 1 shows $\Gamma_v(\theta) = |R_v(\theta)|^2$ for several values of ks. The Brewster angle does not change with surface roughness, but the coherent scattered power decreases very rapidly with increasing roughness.

The power in the incoherent reflected field may be given by a Taylor series in surface slope distributions. In Ulaby *et al.* [7] the Physical Optics solution is called the Scalar Approximation because slopes are ignored in the surface local coordinate system, leading to a decoupling of polarizations in the vector scattering equations. As a result, co-polarized scattering in the plane of incidence is fairly accurate, but cross-polarized scattering is zero. With the inclusion of surface slopes transverse to the plane of incidence in the vectorial solution to the Physical Optics approximation, depolarization in the plane of incidence is predicted when the Taylor series is expanded to the second order in surface slopes. The derivation is given in Appendix A. In the specular scattering direction, the first order terms are zero. The Physical Optics expression for incoherent scattering in the specular direction, which includes the zeroth and the important part of the second order terms, is given by (see last paragraph of Appendix A):

$$\sigma^0_{pq} = 2k^2 \cos^2\theta |a'_{0pq}|^2 I'_0 + 4k^4 s^4 \cos^4\theta (|a'_{lpq}|^2 + |a'_{tpq}|^2) I'_{20} \tag{2}$$

where

$$I'_0 = e^{-4k^2 s^2 \cos^2\theta} \int_0^\infty \left(e^{4k^2 s^2 \cos^2\theta \rho(\xi)} - 1\right) \xi \, d\xi \tag{3}$$

$$I'_{20} = \int_0^\infty \left(\frac{\partial \rho(\xi)}{\partial \xi}\right)^2 e^{-4k^2 s^2 \cos^2\theta (1-\rho(\xi))} \xi \, d\xi \tag{4}$$

and

$$a'_{0hh} = R_{h0} \tag{5}$$
$$a'_{lhh} = R_{h1} \tag{6}$$
$$a'_{0vv} = R_{v0} \tag{7}$$
$$a'_{lvv} = R_{v1} \tag{8}$$
$$a'_{thh} = a'_{tvv} = 0 \tag{9}$$
$$a'_{0vh} = a'_{lvh} = a'_{0hv} = a'_{lhv} = 0 \tag{10}$$
$$a'_{tvh} = (R_{h0}\cos^2\theta + R_{v0})/\sin\theta \tag{11}$$
$$a'_{thv} = -(R_{v0}\cos^2\theta + R_{h0})/\sin\theta \tag{12}$$

The a'_{0pq} terms are the zeroth-order terms (scalar approximation); the a'_{lpq} and a'_{tpq} terms are the second-order terms due to slopes longitudinal and transverse to the plane of incidence. The function $\rho(\xi)$ is the normalized correlation function of the surface, and the parameters $R_{v0}, R_{h0}, R_{v1}, R_{h1}$ are the coefficients of the (field) reflectivity local to the surface when expanded in terms of surface slopes:

$$R_h(x,y) = R_{h0} + R_{h1}Z_l(x,y) + \cdots \tag{13}$$
$$R_v(x,y) = R_{v0} + R_{v1}Z_l(x,y) + \cdots \tag{14}$$

where $Z_l(x,y)$ is the surface slope longitudinal to the direction of the incident wave at the (x,y) lateral coordinates of the surface. The zeroth-order terms are identical to the reflection coefficients for a smooth surface. In particular,

$$R_{h0} = \frac{\eta_2\cos\theta - \eta_1\cos\theta_t}{\eta_2\cos\theta + \eta_1\cos\theta_t} \tag{15}$$
$$R_{v0} = \frac{\eta_1\cos\theta - \eta_2\cos\theta_t}{\eta_1\cos\theta + \eta_2\cos\theta_t} \tag{16}$$
$$R_{h1} = \frac{\eta_2\sin\theta(1-R_{h0}) - \eta_1\frac{k_1\cos\theta}{k_2\cos\theta_t}\sin\theta_t(1+R_{h0})}{\eta_2\cos\theta + \eta_1\cos\theta_t} \tag{17}$$
$$R_{v1} = \frac{\eta_1\sin\theta(1-R_{v0}) - \eta_2\frac{k_1\cos\theta}{k_2\cos\theta_t}\sin\theta_t(1+R_{v0})}{\eta_1\cos\theta + \eta_2\cos\theta_t} \tag{18}$$

where θ_t is related to θ by Snell's Law: $k_1\sin\theta = k_2\sin\theta_t$, and $\eta = \sqrt{\mu/\epsilon}$. These first-order coefficients are different from those found in Ulaby *et al* [7] and Ulaby and Elachi [13] due to the incorporation of a more precise method for expanding the local angle of transmission.

The zeroth-order terms dominate co-polarized scattering except near the Brewster angle, where the zeroth-order terms tend toward zero. For cross-polarization, the zeroth-order terms predict no scattering for all specular angles, and therefore cross-polarized scattering is determined by the second-order terms. Unfortunately, this is still a single-scattering theory, and depolarization is very small compared to other possible sources, such as multiple scattering or volume scattering. Thus it provides a simple estimate of the minimum expected cross-polarized scattering in the specular scattering direction. The co-polarized second-order terms are all negligible except in the vicinity of the Brewster angle, where the zeroth-order terms vanish for vv polarization. The second-order terms all tend toward zero at grazing, and the cross polarized terms tend toward zero at nadir.

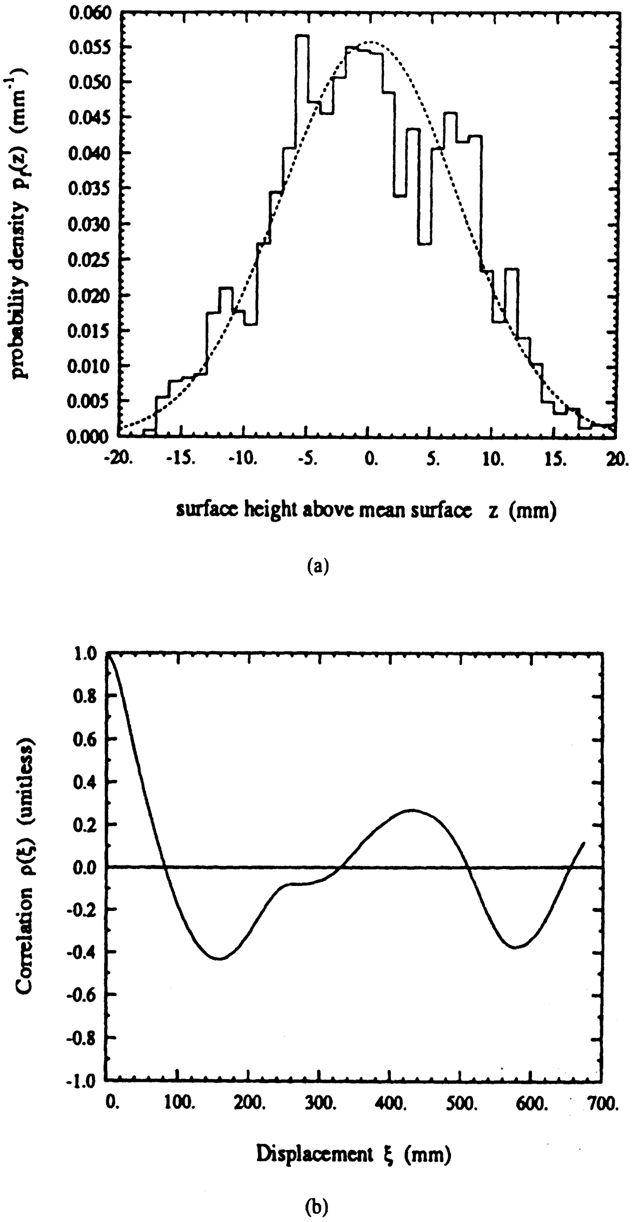

(a)

(b)

Fig. 3. Typical results of surface characterization of one of the surfaces measured in this study: (a) Histogram of measured heights for a slightly rough surface and the Gaussian probability distribution used to model it; a total of 4353 height measurements were made, from which the rms height was calculated to be $s = 6.9$ mm. (b) Measured autocorrelation function of the same surface.

The fact that the Kirchhoff approximation is capable of predicting any cross-polarized single scattering in the plane of incidence is somewhat surprising. However, this is possible because the Physical Optics approximation is used in the derivation; use of the Geometric Optics approximation neglects diffraction and is incapable of predicting cross-polarized scattering. While expressions similar to, but not identical with, those described here for the higher order terms of the Physical Optics model have been presented in the past [14], and have been unsuccessful in matching experimental measurements of

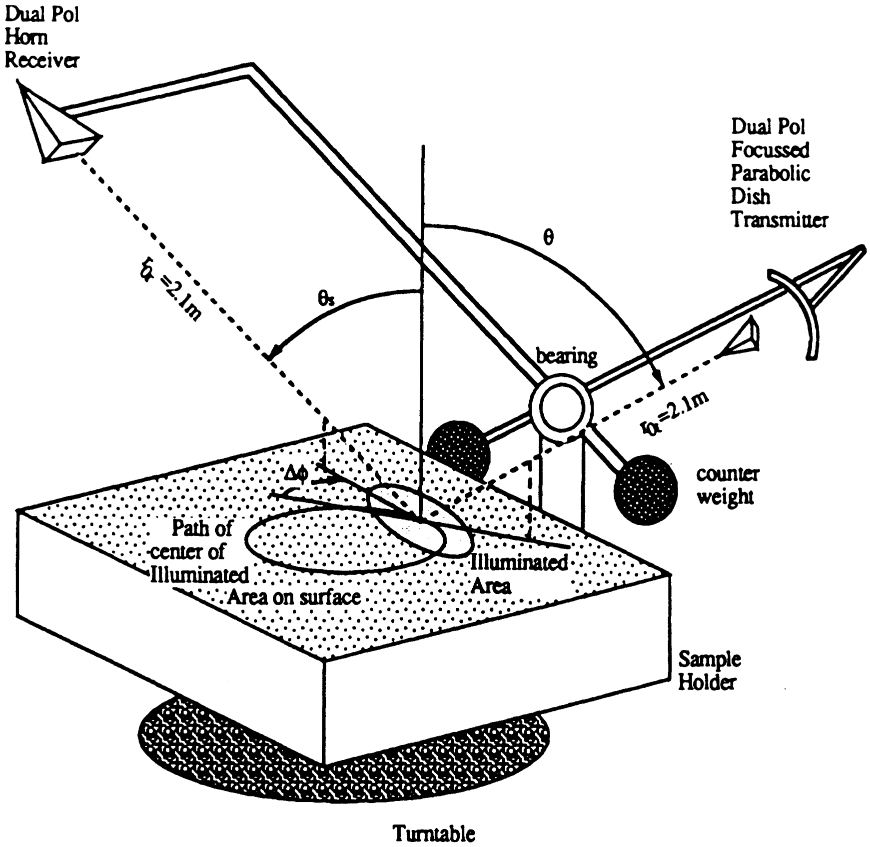

Fig. 4. Diagram of the Bistatic Facility.

the cross-polarized scattering coefficient [15], the authors are not aware of any attempt to use the higher order terms to explain scattering in the vicinity of the Brewster angle.

III. Measurement Description

A. Laser Profiler

The measurements shown in this paper are for random surfaces with varying roughness. The surfaces were characterized by a Laser Profiler, a device engineered at the University of Michigan to measure 2 meter linear or 1 meter by 1 meter square sections of surface profiles. The Profiler is shown in 2 meter linear mode in Fig. 2. Using a Pulsar 50 Electronic Distancemeter manufactured by GEO Fennel, it can measure profiles of surfaces without direct contact. The profiler has a horizontal resolution of 1 mm and a vertical resolution of 2 mm. Fig. 3(a) is an example of the height histogram generated from the profile measured for one of the surfaces, and Fig. 3(b) shows the corresponding correlation function.

B. Bistatic Facility

The configuration shown in Fig. 4 depicts the indoor bistatic radar system used for making the measurements reported in this paper. It is a stepped-frequency (8.5–10 GHz) measurement system capable of measuring the scattering matrix S of the target contained in the area or volume formed by the intersection of the transmit and receive antenna beams. Using an HP8720 vector network analyzer with an amplifier on the transmitting antenna, the system measures a complex voltage for any pair of v or h receive and transmit polarization states. With proper calibration, it is capable of measuring all four complex elements of the scattering matrix of the target surface. The hardware allows the transmitter and receiver to be located independently at any point on a hemispherical shell 2.1 m from the center of the target. In practice, however, measurements are accurate only when both antennas are within 70° of nadir.

The receive antenna is a dual-polarized horn antenna with a beamwidth of 12°, and the transmit antenna is a dual-polarized parabolic dish whose feed was designed such that the main beam of the parabolic dish is focused at a range equal to the distance to the target surface, which is held constant for all measurements. Because of the larger aperture (30 cm diameter), the transmit antenna has a narrow beam of 5°, which dictates the extent of the surface area responsible for the scattered energy. By using a focused beam antenna, we achieve a narrow-beam configuration without having to satisfy the usual far-field criterion. A baffle made of radar absorbing material was placed in the direct path between the transmitter and reciever to insure proper isolation of the two antennas.

To separate the measured signal into its coherent and incoherent components, it is necessary to measure many statistically independent samples of the random surface characterizing the target surface. This is achieved by rotating the sample holder in increments of 10°, thereby realizing 36 spatial samples per full rotation. The spatial correlation of the measured incoherent power indicates that measurements decorrelated every 15°, resulting in 24 independent samples per surface. Measurements of smooth surfaces indicate that phase coherence is maintained between independent samples.

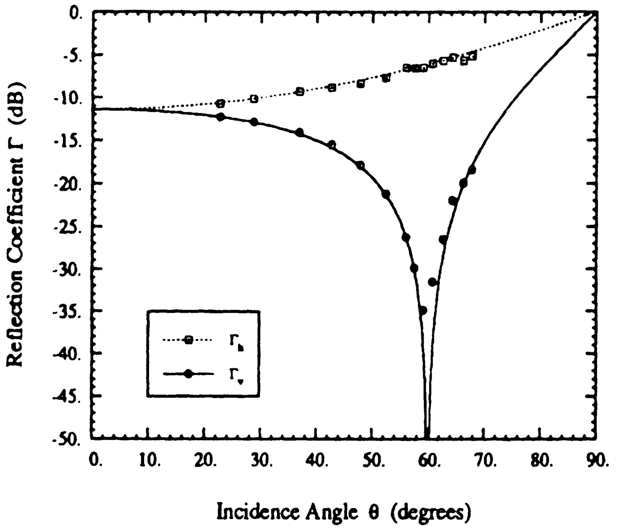

Fig. 5. Measured coherent reflectivity of a smooth surface with $\epsilon = 3.0$ and $ks < 0.2$: squares denote horizontal polarization and circles denote vertical polarization. Continuous curves are predictions based on Physical Optics. The angle of minimum reflectivity for vertical polarization is 60°.

The total path length, from transmitter to target to receiver, has a standard deviation less than 4 mm (7° at 9.25 GHz) for the set of independent samples.

C. Separation of Coherent and Incoherent Power

The Bistatic Facility measures a complex voltage V_m which is proportional to the scattered electric field for each polarization state at each spatially independent sample of the surface. Because the scattered electric field is composed of a coherent component from the mean surface and an incoherent component from the rough surface and/or volume, the measured voltage will also have a coherent and incoherent component: $V_m = V_{\mathrm{coh}} + V_{\mathrm{incoh}}$. These two components can be separated because the incoherent component has a zero mean: $\langle V_{\mathrm{incoh}} \rangle = 0$. Provided a large number of independent samples are measured, the coherent power P^{coh} is proportional to the square of the complex average of the measured voltages:

$$P^{\mathrm{coh}} = |V_{\mathrm{coh}}|^2 = |\overline{V_m}|^2 \tag{19}$$

The incoherent power P^{incoh} is then proportional to the variance of the fluctuating component of the measured voltage:

$$P^{\mathrm{incoh}} = \langle |V_{\mathrm{incoh}}|^2 \rangle = \overline{|V_m - \overline{V_m}|^2} \tag{20}$$

D. Calibration

The bistatic measurement system is calibrated using a bistatic adaptation of the polarimetric backscattering calibration technique developed by Sarabandi and Ulaby [16]. For measurements corresponding to the bistatic specular configuration, a large, flat conducting plate is used as a calibration target. Further verification is obtained by measuring a conducting hemisphere placed on the calibration target. The radar cross section of the hemispherical target was calculated via Physical Optics. Calibration to date has been accurate to within 0.5 dB in magnitude and 10° in co-polarized phase difference at boresight. The system is extremely stable; while the calibration procedure is performed for each day of measurements, calibrations have been good for up to 5 days.

The bistatic facility measures E_{pq}, the p polarized field due to a q polarized transmitted field. The power in this measured field P_{pq}, is composed of a coherent and an incoherent component:

$$P_{pq} = P_{pq}^{\mathrm{coh}} + P_{pq}^{\mathrm{incoh}} \tag{21}$$

$$P_{pq}^{\mathrm{coh}} = P_q^t \frac{|K_{pq}|^2}{(4\pi)^2 (r_{0r} + r_{0t})^2} \Gamma_{pq} \tag{22}$$

$$P_{pq}^{\mathrm{incoh}} = P_q^t \frac{|K_{pq}|^2}{(4\pi)^3} \sigma_{pq}^0 \lambda^2 \int_{A_{\mathrm{ill}}} \frac{g_p^r(x,y) g_q^t(x,y)}{r_r^2(x,y) r_t^2(x,y)} dx dy \tag{23}$$

$$= P_q^t \frac{|K_{pq}|^2}{(4\pi)^3} \sigma_{pq}^0 I_{A_{\mathrm{ill}}\, pq} \tag{24}$$

where the coherent power reflection coefficient, and therefore the coherent power, exists only for co-polarized scattering: $P_{pq}^{\mathrm{coh}} = \Gamma_{pq} = 0$ if $p \neq q$.

The co-polarized coherent power reflection coefficient is calculated by comparing the coherent power from a target to that from a large flat conducting plate, for which $\Gamma_{pp}^{\mathrm{cal}} = 1$ and $\sigma_{pq}^0 = 0$. Thus,

$$\Gamma_{pp} = \frac{P_{pp}^{\mathrm{coh}}}{P_{pp}^{\mathrm{cal}}} \tag{25}$$

The co-polarized differential scattering coefficient is calculated by comparing the incoherent power from a target to that of the calibration power. $I_{A_{\mathrm{ill}} pq}$ was calculated from extensive measurements of the normalized antenna patterns for both antennas, for each of the principal polarization states, over the entire main lobe of the antennas, at the boresight ranges r_{0r} and r_{0t}. Thus,

$$\sigma_{pp}^0 = \frac{4\pi}{(r_{0t} + r_{0r})^2 I_{A_{\mathrm{ill}}\, pp}} \frac{P_{pp}^{\mathrm{incoh}}}{P_{pp}^{\mathrm{cal}}} \tag{26}$$

IV. RESULTS

A. Surface Characterizations

The shape of a random rough surface is described by the surface height distribution function and the surface height correlation function. For a surface whose height is given by $z = f(x, y)$, the surface-height probability density function is given by $p_f(z)$, and is assumed to be Gaussian:

$$p_f(z) = \frac{1}{\sqrt{2\pi} s} e^{-\frac{1}{2}\frac{z^2}{s^2}} \tag{27}$$

Measurements by this and other experimenters [17], [18] indicate that this assumption is appropriate. Fig. 3(a) shows the fit between a histogram of measured surface heights and equation (27). The surface height characteristics can be specified by a single parameter, s, which is the root-mean-squared surface deviation from the mean planar surface located at $z = 0$.

The other statistical descriptor of random rough surfaces is the normalized correlation function, denoted by ρ. It describes

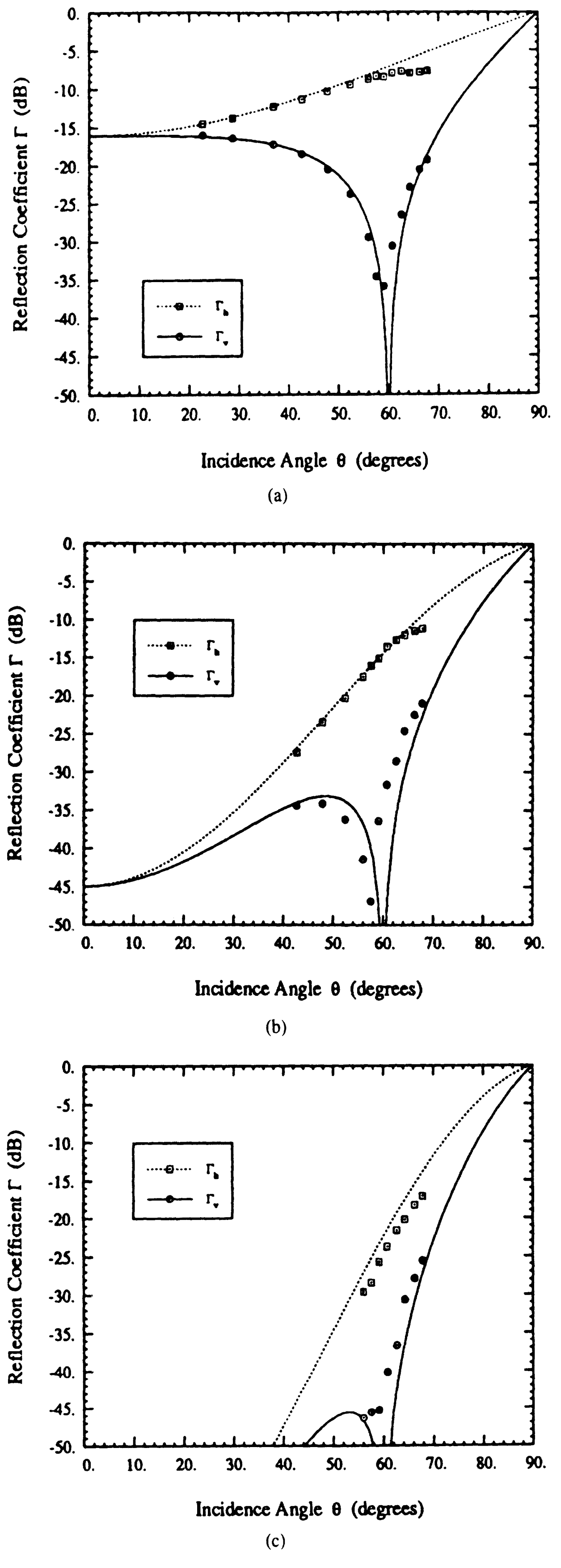

(a)

(b)

(c)

Fig. 6. Measured coherent reflectivity of three rough surfaces. Continuous curves are predictions based on Physical Optics. In all cases, the surfaces have a relative dielectric constant $\epsilon = 3.0$. (a) $ks = 0.515, kl = 5.4$. (b) $ks = 1.39, kl = 10.6$. (c) $ks = 1.94, kl = 11.8$.

the degree to which the height at one location given by $z = f(x, y)$, is correlated to the height at another location, given by $z' = f(x', y')$. For surfaces described by a stationary random process, ρ can be expressed in terms of the lateral separations $u = x - x'$ and $v = y - y'$ between the two locations on the surface. Moreover, if the surface statistics are symmetric under azimuthal rotations, the correlation function can be described by a single variable $\xi = \sqrt{u^2 + v^2}$, which specifies the absolute value of the lateral separation. Unlike the surface height distribution function, the correlation function may take on several forms for naturally occurring randomly rough surfaces. The vast majority of the literature on rough surface scattering assumes that the surface statistics are azimuthally symmetric and Gaussian, while many measurements of commonly occurring surfaces in microwave remote sensing situations indicate that an exponential correlation function may be more appropriate [19].

A correlation function for a surface with a correlation length of 52.5 mm is shown in Fig. 3(b). It was generated by averaging the individual autocorrelations of 3 linear profiles of the surface. Experimentation has shown that only 3 profile measurements averaged together are neccessary to accurately determine the correlation length and shape of this and other surfaces, but many more are needed to demonstrate that the correlation function tends toward zero beyond a few correlation lengths. For the purposes of this paper, the correlation length of a surface is that length at which the normalized correlation function is e^{-1}. As a result of the negative values of the correlation function, several of the integrals used to predict scattering characteristics ((3) and (4)) may yield values which are obviously incorrect. However, only a few surface profiles are needed to determine the shape of the correlation function within one correlation length, and if the rest of the correlation function tends towards zero, this portion of the correlation function dominates the integrals. The effect of the shape of the correlation function within one correlation length can be explored by considering several analytical forms for the correlation function.

B. Coherent Scattering

At the Brewster angle, the reflectivity for the vertical polarization is identically zero for a smooth interface between two lossless dielectric media. Whether or not it remains identically zero for a slightly rough surface is not clear. The Physical Optics approach clearly predicts that this is so; moreover, it predicts that the minimum reflectivity remains at the same incidence angle as for a smooth surface. This can be seen in Fig. 1. However, the Small Perturbation method predicts that the angle of minimum reflection for vertical polarization increases slightly with increasing roughness of the surface [11]. The fact that Physical Optics does not predict a change in angle while the Small Perturbation does is a consequence of the fact that the correction to the Fresnel coefficient is multiplicative for Physical Optics while it is additive for Small Perturbation. Additional terms in the Small Perturbation expansion may move this minimum angle back toward the smooth-surface Brewster angle.

a Fig. 5 shows measurements of the reflection coefficient for a smooth dry surface with $ks < 0.2$ (the rms height s was

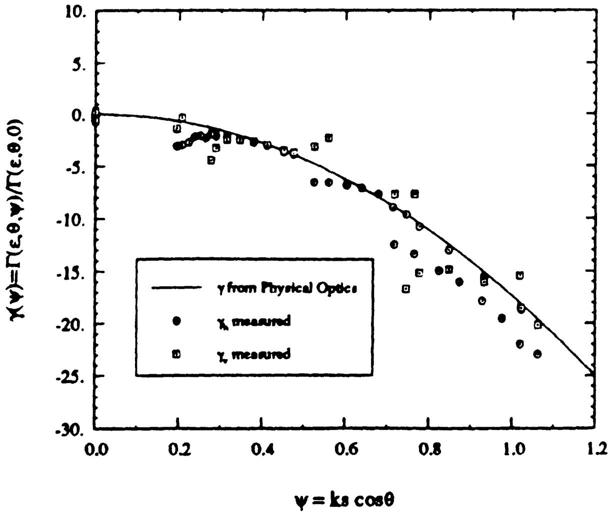

Fig. 7. The reduction of coherent scattering from a surface due to roughness. Shown is the measured coherent reflectivity of several surfaces (all with with $\epsilon' = 3$) but differing roughness parameters ψ, normalized to the reflection coefficient of a smooth surface. The angles of incidence range from 20° to 70° and the roughness ks ranges from 0 to 2. The continuous curve is the Physical Optics prediction for surfaces with Gaussian-height probability densities.

smaller than 1 mm, the measurement precision of the laser profileometer). The curves in Fig. 5 were calculated using the Fresnel reflection coefficient formulas given by (15) and (16) for a surface with a relative dielectric constant $\epsilon = 3.0 + j0$. The dielectric constant for the sand medium was measured by a dielectric probe, which gave a value of $\epsilon' = 3.0$ for the real part and a value of $\epsilon'' < 0.03$ for the imaginary part. Because $\epsilon''/\epsilon' \ll 1$ and the inclusion of ϵ'' as high as 0.05 does not significantly change the results of any of the calculations in this paper, it was ignored. The excellent agreement between the measured data and the calculated curves presented in Fig. 5 provides testimony to the measurement accuracy of the system.

Fig. 6 compares measured values of the power reflection coefficient Γ with curves calculated using Physical Optics (equation (1)) for surfaces with $ks = 0.515, 1.39$, and 1.94. Although good overall agreement is observed between theory and experimental observations, it should be noted that the location of the Brewster angle exhibits a slight shift towards decreasing angle of incidence; the Brewster angle shifts from 60° for the smooth surface shown in Fig. 5 to 58° for the surface with $ks = 1.39$ (Fig. 6(b)) and to about 56° for the surface with $ks = 1.94$ (Fig. 6(c)). The shift is toward decreasing angle of incidence, which is opposite to the direction predicted by the Small Perturbation Method.

By way of summary, Fig. 7 shows the dependence of the q-polarized normalized power reflection coefficient γ_q on the roughness parameter ψ, where

$$\gamma_q(\psi) = \frac{\Gamma_q(\epsilon, \theta, \psi)}{\Gamma_{q0}(\epsilon, \theta, 0)} = \frac{|R_q|^2}{|R_{q0}|^2} \tag{28}$$

$$= e^{4\psi^2} \tag{29}$$

and $\psi = ks\cos\theta$.

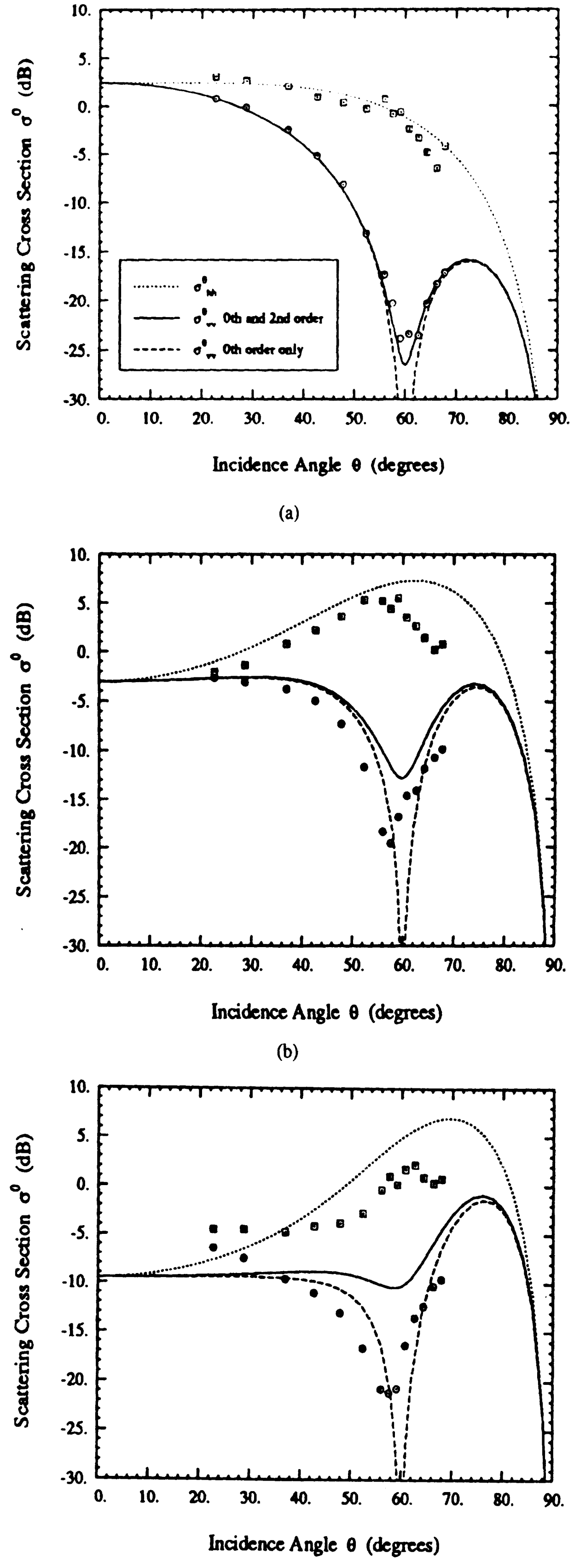

(a)

(b)

(c)

Fig. 8. Measured co-polarized specular scattering coefficient for three rough surfaces. Continuous curves are based on Physical Optics: the dashed curve corresponds to the zeroth-order term for σ^0_{vv}, the solid curve to σ^0_{vv} with both the zeroth-order and second-order terms included; the dotted curve corresponds to σ^0_{hh}. The second-order term is negligible for hh polarization. In all cases, the surfaces have a relative dielectric constant $\epsilon = 3.0$ and an exponential correlation function was used. (a) $ks = 0.515, kl = 5.4$, (b) $ks = 1.39, kl = 10.6$, (c) $ks = 1.94, kl = 11.8$.

C. Incoherent Scattering

As was discussed previously in Section II, the expression given by (2) for the bistatic specular scattering coefficient consists of two terms, a zeroth-order term and a second-order term, with the latter being the result of a new derivation of the Physical Optics model given in Appendix A. Fig. 8(a) shows the measured values of σ_{vv}^0 and σ_{hh}^0 for a slightly rough surface with $ks = 0.515$, plotted as a function of incidence angle, as well as plots for the same quantities calculated in accordance with (2). The calculated curves include a pair for the zeroth-order term alone, and a pair for the sum of the zeroth-order and second-order terms. For *hh* polarization, the second-order term is much smaller than the zeroth-order term, and therefore its contribution is insignificant. The same observation applies to *vv* polarization for angles more than 5° away from the Brewster angle, but in the vicinity of the Brewster angle, the second order term becomes the dominant contribution and it correctly predicts the level of the experimental observations.

Unfortunately, for the rougher surfaces shown in Figs. 8(b) and (c) with $ks = 1.39$ and 1.94, the model overestimates the level of σ^0, particularly for *vv* polarization in the vicinity of the Brewster angle. The measured data fall in between the curves calculated on the basis of the zeroth-order term alone and the curves based on both terms. Thus, despite the improvement that the proposed model provides for the slightly-rough case shown in Fig. 8(a), it is inadequate for very rough surfaces.

V. CONCLUSION

Several measurements of specular scattering from rough surfaces at 10 GHz are presented. They indicate that the Physical Optics predictions for coherent scattering are very good for surface roughness as large as $ks = 2.0$, with the exception that the theory does not predict a shifting of the Brewster angle by a few degrees towards nadir. A theoretical explanation of this phenomenon is unresolved. For co-polarized incoherent scattering, Physical Optics has been shown to be an adequate descriptor for a surface with $ks = 0.515$, but rapidly loses its quantitative predictive value for $ks > 1$.

APPENDIX A. A VECTOR PHYSICAL OPTICS DEVELOPMENT

In Ulaby *et al.* [7], the Physical Optics solution for scattering from a dielectric rough surface is presented under the scalar approximation. This approximation leaves out many terms, some of which change the results of the calculations significantly. In particular, cross-polarized scattering is neglected in the plane of incidence under the scalar approximation. What follows is a full vector solution to the Physical Optics problem, including vector terms which are neglected via the scalar approximation and some higher order terms in the expansion of the solution with respect to surface slope, with the rest of the assumptions remaining the same as in Ulaby *et al.* [7].

The solution starts with the exact Stratton-Chu integral equation for the p-polarized scattered far field due to a q-polarized wave ($\hat{q}E_0e^{-jk\hat{n}_i\cdot\vec{r}}$) incident upon a rough surface:

$$\begin{aligned} E_{pq}^s &= \frac{-jk_se^{-jk_sR_0}}{4\pi R_0}\hat{n}_s \times \int [(\hat{n}\times\vec{E}) - \eta_s\hat{n}_s\times(\hat{n}\times\vec{H})] \\ &\quad \times e^{jk_s\hat{n}_s\cdot\vec{r}}dS && \text{(A.1)} \\ &= \frac{-jk_se^{-jk_sR_0}}{4\pi R_0}E_0\int U_{pq}e^{jk_s(\hat{n}_s-\hat{n}_i)\cdot\vec{r}}dS && \text{(A.2)} \end{aligned}$$

where the singly scattered fields on the surface are calculated via the tangent plane approximation and are given by:

$$\begin{aligned} \hat{n}_1\times\vec{E} &= [R_h(\hat{q}\cdot\hat{t})(\hat{n}_1\times\hat{t}) \\ &\quad + R_v(\hat{n}_1\cdot\hat{n}_i)(\hat{q}\cdot\hat{d})\hat{t}]E_0 && \text{(A.3)} \\ \eta_1\hat{n}_1\times\vec{H} &= [R_h(\hat{n}_1\cdot\hat{n}_i)(\hat{q}\cdot\hat{t})\hat{t} \\ &\quad - R_v(\hat{q}\cdot\hat{d})(\hat{n}_1\times\hat{t})]E_0 && \text{(A.4)} \end{aligned}$$

where $\hat{n}_i$ is the incident wave direction, $\hat{q}$ is the incident wave polarization direction, $\hat{n}_1$ is the unit normal to the surface, $\hat{t} = \hat{n}_i\times\hat{n}_1/|\hat{n}_i\times\hat{n}_1|$, and $\hat{d} = \hat{n}_i\times\hat{t}$. Also, R_v and R_h are the v- and h- polarized Fresnel Reflection coefficients local to a point on the surface. These quantities, and the appropriate vector products, are defined in Ulaby *et al.* [7]; however, the exact expressions for U_{pq} under the single scattering tangent plane approximation do not appear there and hence are given here for reference:

$$\begin{aligned} U_{hh} = \frac{1}{D_1^2D_2}&[R_vZ_t((\sin\theta\sin\Delta\phi + Z_t^s\cos\theta + Z_tZ_l^s\sin\theta) \\ &+ (\cos\theta + Z_l\sin\theta)(\sin\theta\cos\theta_s\sin\Delta\phi \\ &+ Z_t^s\cos\theta\cos\theta_s - Z_t\sin\theta\sin\theta_s)) \\ &- R_h(\sin\theta - Z_l\cos\theta)((\cos\theta + Z_l\sin\theta) \\ &\times(\sin\theta\cos\Delta\phi - Z_l^s\cos\theta) \\ &+ (\sin\theta\cos\theta_s\cos\Delta\phi - Z_l^s\cos\theta\cos\theta_s \\ &+ Z_tZ_t^s\sin\theta\cos\theta_s - Z_l\sin\theta\sin\theta_s \\ &+ (Z_l^2 + Z_t^2)\cos\theta\sin\theta_s))] && \text{(A.5)} \\ U_{vh} = \frac{1}{D_1^2D_2}&[-R_h(\sin\theta - Z_l\cos\theta)((\sin\theta\sin\Delta\phi \\ &+ Z_t^s\cos\theta + Z_tZ_l^s\sin\theta) + (\cos\theta + Z_l\sin\theta) \\ &\times(\sin\theta\cos\theta_s\sin\Delta\phi + Z_t^s\cos\theta\cos\theta_s \\ &- Z_t\sin\theta\sin\theta_s)) \\ &- R_vZ_t((\sin\theta\cos\theta_s\cos\Delta\phi - Z_l^s\cos\theta\cos\theta_s \\ &+ Z_tZ_t^s\sin\theta\cos\theta_s - Z_l\sin\theta\sin\theta_s \\ &+ (Z_l^2 + Z_t^2)\cos\theta\sin\theta_s) \\ &+ (\cos\theta + Z_l\sin\theta) \\ &\times(\sin\theta\cos\Delta\phi - Z_l^s\cos\theta))] && \text{(A.6)} \\ U_{hv} = \frac{1}{D_1^2D_2}&[R_hZ_t((\cos\theta + Z_l\sin\theta) \\ &\times(\sin\theta\cos\Delta\phi - Z_l^s\cos\theta) \\ &+ (\sin\theta\cos\theta_s\cos\Delta\phi - Z_l^s\cos\theta\cos\theta_s \\ &+ Z_tZ_t^s\sin\theta\cos\theta_s - Z_l\sin\theta\sin\theta_s \\ &+ (Z_l^2 + Z_t^2)\cos\theta\sin\theta_s)) \\ &+ R_v(\sin\theta - Z_l\cos\theta) \\ &\times((\sin\theta\sin\Delta\phi + Z_t^s\cos\theta + Z_tZ_l^s\sin\theta) \\ &+ (\cos\theta + Z_l\sin\theta)(\sin\theta\cos\theta_s\sin\Delta\phi \\ &+ Z_t^s\cos\theta\cos\theta_s - Z_t\sin\theta\sin\theta_s))] && \text{(A.7)} \end{aligned}$$

$$\begin{aligned}U_{vv} = \frac{1}{D_1^2 D_2}[&R_h Z_t((\cos\theta + Z_l\sin\theta)\\ &(\sin\theta\cos\theta_s\sin\Delta\phi + Z_t^s\cos\theta\cos\theta_s\\ &- Z_t\sin\theta\sin\theta_s)\\ &+ (\sin\theta\sin\Delta\phi + Z_t^s\cos\theta + Z_tZ_l^s\sin\theta))\\ &- R_v(\sin\theta - Z_l\cos\theta)((\sin\theta\cos\theta_s\cos\Delta\phi\\ &- Z_l^s\cos\theta\cos\theta_s + Z_tZ_t^s\sin\theta\cos\theta_s\\ &- Z_l\sin\theta\sin\theta_s + (Z_l^2 + Z_t^2)\cos\theta\sin\theta_s)\\ &+ (\cos\theta + Z_l\sin\theta)(\sin\theta\cos\Delta\phi - Z_l^s\cos\theta))]\end{aligned} \tag{A.8}$$

where θ and θ_s describe the incident and scattered elevation angles measured from nadir, respectively, $\Delta\phi$ describes the angular change in azimuthal direction between the incident and scattered waves, Z_l and Z_t represent the surface slopes within (longitudinal to) and transverse to the plane of incidence, respectively, Z_l^s and Z_t^s represent the surface slopes within (longitudinal to) and transverse to the plane of the scattered wave, respectively, $D_1 = |\hat{n}_i \times \hat{n}_1| = \sqrt{(\sin\theta - Z_l\cos\theta)^2 + Z_t^2}$, and $D_2 = \sqrt{1 + Z_l^2 + Z_t^2}$.

Unfortunately, the exact expressions for U are not mathematically tractable in the Stratton-Chu integral, as the surface slopes are random functions of the location on the surface. An approximate solution can be obtained by expanding U in a Taylor series in slopes and retaining only the first two terms:

$$U_{pq} = U_{pq}^{(0)} + U_{pq}^{(1)} + \cdots \tag{A.9}$$

$$= \frac{1}{D_2}(a_{0pq} + (a_{lipq}Z_l + a_{tipq}Z_t + a_{lspq}Z_l^s + a_{tspq}Z_t^s)/\sin\theta + \cdots) \tag{A.10}$$

Note that D_2 need not be expanded as it will be cancelled upon integration over $dS = D_2 dx dy$, but D_1 is Taylor expanded as follows:

$$\frac{1}{D_1^2} = \frac{1}{(\sin\theta - Z_l\cos\theta)^2 + Z_t^2} \tag{A.11}$$

$$= \frac{1}{\sin^2\theta}\left(1 - \frac{Z_t^2}{\sin^2\theta} + 2\frac{Z_l}{\tan\theta} + 3\frac{Z_l^2}{\tan^2\theta} + \cdots\right) \tag{A.12}$$

Similarly, the reflection coefficients local to the surface are also expanded in terms of slopes:

$$R_v = R_{v0} + R_{v1}Z_l + \cdots \tag{A.13}$$

$$R_h = R_{h0} + R_{h1}Z_l + \cdots \tag{A.14}$$

The reflection coefficients are not dependent on Z_l^s or Z_t^s, and depend on even powers only of Z_t. The a coefficients in the expansion of U are, for all principal linear polarization combinations, given by:

$$a_{0hh} = -R_{h0}(\cos\theta + \cos\theta_s)\cos\Delta\phi \tag{A.15}$$

$$a_{0vh} = -R_{h0}(1 + \cos\theta\cos\theta_s)\sin\Delta\phi \tag{A.16}$$

$$a_{0hv} = R_{v0}(1 + \cos\theta\cos\theta_s)\sin\Delta\phi \tag{A.17}$$

$$a_{0vv} = -R_{v0}(\cos\theta + \cos\theta_s)\cos\Delta\phi \tag{A.18}$$

$$\begin{aligned}a_{lihh} = &R_{h0}(\sin\theta\sin\theta_s - (1 + \cos\theta\cos\theta_s)\cos\Delta\phi)\\ &- R_{h1}\sin\theta\cos\Delta\phi(\cos\theta + \cos\theta_s)\end{aligned} \tag{A.19}$$

$$a_{lshh} = R_{h0}\cos\theta(\cos\theta + \cos\theta_s) \tag{A.20}$$

$$a_{tihh} = R_{v0}\sin\Delta\phi(1 + \cos\theta\cos\theta_s) \tag{A.21}$$

$$a_{tshh} = 0 \tag{A.22}$$

$$\begin{aligned}a_{livh} = &-R_{h0}\sin\Delta\phi(\cos\theta + \cos\theta_s)\\ &- R_{h1}\sin\theta\sin\Delta\phi(1 + \cos\theta\cos\theta_s)\end{aligned} \tag{A.23}$$

$$a_{lsvh} = 0 \tag{A.24}$$

$$\begin{aligned}a_{tivh} = &R_{h0}\sin\theta\cos\theta\sin\theta_s\\ &- R_{v0}\cos\Delta\phi(\cos\theta + \cos\theta_s)\end{aligned} \tag{A.25}$$

$$a_{tsvh} = -R_{h0}\cos\theta(1 + \cos\theta\cos\theta_s) \tag{A.26}$$

$$\begin{aligned}a_{lihv} = &R_{v0}\sin\Delta\phi(\cos\theta + \cos\theta_s)\\ &+ R_{v1}\sin\theta\sin\Delta\phi(1 + \cos\theta\cos\theta_s)\end{aligned} \tag{A.27}$$

$$a_{lshv} = 0 \tag{A.28}$$

$$\begin{aligned}a_{tihv} = &-R_{v0}\sin\theta\cos\theta\sin\theta_s\\ &+ R_{h0}\cos\Delta\phi(\cos\theta + \cos\theta_s)\end{aligned} \tag{A.29}$$

$$a_{tshv} = R_{v0}\cos\theta(1 + \cos\theta\cos\theta_s) \tag{A.30}$$

$$\begin{aligned}a_{livv} = &R_{v0}(\sin\theta\sin\theta_s - (1 + \cos\theta\cos\theta_s)\cos\Delta\phi)\\ &- R_{v1}\sin\theta(\cos\theta + \cos\theta_s)\cos\Delta\phi\end{aligned} \tag{A.31}$$

$$a_{lsvv} = R_{v0}\cos\theta(\cos\theta + \cos\theta_s) \tag{A.32}$$

$$a_{tivv} = R_{h0}\sin\Delta\phi(1 + \cos\theta\cos\theta_s) \tag{A.33}$$

$$a_{tsvv} = 0 \tag{A.34}$$

A. Differential Radar Cross Section

The elements of the covariance matrix [13] are given by:

$$\langle S_{mn}S_{pq}^*\rangle = \int\int\langle U_{mn}^* U_{pq}^* e^{jk(\hat{n}_s - \hat{n}_i)\cdot(\vec{r} - \vec{r}')}\rangle dS dS' \tag{A.35}$$

from which the differential radar cross section can be derived:

$$\sigma_{pq}^0 = \frac{k^2}{4\pi A_0}\langle S_{pq}S_{pq}^*\rangle \tag{A.36}$$

Using (A.9):

$$U_{mn}U_{pq}^* \approx U_{mn}^{(0)}U_{pq}^{(0)^*} + (U_{mn}^{(0)}U_{pq}^{(1)^*} + U_{mn}^{(1)}U_{pq}^{(0)^*}) + U_{mn}^{(1)}U_{pq}^{(1)^*} \tag{A.37}$$

and evaluating these separately, we can express σ^0 as:

$$\sigma_{pq}^0 \approx \frac{k^2}{4\pi A_0}(\langle S_{pq}S_{pq}^*\rangle_{s^0} + \langle S_{pq}S_{pq}^*\rangle_{s^1} + \langle S_{pq}S_{pq}^*\rangle_{s^2}) \tag{A.38}$$

$$\langle S_{mn}S_{pq}^*\rangle_{s^0} = \int\int\langle U_{mn}^{(0)}U_{pq}^{(0)*} e^{jk(\hat{n}_s - \hat{n}_i)\cdot(\vec{r} - \vec{r}')}\rangle dS dS' \tag{A.39}$$

$$\langle S_{mn}S_{pq}^*\rangle_{s^1} = \int\int\langle (U_{mn}^{(0)}U_{pq}^{(1)*} + U_{mn}^{(1)}U_{pq}^{(0)*}) e^{jk(\hat{n}_s - \hat{n}_i)\cdot(\vec{r} - \vec{r}')}\rangle dS dS' \tag{A.40}$$

$$\langle S_{mn}S_{pq}^*\rangle_{s^2} = \int\int\langle U_{mn}^{(1)}U_{pq}^{(1)*} e^{jk(\hat{n}_s - \hat{n}_i)\cdot(\vec{r} - \vec{r}')}\rangle dS dS' \tag{A.41}$$

To obtain explicit expressions for σ^0_{pq}, the following relations will be used [7]:

$$\left\langle e^{jq_z(z-z')}\right\rangle = e^{-q_z^2 s^2(1-\rho(\xi))} \tag{A.42}$$

$$\left\langle Z_x e^{jq_z(z-z')}\right\rangle = \left\langle Z_x' e^{jq_z(z-z')}\right\rangle = -jq_z s^2 \cos\alpha \frac{\partial\rho(\xi)}{\partial\xi} e^{-q_z^2 s^2(1-\rho(\xi))} \tag{A.43}$$

$$\left\langle Z_y e^{jq_z(z-z')}\right\rangle = \left\langle Z_y' e^{jq_z(z-z')}\right\rangle = -jq_z s^2 \sin\alpha \frac{\partial\rho(\xi)}{\partial\xi} e^{-q_z^2 s^2(1-\rho(\xi))} \tag{A.44}$$

$$\left\langle Z_x Z_x' e^{jq_z(z-z')}\right\rangle = -\cos^2\alpha\left(q_z s^2\frac{\partial\rho(\xi)}{\partial\xi}\right)^2 e^{-q_z^2 s^2(1-\rho(\xi))} \tag{A.45}$$

$$\left\langle Z_y Z_y' e^{jq_z(z-z')}\right\rangle = -\sin^2\alpha\left(q_z s^2\frac{\partial\rho(\xi)}{\partial\xi}\right)^2 e^{-q_z^2 s^2(1-\rho(\xi))} \tag{A.46}$$

$$\left\langle Z_x Z_y' e^{jq_z(z-z')}\right\rangle = \left\langle Z_y Z_x' e^{jq_z(z-z')}\right\rangle = -\sin\alpha\cos\alpha \times\left(q_z s^2\frac{\partial\rho(\xi)}{\partial\xi}\right)^2 e^{-q_z^2 s^2(1-\rho(\xi))} \tag{A.47}$$

as well as the following Bessel function integral identity:

$$\int_{2\pi} \cos(n\alpha+\beta)e^{jx\cos\alpha}d\alpha = 2\pi j^n \cos\beta J_n(x) \tag{A.48}$$

where $q_z = k(\cos\theta + \cos\theta_s)$, s is the rms height, (ξ, α) are the polar coordinates of the difference between the unprimed and primed surface locations, and $\rho(\xi)$ is the normalized surface height correlation function.

B. Zeroth Order Term

The analysis of the zeroth order term is straightforward and yields the traditional coefficients for Physical Optics:

$$\frac{k^2}{4\pi A_0}\langle S_{mn}S^*_{pq}\rangle_{s^0} = \frac{1}{4\pi}k^2 a_{0mn}a^*_{0pq}I_0\frac{1}{4\pi}k^2 a_{0mn}a^*_{0pq}I_0 \tag{A.49}$$

where

$$I_0 = 2\pi e^{-q_z^2 s^2}\int_0^\infty [e^{q_z^2 s^2\rho(\xi)} - 1]J_0(q_t\xi)\xi d\xi \tag{A.50}$$

$$q_t = k\sqrt{\sin^2\theta + \sin^2\theta_s - 2\sin\theta\sin\theta_s\cos\Delta\phi} \tag{A.51}$$

This term represents the expected power in a particular direction due to the correlation of the height of the surface at one point to the height at another point. This term is the largest contribution to σ^0.

C. First Order Term

The first order term in Ulaby *et al.* [7] is that of the scalar approximation. Below is the full vector solution under the tangent plane approximation:

$$\begin{aligned}\frac{k^2}{4\pi A_0}\langle S_{mn}S^*_{pq}\rangle_{s^1} = \frac{-k^2}{4\pi q_z\sin\theta}&[(a_{0mn}a^*_{lipq} + a_{limn}a^*_{0pq})q_{li}\\ &+ (a_{0mn}a^*_{lspq} + a_{lsmn}a^*_{0pq})q_{ls}\\ &+ (a_{0mn}a^*_{tipq} + a_{timn}a^*_{0pq})q_{ti}\\ &+ (a_{0mn}a^*_{tspq} + a_{tsmn}a^*_{0pq})q_{ts}]I_0\end{aligned} \tag{A.52}$$

where

$$q_{li} = k(\sin\theta_s\cos\Delta\phi - \sin\theta) \tag{A.53}$$

$$q_{ti} = k\sin\theta_s\sin\Delta\phi \tag{A.54}$$

$$q_{ls} = k(\sin\theta_s - \sin\theta\cos\Delta\phi) \tag{A.55}$$

$$q_{ts} = k\sin\theta\sin\Delta\phi \tag{A.56}$$

This term represents the expected power in a particular direction due to the correlation of height of the surface at one point to the slope at another point. This term is negligible for scattering in the plane of incidence.

D. Second Order Term

The cross-slope term does not appear in Ulaby *et al* [7], but is nonetheless an analytic term. It is given by:

$$\begin{aligned}&\frac{k^2}{4\pi A_0}\langle S_{mn}S^*_{pq}\rangle_{s^2}\\ &\quad= \frac{k^2 q_z^2 s^4}{4\sin^2\theta}\{[a_{limn}a^*_{lipq} + a_{lsmn}a^*_{lspq}\\ &\qquad + a_{timn}a^*_{tipq} + a_{tsmn}a^*_{tspq}\\ &\qquad + ((a_{lsmn}a^*_{tipq} + a_{timn}a^*_{lspq})\\ &\qquad - (a_{limn}a^*_{tspq} + a_{tsmn}a^*_{lipq}))\sin\Delta\phi\\ &\qquad + ((a_{limn}a^*_{lspq} + a_{lsmn}a^*_{lipq})\\ &\qquad + (a_{timn}a^*_{tspq} + a_{tsmn}a^*_{tipq}))\cos\Delta\phi]I_{20}\\ &\qquad - [(a_{limn}a^*_{lipq} - a_{timn}a^*_{tipq})(q_{li}^2 - q_{ti}^2)\\ &\qquad + (a_{lsmn}a^*_{lspq} - a_{tsmn}a^*_{tspq})(q_{ls}^2 - q_{ts}^2)\\ &\qquad - (a_{limn}a^*_{tipq} + a_{timn}a^*_{lipq})q_{ti}q_{li}\\ &\qquad - (a_{lsmn}a^*_{tspq} + a_{tsmn}a^*_{lspq})q_{ts}q_{ls}\\ &\qquad + ((a_{limn}a^*_{tspq} + a_{tsmn}a^*_{lipq})\\ &\qquad + (a_{lsmn}a^*_{tipq} + a_{timn}a^*_{lspq}))(q_{ti}q_{ls} + q_{li}q_{ts})\\ &\qquad + ((a_{limn}a^*_{lspq} + a_{lsmn}a^*_{lipq})\\ &\qquad - (a_{timn}a^*_{tspq} + a_{tsmn}a^*_{tipq}))\\ &\qquad \times (q_{li}q_{ls} + q_{ti}q_{ts})]I_{22}\}\end{aligned} \tag{A.57}$$

where

$$I_{20} = \int_0^\infty\left(\frac{\partial\rho(\xi)}{\partial\xi}\right)^2 J_0(q_t\xi)e^{-q_z^2 s^2(1-\rho(\xi))}\xi d\xi \tag{A.58}$$

$$I_{22} = \int_0^\infty\left(\frac{\partial\rho(\xi)}{\partial\xi}\right)^2 \frac{J_2(q_t\xi)}{q_t^2}e^{-q_z^2 s^2(1-\rho(\xi))}\xi d\xi \tag{A.59}$$

This term represents the expected power in a particular direction due to the correlation of slope of the surface at one point to the slope at another point. This term is significant for cross polarization in the plane of incidence, and when the angle of incidence is near the Brewster angle for the mean surface.

E. Evaluation of the I Integrals for Common Correlation Functions

The remaining integrals can be further simplified if we assume a form for the correlation function $\rho(\xi)$. In particular, if it is Gaussian, i.e., $\rho(\xi) = e^{-\xi^2/l^2}$, then

$$I_0 = \pi l^2 e^{-q_z^2 s^2} \sum_{i=1}^{\infty} \frac{(q_z s)^{2i}}{i! i} e^{-\frac{q_t^2 l^2}{4i}} \tag{A.60}$$

$$I_{20} = 2e^{-q_z^2 s^2} \sum_{i=1}^{\infty} \frac{i(q_z s)^{2(i-1)}}{(i+1)!(i+1)} e^{-\frac{q_t^2 l^2}{4(i+1)}} \left(1 - \frac{q_t^2 l^2}{4(i+1)}\right) \tag{A.61}$$

$$I_{22} = \frac{1}{2} l^2 e^{-q_z^2 s^2} \sum_{i=1}^{\infty} \frac{i(q_z s)^{2(i-1)}}{(i+1)!(i+1)^2} e^{-\frac{q_t^2 l^2}{4(i+1)}} \tag{A.62}$$

or, if the correlation function is exponential, i.e., $\rho(\xi) = e^{-\xi/l}$, then

$$I_0 = 2\pi l^2 e^{-q_z^2 s^2} \sum_{i=1}^{\infty} \frac{(q_z s)^{2i}}{(i-1)!(i^2 + q_t^2 l^2)^{\frac{3}{2}}} \tag{A.63}$$

$$I_{20} = e^{-q_z^2 s^2} \sum_{i=1}^{\infty} \frac{(i+1)(q_z s)^{2(i-1)}}{(i-1)!(i^2 + q_t^2 l^2)^{\frac{3}{2}}} \tag{A.64}$$

$$I_{22} = 2l^2 e^{-q_z^2 s^2} \sum_{i=1}^{\infty} \frac{(q_z s)^{2(i-1)}\left(\sqrt{(i+1)^2 + q_t^2 l^2} - (i+1)\right)}{(i-1)!((i+1)^2 + q_t^2 l^2)^{\frac{3}{2}} q_t^2 l^2} \times \left(1 - (i+1)\frac{\sqrt{(i+1)^2 + q_t^2 l^2} - (i+1)}{2q_t^2 l^2}\right) \tag{A.65}$$

F. Special Case: Forward Scattering in the Specular Direction

For forward scattering in the specular direction, $\theta_s \to \theta, \Delta\phi \to 0$, and $q_t \to 0$, and the general expressions above simplify considerably:

$$\frac{k^2}{4\pi A_0}\langle S_{mn} S_{pq}^* \rangle_{s^0} = \frac{1}{4\pi} k^2 a_{0mn} a_{0pq}^* I_0 \tag{A.66}$$

$$\frac{k^2}{4\pi A_0}\langle S_{mn} S_{pq}^* \rangle_{s^1} = 0 \tag{A.67}$$

$$\frac{k^2}{4\pi A_0}\langle S_{mn} S_{pq}^* \rangle_{s^2} = \frac{k^4 s^4}{\tan^2\theta}[(a_{limn} + a_{lsmn})(a_{lipq}^* + a_{lspq}^*) + (a_{timn} + a_{tsmn})(a_{tipq}^* + a_{tspq}^*)] I_{20} \tag{A.68}$$

where

$$a_{0hh} = -2R_{h0}\cos\theta \tag{A.69}$$

$$a_{0vh} = a_{0hv} = 0 \tag{A.70}$$

$$a_{0vv} = -2R_{v0}\cos\theta \tag{A.71}$$

$$a_{livv} + a_{lsvv} = -2R_{v1}\sin\theta\cos\theta \tag{A.72}$$

$$a_{livh} + a_{lsvh} = a_{lihv} + a_{lshv} = 0 \tag{A.73}$$

$$a_{lihh} + a_{lshh} = -2R_{h1}\sin\theta\cos\theta \tag{A.74}$$

$$a_{tivh} + a_{tsvh} = -2(R_{h0}\cos^2\theta + R_{v0})\cos\theta \tag{A.75}$$

$$a_{tihv} + a_{tshv} = 2(R_{v0}\cos^2\theta + R_{h0})\cos\theta \tag{A.76}$$

$$a_{tivv} + a_{tsvv} = a_{tihh} + a_{tshh} = 0 \tag{A.77}$$

$$I_0 = 2\pi e^{-q_z^2 s^2} \int_0^{\infty} [e^{q_z^2 s^2 \rho(\xi)} - 1]\xi d\xi \tag{A.78}$$

$$I_{20} = \int_0^{\infty} \left(\frac{\partial\rho(\xi)}{\partial\xi}\right)^2 e^{-q_z^2 s^2 (1-\rho(\xi))} \xi d\xi \tag{A.79}$$

For the principal linear polarizations $pq = hh, hv, vh, vv$, the incoherent specular scattering coefficient can be obtained by setting $mn = pq$ in (A.66) and (A.68) and the resultant expressions in (A.38) This process leads to the expression given in 920.

REFERENCES

[1] K. C. McDonald, M. C. Dobson and F. T. Ulaby, "Using MIMICS to model L-band multi-angle and multi-temporal backscatter from a walnut orchard," *IEEE Transactions on Geoscience and Remote Sensing*, vol. 28, no. 3, pp. 477–491, May 1990.

[2] K. C. McDonald, M. C. Dobson and F. T. Ulaby, "Modeling multi-frequency diurnal backscatter from a walnut orchard," *IEEE Transactions on Geoscience and Remote Sensing*, vol. 29, no. 6, pp. 852–863, 1991.

[3] K. C. McDonald, *Modeling Microwave Backscatter from Tree Canopies*, PhD dissertation, University of Michigan, Ann Arbor, 1991.

[4] F. T. Ulaby, K. Sarabandi, K. C. McDonald, M. Whitt and M. C. Dobson, "Michigan Microwave Conopy Scattering Model," *International Journal of Remote Sensing*, vol. 11, no. 7, pp. 1223–1253, 1990.

[5] M. Whitt, *Microwave Scattering from Periodic Row-Structured Vegetation*, PhD dissertation, University of Michigan, Ann Arbor, 1991.

[6] P. Beckmann and A. Spizzichino, *The Scattering of Electromagnetic Waves from Rough Surfaces*, Pergamon Press, Oxford, 1963.

[7] F. T. Ulaby, R. K. Moore and A. K. Fung, *Microwave Remote Sensing: Active and Passive*, volume 2, Addison-Wesley, Reading, Massachusetts, 1982.

[8] R. L. Cosgriff, W. H. Peake and R. C. Taylor, "Terrain scattering properties for sensor system design," *Technical Report* 181, Ohio State University, 1960.

[9] F. T. Ulaby, T. F. Haddock and M. E. Coluzzi, "Millimeter-wave bistatic radar measurements of sand and gravel," in *Digest, IEEE International Geoscience and Remote Sensing Symposium* (IGARSS'87), pp. 281–286, Ann Arbor, MI, May 1987.

[10] M. Saillard and D. Maystre, "Scattering from metallic and dielectric rough surfaces," *Journal of the Optical Society of America A*, vol. 7, no. 6, pp. 982–990, June 1990.

[11] J.-J. Greffet, "Theoretical model of the shift of the Brewster angle on a rough surface," *Optics Letters*, vol. 17, no. 4, pp. 238–240, February 1992.

[12] S. O. Rice, "Reflection of electromagnetic waves from slightly rough surfaces," *Communications in Pure and Applied Mathematics*, vol. 4, pp. 351–378, 1951.

[13] F. T. Ulaby and E. C. Elachi, *Radar Polarimetry for Geoscience Applications*, Artech House, Norwood, Massachusetts, 1990.

[14] J. C. Leader, "Bidirectional scattering of electromagnetic waves from rough surfaces," *Journal of Applied Physics*, vol. 42, no. 12, pp. 4808–4816, November 1971.

[15] J. C. Leader and W. A. J. Dalton, "Bidirectional scattering of electromagnetic waves from the volume of dielectric materials," *Journal of Applied Physics*, vol. 43, no. 7, pp. 3080–3090, July 1972.

[16] K. Sarabandi and F. T. Ulaby, "A convenient technique for polarimetric calibration of single-antenna radar systems," *IEEE Transactions on Geoscience and Remote Sensing*, vol. 28, no. 6, pp. 1022–1033, November 1990.

[17] K. A. O'Donnell and E. R. Mendez, "Experimental study of scattering from characterized random surfaces," *Journal of the Optical Society of America*, vol. 4, no. 7, pp. 1194–1205, July 1987.

[18] E. R. Mendez and K. A. O'Donnell, "Observation of depolarization and backscattering enhancement in light scattering from Gaussian rendom surfaces," *Optics Communications*, vol. 61, no. 2, pp. 91–95, January 1987.

[19] Y. Oh, K. Sarabandi and F. T. Ulaby, "An empirical model and an inversion technique for radar scattering from bare soil surfaces," *IEEE Transactions on Geoscience and Remote Sensing*, vol. 30, no. 2, pp. 370–381, March 1992.

Roger D. De Roo (S'88) was born in Ridgewood, NJ, on February 29, 1964. He received the B.S. degree in letters and engineering from Calvin College, Grand Rapids, MI, in 1986, and the B.S.E. and M.S.E. degrees from the University of Michigan, Ann Arbor, both in electrical engineering, in 1986 and 1989, respectively.

He is currently a candidate for the Ph.D. degree at the University of Michigan. His research interests include modeling and measurement of bistatic scattering of electromagnetic waves from rough surfaces and modeling electromagnetic scattering from vegetation.

Fawwaz T. Ulaby (M'68-SM'74-F'80) received the B.S. degree in physics from the American University of Beirut, Lebanon, in 1964 and the M.S.E.E. and Ph.D. degrees in electrical engineering from the University of Texas, Austin, TX, in 1966 and 1968, respectively.

Dr. Ulaby is the Williams Professor of Electrical Engineering and Computer Science and the Director of the NASA Center for Space Terahertz Technology at the University of Michigan, Ann Arbor. His current interests include microwave and millimeter-wave remote sensing, radar systems, and radio wave propagation. He is the recipient of numerous awards, including the Eta Kappa Nu Association C. Holmes MacDonald Award as "An Outstanding Electrical Engineering Professor in the United States of America for 1975," the IEEE Geoscience and Remote Sensing Distinguished Achievement Award (1983), the IEEE Centennial Medal (1984), the American Society of Photogrammetry's Presidential Citation for Meritorious Service (1984), the Kuwait Prize in applied science (1986), the NASA Group Achievement Award (1990), and the University of Michigan Distinguished Faculty Achievement Award (1991).

Professor Ulaby served as president of the IEEE Geoscience and Remote Sensing Society (1980–1982), as Executive Editor of its *Transactions* (1983–1985), and as General Chairman of several international symposia. he is a member of URSI Commission F and served on several scientific boards and professional committees.

Electromagnetic Scattering from Slightly Rough Surfaces with Inhomogeneous Dielectric Profiles

Kamal Sarabandi and Tsenchieh Chiu
Radiation Laboratory
Department of Electrical Engineering and Computer Science
The University of Michigan, Ann Arbor, MI 48109-2122
Tel :(313) 936-1575
Email: saraband@eecs.umich.edu

Abstract - Remote sensing of soil moisture using microwave sensors require accurate and realistic scattering models for rough soil surfaces. In the past much effort has been devoted to the development of scattering models for either perfectly conducting or homogeneous rough surfaces. In practice, however, the permittivity of most soil surfaces is nonuniform, particularly in depth, for which analytical solution does not exist. The variations in the permittivity of a soil medium can easily be related to its soil moisture profile and soil type using the existing empirical models. In this paper analytical expressions for the bistatic scattering coefficients of soil surfaces with slightly rough interface and stratified permittivity profile are derived. The scattering formulation is based on a new approach where the perturbation expansion of the volumetric polarization current instead of the tangential fields is used to obtain the scattered field. Basically, the top rough layer is replaced with an equivalent polarization current and using the volumetric integral equation in conjunction with the dyadic Green's function of the remaining stratified half-space medium, the scattering problem is formulated. Closed form analytical expressions for the induced polarization currents to any desired order are derived which are then used to evaluate the bistatic scattered fields up to and including the third order. The analytical solutions for the scattered fields are used to derive the complete second-order expressions for the backscattering coefficients as well as the statistics of phase difference between the scattering matrix elements. The theoretical results are shown to agree well with the backscatter measurements of rough surfaces with known dielectric profiles and roughness statistics.

1 Introduction

Soil moisture, and its temporal and spatial variations are influential parameters in both climatic and hydrologic models. Soil dielectric constant at microwave frequencies exhibits a strong dependence on the soil's moisture content. At L-band, for example, the real part of the dielectric constant ranges from 3 for dry soil to about 25 for saturated soil. This variation can result in a change on the order of 10 dB in the magnitude of the radar backscatter coefficient [1]. With the advent of the polarimetric synthetic aperture radar (SAR), radar remote sensing of soil moisture has attained significant prominence in the past decade. SAR systems are capable of producing the backscatter map of the terrain with high resolution from an airborne or space-borne platform. From the electromagnetic point of view, remote sensing of soil moisture, in the absence of vegetation cover, can be modeled as an inverse scattering problem, where the dielectric constant and surface roughness statistics are to be determined from a set of backscatter measurements.

The problem of wave scattering from random rough surfaces has been the subject of ongoing research over the past several decades because of its arises in many areas of science and engineering. Generally speaking, the available electromagnetic scattering models can be categorized into three major groups: (1) analytical, (2) empirical, and (3) numerical. The analytical scattering solutions for rough surfaces apply when the roughness dimensions of the surface are either much smaller or much larger than the wavelength. For surfaces with small surface rms height and slope, the small perturbation model (SPM) is the most commonly used formalism [2, 3]. In this approach, the surface fields are expanded in terms of a power series in the small roughness parameter and then, using either the Rayleigh hypothesis or the extended boundary condition [4], the expansion coefficients are obtained recursively. The scattering formulations based on SPM exist for dielectric and perfectly conducting rough surfaces. For these surfaces, only first-order expressions for the co-polarized and second-order expressions for the cross-polarized backscattering coefficients are reported [5]. On the other hand, if the irregularities of the surface have relatively small slopes and large radii of curvature, the Kirchhoff approximation (KA) can be used [6]. In this approach, the surface fields at a given point are approximated by those of the local tangent plane. In the past two decades, many attempts have been made to extend the validity region of SPM and KA. Among these, the phase perturbation method (PPM) [7] and the unified perturbation expansion (UPE) [8] for extending the low-frequency techniques, and the integral equation method (IEM) [9] for extending the high-frequency techniques, can be mentioned. In the PPM, the perturbation solution is obtained by expanding the phase of the field instead of the field itself, whereas in the UPE method, the solution is obtained by expanding the field in terms of a parameter (momentum transfer) that remains small over a region larger than the perturbation parameter used in SPM. Scattering formulation based on PPM and UPM are reported only for one-dimensional rough surfaces. The scattering solution based on IE method is obtained by inserting the KA into the surface field integral equation. This method is significant in that it reduces to the SPM solution, thereby seemingly bridging the gap between the low- and high-frequency solutions [10].

In this paper, no attempt is made to extend the validity region of the existing methods; instead another practical aspect of the scattering problem is investigated. In most practical situations, the soil moisture content as a function of depth is non-uniform in depth. The soil moisture profile is usually a complex function of soil type, temperature profile, surface evaporation and moisture content [14]. For radar remote sensing of soil moisture, the effect of the inhomogeneity in the complex permittivity of the soil surface on its backscatter must be understood. For this purpose, analytical expressions for the bistatic scattering coefficients of a slightly rough surface with inhomogeneous dielectric profile are derived. Using the classical perturbation expansion of the electric field, a new volumetric integral equation approach is used to obtain the iterative scattering solutions. In what follows, the theoretical formulation for the scattering problem is given and the closed-form complete second order solution for backscattering coefficients and phase-difference statistics are derived. In Section 3, the theoretical solution will be compared with experimental backscatter measurements collected using the University of Michigan's bistatic indoor facilities.

2 Theoretical Analysis

Consider an inhomogeneous half-space medium with a rough interface as shown in Fig. 1. In the following derivation, it is assumed that the medium is stratified, that is, the relative permittivity is only a function of z, and is given by

$$\epsilon_r(x, y, z) = \epsilon_r(z) \ .$$

Suppose a plane wave is illuminating the rough interface from the upper medium and, with a very high probability, the surface height variation is small compared with the wavelength of the incident wave. To make the solution tractable, the permittivity of the top layer down to a depth of d is considered to be uniform, where -d $<$ min\{surface profile\}. Denote the surface height profile by the function $z = \Delta f(x, y)$, where $f(x, y)$ is a zero-mean stationary random process with a known autocorrelation function, and $\Delta << \lambda$ is a small constant known as the perturbation parameter. The incident wave can be written as

$$\mathbf{E}^i(\bar{r}) = \mathbf{P}_i \, e^{ik_0 \hat{k}^i \cdot \mathbf{r}} \ ,$$

where $\mathbf{P}_i$ denotes the polarization of the incident wave, $k_0 = \frac{2\pi}{\lambda}$ is the free space propagation constant, and $\hat{k}^i$ is the unit vector along the direction of propagation, given by

$$\hat{k}^i = \sin\theta_i \cos\phi_i \hat{x} + \sin\theta_i \sin\phi_i \hat{y} - \cos\theta_i \hat{z} \ .$$

In the absence of the top homogeneous rough layer (with thickness d), the incident wave would be reflected at the smooth interface between the free space and the inhomogeneous half space soil medium. The reflected wave can be expressed by

$$\mathbf{E}^r(\bar{r}) = \mathbf{P}_r \, e^{ik_0 \hat{k}^r \cdot \mathbf{r}} \ ,$$

where $\hat{k}^r$ is the direction of propagation of the reflected wave, given by

$$\hat{k}^r = \hat{k}^i - 2(\hat{z} \cdot \hat{k}^i)\hat{z} \ ,$$

and $\mathbf{P}_r$ is the polarization vector of the reflected wave, which can be obtained from

$$\mathbf{P}_r = r_v(\mathbf{P}_i \cdot \hat{v}_i)\hat{v}_r + r_h(\mathbf{P}_i \cdot \hat{h}_i)\hat{h}_r \ .$$

Here r_v and r_h are the Fresnel reflection coefficients, and the horizontal and vertical unit vectors are given by

$$\hat{h}_s = \frac{\hat{k}_s \times \hat{z}}{|\hat{k}_s \times \hat{z}|}, \qquad \hat{v}_s = \hat{h}_s \times \hat{k}_s \ , \tag{1}$$

where the subscript s can be i or r for the incident and reflected waves. In presence of the homogeneous rough layer, the incident and reflected waves induce a polarization current within the top dielectric layer which is the source of the scattered field. The polarization current in terms of the total field and the permittivity of the layer is

$$\mathbf{J}(\mathbf{r}) = -ik_0 Y_0(\epsilon - 1)\mathbf{E}^t \ , \tag{2}$$

where $Y_0 = \frac{1}{Z_0}$ is the characteristic admittance of the free space, and

$$\mathbf{E}^t = \mathbf{E}^i + \mathbf{E}^r + \mathbf{E}^s \ .$$

The scattered field $\mathbf{E}^s$ can in turn be expressed in terms of the polarization current and is given by

$$\mathbf{E}^s = ik_0 Z_0 \int\limits_{V_{slab}} \bar{\bar{\mathbf{G}}}(\mathbf{r},\mathbf{r}') \cdot \mathbf{J}(\mathbf{r}')\, dv' \ , \tag{3}$$

where $\bar{\bar{\mathbf{G}}}(\mathbf{r},\mathbf{r}')$ is the dyadic Green's function of the half-space inhomogeneous medium (in the absence of the top rough layer). Substituting (3) into (1), the following integral equation for the polarization current can be obtained:

$$\frac{1}{\epsilon - 1}\mathbf{J}(\mathbf{r}) = -ik_0 Y_0(\mathbf{E}^i + \mathbf{E}^r) + k_0^2 \iint\limits_{-\infty}^{\infty} \int\limits_{0}^{d+\Delta f(x',y')} \bar{\bar{\mathbf{G}}}(\mathbf{r},\mathbf{r}') \cdot \mathbf{J}(\mathbf{r}')\, dv' \ . \tag{4}$$

An approximate solution for the integral equation can be obtained using a perturbation technique. By breaking the z' integral into two integrals, one with limits from 0 to d and the other with limits from d to $d + \Delta f(x', y')$, and noting $\Delta f(x', y')$ is a small quantity, up to the Nth order in Δ, (4) can be written as

$$\begin{aligned}\frac{1}{\epsilon - 1}\mathbf{J}(\mathbf{r}) \simeq & -ik_0 Y_0(\mathbf{E}^i + \mathbf{E}^r) + k_0^2 \iint\limits_{-\infty}^{\infty} \int\limits_{0}^{d} \bar{\bar{\mathbf{G}}}(\mathbf{r},\mathbf{r}') \cdot \mathbf{J}(\mathbf{r}')\, dx'dy'dz' \\ & + k_0^2 \sum_{n=0}^{N-1} \iint\limits_{-\infty}^{\infty} \frac{[\Delta f(x',y')]^{n+1}}{(n+1)!} \frac{\partial^n}{\partial z'^n} \left\{ \bar{\bar{\mathbf{G}}}(\mathbf{r},\mathbf{r}'_d) \cdot \mathbf{J}(\mathbf{r}'_d) \right\} dx'dy' \ ,\end{aligned} \tag{5}$$

where $\mathbf{r}'_d = x'\hat{x} + y'\hat{y} + d\hat{z}$. Taking the two-dimensional Fourier transform of both sides of (5) and noting that the integrals in x' and y' are of convolution type, it can be shown that

$$\begin{aligned}\frac{1}{\epsilon - 1}\tilde{\mathbf{J}}(\mathbf{k}_\perp, z) = & - i4\pi^2 k_0 Y_0 \delta(\mathbf{k}_\perp - \mathbf{k}^i_\perp)\left[\mathbf{P}_i e^{-ik^i_z z} + \mathbf{P}_r e^{ik^i_z z}\right] \\ & + k_0^2 \int_0^d \tilde{\bar{\bar{\mathbf{G}}}}(\mathbf{k}_\perp; z, z') \cdot \tilde{\mathbf{J}}(\mathbf{k}_\perp, z')\, dz' + k_0^2 \sum_{n=0}^{N-1} \sum_{m=0}^{n} \frac{\binom{n}{m}\Delta^{n+1}}{(n+1)!} \\ & \cdot \frac{\partial^m}{\partial z'^m}\tilde{\bar{\bar{\mathbf{G}}}}(\mathbf{k}_\perp; z, d) \cdot \left[\frac{\partial^{n-m}}{\partial z'^{n-m}}\tilde{\mathbf{J}}(\mathbf{k}_\perp, d) * \overset{n+1}{\bigotimes} F(\mathbf{k}_\perp)\right] \quad , \end{aligned} \tag{6}$$

where $*$ is the convolution operator, $F(\mathbf{k}_\perp)$ is the Fourier transform of $f(x', y')$, $\overset{n}{\otimes}$ represents n-fold self-convolution $(\overset{n}{\otimes} F = \overbrace{F * F * \cdots * F}^{n})$, $k^i_z = k_0 \cos\theta_i$, and $\tilde{\bar{\bar{\mathbf{G}}}}(\bar{k}_\perp; z, z')$ is the Fourier transform of the Green's function, given by

$$\begin{aligned}\tilde{\bar{\bar{\mathbf{G}}}}(\mathbf{k}_\perp; z, z') = & - \hat{z}\hat{z}\frac{\delta(z - z')}{k_0^2} \\ & + \frac{i}{2k_z}\begin{cases} \left\{\left[r_h \hat{h}(k_z) e^{ik_z z} + \hat{h}(-k_z) e^{-ik_z z}\right] \cdot \hat{h}(-k_z) e^{ik_z z'} \right. \\ \left. + \left[r_v \hat{v}(k_z) e^{ik_z z} + \hat{v}(-k_z) e^{-ik_z z}\right] \cdot \hat{v}(-k_z) e^{ik_z z'}\right\} \\ \qquad\qquad\qquad z < z', \\ \\ \left\{\hat{h}(k_z)\left[r_h \hat{h}(-k_z) e^{ik_z z'} + \hat{h}(k_z) e^{-ik_z z'}\right] e^{ik_z z} \right. \\ \left. + \hat{v}(k_z)\left[r_v \hat{v}(-k_z) e^{ik_z z'} + \hat{v}(k_z) e^{-ik_z z'}\right] e^{ik_z z}\right\} \\ \qquad\qquad\qquad z > z'. \end{cases}\end{aligned} \tag{7}$$

In (7), $k_z = \sqrt{k^2 - k_x^2 - k_y^2}$, $\mathbf{k}_\perp = k_x\hat{x} + k_y\hat{y}$, and $\hat{h}(\pm k_z)$ and $\hat{v}(\pm k_z)$ can be obtained from (1) with $\hat{k}_s = (k_x\hat{x} + k_y\hat{y} \pm k_z\hat{z})/k_0$.

Since the surface height variations are much smaller than the wavelength ($\Delta << \lambda_0$), the induced polarization current on the top rough layer closely resembles that of a smooth layer with the same dielectric constant and thickness d. Under this assumption, the polarization current may be expanded in terms of a convergent perturbation series in Δ, and is given by

$$\mathbf{J}(\mathbf{r}) = \sum_{n=0}^{\infty} \mathbf{J}_n(\mathbf{r})\Delta^n \quad ,$$

where $\mathbf{J}_0(\mathbf{r})$ is the induced polarization current in the unperturbed layer. Then by substituting this expansion into (6) and collecting terms of equal powers in Δ, a recursive set of equations for the components of the polarization current can be obtained, and is given by

$$\begin{aligned}\frac{1}{\epsilon-1}\tilde{\mathbf{J}}_0(\mathbf{k}_\perp,z) =& -i4\pi^2 k_0 Y_0 \delta(\mathbf{k}_\perp-\mathbf{k}_\perp^i)\left[\mathbf{P}_i e^{-ik_z^i z}+\mathbf{P}_r e^{ik_z^i z}\right] \\ & + k_0^2\int_0^d \tilde{\tilde{\mathbf{G}}}(\mathbf{k}_\perp;z,z')\cdot\tilde{\mathbf{J}}_0(\mathbf{k}_\perp,z')\,dz' \ , \end{aligned} \tag{8}$$

$$\frac{1}{\epsilon-1}\tilde{\mathbf{J}}_N(\mathbf{k}_\perp,z) = k_0^2\int_0^d \tilde{\tilde{\mathbf{G}}}(\mathbf{k}_\perp;z,z')\cdot\tilde{\mathbf{J}}_N(\mathbf{k}_\perp,z')\,dz' + k_0^2\tilde{\tilde{\mathbf{G}}}(\mathbf{k}_\perp;z,d)\cdot\tilde{\mathbf{V}}_N \ . \tag{9}$$

Here $\tilde{\mathbf{V}}_N$ is the source function for the Nth-order integral equation with a closed form representation

$$\tilde{\mathbf{V}}_N = \sum_{n=0}^{N-1}\sum_{m=0}^{N-n-1}\frac{\binom{N-n-1}{m}(ik_z)^m}{(N-n)!}\cdot\left[\frac{\partial^{N-n-m-1}}{\partial(z')^{N-n-m-1}}\tilde{\mathbf{J}}_n(\mathbf{k}_\perp,d)\right] * \bigotimes^{N-n} F(\mathbf{k}_\perp) \ .$$

The integral equations so obtained are Fredholm integral equations of the second kind, for which analytical solutions can be obtained. Note that the solution of the zeroth-order equation is the source function for the first-order equation and the Nth-order equation has an excitation function which consists of N-1 lower order polarization currents. To solve (8), let us first split the integral into two integrals : one over the interval $[0,z]$ and the other over the interval $[z,d]$. Extending the integration limits of the second integral over the entire interval $[0,d]$ by adding and subtracting an integral over the interval $[0,z]$ and noting $\hat{h}(k_z)=\hat{h}(-k_z)$, (8) can be written as

$$\begin{aligned}\frac{1}{\epsilon-1}\tilde{\mathbf{J}}_0(\mathbf{k}_\perp,z) =& -i4\pi^2 k_0 Y_0 \delta(\mathbf{k}_\perp-\mathbf{k}_\perp^i)\left[\mathbf{P}_i e^{-ik_z^i z}+\mathbf{P}_r e^{ik_z^i z}\right] - \hat{z}\hat{z}\cdot\tilde{\mathbf{J}}_0(\mathbf{k}_\perp,z) \\ & + \frac{ik_0^2}{2k_z}\int_0^z \Big\{\hat{h}(k_z)\hat{h}(k_z)\left[e^{-ik_z(z'-z)}-e^{ik_z(z'-z)}\right] \\ & + \left[\hat{v}(k_z)\hat{v}(k_z)e^{-ik_z(z'-z)}-\hat{v}(-k_z)\hat{v}(-k_z)e^{ik_z(z'-z)}\right]\Big\}\cdot\tilde{\mathbf{J}}_0(\mathbf{k}_\perp,z')\,dz' \\ & + \frac{ik_0^2}{2k_z}\Big\{\left[r_h e^{ik_z z}+e^{-ik_z z}\right]\hat{h}(k_z)\hat{h}(k_z)+\left[r_v e^{ik_z z}\hat{v}(k_z)+e^{-ik_z z}\hat{v}(-k_z)\right] \\ & \hat{v}(-k_z)\Big\}\cdot\int_0^d \tilde{\mathbf{J}}_0(\mathbf{k}_\perp,z')\,dz' \ . \end{aligned} \tag{10}$$

Noting that the second integral in (10) is a constant function of z and that the first integral is of convolution type in z, (10) is recognized as a vector Volta integral equation that can be solved analytically using the Laplace transformation or Picard's Process of successive approximation [15]. Since the involved integral in (10) is explicit in terms of variable $\mathbf{k}_\perp$, it can be shown that $\tilde{\mathbf{J}}_0(\mathbf{k}_\perp, z)$ is of the form

$$\tilde{\mathbf{J}}_0(\mathbf{k}_\perp, z) = (2\pi)^2 \, \delta(\mathbf{k}_\perp - \mathbf{k}_\perp^i) \, \tilde{\mathbf{J}}_0(z) .$$

The polarization current can be decomposed into its principal components, given by

$$\tilde{\mathbf{J}}_0(z) = J_{0h}(z) \, \hat{h}(k_z^i) + J_{0t}(z) \, \hat{t}(k_z^i) + J_{0z}(z) \, \hat{z} \ ,$$

where $\hat{t}(k_z^i) = \hat{z} \times \hat{h}(k_z^i)$. Evaluating the inner product of (10) with $\hat{h}(k_z^i)$, $\hat{t}(k_z^i)$ and $\hat{z}$, three uncoupled scalar Volta integral equations are obtained. Solutions to the resulted integral equations for the three components of current are of the following form:

$$\begin{aligned}
J_{0h}(z) &= A_h^0 \, e^{ik_{1z}^i z} + B_h^0 \, e^{-ik_{1z}^i z} \ , \\
J_{0t}(z) &= A_v^0 \, e^{ik_{1z}^i z} + B_v^0 \, e^{-ik_{1z}^i z} \ , \\
J_{0z}(z) &= -\frac{k_\rho^i}{k_{1z}} \left\{ A_v^0 \, e^{ik_{1z}^i z} - B_v^0 \, e^{-ik_{1z}^i z} \right\} \ . \qquad (11)
\end{aligned}$$

After a long algebraic manipulation, closed form expressions for the zeroth-order polarization current are obtained

$$\begin{aligned}
J_{0h}(z) &= -i \, \frac{2k_0 k_z^i}{k_z^i + k_{1z}^i} Y_0 \, (\epsilon - 1) \, C_0^h(\mathbf{k}^i, z) \, \left[\mathbf{P}_i \cdot \hat{h}(k_z^i) \right] e^{-ik_z^i d} \ , \\
J_{0t}(z) &= -i \frac{2k_0 k_z^i k_{1z}^i}{k_\rho^i \, (\epsilon k_z^i + k_{1z}^i)} Y_0(\epsilon - 1) \, C_0^v(\mathbf{k}^i, z) \, [\mathbf{P}_i \cdot \hat{z}] \, e^{-ik_z^i d} \ , \\
J_{0z}(z) &= -i \frac{2k_0 k_z^i}{\epsilon k_z^i + k_{1z}^i} Y_0(\epsilon - 1) \, C_1^v(\mathbf{k}^i, z) \, [\mathbf{P}_i \cdot \hat{z}] \, e^{-ik_z^i d} \ ,
\end{aligned}$$

where

$$k_{1z}^i = k_0 \sqrt{\epsilon - \sin^2 \theta_i} \, , \qquad k_\rho^i = k_0 \sin \theta_i \, , \qquad R_h^i = \frac{k_z^i - k_{1z}^i}{k_z^i + k_{1z}^i} \, , \qquad R_v^i = \frac{\epsilon k_z^i - k_{1z}^i}{\epsilon k_z^i + k_{1z}^i} \, ,$$

$$\begin{aligned}
C_n^h(\mathbf{k}, z) &= \frac{(-1)^n \, (R_h - r_h) \, e^{ik_{1z} z} + (R_h r_h - 1) \, e^{-ik_{1z} z}}{R_h \, (R_h - r_h) \, e^{ik_{1z} d} + (R_h r_h - 1) \, e^{-ik_{1z} d}} \ , \\
C_n^v(\mathbf{k}, z) &= \frac{(-1)^n \, (r_v - R_v) \, e^{ik_{1z} z} + (R_v r_v - 1) \, e^{-ik_{1z} z}}{R_v \, (R_v - r_v) \, e^{ik_{1z} d} + (R_v r_v - 1) \, e^{-ik_{1z} d}} \ .
\end{aligned}$$

The source function of (9) can be written as

$$k_0^2 \tilde{\tilde{\mathbf{G}}}(\mathbf{k}_\perp; z, d) \cdot \tilde{\mathbf{V}}_N \triangleq -ik_0 Y_0 \left(\mathbf{q}_{Ni} e^{-ik_z z} + \mathbf{q}_{Nr} e^{ik_z z} \right) \ , \qquad (12)$$

where

$$\mathbf{q}_{Ni} = \frac{-Z_0 k_0}{2k_z} e^{ik_z d} \cdot \left\{ \left(\hat{h}(k_z) \cdot \tilde{\mathbf{V}}_N \right) \hat{h}(k_z) + \left(\hat{v}(-k_z) \cdot \tilde{\mathbf{V}}_N \right) \hat{v}(-k_z) \right\} \ ,$$
$$\mathbf{q}_{Nr} = \frac{-Z_0 k_0}{2k_z} e^{ik_z d} \cdot \left\{ \left(\hat{h}(k_z) \cdot \tilde{\mathbf{V}}_N \right) \hat{h}(k_z) + \left(\hat{v}(-k_z) \cdot \tilde{\mathbf{V}}_N \right) \hat{v}(k_z) \right\} \ .$$

Noted that the vector integral equation (9) and the source function for the Nth-order polarization current are identical to those of the zeroth-order polarization current, and therefore a similar solution can be easily obtained. By decomposing the Nth-order polarization current in terms of its three principle components, it can be shown that

$$\tilde{J}_{Nh}(\mathbf{k}_\perp, z) = \frac{ik_0^2 (\epsilon - 1)}{k_z + k_{1z}} C_0^h(\mathbf{k}, z) \left[\tilde{\mathbf{V}}_N \cdot \hat{h}(k_z) \right] \ ,$$
$$\tilde{J}_{Nt}(\mathbf{k}_\perp, z) = \frac{ik_0 k_{1z} (\epsilon - 1)}{\epsilon k_z + k_{1z}} C_0^v(\mathbf{k}, z) \left[\tilde{\mathbf{V}}_N \cdot \hat{v}(-k_z) \right] \ ,$$
$$\tilde{J}_{Nz}(\mathbf{k}_\perp, z) = \frac{ik_0 k_\rho (\epsilon - 1)}{\epsilon k_z + k_{1z}} C_1^v(\mathbf{k}, z) \left[\tilde{\mathbf{V}}_N \cdot \hat{v}(-k_z) \right] \ .$$

2.1 Scattering Coefficients

Once the polarization current is obtained, the scattered field in region $z > d$ can be obtained from (3). Assuming that the surface perturbation is localized and the observation point $\mathbf{r} = r(\sin\theta_s \cos\phi_s \hat{x} + \sin\theta_s \sin\phi_s \hat{y} + \cos\theta_s \hat{z})$ is far from the scatterer, the far field approximation can be used to find the scattered fields. Using the stationary phase approximation in the far fields region, the Green's function is reduced to

$$\bar{\bar{\mathbf{G}}}(\mathbf{r}, \mathbf{r}') = \frac{e^{ik_0 r}}{4\pi r} \left\{ \left[\hat{h}(k_z^s) \hat{h}(k_z^s) r_h^s + \hat{v}(k_z^s) \hat{v}(-k_z^s) r_v^s \right] e^{-i\mathbf{K}^s \mathbf{r}'} + \left[\hat{h}(k_z^s) \hat{h}(k_z^s) + \hat{v}(k_z^s) \hat{v}(k_z^s) \right] e^{-i\mathbf{k}^s \mathbf{r}'} \right\} \ . \tag{13}$$

Substituting (13) and the polarization currents into (3) and expanding the integral similar to those used in (5), the Nth-order scattered field is given by a power series in $\Delta f(x,y)$ (similar to (3)). In this process, the Nth-order scattered field components are found to be

$$\mathbf{E}_N^s(\mathbf{r}) \cdot \hat{h}(k_z^s) = ik_0 Z_0 \Delta^N \frac{e^{ik_0 r}}{4\pi r} e^{-ik_z^s d} \sum_{n=0}^{N-1} \sum_{m=0}^{N-n-1} \frac{\binom{N-n-1}{m} (ik_z^s)^m}{(N-n)!} \left[R_h^s + (-1)^m \right] \cdot C_m^h(\mathbf{k}^s, d) \left[\frac{\partial^{N-n-m-1}}{\partial (z')^{N-n-m-1}} \tilde{\mathbf{J}}_n(\mathbf{k}_\perp^s, d) \right] * \bigotimes^{N-n} F(\mathbf{k}_\perp^s) \cdot \hat{h}(k_z^s) \ , \tag{14}$$

$$\mathbf{E}^s_N(\mathbf{r}) \cdot \hat{v}(k^s_z) = i k_0 Z_0 \Delta^N \frac{e^{ik_0 r}}{4\pi r} e^{-ik^s_z d} \sum_{n=0}^{N-1} \sum_{m=0}^{N-n-1} \frac{\binom{N-n-1}{m} (ik^s_z)^m}{(N-n)!} \Bigg\{ \left[R^s_v - (-1)^m\right]$$

$$\cdot\, C^v_m(\mathbf{k}^s, d) \cos\theta_s \, \hat{t}(k^s_z) + \left[R^s_v + (-1)^m\right] C^v_{m+1}(\mathbf{k}^s, d) \sin\theta_s \, \hat{z} \Bigg\}$$

$$\cdot \left[\frac{\partial^{N-n-m-1}}{\partial (z')^{N-n-m-1}} \tilde{\mathbf{J}}_n(\mathbf{k}^s_\perp, d) \right] * \bigotimes^{N-n} F(\mathbf{k}^s_\perp) \ . \tag{15}$$

The polarimetric response of a target can be obtained from its complex scattering matrix, defined by

$$\mathbf{E}^s = \frac{e^{ikr}}{r} \bar{\bar{\mathbf{S}}}\, \mathbf{E}^i \ .$$

The elements of the bistatic scattering matrix can simply be computed by setting $\mathbf{P}_i = \hat{h}(k^i_z)$ and $\mathbf{P}_i = \hat{v}(k^i_z)$ in (14) and (15). For distributed targets, such as rough surfaces, the quantities of interest are the elements of the differential covariance matrix, defined by

$$\sigma^0_{ijpq} = \lim_{A\to\infty} \frac{4\pi}{A} \left\langle S_{ij} S^*_{pq} \right\rangle \ , \qquad\qquad i,\, j,\, p,\, q \in \{h,\, v\} \, . \tag{16}$$

Here $\langle\cdot\rangle$ denotes ensemble averaging. These elements are in general complex quantities, except when $i = p$ and $j = q$, in which case the elements are the usual scattering coefficients. In the perturbation analysis, each element of the scattering matrix can be evaluated up to the Nth-order, that is

$$S_{ij} = \sum_{n=1}^{N} S^{(n)}_{ij} \Delta^n \ , \qquad\qquad i,\, j \in \{h,\, v\} \, . \tag{17}$$

It turns out that simple expressions for the first-order elements can be obtained and are given by

$$S^{(1)}_{hh} = \frac{k_0^2 k^i_z k^s_z (\epsilon - 1) e^{-i(k^i_z + k^s_z)d}}{\pi (k^i_z + k^i_{1z})(k^s_z + k^s_{1z})} C^h_0(\mathbf{k}^s, d)\, C^h_0(\mathbf{k}^i, d) \cos(\phi_s - \phi_i)\, F(\mathbf{k}^s_\perp - \mathbf{k}^i_\perp) \ , \tag{18}$$

$$S^{(1)}_{hv} = \frac{k_0 k^i_z k^s_z k^i_{1z} (\epsilon - 1) e^{-i(k^i_z + k^s_z)d}}{\pi (\epsilon k^i_z + k^i_{1z})(k^s_z + k^s_{1z})} C^h_0(\mathbf{k}^s, d)\, C^v_0(\mathbf{k}^i, d) \sin(\phi_s - \phi_i)\, F(\mathbf{k}^s_\perp - \mathbf{k}^i_\perp) \ , \tag{19}$$

$$S^{(1)}_{vh} = \frac{k_0 k^i_z k^s_z k^s_{1z} (\epsilon - 1) e^{-i(k^i_z + k^s_z)d}}{\pi (\epsilon k^s_z + k^s_{1z})(k^i_z + k^i_{1z})} C^h_0(\mathbf{k}^i, d)\, C^v_0(\mathbf{k}^s, d) \sin(\phi_s - \phi_i)\, F(\mathbf{k}^s_\perp - \mathbf{k}^i_\perp) \ , \tag{20}$$

$$S^{(1)}_{vv} = \frac{k^i_z k^i_{1z} (\epsilon - 1) e^{-i(k^i_z + k^s_z)d}}{\pi (\epsilon k^i_z + k^i_{1z})(\epsilon k^s_z + k^s_{1z})} \Bigg[-k^s_z k^s_{1z} C^v_0(\mathbf{k}^s, d) C^v_0(\mathbf{k}^i, d) \cos(\phi_s - \phi_i) + \frac{\epsilon k^s_z k^s_\rho k^i_\rho}{k^i_{1z}}$$

$$\cdot\, C^v_1(\mathbf{k}^s, d) C^v_1(\mathbf{k}^i, d) \Bigg] F(\mathbf{k}^s_\perp - \mathbf{k}^i_\perp) \ . \tag{21}$$

In these expressions $F(\mathbf{k}_\perp^s - \mathbf{k}_\perp^i)$ is the only indeterministic factor and therefore the elements of the differential covariance matrix can easily be obtained by noting that

$$\lim_{A\to\infty} \frac{1}{A} \left\langle \left| \Delta F(\mathbf{k}_\perp^s - \mathbf{k}_\perp^i) \right|^2 \right\rangle = W(\mathbf{k}_\perp^s - \mathbf{k}_\perp^i) , \tag{22}$$

where $W(\mathbf{k}_\perp)$ is the power spectral density of the surface.

To examine the validity of the first-order results, a special case is considered. In the case of backscattering ($\mathbf{k}_\perp^s = -\mathbf{k}_\perp^i$) and for a homogeneous profile where $R_v = r_v$ and $R_h = r_h$, the first-order backscattering coefficients are given by

$$\begin{aligned}
\sigma_{hhhh}^0 &= \frac{4}{\pi} k_0^4 \cos^4\theta_i \left| R_h^i \right|^2 W(-2\mathbf{k}_\perp^i) , \\
\sigma_{vvvv}^0 &= \frac{4}{\pi} \cos^4\theta_i \left| \frac{(k_1^2 - k_0^2)\left(k_{1z}^2 + k_1^2 \sin^2\theta_i\right)}{(k_{1z}^i + \epsilon k_z^i)^2} \right|^2 W(-2\mathbf{k}_\perp^i) , \\
\sigma_{hvhv}^0 &= \sigma_{vhvh}^0 = 0 ,
\end{aligned}$$

which are in agreement with the results reported in the literature [5]. Before we proceed with the higher order scattering solutions, the following observations are in order. The analysis is simplified if we assume that the surface height profile $f(x,y)$ is a Gaussian random field. There is some evidence that this assumption is reasonable for some surfaces of practical importance [1]. Since Fourier transformation is a linear operation, $F(\mathbf{k}_\perp)$ is also Gaussian. It is well known that the following identities hold for a zero-mean jointly Gaussian random vector $\{X_1, \ldots, X_n\}$:

$$\langle X_i X_j X_k \rangle = 0 , \tag{23}$$

$$\langle X_i X_j X_k X_l \rangle = \langle X_i X_j \rangle \langle X_k X_l \rangle + \langle X_i X_k \rangle \langle X_j X_l \rangle + \langle X_i X_l \rangle \langle X_j X_k \rangle . \tag{24}$$

On the other hand, it can be shown that

$$S_{ij}^{(1)} \propto F(\mathbf{k}_\perp^s - \mathbf{k}_\perp^i) , \tag{25}$$

$$S_{ij}^{(2)} \propto \int_{-\infty}^{\infty} d\mathbf{k}_\perp \, F(\mathbf{k}_\perp^s - \mathbf{k}_\perp) F(\mathbf{k}_\perp - \mathbf{k}_\perp^i) \, I_{ij}^{(2)}(\mathbf{k}_\perp) , \tag{26}$$

$$S_{ij}^{(3)} \propto \iint_{-\infty}^{\infty} d\mathbf{k}_\perp d\mathbf{k}'_\perp \, F(\mathbf{k}_\perp^s - \mathbf{k}_\perp) F(\mathbf{k}_\perp - \mathbf{k}'_\perp) F(\mathbf{k}'_\perp - \mathbf{k}_\perp^i) \, I_{ij}^{(3)}(\mathbf{k}_\perp, \mathbf{k}'_\perp) , \tag{27}$$

where $I_{ij}^{(2)}$ and $I_{ij}^{(3)}$ are functions of polarization currents (see (18)~(21) and Appendix A). For the evaluation of the covariance matrix, we confine our interest in perturbation terms up to Δ^4. Substituting (25)~(27) in (17) and then using (23), the elements of covariance matrix simplify to

$$\left\langle S_{ij} S_{pq}^* \right\rangle \approx \left\langle S_{ij}^{(1)} S_{pq}^{(1)*} \right\rangle \Delta^2 + \left[\left\langle S_{ij}^{(2)} S_{pq}^{(2)*} \right\rangle + \left\langle S_{ij}^{(1)} S_{pq}^{(3)*} \right\rangle + \left\langle S_{ij}^{(3)} S_{pq}^{(1)*} \right\rangle \right] \Delta^4 . \tag{28}$$

Noting that property (23) is valid for any odd number of random variables, the elements of covariance matrix are only functions of even power of Δ. Therefore the next higher order of approximation in calculation of $\left\langle S_{ij} S^*_{pq} \right\rangle$ can be obtained by inclusion of products of the first and the fifth, the second and the fourth, and the third-order scattering terms. However, evaluation of high-order scattered fields such as fourth and fifth order are rather complex and tedious. Noting that Δ is a small quantity compared to the wavelength, the benefit of inclusion of Δ^6 term is not significant. This argument cannot be used for the second order solution (Δ^4 term), since this term is the dominant factor for some important scattering parameters such as cross-polarized backscattering coefficient and co-polarized degree of correlation.

The scattering matrix elements up to third order are derived. These expressions are very lengthy and are not included in this paper. Interested readers are referred to reference [11]. Using these expressions in (28), the elements of the covariance matrix can be obtained. The ensemble averaging process can be carried out easily using (24), and

$$\Delta^2 \langle F(\mathbf{k}_\perp) F^*(\mathbf{k}'_\perp) \rangle = \Delta^2 \langle F(\mathbf{k}_\perp) F(-\mathbf{k}'_\perp) \rangle = (2\pi)^2 \delta(\mathbf{k}_\perp - \mathbf{k}'_\perp) W(\mathbf{k}_\perp) \,. \tag{29}$$

Using the above mentioned properties, and noting that in backscatter direction ($\phi_s = \phi_i + \pi$, $\theta_s = \theta_i$) $S^{(1)}_{hv} = S^{(1)}_{vh} = 0$, the cross-polarized backscattering coefficients can be obtained and are given by

$$\begin{aligned}\sigma^0_{hvhv} = \sigma^0_{vhvh} = {} & \frac{|k_0 k^i_z (\epsilon - 1)^2|^2}{16\pi^3} \left| \left(1 - R^i_v\right) \left(1 + R^i_h\right) C^h_0(\mathbf{k}^i, d) C^v_0(\mathbf{k}^i, d) \right|^2 \\ & \cdot \int_{-\infty}^{\infty} W(\mathbf{k}_\perp - \mathbf{k}^i_\perp) W(\mathbf{k}_\perp + \mathbf{k}^i_\perp) \sin^2(\phi - \phi_i) \cos^2(\phi - \phi_i) \\ & \cdot \left| \frac{k_0^2}{k_z + k_{1z}} C^h_0(\mathbf{k}, d) - \frac{k_z k_{1z}}{k_{1z} + \epsilon k_z} C^v_0(\mathbf{k}, d) \right|^2 d\mathbf{k}_\perp \,,\end{aligned} \tag{30}$$

which satisfies the reciprocity condition. To examine the validity of (30), a homogeneous profile is considered having $R_h = r_h$ and $R_v = r_v$. In this case

$$\begin{aligned}\sigma^0_{hvhv} = \sigma^0_{vhvh} = {} & \frac{2}{\pi^3} \left| \frac{k_0 (k^i_z)^2 k^i_{1z} \left(k_1^2 - k_0^2\right)^2}{\left(k_0^2 k^i_{1z} + k_1^2 k^i_z\right) \left(k^i_z + k^i_{1z}\right)} \right|^2 \\ & \cdot \int \left| \frac{\left(k^i_x k_y - k^i_y k_x\right) \left(k^i_x k_x + k^i_y k_y\right)}{(k^i_\rho)^2 \left(k_0^2 k_{1z} + k_1^2 k_z\right)} \right|^2 W(\mathbf{k}_\perp - \mathbf{k}^i_\perp) W(\mathbf{k}_\perp + \mathbf{k}^i_\perp) \, d\mathbf{k}_\perp \,,\end{aligned} \tag{31}$$

which is in agreement with result reported in [5].

2.2 Phase Statistics

Traditionally, scattering models for rough surfaces provide formulations for co- and cross-polarized scattering coefficients. With the advances in the development of polarimetric radar, the statistics of the phase difference of scattering matrix elements can be measured and used in inversion algorithms to retrieve the target parameters. In a polarimetric backscatter measurement, apart from the backscattering coefficients, the co- and cross-polarized phase differences, defined by $\phi_c = \phi_{hh} - \phi_{vv}$ and $\phi_x = \phi_{hv} - \phi_{vv}$, are two additional independent parameters which can be used in an inversion process. In a recent paper [12], it was shown that the statistics of the phase difference can be derived from the elements of the target covariance matrix $(\langle S_{ij} S_{pq}^* \rangle)$ and that the pdf of each phase-difference can be fully determined in terms of two parameters : (1) coherent phase difference (ζ) and (2) degree of correlation (α). The coherent phase difference is the phase difference at which the pdf assumes its maximum. The degree of correlation is a real number that can vary from 0 to 1 and is proportional to the spread of the pdf around ζ, where $\alpha = 0$ corresponds to a uniform distribution and $\alpha = 1$ corresponds to a delta function. In terms of covariance matrix elements, ζ and α are given by

$$\zeta = \tan^{-1} \frac{Im\left[\langle S_{ij} S_{vv}^* \rangle\right]}{Re\left[\langle S_{ij} S_{vv}^* \rangle\right]}, \qquad \alpha = \sqrt{\frac{|\langle S_{ij} S_{vv}^* \rangle|^2}{\langle |S_{ij}|^2 \rangle \langle |S_{vv}|^2 \rangle}}, \tag{32}$$

where subscript $ij = hh$ for co-polarized and $ij = vh$ or hv for cross-polarized phase difference respectively. Referring to (18)–(21) it can easily be shown that $\alpha_c = 1$ and $\alpha_x = 0$ for the first-order scattering solution. Hence α_c and α_x do not contain any information about the surface power spectral density or the surface dielectric constant. Noting that to the first-order solutions, elements of the covariance matrix are linearly proportional to the power spectral density, ζ_c is only a function of the surface dielectric profile.

To characterize the dependency of α_c and α_x on the surface power spectral density, we have to resort to the second-order scattering solution. Combining the first-order solution given by (18)–(21) and the second-order and third-order solutions, closed form expressions for the parameters of phase-difference statistics can be obtained. It is found that α_x vanishes when the surface power spectral density is azimuthally symmetric, that is, if $W(k_x, k_y) = W(\sqrt{k_x^2 + k_y^2})$. This is usually the case for most practical situations, which implies the co- and cross-polarized backscattered fields are mutually uncorrelated.

3 Data Simulation and Experimental Results

In the previous section, an analytical model for predicting polarimetric scattering behavior of inhomogeneous rough surfaces based on a perturbation expression of induced polarization current was obtained. Here, data simulation based on the complete second-order analytical model is carried out to investigate the sensitivity of the radar backscatter measurements to physical parameters of the surface, such as the surface dielectric profile and surface power spectral density. Also, polarimetric backscatter measurements were conducted to examine the significance of the second-order solution on the overall backscatter response as a function of surface parameters and radar attributes.

Figures 2a and 2b demonstrate the significance of the second-order solution, where the ratio of the first-order to the complete co-polarized second-order solutions $(\sigma^{0(1)})/\sigma^{0(2)})$ are plotted versus incidence angle. An exponential correlation function given by

$$\rho(x,y) = s^2\, e^{-\frac{\sqrt{x^2+y^2}}{l}}\,, \tag{33}$$

where s is the rms height and l is the surface correlation length, is used in these simulations. In Figs. 2a and 2b, ks and kl are varied as free parameters, and the soil surface is assumed to be a homogeneous medium with $\epsilon = 8.0 + i\,2.51$. This dielectric constant corresponds to a moist soil surface with volumetric moisture content $m_v = 0.2$ and is computed using the empirical formula given in [13] at 1.25 GHz with $S = 0.1$ and $C = 0.3$. It is shown that the second-order scattering term is more sensitive to variations in rms height(s) than it is to the surface correlation length (l). The sensitivity to s is higher at lower angles of incidence for σ^0_{vvvv} unlike σ^0_{hhhh}. Figures 3a and 3b show the ratio of the first-order to the complete co-polarized second-order solutions of the homogeneous rough surface as a function of soil moisture at $\theta = 45^\circ$. Here it is shown that as the soil moisture increases from 0.01 ($\epsilon = 2.21 + i\,0.002$) to 0.4 ($\epsilon = 14.68 + i\,7.5$), the contribution from the second-order scattering term to the overall backscattering increases slightly. This effect is more pronounced for σ^0_{hhhh}. Figures 2 and 3 demonstrate that the inclusion of the second-order solution is more important for calculation of σ^0_{hhhh} than for σ^0_{vvvv}. Figures 4 and 5 show the co-polarized coherent phase difference ζ_c calculated from the first-order and complete second-order solutions for the homogeneous surface as a function of incidence angle and soil moisture. To the first order, ζ_c is independent of surface roughness parameters, however, the second-order solution shows a weak dependency on ks and kl. It is interesting to note that the sensitivity to roughness parameters disappears for incidence angles larger than 50^o. As shown in Fig. 5, ζ_c is relatively insensitive to moisture content for a homogeneous surface.

As mentioned before, the second-order solution is the dominant component for the cross-polarized backscattering coefficient. σ^0_{hvhv} is directly proportional to the square of the rms height, thus the dependency to s is not examined. Figure 6 shows σ^0_{hvhv} of the homogeneous surface as a function of incidence angle for different values of kl and m_v while $ks = 0.2$ is kept constant. Note that σ^0_{hvhv} increases with increasing dielectric constant and decreases with increasing surface correlation length. The co-polarized degree of correlation is another potential parameter that can be used in retrieval of surface physical parameters. The first-order scattering solution predict $\alpha_c = 1$ independent of the surface physical parameters. Figures 7 and 8 show α_c for the homogeneous rough surface as a function of incidence angle and dielectric constant for different values of ks and kl. Note that α_c, in general, has a decreasing trend with increasing incidence angle, rms height, and soil moisture. It is also noted that α_c increases when kl is decreased. The total dynamic range of α_c as a function of the surface parameters is rather limited.

Next we examine the sensitivity of the polarimetric backscatter data to the surface dielectric inhomogeneity. Three dielectric profiles are considered here: (1) exponentially increasing moisture with depth, (2) exponentially decreasing moisture with depth, and (3) a two-layer step profile, as shown in Fig. 9. The exponential profiles are chosen according to [14] and are given by:

$$m_v(z) = \begin{cases} m_{vs} + \Delta m_v \, \frac{e^{\beta z}-1}{e^{-\beta d}-1} & -d \leq z \leq 0 \, , \\ m_v(z) = m_v(-d) & z \leq -d \, , \end{cases}$$

where m_{vs} is the surface moisture content and Δm_v is the increment of moisture at a depth d below the surface. The moisture content below depth d is considered to be uniform. In all cases the backscatter parameters are compared with a homogeneous profile having a dielectric constant equal to that of the inhomogeneous profile at the interface. Figures 10 and 11 show the backscattering coefficients for a surface with the increasing and decreasing exponential dielectric profiles and having $ks = 0.2$, $kl = 2$. Note that the backscattering coefficients are insensitive to moisture profiles, and the backscattering coefficients are basically indistinguishable from those of the homogeneous profile having the same dielectric constant as that of the inhomogeneous profile at the interface. This is due to the tapered impedance matching nature of the profile. However, this is not the case for the step profile as shown in Fig. 12. The difference in σ^o, depending on the incidence angle, can be as high as 10 dB. The only sensitive parameter to moisture variations in depth for continuous profiles is the co-polarized coherent phase difference as is shown in Fig. 13, where ζ_c for the homogeneous, increasing, and step moisture profiles are shown. ζ_c does not shown any sensitivity for decreasing profiles. It should be pointed out that the calculation of the complete second-order solution involves numerical evaluation of two-fold integrals. To provide a feeling for the required computation time, the calculation of backscattering coefficients and phase difference statistics for one incidence angle would take about one minute on a Sun workstation Ultra 2.

The validity of the analytical results are also examined by conducting backscatter measurements. The backscatter measurements were performed polarimetrically using the indoor bistatic facilities of the Radiation Laboratory at the University of Michigan [16]. The backscatter data were collected from a rough layer of sand above a perfectly conducting ground plane at center frequency 9.25 GHz with a bandwidth of 1.5 GHz. A $6' \times 6'$ sand-box on top of a computer controlled turntable was used to contain the sand layer. The antenna footprint covered an area of about $0.27 \sec\theta \; m^2$ on the sand-box and collection of independent backscatter data was facilitated by rotating the sand-box at steps of 5^o. The wide bandwidth of the radar system was used to range-gate the possible unwanted radar backscatter from the sand-box walls and edges. A simplified block diagram of the measurement system is shown in Fig. 14.

An uniform sand with maximum particle dimension of 0.15 mm was chosen to minimize the effect of volume scattering from the sand layer. The effective dielectric constant of the sand medium was measured to be $\epsilon_r = 2.7 + i\,0.05$. The radar was calibrated polarimetrically using STCT [17]. To generate a desired roughness over the sand surface repeatedly, a template was made. The imprint of the template on the surface generated a rough surface with almost an exponential auto-correlation function with $ks = 0.122$ and $kl = 2.69$. The surface roughness statistics were measured using a laser ranging system with a range resolution of 0.1 mm. The backscatter measurements conducted for two layers having thicknesses $d = 2.52$ cm and $d = 3.53$ cm over the angular range $20^o \sim 50^o$.

Figures 15a and 15b show the measured and simulated σ^0 versus incidence angle. All the measured results are shown to be in a very good agreement with the complete second order solution except for the cross-polarized responses at $\theta = 50^o$. For these cases we were limited by the system noise floor. Figures 16a and 16b show the response of the co-polarized coherent phase difference as a function of incidence angle. Both the first-order and second-order solutions are shown and it is obvious that the second-order contribution is insignificant at angles below 40^o.

Figures 17a and 17b compare the measured and theoretical ratio of $\sigma^0_{hhhh}/\sigma^0_{vvvv}$, versus incidence angle. Here it is shown that at high incidence angles first-order results are incapable of accurate prediction of backscattering coefficients whereas the second-order solution provide satisfactory results. Figures 18a and 18b show the the measured and calculated co-polarized degree of correlation versus incidence angle, where a relatively good agreement has been obtained considering the difficulties in the accurate measurement of α [18].

4 Conclusions

In this paper, a bistatic polarimetric scattering model for random dielectric surfaces with inhomogeneous permittivity profiles and small surface roughnesses is developed using a perturbation expansion of volumetric polarization current. A complete second-order solution for the backscattering coefficients and the statistics of the phase difference between the elements of scattering matrix is obtained. The validity of the model is verified in a limiting case, where it is shown that the formulation for surface with inhomogeneous permittivity profile reduces to the known formulation for homogeneous rough surfaces. Also, polarimetric backscatter measurements from rough surfaces with known dielectric profiles and roughness statistics were collected and compared with the theoretical calculations. Comparisons with the measured data show excellent agreement. The sensitivity analysis in terms of the surface physical parameters is also performed. It is shown that, in general, the backscatter parameters, such as backscattering coefficients and phase-difference statistics, are more sensitive to ks than kl. The contribution of the second-order solution for calculation of σ^o_{hhhh} is more significant than that for the calculation of σ^o_{vvvv}. The contribution of the second-order solution to overall σ^o_{hhhh} can be as high as 2 dB for $ks \leq 0.3$. It is shown that for continuous inhomogeneous profiles, the backscattering coefficients are insensitive to the variations of moisture content as a function of depth. In the other words, the backscattering coefficients of a surface with a continuous soil moisture profile are equal to those of a homogeneous surface having a moisture content equivalent to that of the inhomogeneous profile at the interface. The only backscatter parameter sensitive to moisture profile is the co-polarized coherent phase difference (ζ_c). However, both the backscattering coefficients and phase-difference statistics are very sensitive to step discontinuities in moisture profile.

Acknowledgment: This research was supported by NASA, under Contract NAGW-2151.

References

[1] Y. Oh, K. Sarabandi, and F.T. Ulaby, "An empirical model and an inversion technique for radar scattering from bare soil surfaces," *IEEE Trans. Geosci. Remote Sensing,* vol. 30, pp. 370-382, Mar. 1992.

[2] S.O. Rice, "Reflection of electromagnetic wave by slightly rough surfaces," *Communication in Pure and Applied Mathematics,* vol. 4, pp. 351-378, 1951.

[3] M. Nieto-Vesperinas, "Depolarization of electromagnetic waves scattered from slightly rough random surfaces: A study by means of the extinction theorem," *J. Opt. Soc.,* 72(5), pp. 539-547, 1982.

[4] G.S. Agarwal, "Interaction of electromagnetic waves at rough dielectric surfaces," *Phys. Rev. B,* no. 15, pp. 2371-2383, 1977.

[5] L. Tsang, J. Kong, and R.T. Shin, *Theory of Microwave Remote Sensing,* John Wiley and Sons, New York, 1985.

[6] P. Beckmann and A. Spizzichino, *The Scattering of Electromagnetic Waves from Rough Surfaces*, Pergamon, New York, 1963.

[7] D. Winebrenner and A. Ishimaru, "Investigation of a surface field phase perturbation technique for scattering from rough surfaces," *Radio Science,* vol. 20, no. 2, pp. 161-170, Mar-Apr, 1985.

[8] E. Rodriguez and Y. Kim, "A unified perturbation expansion for surface scattering," *Radio Science,* vol. 27, no. 1, pp. 79-93, Jan-Feb, 1992.

[9] A.K. Fung and G.W. Pan, "A scattering models for perfectly conducting random surfaces: I. model development, II. range of validity," *IEEE Trans. Geosci. Remote Sensing,* vol. 8, no. 11, pp. 1579-1605, 1987.

[10] A.K. Fung, Z. Li, and K.S. Chen, "Backscattering from a randomly rough dielectric surface," *IEEE Trans. Geosci. Remote Sensing,* vol. 30, pp. 356-369, Mar. 1992.

[11] T. Chiu and K. Sarabandi, "Scattering solutions for slightly rough surfaces with inhomogeneous dielectric profiles," Radiation Laboratory Report no. RL-946, the University of Michigan, 1997.

[12] K. Sarabandi, "Derivation of phase statistics from the Mueller matrix," *Radio Science,* vol. 27, no. 5, pp. 553-560, September-October 1992.

[13] M.T. Hallikainen, F.T. Ulaby, M.C. Dobson, M.A. El-Rayes, and L. Wu, "Microwave dielectric behavior of wet soil — part I: empirical models and experimental observations," *IEEE Trans. Geosci. Remote Sensing,* vol. GE-23, no. 1, pp. 25-34, January 1985.

[14] E.G. Njoku, and J. Kong, "Theory for passive microwave remote sensing of near-surface soil moisture," *J. Geophys. Res.,* vol. 28, pp. 1022-1033, 1990.

[15] F.G. Tricomi, *Integral Equations*, New York: Interscience Publishers, 1957.

[16] R. DeRoo, R. Hartikka, N. Peplinski, and A. Zambetti, , Bistatic Measurement Facility User's Manual, Radiation Laboratory, the University of Michigan, August, 1994.

[17] K. Sarabandi and F.T. Ulaby, "A convenient technique for polarimetric calibration of radar systems," *IEEE Trans. Geosci. Remote Sensing,* vol. GE-23, no. 1, pp. 25-34, January 1985.

[18] K. Sarabandi, Y. Oh, and F.T. Ulaby, "Measurement and calibration of differential Mueller matrix of distributed targets," *IEEE Trans. Antennas Propagat.,* vol. 40, pp. 1524-1532, Dec. 1992.

List of Figures

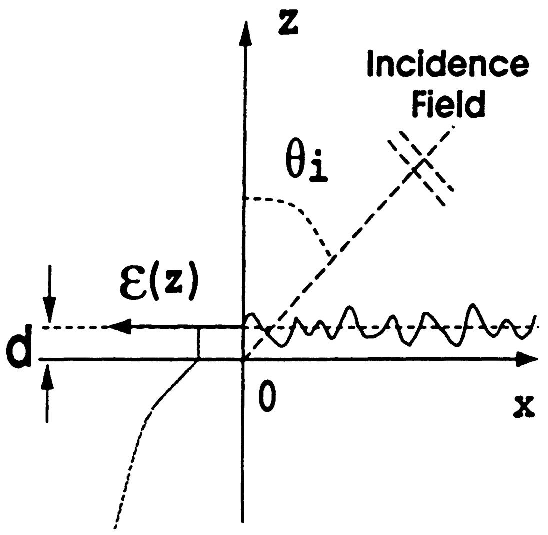

Figure 1: An inhomogeneous half-space medium with a rough interface. Left side of this figure shows the dielectric profile.

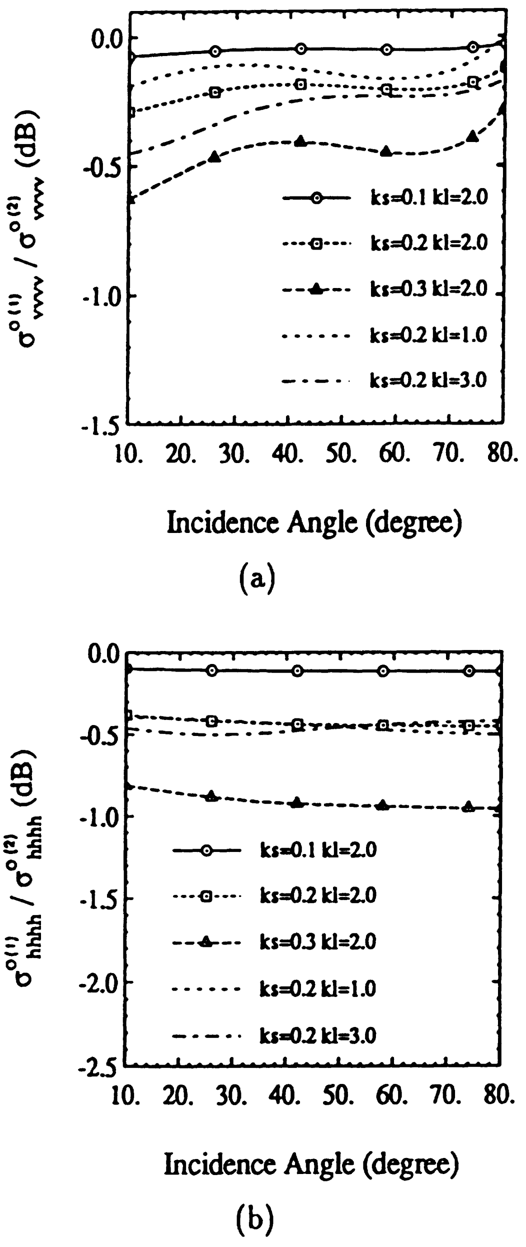

(a)

(b)

Figure 2: Ratio of the first-order to the complete second-order solution of a homogeneous rough surface with $m_v = 0.2$ ($\epsilon = 8.0 + i\,2.51$ at 1.25 GHz) as a function of incidence angle for different values of ks and kl.

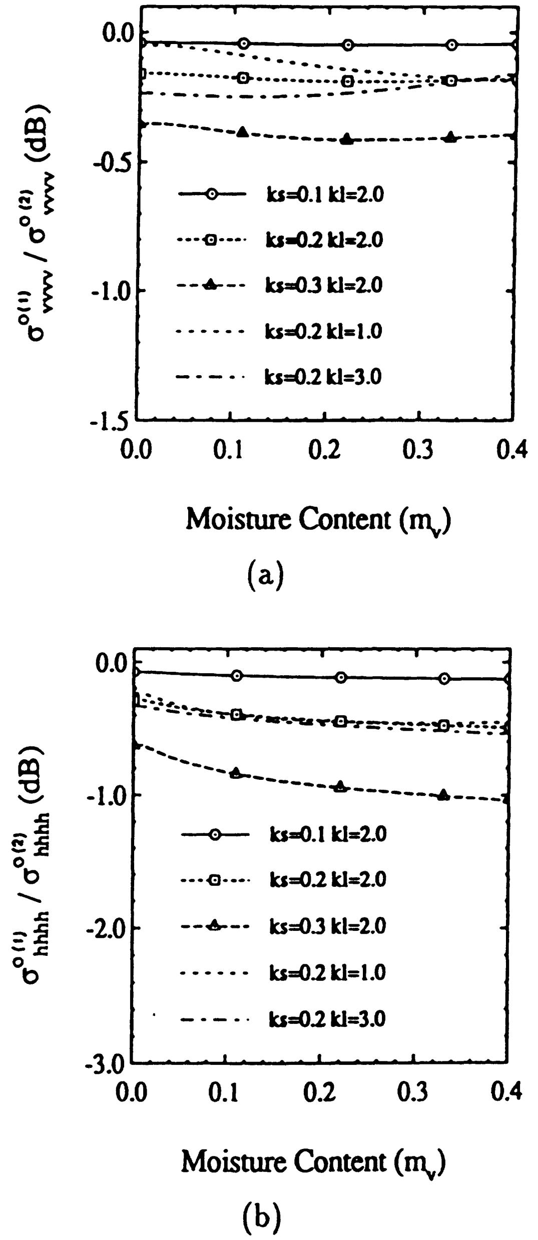

Figure 3: Ratio of the first-order to the complete second-order solution of a homogeneous rough surface as a function of moisture content for different values of ks and kl at $\theta = 45^o$.

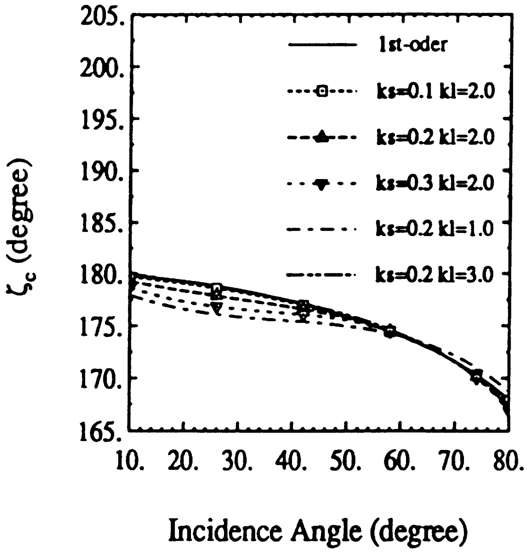

Figure 4: Co-polarized coherent phase difference of homogeneous rough surface with $m_v = 0.2$ ($\epsilon = 8.0 + i\,2.51$ at 1.25 GHz) as a function of incidence angle for different values of ks and kl.

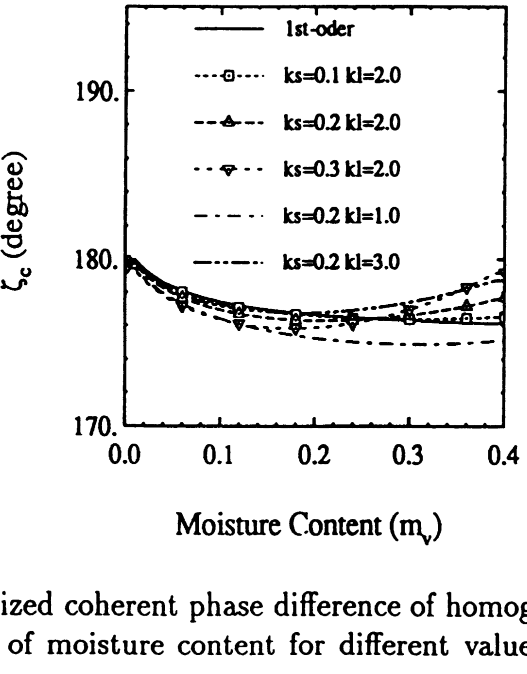

Figure 5: Co-polarized coherent phase difference of homogeneous rough surface as a function of moisture content for different values of ks and kl at $\theta = 45°$.

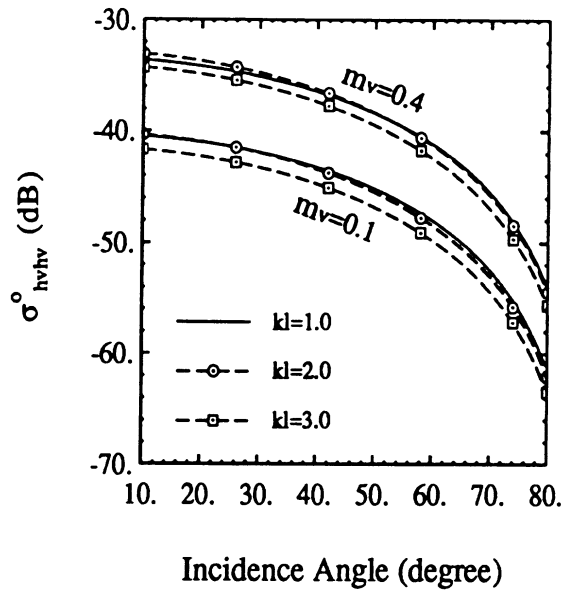

Figure 6: Variations of cross-polarized backscattering coefficient as a function of incidence angle, moisture content ($\epsilon = 4.89 + i\,0.92$ for $m_v = 0.1$ and $\epsilon = 14.68 + i\,7.5$ for $m_v = 0.4$ at 1.25 GHz) and correlation length for a surface with $ks = 0.2$.

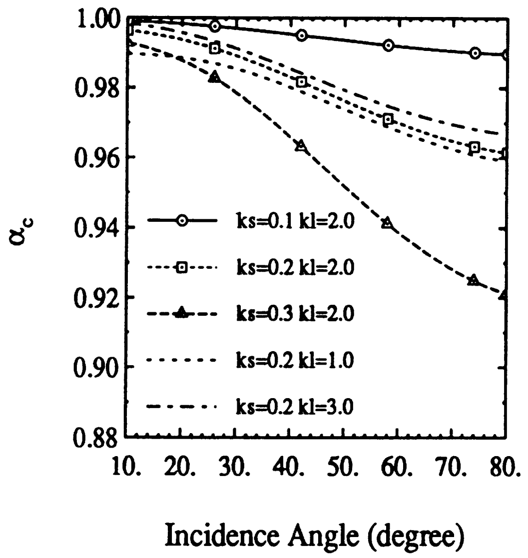

Figure 7: Sensitivity of co-polarized degree of correlation to incidence angle for different values of ks and kl and moisture content $m_v = 0.2$ ($\epsilon = 8.0 + i\,2.51$ at 1.25 GHz).

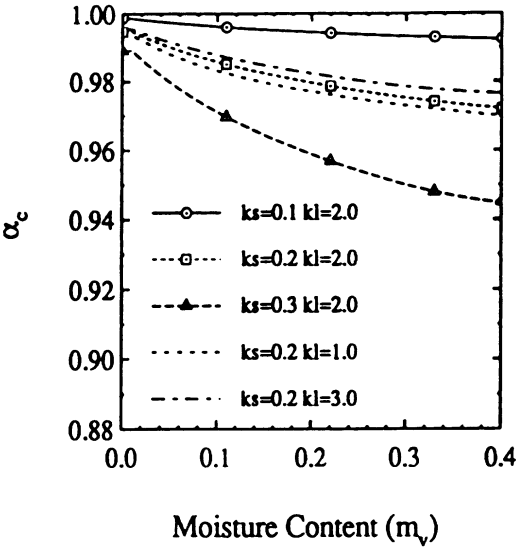

Figure 8: Sensitivity of co-polarized degree of correlation to soil moisture content for different values of ks and kl at $\theta = 45^o$. α_c does not show much sensitivity to kl.

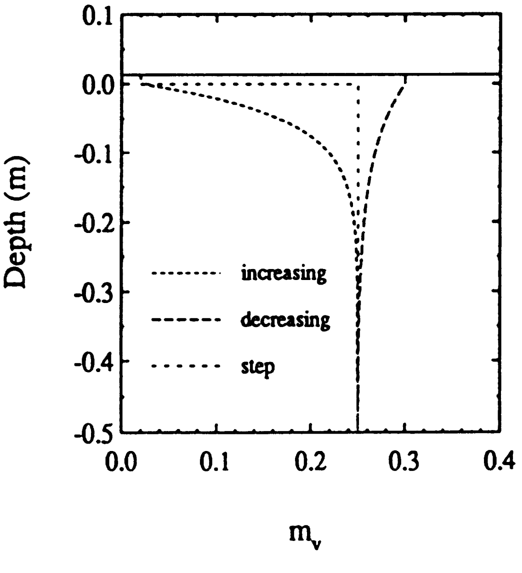

Figure 9: Three different moisture profiles used in the backscattering simulations: increasing exponential with $\beta = 20$, decreasing exponential with $\beta = 10$, and step.

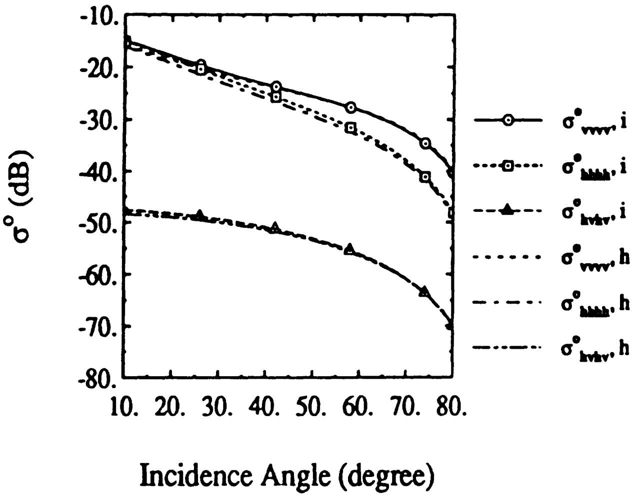

Figure 10: Comparison of backscattering coefficients calculated for the homogeneous and increasing exponential moisture profiles for a rough surface with $ks = 0.2$ and $kl = 2$.

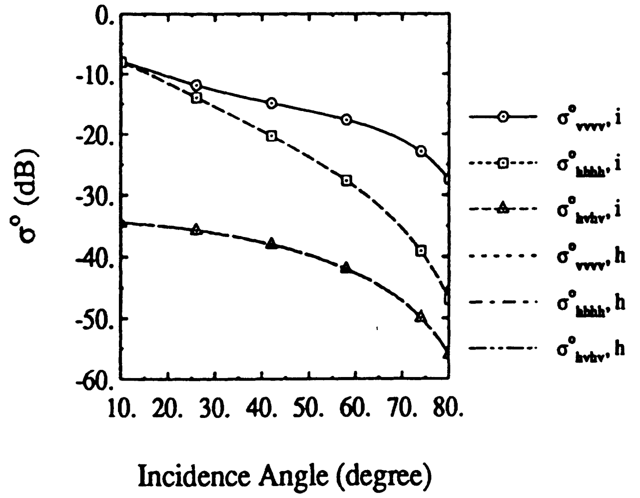

Figure 11: Comparison of backscattering coefficients calculated for the homogeneous and decreasing exponential moisture profiles for a rough surface with $ks = 0.2$ and $kl = 2$.

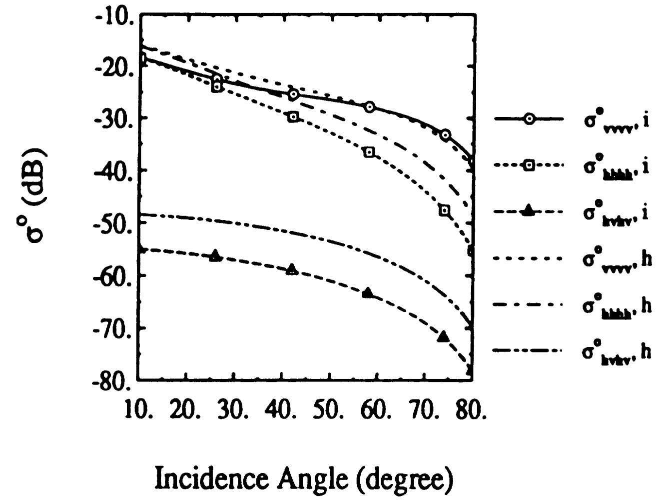

Figure 12: Comparison of backscattering coefficients calculated for the homogeneous and step moisture profiles for a rough surface with $ks = 0.2$ and $kl = 2$.

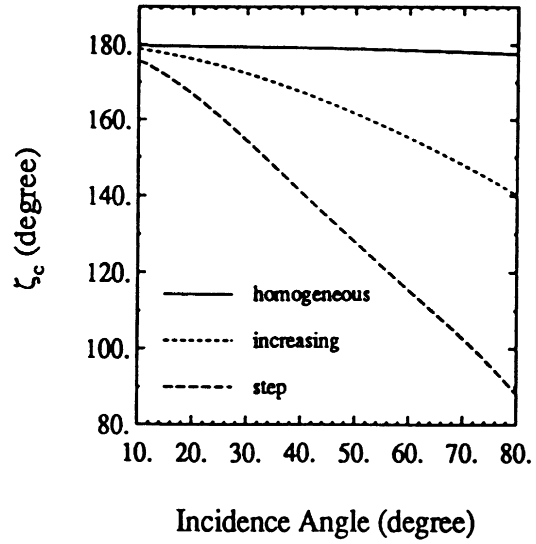

Figure 13: Co-polarized coherent phase difference calculated for the homogeneous, increasing exponential, and step moisture profiles for a rough surface with $ks = 0.2$ and $kl = 2$.

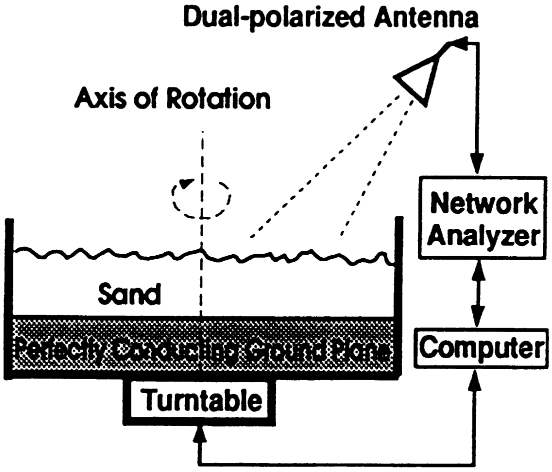

Figure 14: Simplified block diagram of the experimental setup.

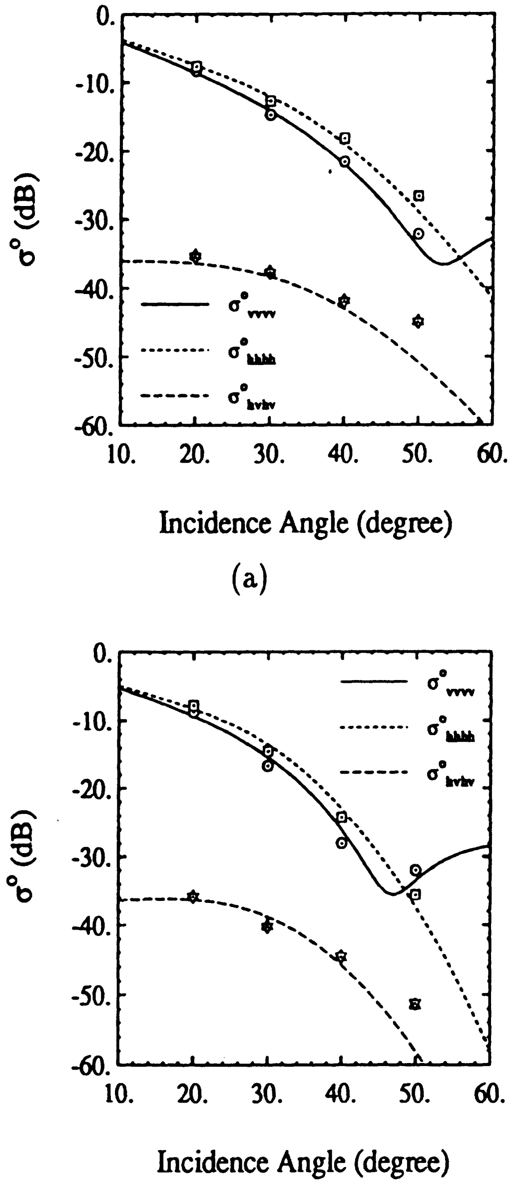

(a)

(b)

Figure 15: Comparison of the measured and the complete second-order simulated backscatter for a sand layer of thickness 2,52 cm (a) and 3.53 cm (b) above a perfectly conducting ground plane at 9.25 GHz. Symbols represent the measured quantities and the lines are the theoretical calculations.

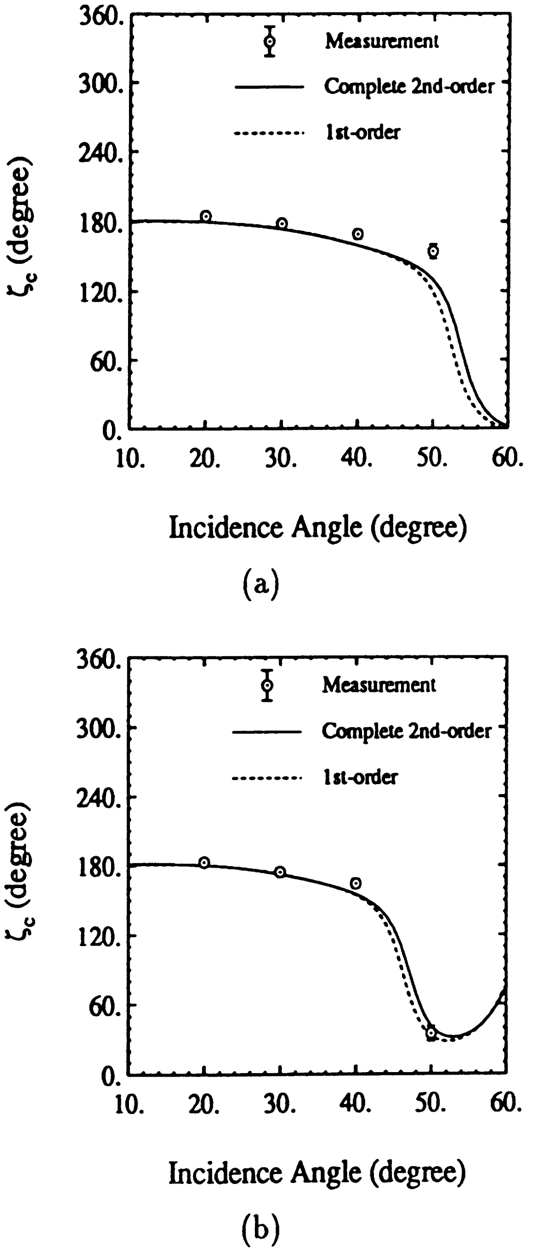

(a)

(b)

Figure 16: Comparison of the measured and the calculated co-polarized coherent phase difference for a sand layer of thickness 2,52 cm (a) and 3.53 cm (b) above a perfectly conducting ground plane at 9.25 GHz.

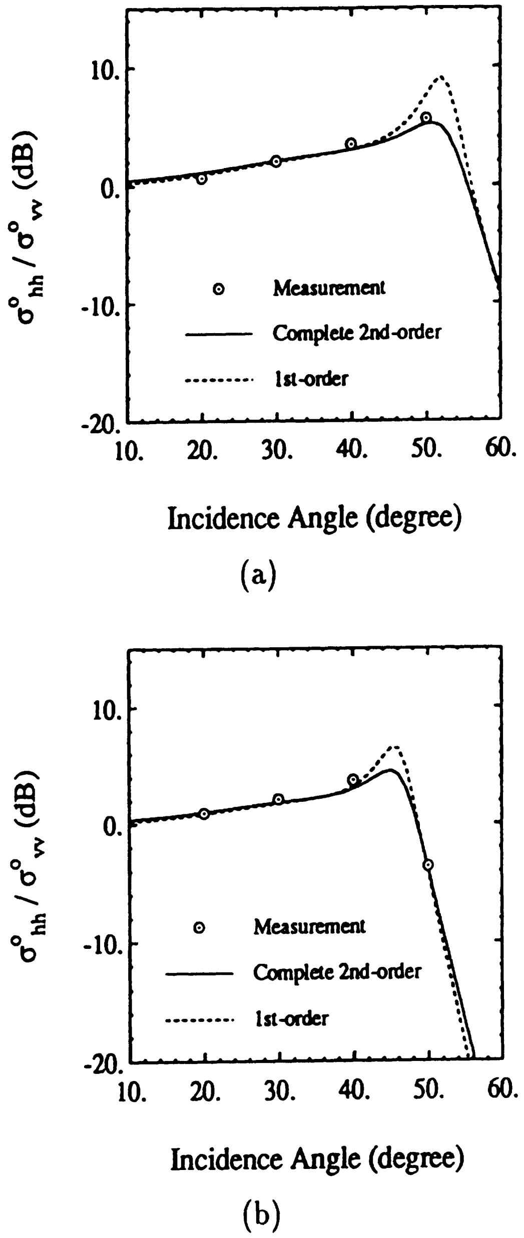

Figure 17: Comparison of the measured and the calculated $\sigma^o_{hhhh}/\sigma^o_{vvvv}$ for a sand layer of thickness 2,52 cm (a) and 3.53 cm (b) above a perfectly conducting ground plane at 9.25 GHz.

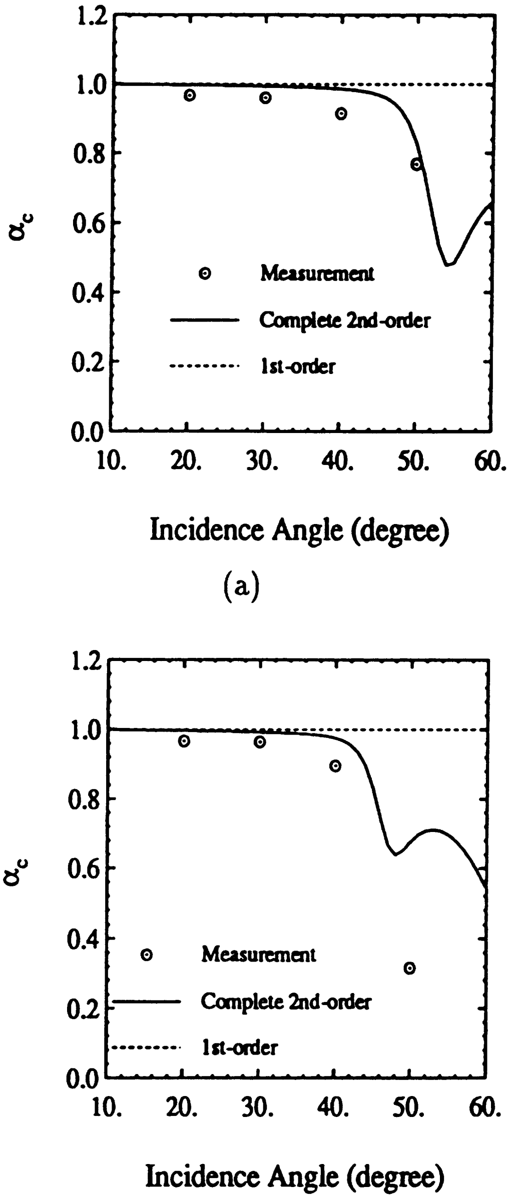

(a)

(b)

Figure 18: Comparison of the measured and the calculated co-polarized degree of correlation for a sand layer of thickness 2,52 cm (a) and 3.53 cm (b) above a perfectly conducting ground plane at 9.25 GHz.

A Numerical Simulation of Scattering from One-Dimensional Inhomogeneous Dielectric Random Surfaces

Kamal Sarabandi, *Senior Member, IEEE*, Yisok Oh, *Student Member, IEEE*, and Fawwaz T. Ulaby, *Fellow, IEEE*

***Abstract*—In this paper, an efficient numerical solution for the scattering problem of inhomogeneous dielectric rough surfaces is presented. The inhomogeneous dielectric random surface represents a bare soil surface and is considered to be comprised of a large number of randomly positioned dielectric humps of different sizes, shapes, and dielectric constants above an impedance surface. Clods with nonuniform moisture content and rocks are modeled by inhomogeneous dielectric humps and the underlying smooth wet soil surface is modeled by an impedance surface. In this technique, an efficient numerical solution for the constituent dielectric humps over an impedance surface is obtained using Green's function derived by the exact image theory in conjunction with the method of moments. The scattered field from a sample of the rough surface is obtained by summing the scattered fields from all the individual humps of the surface coherently ignoring the effect of multiple scattering between the humps. The statistical behavior of the scattering coefficient σ° is obtained from the calculation of scattered fields of many different realizations of the surface. Numerical results are presented for several different roughnesses and dielectric constants of the random surfaces. The numerical technique is verified by comparing the numerical solution with the solution based on the small perturbation method and the physical optics model for homogeneous rough surfaces. This technique can be used to study the behavior of scattering coefficient and phase difference statistics of rough soil surfaces for which no analytical solution exists.**

I. INTRODUCTION

INVESTIGATION of the radar scattering response of natural surfaces is an important problem in remote sensing because of its potential in retrieving desired physical parameters of the surface, namely its soil moisture content and surface roughness. Soil moisture is a key ingredient of the biochemical cycle and an important variable in hydrology and land processes. Although the problem of electromagnetic wave scattering from random surfaces has been investigated for many years, because of its complexity, theoretical solutions exist only for simple limiting cases. Among the existing theoretical models the small perturbation method (SPM) [1] and the Kirchhoff approximation (KA) [2] can be mentioned, which are applicable for homogeneous surfaces over a restricted regions of validity. Numerous techniques based on the basic assumptions of the SPM and KA have been developed in past in an attempt to improve the region of validity of these models; however, they all have the basic limitations of the original models [3]. Other theoretical models such as the phase perturbation technique [4] and the integral equation method [5] are not applicable, for inhomogeneous surfaces and their regions of validity have not been fully determined yet. A scattering formulation for rough surfaces with variable surface impedance exist [6]; however, the solution is not applicable to soil surfaces with low dielectric constant. Several numerical solutions of the scattering problem have been proposed to identify the region of validity and accuracy of these theoretical models. Scattering solution for a perfectly conducting random surface using the method of moments has been suggested by Axline and Fung [7]. In this method a tapered incident field is used as the excitation to eliminate the edge effect contribution.

A numerical solution for homogeneous dielectric random surfaces has been reported [8] where again a tapered illumination is used to limit the size of the scatterer. The accuracy of the numerical solution with tapered illumination decreases with increasing incidence angle. To our knowledge, numerical scattering solution for inhomogeneous rough surfaces does not exist.

Analysis of microwave backscatter observations by Oh *et al.* [9] reveals that the existing theoretical models cannot adequately explain the scattering behavior of soil surfaces. The deviation between theoretical predictions and experimental data is attributed to three factors. First, the roughness parameters are often outside the region of validity of the theoretical models. Second, the autocorrelation functions measured from natural surfaces are very complicated and are not Gaussian or exponential correlation functions. Finally, the most important reason is that the natural surfaces are not homogeneous in most cases, i.e., the moisture content is not uniform in depth. The top rough layer which includes clods and rocks is usually dry and the underlying soil layer is moist and smooth.

In this paper, we model a soil surface as an inhomogeneous dielectric random surface comprised of a large number of randomly positioned two-dimensional dielectric humps of different sizes, shapes, and dielectric constants all lying above an impedance surface. At microwave frequencies, the moist and smooth underlying soil layer can be modeled as an impedance surface, and the irregularities above it can be treated as dielectric humps of different dielectric constants and shapes. For the field scattered by a single dielectric hump over an impedance surface, we have an available efficient numerical solution that uses the exact image theory for the

---

Manuscript received November 15, 1994. This work was supported by NASA under Contract NAGW 2151.

The authors are with the Radiation Laboratory, Department of Electrical Engineering and Computer Science, University of Michigan, Ann Arbor, MI 48109 USA.

Publisher Item Identifier S 0196-2892(96)00996-5.

Green's function in conjunction with the method of moments [10]. In the solution of a single hump, it has been shown that the bistatic scattered field is very weak at points in close proximity to the impedance surface; thus, the effects of multiple scattering between humps can be ignored. In this case, the scattered field from a collection of randomly positioned dielectric humps can easily be obtained by summing the scattered field of all the constituent humps coherently. The scattering coefficients (σ°) is obtained by a Monte Carlo simulation.

In Section II, we summarize the procedure for the numerical solution of a single hump above an impedance surface. Section III outlines the procedures used for generating the random surfaces and for evaluating the statistics of the scattered field. Numerical results and their comparison with theoretical models are presented in Section IV.

II. SCATTERING FROM INDIVIDUAL HUMPS

In this section, we briefly review the procedure for the numerical solution of scattering from a two-dimensional dielectric object above a uniform impedance surface [10]. The radiated field for a dipole source above a dissipative half-space medium (Green's function) is usually evaluated using the Sommerfeld integral [11]. This infinite integral, in general, is highly oscillatory and computationally rather inefficient. In [10], the Green's function of an impedance surface was derived in terms of rapidly converging integrals using appropriate integral transforms. The scattering problem was then formulated by integral equations which were solved numerically using the method of moments.

Suppose a dielectric object, possibly inhomogeneous, is located above an impedance surface and is illuminated by a plane wave. The incident field $\boldsymbol{E}^i$ induces conduction and displacement currents in the dielectric object which together are known as the polarization current $\boldsymbol{J}_e$. The polarization current can be represented in terms of the total electric field inside the dielectric object, which is comprised of the incident, reflected, and scattered fields denoted by $\boldsymbol{E}^i$, $\boldsymbol{E}^r$, and $\boldsymbol{E}^s$, respectively. Thus

$$\boldsymbol{J}_e(\overline{\rho}) = -ik_0Y_0[\epsilon(\overline{\rho}) - 1][\boldsymbol{E}^i(\overline{\rho}) + \boldsymbol{E}^r(\overline{\rho}) + \boldsymbol{E}^s(\overline{\rho})] \tag{1}$$

where $k_0 = \omega\sqrt{\mu_0\epsilon_0}$, $Y_0 = \sqrt{\epsilon_0/\mu_0}$, and $\epsilon(\overline{\rho})$ is the relative dielectric constant of the object at the point $\overline{\rho} = x\hat{x} + y\hat{y}$. The fields $\boldsymbol{E}^i$, $\boldsymbol{E}^r$, and $\boldsymbol{E}^s$ are, respectively, given by

$$\boldsymbol{E}^i(\overline{\rho}) = (E_h^i\hat{h}_i + E_v^i\hat{v}_i)\exp[ik_0\hat{k}_i \cdot \overline{\rho}] \tag{2}$$

$$\boldsymbol{E}^r(\overline{\rho}) = (R_hE_h^i\hat{h}_r + R_vE_v^i\hat{v}_r)\exp[ik_0\hat{k}_r \cdot \overline{\rho}] \tag{3}$$

$$\boldsymbol{E}^s(\overline{\rho}) = ik_0Z_0\int_S \overline{\overline{G}}(\overline{\rho}, \overline{\rho}') \cdot \boldsymbol{J}_e(\overline{\rho}')\,d\overline{\rho}' \tag{4}$$

where E_h^i and E_v^i are the horizontal (E-polarized) and vertical (H-polarized) components of the incident field, respectively. R_h and R_v are the horizontal and vertical Fresnel reflection coefficients and $\overline{\overline{G}}(\overline{\rho}, \overline{\rho}')$ is the dyadic Green's function of the problem.

There is no known exact solution for the integral equation given by (1). Hence, an approximate numerical solution of this equation must be obtained using the method of moments. This is done by dividing the cross section of the dielectric structure into N_c sufficiently small rectangular cells such that the dielectric constant and the polarization current over each cell can be approximated by constant values. Using the point-matching technique, the integral equation can be cast into a matrix equation of the following form:

$$\begin{bmatrix} [\mathcal{Z}_{xx}] & [\mathcal{Z}_{xy}] & 0 \\ [\mathcal{Z}_{yx}] & [\mathcal{Z}_{yy}] & 0 \\ 0 & 0 & [\mathcal{Z}_{zz}] \end{bmatrix} \begin{bmatrix} [\mathcal{I}_x] \\ [\mathcal{I}_y] \\ [\mathcal{I}_z] \end{bmatrix} = \begin{bmatrix} [\mathcal{V}_x] \\ [\mathcal{V}_y] \\ [\mathcal{V}_z] \end{bmatrix} \tag{5}$$

where $[\mathcal{Z}_{pq}]$ is the impedance matrix, $[\mathcal{I}_p]$ is the unknown vector whose entries are the values of the polarization current at the center of each cell, and $[\mathcal{V}_p]$ is the excitation vector with $p = x$, y, or z. The entries of $[\mathcal{V}_p]$ are simply given by

$$\begin{aligned} v_{p,n} = {} & ik_0Y_0[\epsilon(x_n, y_n) - 1] \\ & \cdot \{[\boldsymbol{E}_p^i(x_n, y_n) + \boldsymbol{E}_p^r(x_n, y_n)]\} \cdot \hat{p} \end{aligned} \tag{6}$$

and the entries of $[\mathcal{Z}_{pq}]$ can be evaluated from

$$\begin{aligned} z_{pqmn} = {} & -\delta_{pq}\delta_{mn} + k_0^2[\epsilon(x_n, y_n) - 1] \\ & \cdot \int_{\Delta S_m} [G_{pq}(x_n, y_n; x_m, y_m) \\ & + G_{rpq}(x_n, y_n; x_m, y_m)]\,ds_m \end{aligned} \tag{7}$$

where δ_{pq} and δ_{mn} are the Kronecker delta functions, and $p, q = x, y$, or z.

Explicit expressions for the elements of the impedance matrix are given in [10] where off-diagonal elements are obtained by approximating the Green's function via its Taylor series expansion around the midpoint of each cell and then the integration over the cell surface is performed analytically. For diagonal elements the free-space Green's function is approximated by its small argument expansion and then integration is performed analytically.

III. MONTE CARLO SIMULATION OF ROUGH SURFACE SCATTERING

The Monte Carlo scattering simulation of rough surfaces made up of a finite collection of dielectric humps involves in five major steps as shown in Fig. 1. The first step is to choose the type (size, shape, and dielectric constant, etc.) and number of constituent humps. The second step deals with generating a surface sample by positioning a large number of humps with a prescribed probability. The third step in this algorithm is to compute the inverse impedance matrices for all constituent humps using the numerical method explained in the previous section. Next the scattered field from the surface is computed by coherent summation of the scattered fields from all of the humps in the surface sample. Finally the scattering coefficient σ° is obtained by repeating the fourth step for a large number of independently generated surface samples.

The types of constituent humps which in addition to their probability of occurrence fully characterize the statistics of a random surface. Fig. 2 shows the geometry and dielectric profiles of different types of dielectric humps which can be handled by this algorithm. For example, Fig. 2(a) shows a typical hump for a dry clod above a moist and smooth underlying soil layer ($\epsilon_0 < \epsilon_1 < \epsilon_2$) and Fig. 2(b) shows the same

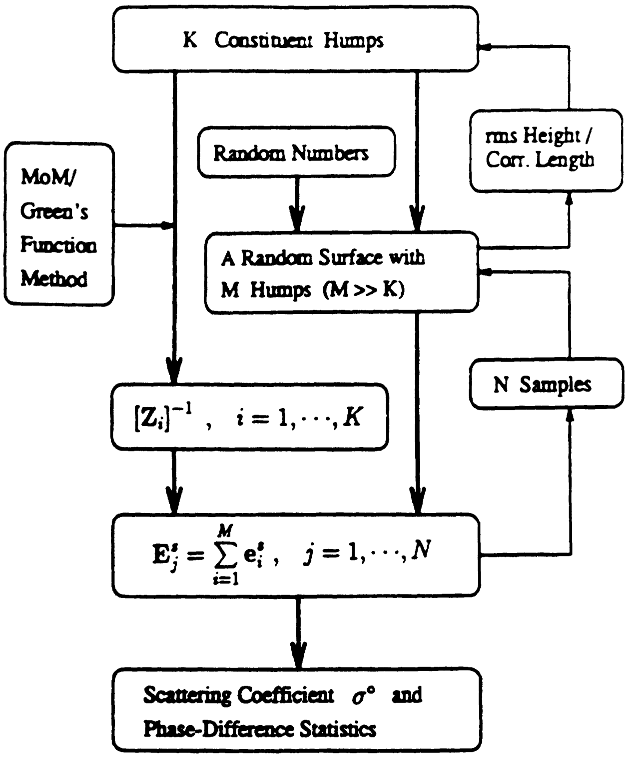

Fig. 1. Flow chart of the Monte Carlo simulation for the rough surface problem.

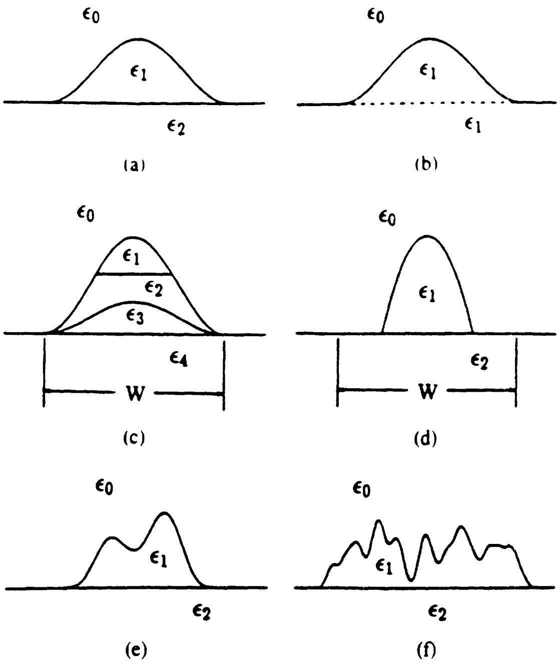

Fig. 2. Hump types considered in this paper.

hump when the clod and underlying layer are both moist (a homogeneous surface). The hump itself may be considered to be inhomogeneous as shown in Fig. 2(c). Isolated irregularities such as rocks above a flat surface can be represented by the hump shown in Fig. 2(d) where the bump occupies only a part of the total width allocated for an individual hump. When the surface is rough with a short correlation length, the geometry of the humps are more complicated and two examples are shown in Fig. 2(e) and (f). The profiles of Fig. 2(a)–(e) used in this paper are given by the following functional forms

$$y(x) = \frac{W}{A}\cos^2\left(\frac{\pi x}{W}\right), \quad -\frac{W}{2} \le x \le \frac{W}{2}, \quad \text{for (a)–(c)} \tag{8}$$

$$y(x) = A\left(1 - \frac{x^2}{B^2}\right), \quad -B \le x \le B,\ B \le W, \quad \text{for (d)} \tag{9}$$

and

$$y(x) = AF_1(x) + BF_2(x)$$

with

$$\left.\begin{aligned} F_1(x) &= \cos^n\left(\frac{\pi x}{W} - \frac{\pi}{2}\right)\left(\frac{x}{W}\right)^m \\ F_2(x) &= \cos^n\left(\frac{\pi x}{W} - \frac{\pi}{2}\right)\left(1 - \frac{x}{W}\right)^m \end{aligned}\right\} \quad 0 \le x \le W, \quad \text{for (e)} \tag{10}$$

where A and B are constants, n and m are integers, and W is width of a hump. The set of constituent humps for a surface can be constructed by choosing a finite number of parameters in the desired functionals and the desired dielectric constants. The profile of Fig. 2(f) is very complicated and should be obtained numerically by the procedure outlined in [8]. In this procedure the hump profile is obtained from a sequence of independent Gaussian deviates with zero mean and unit variance which are correlated by a set of weighting factors derived from the desired correlation function.

Suppose the set of individual humps includes K different humps (including size, shape, and dielectric constant) and the profiles of the humps in the set are represented by $f_i(x)$, $i = 1, \cdots, K$. Then a sequence of random numbers ranging from 1 to K, which is generated by a random number generator with the prescribed probability distribution, is used to position a large number of humps randomly to construct a surface sample. If the total number of humps (M) in the surface sample is much larger than the number of constituent humps (K) and the random number generator has a uniform distribution, the probability of the occurrence of each hump in the surface will be about M/K. A functional form of the generated surface profile can be represented by

$$y(x) = \sum_{m=1}^{M} f_{i_m}\left(x - \sum_{l=1}^{m-1} W_{i_l}\right) \tag{11}$$

where $i_m, i_l \in \{1, \cdots, K\}$ and W_{i_l} represents the width of the hump of the i_lth type. The roughness parameters, rms height s, correlation length l, and rms slope m, can be computed either numerically or analytically from the surface profile given in (11). However, the analytical computation is only possible for simple functional forms and simple probability distribution functions. Assuming perfect randomness, the average height of the surface can be computed from

$$\bar{y}(x) = \frac{1}{L}\sum_{i=1}^{K} p_i \int_0^{W_i} f_i(x)\, dx \tag{12}$$

where $L = \sum_{i=1}^{K} p_i W_i$ and p_i is the probability of occurrence of the hump of ith type. The rms height s and the rms slope

m, respectively, can be evaluated from

$$
\begin{aligned}
s &= \langle [y(x) - \overline{y}(x)]^2 \rangle^{1/2} \\
&= \left\{ \frac{1}{L} \sum_{i=1}^{K} \int_0^{W_i} [p_i f_i(x) - \overline{y}(x)]^2 \, dx \right\}^{1/2} \qquad (13)
\end{aligned}
$$

and

$$
\begin{aligned}
m &= \left\langle \left[\frac{dy(x)}{dx} - \left\langle \frac{dy(x)}{dx} \right\rangle \right]^2 \right\rangle^{1/2} \\
&= \left\{ \frac{1}{L} \sum_{i=1}^{K} w_i \int_0^{W_i} [f_i'(x)]^2 \, dx \right\}^{1/2}. \qquad (14)
\end{aligned}
$$

Assuming the surface has a Gaussian correlation function, the correlation length l in terms of rms height and rms slope is given by

$$
l = \sqrt{2} \, \frac{s \, (\text{rms height})}{m \, (\text{rms slope})}. \qquad (15)
$$

It is often required to generate a random surface of given rms height s and correlation length l. In that case the required surface can be obtained by an iterative process where some initial values for the hump parameters are chosen. Then the roughness parameters are calculated and compared with the desired ones. Depending on the difference between the calculated s and l and the desired s and l the hump parameters are modified and this process is repeated until the difference is below a tolerable error.

Once the set of individual humps for a random surface with given s and l is formed the impedance matrices, $[\mathcal{Z}_{pq}]_i$, $i = 1, \cdots, K$, can be computed using the method of moments described in the previous section. Since the scattered field of a hump near the impedance surface is very weak the effect of multiple interaction between humps in a surface sample can be ignored. Therefore, by inverting and storing the impedance matrices of the constituent humps the scattered field of any surface sample comprised of M humps ($M \gg K$) and for any incidence and observation directions can be computed very efficiently. For a given direction of incidence the polarization current in the jth hump for the vertical and horizontal polarization, respectively, are given by

$$
\begin{bmatrix} [\mathcal{I}_x] \\ [\mathcal{I}_y] \end{bmatrix}_j = \begin{bmatrix} [\mathcal{Z}_{xx}] & [\mathcal{Z}_{xy}] \\ [\mathcal{Z}_{yx}] & [\mathcal{Z}_{yy}] \end{bmatrix}_{i_j}^{-1} \begin{bmatrix} [\mathcal{V}_x] \\ [\mathcal{V}_y] \end{bmatrix}_j \qquad (16)
$$

and

$$
[\mathcal{I}_z]_j = [\mathcal{Z}_{zz}]_{i_j}^{-1} [\mathcal{V}_z]_j \qquad (17)
$$

where $j \in \{1, \cdots, M\}$ and $i_j \in \{1, \cdots, K\}$ representing the hump of the ith type. The excitation vector $[\mathcal{V}]_j$ is computed from (6) where the position vector $\overline{\rho}$ is specified by the discretization procedure and the profile function (11). The electric polarization current induced inside the surface sample can be represented by

$$
\begin{aligned}
[\mathcal{J}_p] &= [\, [\mathcal{I}_p]_1^T, \cdots, [\mathcal{I}_p]_i^T, \cdots, [\mathcal{I}_p]_M^T \,]^T, \\
p &= x, y, z \qquad (18)
\end{aligned}
$$

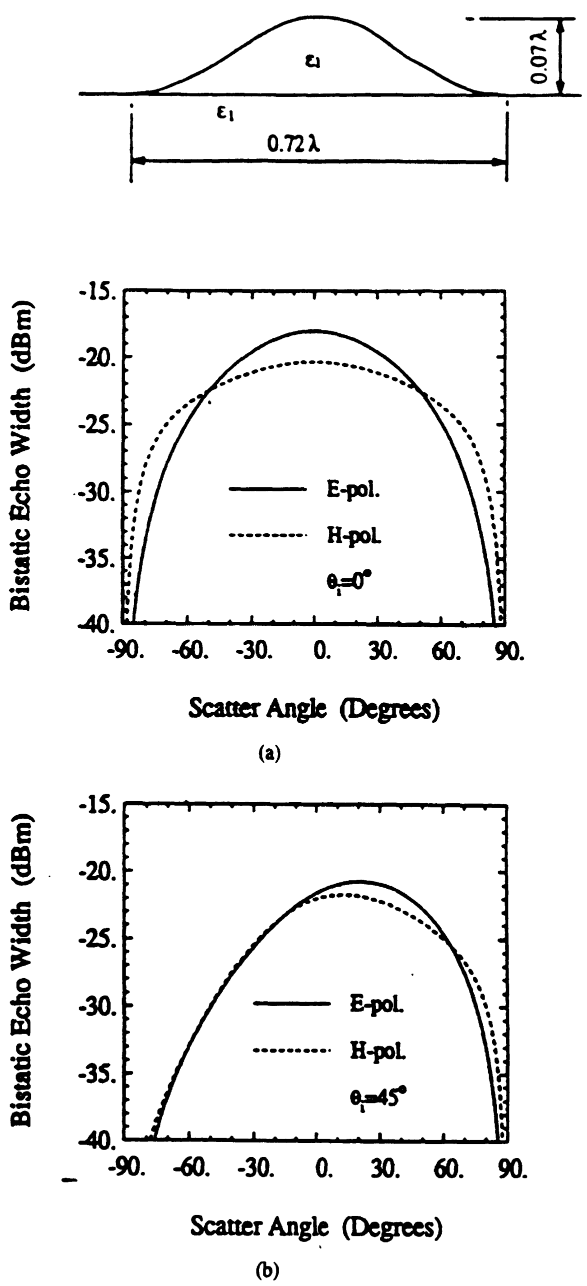

Fig. 3. Bistatic echo width of a squared-cosine hump of $\epsilon_1 = 15 + i3$, $W = 0.72\lambda$, $H = 0.07\lambda$ over an impedance surface of $\eta = 0.254 - i0.025$ at (a) $\theta_i = 0°$ and (b) $\theta_i = 45°$ at $f = 5$ GHz for E- and H-polarizations.

where $[\mathcal{I}_p]_i$ is the p-polarized current inside the ith hump. The radiated far field can be evaluated from

$$
E_{pp}^s = \sqrt{\frac{2}{\pi k_0 \rho}} \, e^{i(k_0 \rho - \pi/4)} S_{pp}, \quad pp = hh \text{ or } vv \qquad (19)
$$

where S_{pp} is the far field amplitude given by

$$
\begin{aligned}
S_{hh} &= -\frac{k_0 Z_0}{4} \sum_{n=1}^{N_t} J_z(x_n, y_n) \, \Delta x_n \, \Delta y_n \, e^{-ik_0 \sin \theta_s x_n} \\
&\quad \cdot [e^{-ik_0 \cos \theta_s y_n} + R_E(\theta_s) e^{ik_0 \cos \theta_s y_n}] \qquad (20) \\
S_{vv} &= \frac{k_0 Z_0}{4} \sum_{n=1}^{N_t} \Delta x_n \, \Delta y_n \, e^{-ik_0 \sin \theta_s x_n} \\
&\quad \cdot \{J_x(x_n, y_n) \cos \theta_s \\
&\quad \cdot ([e^{-ik_0 \cos \theta_s y_n} - R_H(\theta_s) e^{ik_0 \cos \theta_s y_n})
\end{aligned}
$$

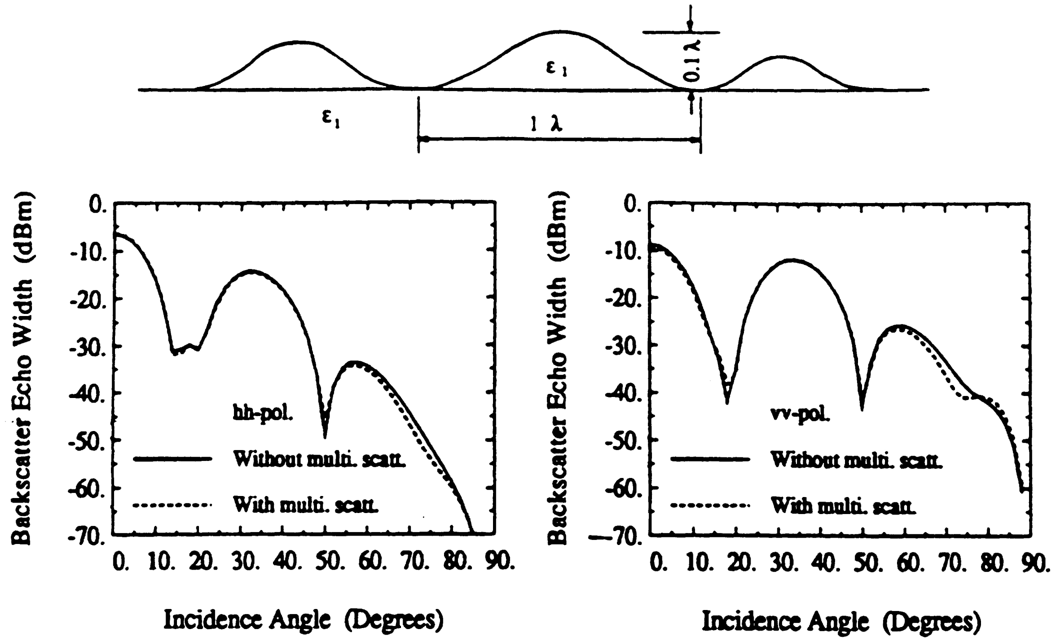

(a) (b)

Fig. 4. Multiple scattering effect on the backscatter echo width of a surface segment consisting of three squared-cosine humps with $\epsilon_1 = 15 + i3$ at $f = 5$ GHz for both (a) HH-polarization and (b) VV-polarization.

$$- J_y(x_n, y_n) \sin \theta_s \cdot \left(e^{-ik_0 \cos \theta_s y_n} + R_H(\theta_s) e^{ik_0 \cos \theta_s y_n}\right)\}. \tag{21}$$

Here N_t is the total number of cell in the surface sample.

The statistical behavior of the scattered field are obtained from the scattered fields E^s_{pp} of many independent surface samples. For sufficiently large N_s surface samples the incoherent scattering coefficient is computed from

$$\sigma^\circ_{pp} = \lim_{\rho \to \infty} \frac{2\pi\rho}{N_s L_{av}} \left[\sum_{j=1}^{N_s} |E^s_{pp,j}|^2 - \frac{1}{N_s} \left| \sum_{j=1}^{N_s} E^s_{pp,j} \right|^2 \right]$$
$$pp = hh,\ vv \tag{22}$$

where $L_{av} = (1/N_s) \sum_{j=1}^{N_s} L_j$, and L_j is the total length of jth random surface.

IV. Numerical Results

To demonstrate the performance of the technique proposed in this paper, we shall use it to compute the scattering for some sample surfaces and then compare the results with those predicted by the available theoretical scattering models, when conditions apply. First, we consider a surface with homogeneous dielectric humps as shown in Fig. 2(a). The functional form of the humps are given by (8) where the parameters A and W are varied to generate the set of the constituent humps. Keeping A as a constant controlling the height and varying W, a set of similar humps can be generated. A random number generator with output $i \in \{1, \cdots, K\}$ selects the parameter $W_i = B\lambda i$, where B is a constant controlling the width of the humps and λ is the wavelength. In this example, the hump parameters were chosen according to Table I and the random number generator was given a uniform distribution with $K = 10$. Before presenting the statistical scattering behavior of the surface, it is useful to demonstrate the validity of the assumption regarding the significance of the effects of multiple scattering among the humps. Fig. 3(a) and (b) show the bistatic echo width of a squared-cosine hump with $W = 0.72\lambda$, $H = 0.07\lambda$, $\epsilon_1 = 15 + i3$ above a surface with $\eta = 0.254 - i0.025$ (which corresponds to $\epsilon_2 = 15 + i3$) at 5 GHz when the incidence angle $\theta_i = 0°$ and $\theta_i = 45°$, respectively. It is shown that the bistatic echo widths at the large scatter angles (near the surface) are very weak which implies that the effect of multiple scattering between humps can be ignored. In order to illustrate the effect of multiple scattering, a surface segment consisting of three squared-cosine humps with $\epsilon_1 = 15 + i3$ above an impedance surface with $\eta = 0.254 - i0.025$ was considered (see Fig. 4). Dimensions of three humps are, respectively, given by: $W_1 = 0.8\lambda$, $H_1 = 0.08\lambda$; $W_2 = 1.0\lambda$, $H_2 = 0.1\lambda$, and $W_3 = 0.6\lambda$, $H_3 = 0.06\lambda$. The backscatter echo widths of the surface segment were computed twice. In one case the scattered field was computed from the polarization current of isolated humps (ignoring the effect of mutual coupling) and in the other case the polarization current of the three-hump structure was obtained directly from the method of moments solution (including the effect of mutual coupling). Fig. 4(a) and (b) show that the effect of multiple scattering is negligible for both polarizations. As long as the ratio of rms height to correlation length of the surface (s/l) is small, this approximation provides accurate results. For most natural surfaces $s/l < 0.3$ which satisfies this condition [9]. However, if the ratio (s/l) is relatively large, the hump type of Fig. 2(f) must be used to include the effect of multiple scattering at the expense of computation time.

The rms surface height s and the rms surface slope m for this surface can be computed from (13) and (14), respectively,

TABLE I
ROUGHNESS PARAMETERS CORRESPONDING TO CONSTANTS A AND B

Case	A	B	Approx. † s (in cm)	Approx. † l (in cm)	Exact ‡ s (in cm)	Exact ‡ l (in cm)	At 5 GHz ks	At 5 GHz kl	Remarks
1	30	0.20	0.115	2.21	0.115	2.03	0.12	2.13	SPM region
2	30	0.36	0.208	3.98	0.207	3.63	0.22	3.80	
3	30	0.70	0.405	7.74	0.405	7.15	0.42	7.49	PO region

† Approximation by equations (23), (24) and (15).

‡ Numerical evaluation with 4000 humps,

s : rms surface height,

l : correlation length.

TABLE II
CONSTANTS USED IN THE NUMERICAL COMPUTATIONS

Case No.	Individual hump size: Width min. (λ)	Width max. (λ)	Height min. (λ)	Height max. (λ)	No. of humps for each surface segment	Length of surface segment (λ)	No. of segments for a surface
1	0.2	2.0	0.0066	0.066	40	44	100
2	0.36	3.6	0.012	0.12	40	79	100
3	0.7	7.0	0.023	0.233	40	154	100

and are given by

$$s = \left[\frac{1}{L_W}\sum_{i=1}^{K}\left(\frac{3}{8}\frac{W_i^3}{A^2} - \frac{W_i^2}{A}\bar{y} + W_i\bar{y}^2\right)\right]^{1/2} \tag{23}$$

$$m = \frac{\pi}{\sqrt{2}A} \tag{24}$$

where

$$\bar{y} = \frac{1}{2AL_W}\sum_{i=1}^{K} W_i^2$$

and

$$L_W = \sum_{i=1}^{K} W_i.$$

It should be noted that the rms surface slope m of this surface depends only on the constant A. Therefore, for a fixed value of A, both the rms height and the correlation length increase at the same rate with increasing B. Table I shows several values of roughness parameters, s and l, corresponding to different values of A and B.

A random number generator was used to select and position 4000 squared-cosine humps over the impedance surface ($\eta = 0.254 - i0.025$). Then this surface was divided into 100 segments to obtain 100 independent surface samples each having 40 humps. The length of the surface segment was chosen to be about 44λ to 154λ depending on the correlation length of the surface, corresponding to the size of individual humps. Table II summarizes the characteristics of the surfaces and their constituent humps used in the examples considered in this study.

The backscattering coefficients for the surface at 5 GHz with $ks = 0.12$ and $kl = 2.13$ (Case 1 in Tables I and II) are computed by the Monte Carlo simulation technique for

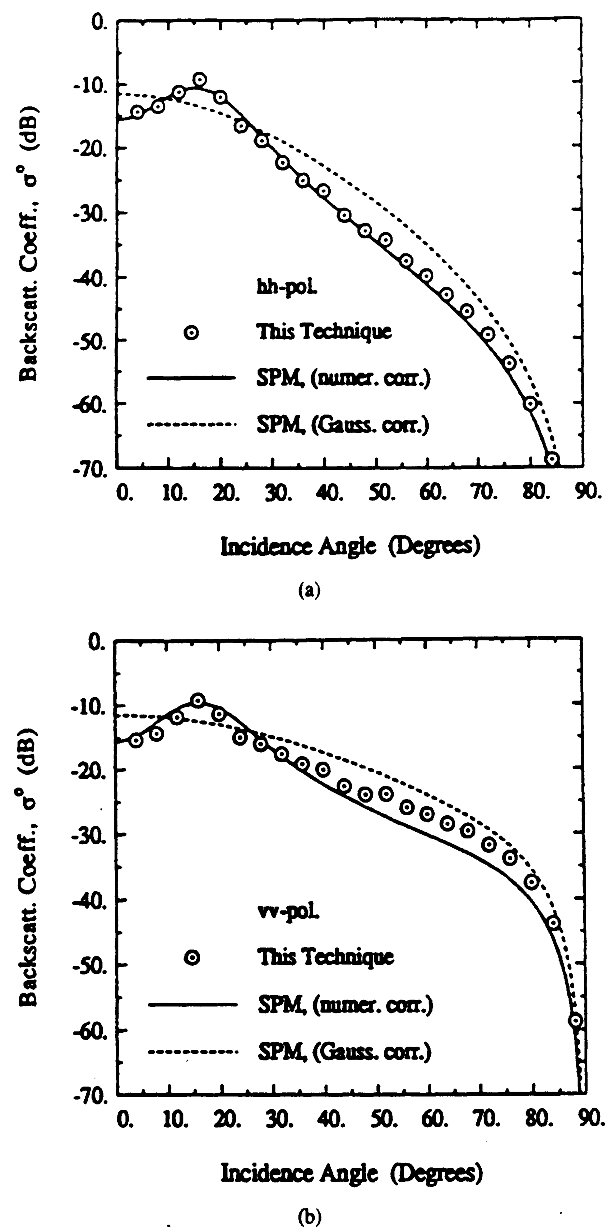

(a)

(b)

Fig. 5. Backscattering coefficient σ^0 of the random surface with $ks = 0.12$, $kl = 2.13$, and $\epsilon_1 = \epsilon_2 = 15 + i3$ as computed by the SPM and the numerical technique. (a) HH-polarization. (b) VV-polarization.

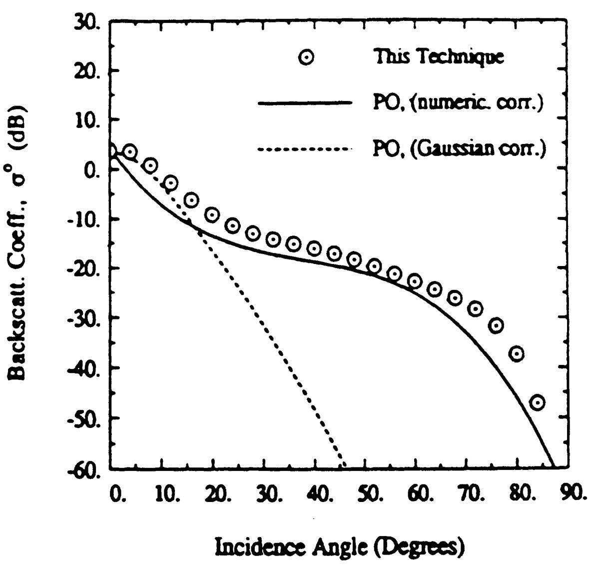

Fig. 6. Backscattering coefficient σ^0 of the random surface with $ks = 0.42$, $kl = 7.49$, and $\epsilon_1 = \epsilon_2 = 15 + i3$ as computed by the PO model and the numerical technique for HH-polarization.

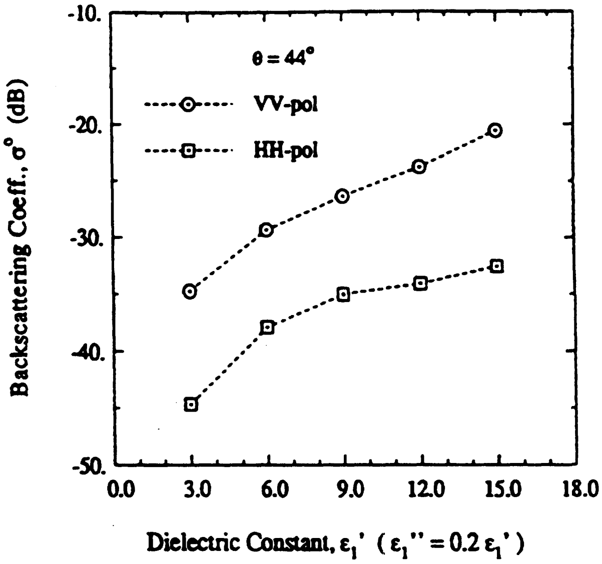

Fig. 7. The sensitivity of the backscattering coefficient σ^0 to the dielectric constant in case of $ks = 0.22$, $kl = 3.8$, and $\epsilon_2 = 15 + i3$ at $\theta = 44°$.

a homogeneous surface with $\epsilon_1 = \epsilon_2 = 15 + i3$ (Fig. 2(b)), and compared with the analytical results based on the SPM. The comparisons are shown in Fig. 5(a) and (b). For the SPM solution, the scattering coefficient σ^0 is proportional to the roughness spectrum (Fourier transform of the correlation function). Both the actual and Gaussian correlation functions are used in the calculation of the backscattering coefficients using the SPM. It is shown that the Monte Carlo simulation agrees very well with the SPM prediction when the actual correlation function is used. The discrepancies between the Monte Carlo simulation and the SPM with Gaussian correlation function indicate the importance of the tail section of the correlation function in the estimation of σ^0.

The numerical simulation was also performed for a surface at 5 GHz with $ks = 0.42$, $kl = 7.49$ (Case 3 in Tables I and II), and $\epsilon_1 = \epsilon_2 = 15 + i3$. The roughness parameters of this surface fall within the validity region of the physical optics (PO) model; therefore, the numerical solution can be compared with the PO solution. The scattering coefficient σ^0_{hh} predicted by the PO model using the actual correlation function agrees very well with the results computed by the numerical technique (see Fig. 6). In this figure the PO solution using a Gaussian correlation function with the same correlation length as the actual correlation function is also compared with the numerical simulation. It is shown that the agreement is good only for low incidence angles ($\theta_i \leq 20°$) and the discrepancy between the two solutions becomes rather significant for higher incidence angles. In this case, similar to the previous case (SPM), it is shown that the tail of the correlation function plays an important role in determining the angular patterns of the backscattering coefficients.

With the success of the Monte Carlo simulation in predicting the scattering behavior of rough surfaces in the small perturbation and physical optics regions, the numerical model can be used to study complex surfaces with intermediate roughness parameters and inhomogeneous dielectric profiles. For example, the sensitivity of radar backscatter to the moisture content of the top layer for the Case 2 random surface is shown in Fig. 7 at $\theta = 44^\circ$.

V. CONCLUSION

In this paper an efficient Monte Carlo simulation technique is proposed for computing electromagnetic scattering by inhomogeneous one-dimensional rough surfaces. The surface irregularities are represented by inhomogeneous dielectric humps of different shapes and the underlying layer is represented by an impedance surface. A moment-method procedure, in conjunction with the exact image theory, is used for calculation of the field scattered by the dielectric humps. It was shown that the scattered field near the impedance surface is weak, and hence, the effect of multiple scattering between humps can be ignored.

To check the validity of the Monte Carlo simulation, the numerical results were compared with the existing analytical solutions for surfaces at extreme roughness conditions. A smooth surface that satisfies the validity region of the SPM and a surface that satisfies the validity region of the PO model were considered, and in both cases excellent agreements were obtained between the analytical results and those computed using the proposed technique. It was found that away from normal incidence, the tail of the correlation function plays an important role in the determination of the backscattering coefficients.

The analysis presented in this paper is only for one-dimensional surfaces and therefore is incapable of predicting the cross-polarized scattering coefficients. A numerical simulation for a two-dimensional rough surface using a similar method is computationally tractable.

REFERENCES

[1] S. O. Rice, "Reflection of electromagnetic waves by slightly rough surfaces," *Commun. Pure Appl. Math.*, vol. 4, pp. 351–378, 1951.

[2] P. Beckmann and A. Spizzichino, *The Scattering of Electromagnetic Waves from Rough Surfaces.* Norwood, MA: Artech House, 1987.

[3] G. S. Brown, "Backscattering from a Gaussian distributed perfectly conducting rough surface," *IEEE Trans. Antennas Propagat.*, vol. AP-26, pp. 472–482, May 1978.

[4] D. Winebemer and A. Ishimaru, "Investigation of a surface field phase perturbation technique for scattering from rough surfaces," *Radio Sci.*, vol. 20, pp. 161–170, Mar. 1985.

[5] A. K. Fung and G. W. Pan, "A scattering model for perfectly conducting random surfaces: I. Model development and II. Range of validity," *Int. J. Remote Sensing*, vol. 8, no. 11, pp. 1579–1605, 1987.

[6] E. Bahar, "Radio wave propagation over a rough variable impedance boundary: Part I. Full-wave analysis," *IEEE Trans. Antennas Propagat.*, vol. AP-20, pp. 354–362, May 1972.

[7] R. M. Axline and A. K. Fung, "Numerical computation of scattering from a perfectly conducting random surface," *IEEE Trans. Antennas Propagat.*, vol. AP-26, pp. 482–488, May 1978.

[8] A. K. Fung and M. F. Chen, "Numerical simulation of scattering from simple and composite random surfaces," *J. Opt. Soc. Amer. A*, vol. 2, no. 12, pp. 2274–2284, Dec. 1985.

[9] Y. Oh, K. Sarabandi, and F. T. Ulaby, "An empirical model and an inversion technique for radar scattering from bare soil surfaces," *IEEE Trans. Geosci. Remote Sensing*, vol. 30, pp. 370–382, Mar. 1992.

[10] K. Sarabandi, "Scattering from dielectric structures above impedance surfaces and resistive sheets," *IEEE Trans. Antennas Propagat.*, vol. 40, pp. 67–78, Jan. 1992.

[11] J. A. Stratton, *Electromagnetic Theory.* New York: McGraw-Hill, 1941.

[12] A. K. Fung and M. F. Chen, "Numerical simulation of scattering from simple and composite random surfaces," *J. Opt. Soc. Amer.*, vol. 2, no. 12, pp. 2274–2284, Dec. 1985.

[13] F. T. Ulaby, M. K. Moore, and A. K. Fung, *Microwave Remote Sensing, Active and Passive*, vol. 2 and 3. Norwood, MA: Artech House, 1986.

Kamal Sarabandi (S'87–M'90–SM'93) received the B.S. degree in electrical engineering from Sharif University of Technology, Tehran, Iran, in 1980. He entered the graduate program at the University of Michigan in 1984 and received the M.S.E. degree in electrical engineering in 1986, and the M.S. degree in mathematics and the Ph.D. degree in electrical engineering in 1989.

From 1980–1984, he was a Microwave Engineer with the Telecommunication Research Center in Iran. He is presently an Assistant Professor in the Department of Electrical Engineering and Computer Science at the University of Michigan. He has 15 years of experience with microwave sensors and radar systems. In the past six years, he has served as Principal Investigator and Co-Investigator on many projects sponsored by NASA, JPL, ARO, DARPA, etc., all related in one way or the other to the radar remote sensing of environment. He has published four book chapters and more than fifty papers in refereed journals on electromagnetic scattering, random media modeling, microwave measurement techniques, radar calibration, application of neural networks in inverse scattering problems, and microwave sensors. He has also had more than 80 papers and presentations in national and international conferences and symposia on similar subjects.

Dr. Sarabandi is listed in *Who's Who in Electromagnetics* and is the Chairman of Geoscience and Remote Sensing Society Southeastern Michigan chapter.

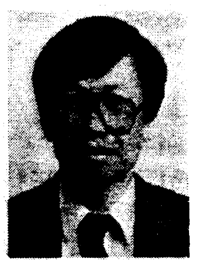

Yisok Oh (S'88) received the B.S. degree from Yonsei University, Seoul, Korea, in 1982, the M.S. degree from the University of Missouri, Rolla, in 1988, and the Ph.D. degree from the University of Michigan, Ann Arbor, in 1993, all in electrical engineering.

He is presently an Assistant Professor in the Department of Radio Engineering at the Hong IK University. His research interests include electromagnetic wave scattering from random surfaces and microwave remote sensing.

Fawwaz T. Ulaby (M'68–SM'74–F'80), for a photograph and biography, see p. 99 of the January 1996 issue of this TRANSACTIONS.

IEEE TRANSACTIONS ON ANTENNAS AND PROPAGATION, VOL. 40, NO. 1, JANUARY 1992

Scattering from Dielectric Structures Above Impedance Surfaces and Resistive Sheets

Kamal Sarabandi

Abstract—**Interest in understanding of electromagnetic interaction with rough surfaces has prompted the study of scattering from typical dielectric humps over impedance surfaces. It is shown that the Green's function of the problem for a resistive sheet resembles that of the impedance surface. Hence both problems are considered here. In this paper a numerical solution for the scattered field of a two-dimensional dielectric object, possibly inhomogeneous, with arbitrary cross section above the impedance surface or resistive sheet is sought. First the Green's function of the problem is derived based on the exact image theory. This form of the Green's function is amenable to numerical computation. Then the induced polarization currents are calculated by casting the integral equations into a matrix equation via the method of moments. Numerical problems in calculation of the Green's function when both source and observation points are close to the surface are discussed. Comparison of numerical results for both transverse electric (TE) and transverse magnetic (TM) cases with a perturbation solution shows excellent agreement between the two methods.**

I. Introduction

APPLICATION of electromagnetic waves as a means of retrieving the desired surface parameters of the earth is a matter of increasing concern. For example, soil moisture content and surface roughness are two such parameters. The problem of electromagnetic wave scattering by rough surfaces has long been studied and because of its complexity satisfactory models exist only for a limited cases. The existing models are applicable to two extreme roughness conditions. In the so-called small perturbation model both the correlation length and root mean square (rms) height must be smaller than a wavelength [1]. For the other extreme, known as the Kirchoff model, however, both the correlation length and rms height must be much larger than a wavelength while the rms slope must be reasonably small [1]. To achieve analytical expressions for the scattering coefficients, the random surface medium is assumed to be homogeneous and to have a Gaussian autocorrelation function.

Measurement of natural surfaces at microwave frequencies shows that the existing models are inadequate to explain the scattering behavior for two main reasons [2]. First, the roughness parameters are usually outside the region of validity of the mentioned models. Second, natural surfaces are not homogeneous, that is the moisture content in most cases is not uniform in depth. The top rough layer includes clods and rocks that are usually dry and keep the moisture of the underlying layer from evaporating. The moist smooth underlying soil layer at microwave frequencies can be modeled by an impedance surface and irregularities at the top by dielectric humps of different dielectric constants. To simulate the electromagnetic scattering behavior of such surfaces, the scattering solution of an isolated hump is needed.

In this paper we seek a numerical solution of a two-dimensional dielectric object with arbitrary cross section above a uniform impedance surface when the object is illuminated by a plane wave. The geometry of the problem is depicted in Fig. 1. Common practice in obtaining the Green's function for scattering and antenna problems in the presence of a half-space medium is through calculation of a Sommerfeld-type integral [3]. These infinite integrals, in general, are highly oscillatory and computationally rather inefficient. Although many techniques have been developed to speed up their calculation for three-dimensional problems [4], [5] they are of little use for two-dimensional problems. Numerical solutions for two-dimensional scattering problems in the presence of a half-space medium have been limited to small scatterers or low frequencies mainly because of difficulties in computing the Green's function [6], [7]. Here, the Green's function of an impedance surface (or resistive sheet) is derived in terms of rapidly converging integrals using appropriate integral transforms. Useful asymptotic expressions of the Green's function are also given. The scattering problem is then formulated by integral equations which are solved numerically using the method of moments.

II. Derivation of Green's Function Using Exact Image Theory

The first step toward calculating the scattered field of an object is to derive the dyadic Green's function of the problem. Since the Green's function is used in a numerical solution of the scattering problem, it should be efficiently calculable. An integral representation for the image of a line source above an impedance surface or a resistive sheet is derived using integral transforms similar to those employed by Lindell and Alanen in derivation of the exact image theory [8]. Interested readers are also referred to [9]–[11] for detailed discussion of the exact image theory. The new representation for the Green's function has an excellent rate of convergence for most practical purposes and can be computed very easily.

The fields generated by a two-dimensional ($\partial / \partial z = 0$) distribution of electric current ($\mathbf{J}_e(x, y)$) in terms of the

Manuscript received March 26, 1991; revised October 3, 1991. This work was supported by NASA under Contract NAGW-2151.

The author is with the Radiation Laboratory, Department of Electrical Engineering and Computer Science, University of Michigan, Ann Arbor, MI 48109-2122.

IEEE Log Number 9105277.

0018-926X/92$03.00

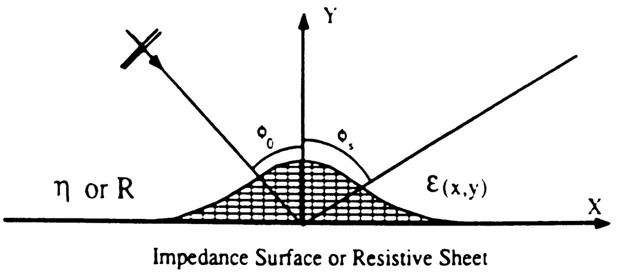

Fig. 1. Geometry for the scattering problem of a dielectric cylinder above a uniform resistive or impedance sheet.

associated Hertz vector potential are given by

$$E_x = k_0^2\left(1 + \frac{1}{k_0^2}\frac{\partial^2}{\partial x^2}\right)\Pi_x + \frac{\partial^2}{\partial x\,\partial y}\Pi_y,$$

$$E_y = \frac{\partial^2}{\partial y\,\partial x}\Pi_x + k_0^2\left(1 + \frac{1}{k_0^2}\frac{\partial^2}{\partial y^2}\right)\Pi_y, \qquad (1)$$

$$E_z = k_0^2\Pi_z.$$

The Hertz vector potential associated with an infinite current filament located at point (x', y') in free space with amplitude I_p and orientation $\hat{p}$ is of the form

$$\Pi_p(x,y) = \frac{-Z_0}{4k_0}H_0^{(1)}\left(k_0\sqrt{(x-x')^2 + (y-y')^2}\right)I_p, \qquad p = x, y \text{ or } z \qquad (2)$$

where $H_0^{(1)}$ is the Hankel function of the first kind and zeroth order and Z_0 is the free space characteristic impedance. The corresponding field components can be obtained by inserting (2) into (1) and then by employing the identity

$$H_0^{(1)}\left(k_0\sqrt{(x-x')^2 + (y-y')^2}\right) = \frac{1}{\pi}\int_{-\infty}^{+\infty}\frac{e^{ik_y|y-y'| - ik_x(x-x')}}{k_y}\,dk_x \qquad (3)$$

the resulting fields can be expressed in terms of a continuous spectrum of plane waves. In (3) $k_y = \sqrt{k_0^2 - k_x^2}$ and the branch of the square root is chosen such that $\sqrt{-1} = i$.

In the presence of the impedance surface or the resistive sheet, when the current filament is in the upper half-space, each plane wave is reflected at the interface according to the appropriate reflection coefficient. It should be noted that the incidence angle of each plane wave, in general, is complex and is given by $\gamma = \arctan(k_x/k_y)$. The net effect of the impedance surface or resistive sheet on the radiated field can be obtained by superimposing all of the reflected plane waves of the form $R_q(\gamma)e^{ik_y(y+y') - ik_x(x-x')}$, where $R_q(\gamma)$ is the reflection coefficient corresponding to incident polarization $q = E$ or H and the surface type. The total reflected field can now be obtained by noting that

$$E_x^r = -R_H(\gamma)E_x^i, \quad E_y^r = R_H(\gamma)E_y^i, \quad E_z^r = R_E(\gamma)E_z^i$$

and since the direction of propagation along the y axis is reversed for the reflected waves, the operator $\partial/\partial y$ for the x and y components of the reflected field must be replaced with $-\partial/\partial y$. Thus, in matrix notation the total field in the upper half-space can be represented by

$$\mathbf{E} = \begin{bmatrix} G_{xx} & G_{xy} & 0 \\ G_{yx} & G_{yy} & 0 \\ 0 & 0 & G_{zz} \end{bmatrix}\begin{bmatrix} I_x \\ I_y \\ I_z \end{bmatrix} \qquad (4)$$

where

$$G_{xx} = -\frac{k_0 Z_0}{4}\left(1 + \frac{1}{k_0^2}\frac{\partial^2}{\partial x^2}\right)\cdot\left[H_0^{(1)}\left(k_0\sqrt{(x-x')^2 + (y-y')^2}\right) - Q_H\right]$$

$$G_{xy} = -\frac{Z_0}{4k_0}\frac{\partial^2}{\partial x\,\partial y}\cdot\left[H_0^{(1)}\left(k_0\sqrt{(x-x')^2 + (y-y')^2}\right) + Q_H\right]$$

$$G_{yx} = -\frac{Z_0}{4k_0}\frac{\partial^2}{\partial y\,\partial x}\cdot\left[H_0^{(1)}\left(k_0\sqrt{(x-x')^2 + (y-y')^2}\right) - Q_H\right]$$

$$G_{yy} = -\frac{k_0 Z_0}{4}\left(1 + \frac{1}{k_0^2}\frac{\partial^2}{\partial y^2}\right)\cdot\left[H_0^{(1)}\left(k_0\sqrt{(x-x')^2 + (y-y')^2}\right) + Q_H\right]$$

$$G_{zz} = -\frac{k_0 Z_0}{4}\cdot\left[H_0^{(1)}\left(k_0\sqrt{(x-x')^2 + (y-y')^2}\right) + Q_E\right] \qquad (5)$$

are the elements of the dyadic Green's function $(\mathbf{G}(x, y; x', y'))$ for the two-dimensional impedance surface or resistive sheet problem. In (5) the quantity $Q_{\substack{H\\E}}$ is given by

$$Q_{\substack{H\\E}}(x, y; x', y') = \frac{1}{\pi}\int_{-\infty}^{+\infty} R_{\substack{H\\E}}(\gamma)\cdot\frac{e^{ik_y(y+y') - ik_x(x-x')}}{k_y}\,dk_x \qquad (6)$$

and the expressions for the reflection coefficients of the impedance surface and resistive sheet are respectively given by [12]

$$R_E(\gamma) = \frac{\eta\cos\gamma - 1}{\eta\cos\gamma + 1} \qquad R_H(\gamma) = \frac{\cos\gamma - \eta}{\cos\gamma + \eta} \qquad (7)$$

$$R_E(\gamma) = \frac{-1}{1 + 2R\cos\gamma} \qquad R_H(\gamma) = \frac{1}{1 + 2R\sec\gamma} \qquad (8)$$

where η is the normalized impedance of the impedance surface $(\eta = Z/Z_0)$ and R is the normalized resistivity of the resistive sheet. For example the resistivity of an infinitesimally thin dielectric layer of thickness τ and permittivity ϵ is given by [13]

$$R = \frac{i}{k_0 \tau (\epsilon - 1)}.$$

If an electric current distribution $\mathbf{J}_e$ occupies region S in the upper half-space, the radiated electric field at any point in the upper half-space can be obtained from:

$$\mathbf{E}^s(x, y) = \int_S \mathbf{G}(x, y; x', y') \cdot \mathbf{J}(x', y')\, dx'\, dy'. \quad (9)$$

The first term within brackets in (5) represents the effect of the current filament in the absence of the impedance surface while the second term is due to the image of the current filament. Unfortunately, the integral representing the contribution of the image does not have a closed form and its convergence rate is very poor. To achieve the image contribution in an efficient way consider the following transformation:

$$\int_0^{+\infty} e^{-\alpha \nu} e^{-k_y \nu}\, d\nu = \frac{1}{\alpha + k_y},$$

$$\text{provided } \operatorname{Re}[\alpha] > -\operatorname{Re}[k_y]. \quad (10)$$

The choice of the branch cut for k_y guarantees that $\operatorname{Re}[k_y]$ is nonnegative as k_x takes any real number, therefore the sufficient condition for (10) is

$$\operatorname{Re}[\alpha] > 0.$$

The expressions for the reflection coefficients can be written in terms of k_y by substituting $\cos\gamma = k_y / k_0$. For the case of a resistive sheet with an E-polarized incident wave we can define α to be $k_0/2R$, noting that the above condition is satisfied ($\operatorname{Re}[\alpha] = k_0^2 \tau \epsilon''/2 > 0$). In view of the transformation (10) the integral representing the image contribution in the upper half-space can be written as

$$\int_{-\infty}^{+\infty} \frac{-1}{\left(1 + \dfrac{k_y}{\alpha}\right) k_y} e^{i k_y (y + y') - i k_x (x - x')}\, dk_x$$

$$= \int_0^{+\infty} -\alpha e^{-\alpha \nu} \left[\int_{-\infty}^{+\infty} \frac{e^{i k_y (y + y' + i\nu) - i k_x (x - x')}}{k_y}\, dk_x \right] d\nu.$$

Employing the identity given by (3), the zz-component of the dyadic Green's function for the resistive sheet problem in the upper half-space can be obtained from

$$G_{zz}^{+} = \frac{-k_0 Z_0}{4} \Bigg[H_0^{(1)}\left(k_0 \sqrt{(x - x')^2 + (y - y')^2}\right) - \int_0^{+\infty} \alpha e^{-\alpha \nu} \cdot H_0^{(1)}\left(k_0 \sqrt{(x - x')^2 + (y + y' + i\nu)^2}\right) d\nu \Bigg]. \quad (11)$$

In a similar manner for the lower half-space the zz-component becomes

$$G_{zz}^{-} = \frac{-k_0 Z_0}{4} \Bigg[H_0^{(1)}\left(k_0 \sqrt{(x - x')^2 + (-y + y')^2}\right) - \int_0^{+\infty} \alpha e^{-\alpha \nu} \cdot H_0^{(1)}\left(k_0 \sqrt{(x - x')^2 + (-y + y' + i\nu)^2}\right) d\nu \Bigg]. \quad (12)$$

This integral representation converges very fast because both functions in the integrand are exponentially decaying. Also from this representation it can be deduced that the image of a line current above a resistive sheet is a half-plane current with exponential distribution and is located in the complex y-plane occupying the region $-y' - i\infty < y < -y'$ (see Fig. 2).

Similarly by defining $\beta = 2Rk_0$ for the case of H-polarization the quantity Q_H in (6) for a resistive sheet in the upper half-space is given by

$$Q_H = H_0^{(1)}\left(k_0 \sqrt{(x - x')^2 + (y + y')^2}\right) - \int_0^{+\infty} \beta e^{-\beta \nu} \cdot H_0^{(1)}\left(k_0 \sqrt{(x - x')^2 + (y + y' + i\nu)^2}\right) d\nu. \quad (13)$$

In the corresponding case of an impedance surface the dyadic Green's function can be obtained from (5) with the following expressions for the quantities Q_E and Q_H

$$Q_E = H_0^{(1)}\left(k_0 \sqrt{(x - x')^2 + (y + y')^2}\right) - 2\int_0^{+\infty} \alpha' e^{-\alpha' \nu} \cdot H_0^{(1)}\left(k_0 \sqrt{(x - x')^2 + (y + y' + i\nu)^2}\right) d\nu \quad (14)$$

$$Q_H = H_0^{(1)}\left(k_0 \sqrt{(x - x')^2 + (y + y')^2}\right) - 2\int_0^{+\infty} \beta' e^{-\beta' \nu} \cdot H_0^{(1)}\left(k_0 \sqrt{(x - x')^2 + (y + y' + i\nu)^2}\right) d\nu. \quad (15)$$

The quantities α' and β' in (14) and (15) in terms of the normalized surface impedance are, respectively, given by

$$\alpha' = \frac{k_0}{\eta}, \quad \beta' = k_0 \eta.$$

The validity of the new image representation can be checked by considering some special limiting cases. For example consider the resistive sheet problem for E-polarization. Suppose the resistivity is very small (approaching perfect conductivity) which implies that $|\alpha| \gg 1$. In this case contribution to the integral in (11) comes mostly from point $\nu = 0$

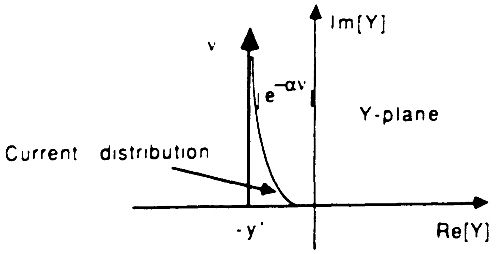

Fig. 2. The location of the image of the line source in the complex Y plane.

and therefore

$$\int_0^{+\infty} \alpha e^{-\alpha\nu} H_0^{(1)}\left(k_0\sqrt{(x-x')^2+(y+y'+i\nu)^2}\right) d\nu$$

$$\approx H_0^{(1)}\left(k_0\sqrt{(x-x')^2+(y+y')^2}\right)\int_0^{+\infty}\alpha e^{-\alpha\nu}\,d\nu$$

$$= H_0^{(1)}\left(k_0\sqrt{(x-x')^2+(y+y')^2}\right)$$

which is the image for the perfectly conducting case. The asymptotic behavior of the integral in terms of a convergent series of inverse power of α can also be obtained by performing integration by parts repeatedly, that is

$$\int_0^{+\infty} \alpha e^{-\alpha\nu} H_0^{(1)}\left(k_0\sqrt{(x-x')^2+(y+y'+i\nu)^2}\right) d\nu = \sum_{n=0}^{\infty}\left(\frac{-1}{\alpha}\right)^n h^{(n)}(0) \quad (16)$$

where $h^{(n)}(0)$ is the nth derivative of $H_0^{(1)}(k_0\sqrt{(x-x')^2+(y+y'+i\nu)^2})$ with respect to ν evaluated at zero. The first order of approximation is

$$\sum_{n=0}^{\infty}\left(\frac{-1}{\alpha}\right)^n h^{(n)}(0) \approx h(0) - h'(0)\frac{1}{\alpha} \approx h\left(\frac{-1}{\alpha}\right)$$

$$= H_0^{(1)}\left(k_0\sqrt{(x-x')^2+\left(y+y'-\frac{i}{\alpha}\right)^2}\right)$$

which is a line image located in the complex plane at $y = -y' + i/\alpha$. As it is important in the scattering problems, the other asymptotic behavior of interest is the far field approximation where the point of observation is far from the image point, i.e., $\rho_2 = \sqrt{(x-x')^2+(y+y')^2} \gg \lambda_0$. In this condition

$$\sqrt{(x-x')^2+(y+y'+i\nu)^2} \approx \rho_2\left(1+\frac{i\nu\cos\phi_2}{\rho_2}\right)$$

where we have assumed that $\rho_2 \gg \nu$. The validity of this assumption comes from the fact that the integrand of (16) is approximately zero if $\nu > \nu_{\max}$ for some finite $\nu_{\max}$. Now by using the large argument expansion of the Hankel function and then substituting for α we get

$$\lim_{\rho_2\to\infty}\int_0^{+\infty} -\alpha e^{-\alpha\nu} \cdot H_0^{(1)}\left(k_0\sqrt{(x-x')^2+(y+y'+i\nu)^2}\right) d\nu$$

$$\approx \sqrt{\frac{2}{\pi k_0\rho_2}}\, e^{i(k_0\rho_2-\pi/4)}\frac{-1}{1+2R\cos\phi}.$$

Note that the last term in the above equation is the plane wave reflection coefficient for the E-polarization case. This result is identical to the asymptotic value of the integral given by (6) evaluated using the saddle point technique. In applying the saddle point technique the poles associated with the reflection coefficient function ($R_q(\gamma)$) may be captured when the contour is deformed. The contribution of these poles gives rise to surface waves, but their effect can be ignored if the surface is lossy and the observation point is away from the interface. Also, the large-argument expansion of the Hankel function can be used for the distant approximation. Now it can easily be shown that for an electric current distribution $\mathbf{J}_e$, the radiated far field does not have a $\hat{\rho}$ component and the far-field amplitude defined by

$$\mathbf{E} = \sqrt{\frac{2}{\pi k_0\rho}}\, e^{i(k_0\rho-\pi/4)}\mathbf{S}$$

has the following components:

$$S_\phi = \frac{k_0Z_0}{4}\left\{\int_S \cos\phi J_x(x',y') \cdot e^{-ik_0\sin\phi x'}\left[e^{-ik_0\cos\phi y'} - R_H(\phi)e^{ik_0\cos\phi y'}\right]dx'\,dy' - \int_S \sin\phi J_y(x',y') \cdot e^{-ik_0\sin\phi x'}\left[e^{-ik_0\cos\phi y'} + R_H(\phi)e^{ik_0\cos\phi y'}\right]dx'\,dy'\right\} \quad (17)$$

$$S_z = -\frac{k_0Z_0}{4}\int_S J_z(x',y') \cdot e^{-ik_0\sin\phi x'}\left[e^{-ik_0\cos\phi y'} + R_E(\phi)e^{ik_0\cos\phi y'}\right]dx'\,dy'.$$

III. Derivation of Integral Equations

Suppose a dielectric object, possibly inhomogeneous, is located above an impedance surface (resistive sheet) and is illuminated by a plane wave. The direction of propagation of the plane wave is denoted by the angle ϕ_0 measured from the normal to the surface. Therefore the incident wave for E- and H-polarization cases may be represented by

$$\mathbf{E}^i = \hat{z}e^{ik_0(\sin\phi_0 x-\cos\phi_0 y)},$$

$$\mathbf{E}^i = (\cos\phi_0\hat{x}+\sin\phi_0\hat{y})e^{ik_0(\sin\phi_0 x-\cos\phi_0 y)}.$$

The incident field induces conduction and displacement currents in the dielectric object which together are known as the polarization current. The polarization current in terms of the total electric field ($\mathbf{E}^t$) inside the dielectric object is given by

$$\mathbf{J}_e = -ik_0 Y_0(\epsilon(x, y) - 1)\mathbf{E}^t \tag{18}$$

where $\epsilon(x, y)$ represents the relative dielectric constant of the object. The total field is comprised of the incident, reflected, and scattered fields which are, respectively, denoted by $\mathbf{E}^i$, $\mathbf{E}^r$, and $\mathbf{E}^s$, then

$$\mathbf{E}^t = \mathbf{E}^i + \mathbf{E}^r + \mathbf{E}^s. \tag{19}$$

In the E-polarization case where the electric field is perpendicular to the plane of incidence the incident field excites a z-directed polarization current, which leads to a scattered field in the z direction. For the H-polarization case, however, the polarization current and the scattered field are in the transverse plane and therefore the integral equations for E- and H-polarization cases are decoupled. Using (9) for the scattered field and (19) for the total field with (18) the following integral equations for the polarization currents can be derived

$$\begin{aligned} J_z(x, y) = -ik_0 Y_0(\epsilon(x, y) - 1)\Big\{ & e^{ik_0 \sin\phi_0 x} \\ & \cdot \left(e^{-ik_0 \cos\phi_0 y} + R_E(\phi_0) e^{ik_0 \cos\phi_0 y}\right) \\ & + \int\!\!\int_s J_z(x', y') G_{zz}(x, y; x', y')\, dx'\, dy' \Big\}. \end{aligned} \tag{20}$$

$$\begin{aligned} J_x(x, y) = -ik_0 Y_0(\epsilon(x, y) - 1)\Big\{ & \cos\phi_0 e^{ik_0 \sin\phi_0 x} \\ & \cdot \left(e^{-ik_0 \cos\phi_0 y} - R_H(\phi_0) e^{ik_0 \cos\phi_0 y}\right) \\ & + \int\!\!\int_s \left[J_x(x', y') G_{xx}(x, y; x', y') \right. \\ & \left. + J_y(x', y') G_{xy}(x, y; x', y')\right] dx'\, dy' \Big\} \end{aligned} \tag{21}$$

$$\begin{aligned} J_y(x, y) = -ik_0 Y_0(\epsilon(x, y) - 1)\Big\{ & \sin\phi_0 e^{ik_0 \sin\phi_0 x} \\ & \cdot \left(e^{-ik_0 \cos\phi_0 y} + R_H(\phi_0) e^{ik_0 \cos\phi_0 y}\right) \\ & + \int\!\!\int_s \left[J_x(x', y') G_{yx}(x, y; x', y') \right. \\ & \left. + J_y(x', y') G_{yy}(x, y; x', y')\right] dx'\, dy' \Big\}. \end{aligned} \tag{22}$$

IV. The Method of Moments Solution

There is no known exact solution for the integral equations that were developed in the previous section. In this section an approximate numerical solution of these equations is obtained by employing the method of moments.

Let us divide the cross section of the dielectric structure into N sufficiently small rectangular cells such that the dielectric constant and the polarization current can be approximated by constant values over each cell. First consider the integral equation (20), which corresponds to the E-polarization case. Using the point matching technique the integral equation can be cast into a matrix equation of the following form:

$$[\mathcal{Z}][\mathcal{J}] = [\mathcal{V}] \tag{23}$$

where $[\mathcal{Z}]$ is the impedance matrix, $[\mathcal{J}]$ is the unknown vector whose entries are the value of polarization current at the center of each cell, i.e., (x_n, y_n), and finally $[\mathcal{V}]$ is the excitation vector whose entries are given by

$$\begin{aligned} v_n = ik_0 Y_0(\epsilon(x_n, y_n) - 1) & \\ \cdot e^{ik_0 \sin\phi_0 x_n} & \left(e^{-ik_0 \cos\phi_0 y_n} + R_E(\phi_0) e^{ik_0 \cos\phi_0 y_n}\right). \end{aligned}$$

The off-diagonal elements of the impedance matrix can be obtained by approximating the Green's function via its Taylor series expansion around the midpoint of each cell and then performing the integration analytically. This technique allows us to choose very small cell sizes without incurring too much error because of the adjacent cells. For diagonal elements the free space Green's function is approximated by its small argument expansion and then integration is performed analytically over the cell area. This allows us to choose rectangular shape cells instead of squares that are approximated by circles of equal areas in the traditional method [14]. In order to give the expressions for elements of the impedance matrix, let us define the following functions

$$\begin{aligned} U_{mn}^q = & -H_0^{(1)}(k_0 r_{mn}^q) \cos^2\theta_{mn}^q \\ & + \frac{H_1^{(1)}(k_0 r_{mn}^q)}{k_0 r_{mn}^q} \left(\cos^2\theta_{mn}^q - \sin^2\theta_{mn}^q\right) \end{aligned} \tag{24}$$

$$\begin{aligned} V_{mn}^q = & -H_0^{(1)}(k_0 r_{mn}^q) \sin^2\theta_{mn}^q \\ & + \frac{H_1^{(1)}(k_0 r_{mn}^q)}{k_0 r_{mn}^q} \left(\sin^2\theta_{mn}^q - \cos^2\theta_{mn}^q\right) \end{aligned} \tag{25}$$

where r_{mn}^q and θ_{mn}^q are the distance and the angle from the source, its mirror image, and its continuous image points to the observation point which are given by

$$r_{mn}^q = \begin{cases} \sqrt{(x_m - x_n)^2 + (y_m - y_n)^2}, & \text{if } q = s \\ \sqrt{(x_m - x_n)^2 + (y_m + y_n)^2}, & \text{if } q = i \\ \sqrt{(x_m - x_n)^2 + (y_m + y_n + i\nu)^2}, & \text{if } q = c \end{cases}$$

$$\theta_{mn}^q = \begin{cases} \arctan\left(\dfrac{y_m - y_n}{x_m - x_n}\right), & \text{if } q = s \\ \arctan\left(\dfrac{y_m + y_n}{x_m - x_n}\right), & \text{if } q = i \\ \arctan\left(\dfrac{y_m + y_n + i\nu}{x_m - x_n}\right), & \text{if } q = c. \end{cases}$$

The diagonal entries of the impedance matrix for resistive sheet are given by

$$z_{nn} = -1 - \frac{1}{\pi}\left(\epsilon(x_n, y_n) - 1\right)\Bigg\{\frac{k_0^2\,\Delta x_n\,\Delta y_n}{2}\cdot\left[\ln\left(\frac{k_0}{4}\sqrt{\Delta x_n^2 + \Delta y_n^2}\right) + \gamma - \frac{i\pi}{2} - \frac{3}{2}\right] + \left(\frac{k_0\,\Delta x_n}{2}\right)^2 \arctan\left(\frac{\Delta y_n}{\Delta x_n}\right) + \left(\frac{k_0\,\Delta y_n}{2}\right)^2\left(\frac{\pi}{2} - \arctan\left(\frac{\Delta y_n}{\Delta x_n}\right)\right)\Bigg\} - \frac{ik_0^2\,\Delta x_n\,\Delta y_n}{4}\left(\epsilon(x_n, y_n) - 1\right)\alpha\cdot\int_0^{\infty} e^{-\alpha\nu} H_0^{(1)}(k_0 r_{nn}^c)\,d\nu \tag{26}$$

and the nondiagonal entries are expressed by

$$z_{mn} = \frac{ik_0^2\,\Delta x_n\,\Delta y_n}{4}\left(\epsilon(x_m, y_m) - 1\right)\Bigg\{H_0^{(1)}(k_0 r_{mn}^s) + \frac{(k_0\,\Delta x_n)^2}{24}U_{mn}^s + \frac{(k_0\,\Delta y_n)^2}{24}V_{mn}^s - \alpha\int_0^{\infty} e^{-\alpha\nu} H_0^{(1)}(k_0 r_{mn}^c)\,d\nu\Bigg\}. \tag{27}$$

Here, Δx_n and Δy_n are the dimensions of the nth rectangular cell and $\gamma = 0.57721$ is Euler's constant. The entries of the impedance matrix for the impedance surface can also be obtained in asimilar fashion by adding the mirror contribution, replacing α with α' and doubling the integrals in (26) and (27).

The integrals in (26) and (27) are evaluated numerically using the Gauss-Legendre quadrature technique [15]. It should be mentioned here that when the observation and source points are both close to the surface ($k_0(y_m + y_n) \ll 1$) for some value of $\nu = \nu_0$, the distance function $r_0 = \sqrt{(x_m - x_n)^2 + (y_m + y_n + i\nu_0)^2}$ becomes very small. Consequently the integrand of the integral representing the image contribution varies very rapidly around this point. In order to evaluate the integral accurately, the contribution of the integrand around ν_0 should be evaluated analytically. The integrand achieves its maximum when the absolute value of the distance function is minimum. This minimum occurs at

$$\nu_0 = \sqrt{(x_m - x_n)^2 - (y_m + y_n)^2}. \tag{28}$$

If the argument of the square root in (28) is negative, then the distance function takes its minimum at $\nu_0 = 0$. Fig. 3 shows the integrand function in (27) when both observation and source points are very close to the surface. The analytical evaluation of the integral around the point ν_0 can be performed by using the small argument expansion of the Hankel function, i.e.,

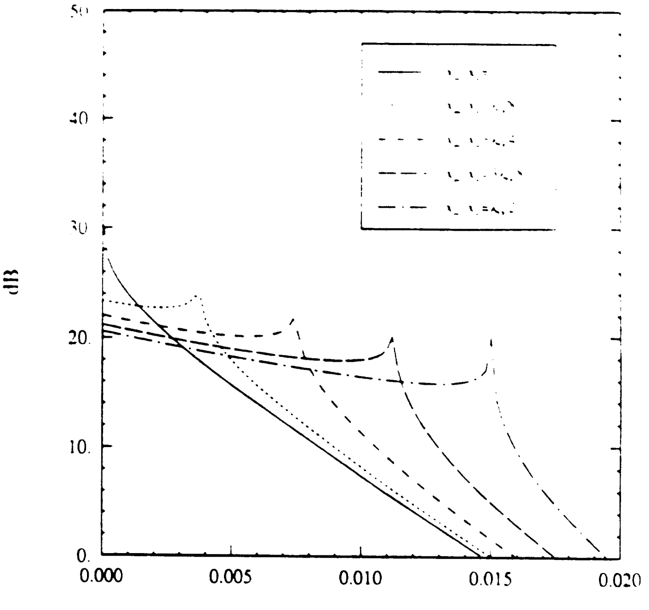

Fig. 34. The absolute value of the integrand function in (30) for $R = 0.18 + i0.37$ at 10 GHz, $y_m + y_n = 6 \times 10^{-5}\,\lambda_0$, and five values of $x_m - x_n$.

$$\int_{\nu_0 - \Delta\nu}^{\nu_0 + \Delta\nu} e^{-\alpha\nu} H_0^{(1)}(k_0 r_{mn}^c)\,d\nu = e^{-\alpha\nu_0}\left[2\,\Delta\nu\left(1 + \frac{i2\gamma}{\pi}\right) + \frac{i2}{\pi}I_1\right]$$

where

$$I_1 = \frac{i}{2}(y_m + y_n + i\nu_0)\cdot\ln\frac{r_0^2 - \Delta\nu^2 - i2\,\Delta\nu(y_m + y_n + i\nu_0)}{r_0^2 - \Delta\nu^2 + i2\,\Delta\nu(y_m + y_n + i\nu_0)} + \frac{x_m - x_n}{2}\ln\frac{r_0^2 + \Delta\nu^2 + 2\,\Delta\nu(x_m - x_n)}{r_0^2 + \Delta\nu^2 - 2\,\Delta\nu(x_m - x_n)} - \Delta\nu\left[2 - \ln\frac{k_0^2}{4}\cdot\sqrt{(r_0^2 - \Delta\nu^2)^2 + 4\Delta\nu^2(y_m + y_n + i\nu_0)^2}\right].$$

For self-cell (diagonal element) calculation we note that $x_m = x_n$, which renders $\nu_0 = 0$ and

$$\int_0^{\Delta\nu} e^{-\alpha\nu} H_0^{(1)}(k_0 r_{mn}^c)\,d\nu = \Delta\nu\left(1 + \frac{i2\gamma}{\pi}\right) + \frac{2}{\pi}I_1'$$

where

$$I_1' = (y_m + y_n)\ln\frac{y_m + y_n + i\,\Delta\nu}{y_m + y_n} + i\,\Delta\nu\left[\ln\frac{k_0(y_m + y_n + i\,\Delta\nu)}{2} - 1\right].$$

In the H-polarization case, using the same partitioning of the cross section of the dielectric body, the coupled integral equations (21) and (22) can be cast into a matrix equation similar to (23) where

$$[\mathcal{J}] = \begin{bmatrix} \mathcal{J}_x \\ \mathcal{J}_y \end{bmatrix}, \quad [\mathcal{Z}] = \begin{bmatrix} \mathcal{Z}_1 & \mathcal{Z}_2 \\ \mathcal{Z}_3 & \mathcal{Z}_4 \end{bmatrix}, \quad \text{and}$$

$$[\mathcal{V}] = \begin{bmatrix} \mathcal{V}_x \\ \mathcal{V}_y \end{bmatrix}.$$

The elements of the excitation vector are given by ($n = 1, \cdots, N$)

$$v_n = ik_0 Y_0(\epsilon(x_n, y_n) - 1)\cos\phi_0 \cdot e^{ik_0 \sin\phi_0 x_n}\left(e^{-ik_0\cos\phi_0 y_n} - R_H(\phi_0) e^{ik_0 \cos\phi_0 y_n}\right)$$

$$v_{n+N} = ik_0 Y_0(\epsilon(x_n, y_n) - 1)\sin\phi_0 \cdot e^{ik_0 \sin\phi_0 x_n}\left(e^{-ik_0\cos\phi_0 y_n} + R_H(\phi_0) e^{ik_0 \cos\phi_0 z_m}\right).$$

Here again the entries of the impedance matrix are obtained by expansion of the Green's function over each cell as explained in the E-polarization case. Since the Green's function has a higher degree of singularity in this case, these expansions are even more important to use in order to avoid anomalous errors.

For the resistive sheet the nondiagonal elements of the impedance matrix are given by

$$z_{1mn} = \frac{ik_0^2 \Delta x_n \Delta y_n}{4}(\epsilon(x_m, y_m) - 1) \cdot \left\{A_{mn}^s - A_{mn}^i + \beta\int_0^\infty e^{-\beta\nu} A_{mn}^c \, d\nu\right\} \tag{29}$$

$$z_{2mn} = \frac{ik_0^2 \Delta x_n \Delta y_n}{4}(\epsilon(x_m, y_m) - 1) \cdot \left\{B_{mn}^s + B_{mn}^i - \beta\int_0^\infty e^{-\beta\nu} B_{mn}^c \, d\nu\right\} \tag{30}$$

$$z_{3mn} = \frac{ik_0^2 \Delta x_n \Delta y_n}{4}(\epsilon(x_m, y_m) - 1) \cdot \left\{B_{mn}^s - B_{mn}^i + \beta\int_0^\infty e^{-\beta\nu} B_{mn}^c \, d\nu\right\} \tag{31}$$

$$z_{4mn} = \frac{ik_0^2 \Delta x_n \Delta y_n}{4}(\epsilon(x_m, y_m) - 1) \cdot \left\{C_{mn}^s + C_{mn}^i - \beta\int_0^\infty e^{-\beta\nu} C_{mn}^c \, d\nu\right\} \tag{32}$$

where A_{mn}^q, B_{mn}^q, and C_{mn}^q are given in the Appendix. Noting that $\cos\theta_{nn}^i = \cos\theta_{nn}^c = 0$ and $\sin\theta_{nn}^i = \sin\theta_{nn}^c = 1$, the diagonal elements are of the following form:

$$z_{1nn} = -1 - \frac{1}{\pi}(\epsilon(x_n, y_n) - 1)\left\{\frac{k_0^2 \Delta x_n \Delta y_n}{4} \cdot \left[\ln\left(\frac{k_0}{4}\sqrt{\Delta x_n^2 + \Delta y_n^2}\right) + \gamma - \frac{i\pi}{2} - \frac{3}{2}\right] + 2\arctan\left(\frac{\Delta y_n}{\Delta x_n}\right) + \left(\frac{k_0 \Delta y_n}{2}\right)^2 \cdot \left(\frac{\pi}{2} - \arctan\left(\frac{\Delta y_n}{\Delta x_n}\right)\right)\right\}$$
$$+ \frac{ik_0^2 \Delta x_n \Delta y_n}{4}(\epsilon(x_n, y_n) - 1) \cdot \left\{-A_{nn}^i + \beta\int_0^\infty e^{-\beta\nu} A_{nn}^c \, d\nu\right\}. \tag{33}$$

$$z_{2nn} = z_{3nn} = 0 \tag{34}$$

$$z_{4nn} = -1 - \frac{1}{\pi}(\epsilon(x_n, y_n) - 1)\left\{\frac{k_0^2 \Delta x_n \Delta y_n}{4} \cdot \left[\ln\left(\frac{k_0}{4}\sqrt{\Delta x_n^2 + \Delta y_n^2}\right) + \gamma - \frac{i\pi}{2} - \frac{3}{2}\right] + 2\left(\frac{\pi}{2} - \arctan\left(\frac{\Delta y_n}{\Delta x_n}\right)\right) + \left(\frac{k_0 \Delta x_n}{2}\right)^2 \arctan\left(\frac{\Delta y_n}{\Delta x_n}\right)\right\}$$
$$+ \frac{ik_0^2 \Delta x_n \Delta y_n}{4}(\epsilon(x_n, y_n) - 1) \cdot \left\{C_{nn}^i - \beta\int_0^\infty e^{-\beta\nu} C_{nn}^c \, d\nu\right\}. \tag{35}$$

Upon comparing (13) and (15) the expressions for the elements of the impedance matrix for the impedance surface can be obtained by doubling the integral expressions, and replacing β by β' in (29)-(35).

The distance function in the integrand of all the integrals in the elements of the impedance matrix assumes a very small number when the observation and source points are both close to the surface of the resistive sheet. Since the singularity of the integrands in this case are much higher than the E polarization case, analytical evaluation of the integrals around the point ν_0 is even more critical. Fig. 4 shows the variation of the integrand as a function of ν for some typical values of source and observation points, and also compares the integrand with its approximation. It should be noted here that the phase of the integrand varies very rapidly around ν_0 resulting in a faster variation of the integrand than what is shown in Fig. 4. If the integral in (29) around the $\Delta\nu$ neighborhood of ν_0 is denoted by S_1 then

$$S_1 = e^{-\beta\nu_0}\left\{H_0^{(1)}(k_0 r_0)(y_m + y_n + i\nu_0)^2 - \left[\left(\frac{i}{2\pi} - \frac{i\gamma}{\pi} - \frac{1}{2}\right) - \frac{i}{\pi}\ln\frac{k_0 r_0}{2}\right] \cdot \left[(x_m - x_n)^2 - (y_m + y_n + i\nu_0)^2\right]\right\} I_2$$
$$- e^{-\beta\nu_0}\frac{2i}{\pi k_0^2}\left[(x_m - x_n)^2 - (y_m + y_n + i\nu_0)^2\right] I_3$$

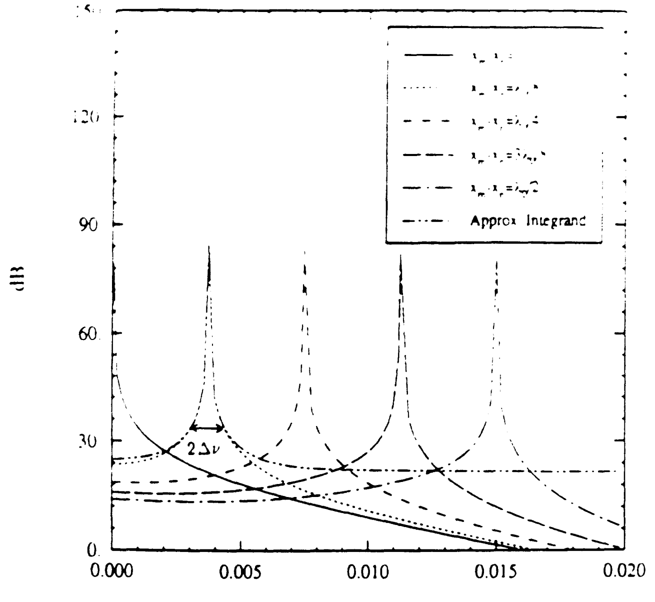

Fig. 4. The absolute value of the integrand function in (38) and its approximation for $R = 0.18 + i0.37$ at 10 GHz, $y_m + y_n = 6 \times 10^{-5}\,\lambda_0$, and five values of $x_m - x_n$.

where

$$I_2 = \frac{1}{2(x_m - x_n)} \ln \frac{r_0^2 + \Delta\nu^2 + 2(x_m - x_n)\,\Delta\nu}{r_0^2 + \Delta\nu^2 - 2(x_m - x_n)\,\Delta\nu},$$

$$I_3 = \frac{\Delta\nu}{(x_m - x_n)^2} \cdot \frac{r_0^2 - \Delta\nu^2 - 2(y_m + y_n + i\nu_0)^2}{(r_0^2 - \Delta\nu^2)^2 + 4\Delta\nu^2(y_m + y_n + i\Delta\nu_0)^2} + \frac{1}{4(x_m - x_n)^3} \ln \frac{r_0^2 + \Delta\nu^2 + 2(x_m - x_n)\,\Delta\nu}{r_0^2 + \Delta\nu^2 - 2(x_m - x_n)\,\Delta\nu}.$$

In evaluation of the diagonal elements, we set $x_m = x_n$, which leads to $\nu_0 = 0$ and the integral in (33) is approximated by

$$S_1' = \frac{i2}{\pi k_0^2} I_3' + \frac{i}{\pi} I_2' + \left(\frac{i}{2\pi} + \frac{i\gamma}{\pi} - \frac{1}{2} \right) \Delta\nu,$$

where

$$I_2' = -i\left[(y_m + y_n) \ln \frac{y_m + y_n + i\,\Delta\nu}{y_m + y_n} + i\,\Delta\nu \ln \frac{k_0(y_m + y_n + i\,\Delta\nu)}{2} - i\,\Delta\nu \right]$$

$$I_3' = \frac{\Delta\nu}{(y_m + y_n)(y_m + y_n + i\,\Delta\nu)}.$$

To extract the contribution of the integrand in (30) around ν_0 we use similar approximations as in (29). If this integral is denoted by S_2, then

$$S_2 = e^{-\beta\nu_0}(x_m - x_n)(y_m + y_n + i\nu_0) \cdot \left\{ \left[H_0^{(1)}(k_0 r_0) + \left(\frac{i}{\pi} - \frac{i2\gamma}{\pi} - 1 \right) - \frac{i2}{\pi} \ln \frac{k_0 r_0}{2} \right] I_2 + \frac{4i}{\pi k_0^2} I_3 \right\}.$$

The integral in (31) around the point ν_0 is approximated by S_3 where $S_3 = S_2$, and similarly for the integral in (32) if S_4 represents the integral around ν_0 then

$$S_4 = e^{-\beta\nu_0}\left\{ H_0^{(1)}(k_0 r_0)(x_m - x_n)^2 + \left[\left(\frac{i}{2\pi} - \frac{i\gamma}{\pi} - \frac{1}{2} \right) - \frac{i}{\pi} \ln \frac{k_0 r_0}{2} \right] \cdot \left[(x_m - x_n)^2 - (y_m + y_n + i\nu_0)^2 \right] \right\} I_2 + e^{-\beta\nu_0} \frac{2i}{\pi k_0^2} \left[(x_m - x_n)^2 - (y_m + y_n + i\nu_0)^2 \right] I_3.$$

When $x_m = x_n$, then $\nu_0 = 0$ and this integral is represented by

$$S_4' = -\frac{i2}{\pi k_0^2} I_3' + \frac{i}{\pi} I_2' - \left(\frac{i}{2\pi} - \frac{i\gamma}{\pi} - \frac{1}{2} \right) \Delta\nu.$$

Once the system of linear equations for the polarization current has been solved the scattered field from the dielectric structure at any point in the upper half-space can be obtained by means of (17) for both E- and H-polarization cases.

V. NUMERICAL RESULTS

In this section the results based on the numerical solution are presented. As a verification of the numerical code we first compare the numerical solution of scattering echo width of a dielectric hump over a resistive sheet with a perturbation solution of the problem [16]. Consider a homogeneous dielectric hump with dielectric constant $\epsilon = 36 + i17$ over a resistive sheet with resistivity $R = 0.18 + i0.37$. Suppose the functional form of the hump is given by

$$y = \frac{w^2}{x^2 + w^2} \Delta$$

and that the hump is illuminated by a plane wave at 10 GHz ($\lambda_0 = 3$ cm). Figs. 5–8 show the bistatic echo width and the phase of the far-field amplitude of the hump for $\Delta = 3\lambda_0/1000$, $w = \lambda_0/15$, and $w = \lambda_0/25$ at incidence angles $\phi_0 = 0°$ and $\phi_0 = 45°$ for both polarizations. In each figure the results based on the perturbation technique are compared with the numerical results. The agreement is very good in spite of the fact that the perturbation solution is only a first order one. For thicker dielectric humps (larger Δ) the perturbation technique cannot be used and the moment method is the only available method of solution.

With confidence in the numerical code we now consider

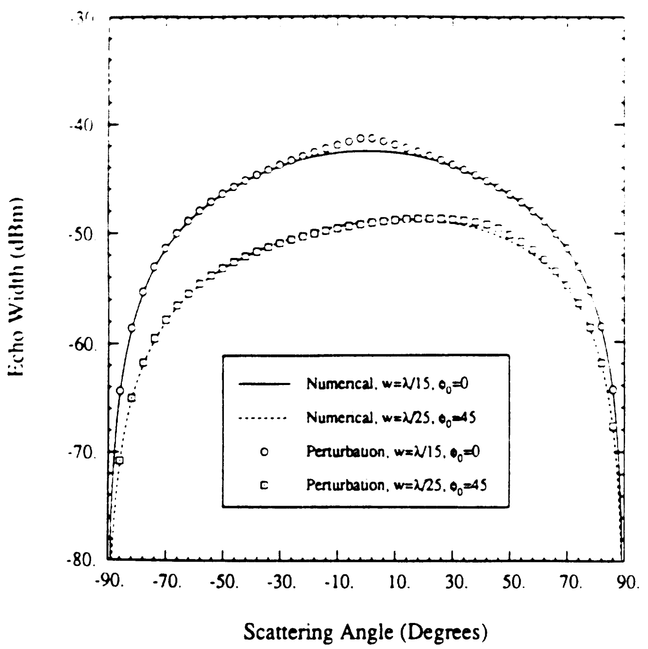

Fig. 5. Bistatic echo width of a dielectric hump with $\epsilon = 36 + i17$, and $\Delta = 3\lambda_0/1000$ over a resistive sheet with $R = 0.18 + i0.37$ at $f = 10$ GHz for E-polarization.

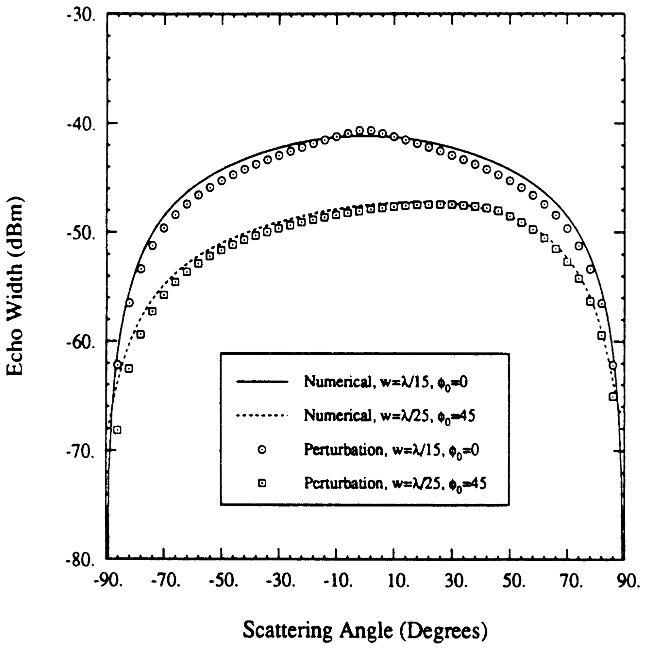

Fig. 6. Bistatic echo width of a dielectric hump with $\epsilon = 36 + i17$, and $\Delta = 3\lambda_0/1000$ over a resistive sheet with $R = 0.18 + i0.37$ at $f = 10$ GHz for H-polarization.

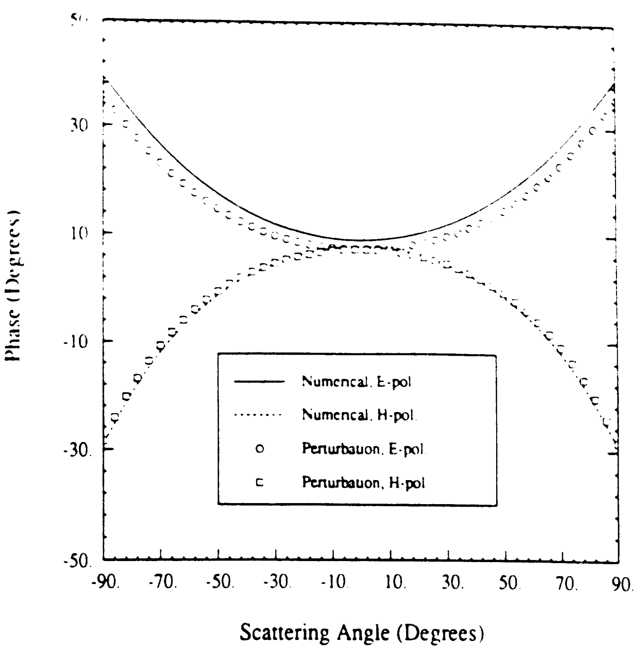

Fig. 7. Phase of far-field amplitude of a dielectric hump with $\epsilon = 36 + i17$, and $\Delta = 3\lambda_0/1000$ over a resistive sheet with $R = 0.18 + i0.37$ at $f = 10$ GHz and $\phi_0 = 0$ for E- and H-polarization.

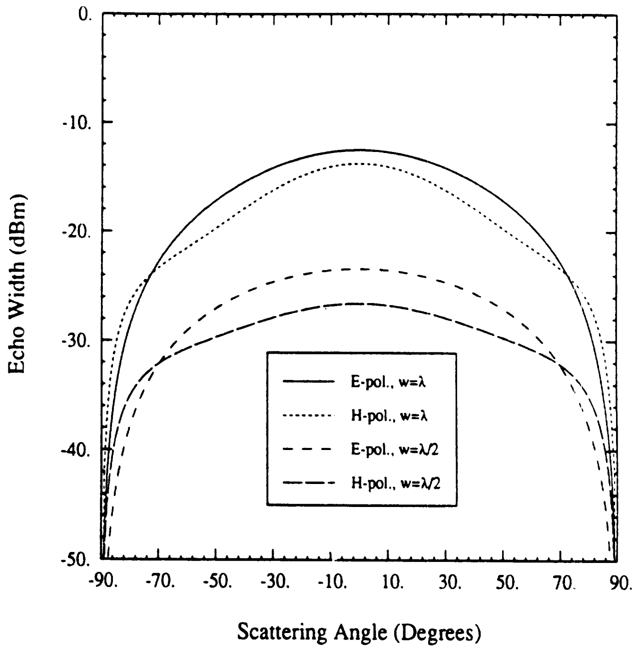

Fig. 8. Bistatic echo width of triangular humps with $\epsilon = 3 + i1$, over an impedance surface with $\eta = 0.21 - i0.04$ at $f = 10$ GHz for E- and H-polarization.

several examples with impedance surfaces. In all of the following examples the impedance of the surface is taken to be $\eta = 0.21 - i.04$ and the dielectric hump is assumed to be an isosceles triangle with base w and altitude $w/4$. The triangular humps are also considered to be homogeneous with $\epsilon = 3 + i1$ placed over the impedance surface. Figs. 8 and 9, respectively, show the bistatic echo width and phase of the far-field amplitude for two different sizes of triangular humps at normal incidence ($\phi_0 = 0°$) and $\lambda = 3$ cm. The angular dependency of the backscattering echo width of the same humps is shown in Fig. 10.

VI. CONCLUSION

An efficient numerical technique has been developed to compute the scattering behavior of inhomogeneous dielectric cylinders of arbitrary cross section above impedance surfaces and resistive sheets. The efficiency of this method is accomplished by deriving new expressions for the Green's function of the problem. Using an appropriate integral transformation the ordinary integral representation of the Green's function containing a highly oscillatory integrand was transformed into a new integral form that is rapidly convergent. Useful asymptotic expressions of the Green's function were also derived. Analytical treatment for singular behavior of Green's

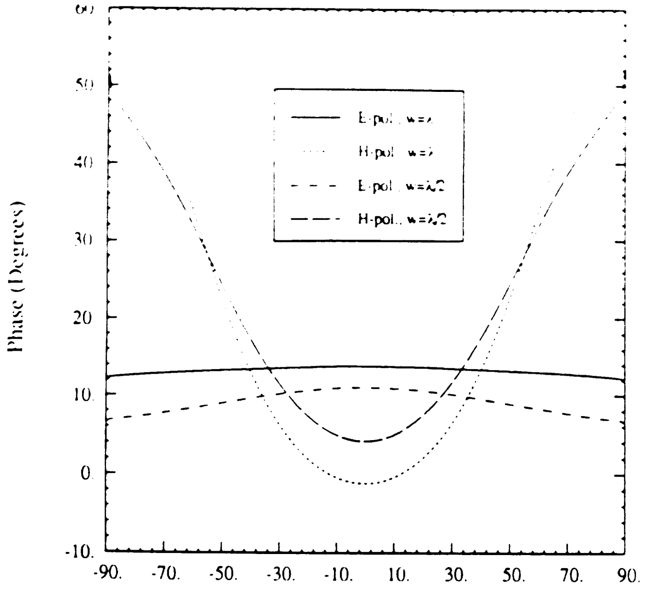

Fig. 9. Phase of far-field amplitude of triangular humps with $\epsilon = 3 + i1$, over an impedance surface with $\eta = 0.21 - i0.04$ at $f = 10$ GHz and $\phi_0 = 0$ for E- and H-polarization.

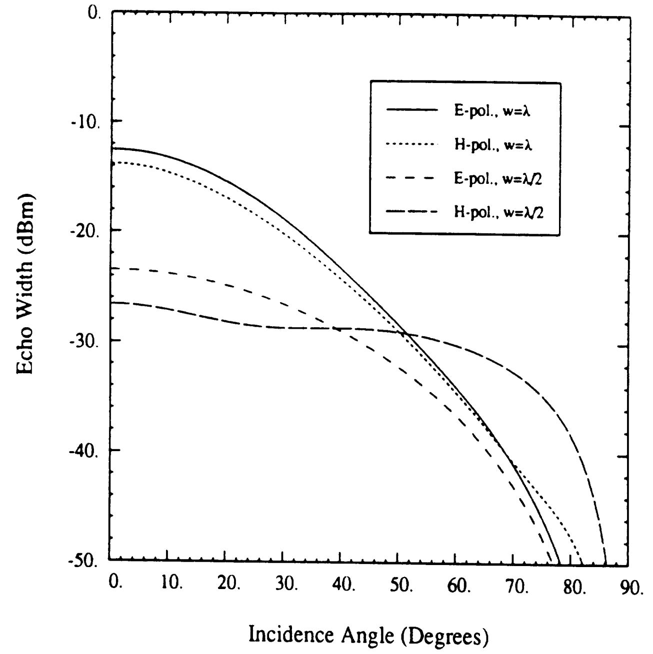

Fig. 10. Backscattering echo width of triangular humps with $\epsilon = 3 + i1$, over an impedance surface with $\eta = 0.21 - i0.04$ at $f = 10$ GHz for E- and H-polarization.

function when both the source and the observation points are close to the surface is given.

Several numerical examples are presented for resistive sheet and impedance surface problems. The accuracy of the numerical code is checked by comparing the numerical solution of scattering from a very thin dielectric hump above a resistive sheet with a perturbation method. Excellent agreement is obtained in all test cases.

APPENDIX

The following functions are defined to simplify the expressions for the elements of the impedance matrix in the H-polarization case

$$A_{mn}^q = H_0^{(1)}(k_0 r_{mn}^q)\sin^2\theta_{mn}^q + \frac{H_1^{(1)}(k_0 r_{mn}^q)}{(k_0 r_{mn}^q)} \cdot (2\cos^2\theta_{mn}^q - 1) + \frac{(\Delta x_n)^2}{24}\left(\frac{\partial^2}{\partial x^2} + k_0^2\right)U_{mn}^q + \frac{(\Delta y_n)^2}{24}\left(\frac{\partial^2}{\partial x^2} + k_0^2\right)V_{mn}^q$$

$$B_{mn}^q = -H_0^{(1)}(k_0 r_{mn}^q) + \frac{2H_1^{(1)}(k_0 r_{mn}^q)}{(k_0 r_{mn}^q)}\cos\theta_{mn}^q \sin\theta_{mn}^q + \frac{(\Delta x_n)^2}{24}\frac{\partial^2}{\partial x\,\partial y}U_{mn}^q + \frac{(\Delta y_n)^2}{24}\frac{\partial^2}{\partial x\,\partial y}V_{mn}^q$$

$$C_{mn}^q = H_0^{(1)}(k_0 r_{mn}^q)\cos^2\theta_{mn}^q + \frac{H_1^{(1)}(k_0 r_{mn}^q)}{(k_0 r_{mn}^s)} \cdot (2\sin^2\theta_{mn}^q - 1) + \frac{(\Delta x_n)^2}{24}\left(\frac{\partial^2}{\partial y^2} + k_0^2\right)U_{mn}^q + \frac{(\Delta y_n)^2}{24}\left(\frac{\partial^2}{\partial y^2} + k_0^2\right)V_{mn}^q$$

where the derivatives of the functions defined by (24) and (25) are given by

$$\frac{\partial^2}{\partial x^2}U_{mn}^q = k_0^2\left\{H_0^{(1)}(k_0 r_{mn}^q)\left[\cos^2\theta_{mn}^q\left(\frac{1}{4}\cos^2\theta_{mn}^q + \frac{1}{8}\right) + \frac{2\sin^2\theta_{mn}^q}{(k_0 r_{mn}^q)^2}(4\cos^2\theta_{mn}^q - 1)\right] + H_1^{(1)}(k_0 r_{mn}^q)\left[\frac{5}{k_0 r_{mn}^q}\cos^2\theta_{mn}^q \sin^2\theta_{mn}^q - \frac{4\sin^2\theta_{mn}^q}{(k_0 r_{mn}^q)^3}(4\cos^2\theta_{mn}^q - 1)\right] + H_2^{(1)}(k_0 r_{mn}^q)\left[-\frac{1}{2}\cos^4\theta_{mn}^q + \frac{\sin^2\theta_{mn}^q}{(k_0 r_{mn}^q)^2}(-10\cos^2\theta_{mn}^q + 1)\right] + H_4^{(1)}(k_0 r_{mn}^q)\left[\frac{1}{8}\cos^2\theta_{mn}^q(2\cos^2\theta_{mn}^q - 1)\right]\right\}$$

$$\frac{\partial^2}{\partial y^2}U_{mn}^q = k_0^2\left\{H_0^{(1)}(k_0 r_{mn}^q)\left[\sin^2\theta_{mn}^q\left(\frac{1}{4}\cos^2\theta_{mn}^q + \frac{1}{8}\right) + \frac{2\cos^2\theta_{mn}^q}{(k_0 r_{mn}^q)^2}(1 - 4\sin^2\theta_{mn}^q)\right] + H_1^{(1)}(k_0 r_{mn}^q)\left[-\frac{4}{k_0 r_{mn}^q}\cos^2\theta_{mn}^q \sin^2\theta_{mn}^q\right.\right.$$

$$
\begin{aligned}
&+\frac{4\cos^2\theta^q_{mn}}{(k_0r^q_{mn})^3}(4\sin^2\theta^q_{mn}-1)\Bigg]\\
&+H^{(1)}_2(k_0r^q_{mn})\Bigg[-\frac{1}{2}\sin^2\theta^q_{mn}\cos^2\theta^q_{mn}\\
&+\frac{\cos^2\theta^q_{mn}}{(k_0r^q_{mn})^2}(10\sin^2\theta^q_{mn}-1)\Bigg]\\
&+H^{(1)}_4(k_0r^q_{mn})\left[\frac{1}{8}\sin^2\theta^q_{mn}(2\cos^2\theta^q_{mn}-1)\right]\Bigg\}
\end{aligned}
$$

$$
\begin{aligned}
\frac{\partial^2}{\partial x\,\partial y}U^q_{mn} &= k_0^2\sin\theta^q_{mn}\cos\theta^q_{mn}\\
&\cdot\Bigg\{H^{(1)}_0(k_0r^q_{mn})\Bigg[\frac{1}{4}\cos^2\theta^q_{mn}+\frac{1}{8}\\
&+\frac{4}{(k_0r^q_{mn})^2}(2\sin^2\theta^q_{mn}-1)\Bigg]\\
&+H^{(1)}_1(k_0r^q_{mn})\Bigg[\frac{1}{k_0r^q_{mn}}(2-5\cos^2\theta^q_{mn})\\
&+\frac{8}{(k_0r^q_{mn})^3}(2\cos^2\theta^q_{mn}-1)\Bigg]\\
&+H^{(1)}_2(k_0r^q_{mn})\Bigg[-\frac{1}{2}\cos^2\theta^q_{mn}\\
&+\frac{5}{(k_0r^q_{mn})^2}(2\cos^2\theta^q_{mn}-1)\Bigg]\\
&+H^{(1)}_4(k_0r^q_{mn})\left[\frac{1}{8}(2\cos^2\theta^q_{mn}-1)\right]\Bigg\}
\end{aligned}
$$

$$
\begin{aligned}
\frac{\partial^2}{\partial x^2}V^q_{mn} &= k_0^2\Bigg\{H^{(1)}_0(k_0r^q_{mn})\Bigg[\cos^2\theta^q_{mn}\left(\frac{1}{4}\sin^2\theta^q_{mn}+\frac{1}{8}\right)\\
&+\frac{2\sin^2\theta^q_{mn}}{(k_0r^q_{mn})^2}(1-4\cos^2\theta^q_{mn})\Bigg]\\
&+H^{(1)}_1(k_0r^q_{mn})\Bigg[\frac{\sin^2\theta^q_{mn}}{k_0r^q_{mn}}(-5\cos^2\theta^q_{mn}+1)\\
&+\frac{4\sin^2\theta^q_{mn}}{(k_0r^q_{mn})^3}(4\cos^2\theta^q_{mn}-1)\Bigg]\\
&+H^{(1)}_2(k_0r^q_{mn})\Bigg[-\frac{1}{2}\sin^2\theta^q_{mn}\cos^2\theta^q_{mn}\\
&+\frac{\sin^2\theta^q_{mn}}{(k_0r^q_{mn})^2}(10\cos^2\theta^q_{mn}-1)\Bigg]\\
&+H^{(1)}_4(k_0r^q_{mn})\left[\frac{1}{8}\cos^2\theta^q_{mn}(2\sin^2\theta^q_{mn}-1)\right]\Bigg\}
\end{aligned}
$$

$$
\begin{aligned}
\frac{\partial^2}{\partial y^2}V^q_{mn} &= k_0^2\Bigg\{H^{(1)}_0(k_0r^q_{mn})\Bigg[\sin^2\theta^q_{mn}\left(\frac{1}{4}\sin^2\theta^q_{mn}+\frac{1}{8}\right)\\
&+\frac{2\cos^2\theta^q_{mn}}{(k_0r^q_{mn})^2}(4\sin^2\theta^q_{mn}-1)\Bigg]\\
&+H^{(1)}_1(k_0r^q_{mn})\Bigg[\frac{5}{k_0r^q_{mn}}\sin^2\theta^q_{mn}\cos^2\theta^q_{mn}\\
&-\frac{4\cos^2\theta^q_{mn}}{(k_0r^q_{mn})^3}(4\sin^2\theta^q_{mn}-1)\Bigg]\\
&+H^{(1)}_2(k_0r^q_{mn})\Bigg[-\frac{1}{2}\sin^4\theta^q_{mn}\\
&-\frac{\cos^2\theta^q_{mn}}{(k_0r^q_{mn})^2}(10\sin^2\theta^q_{mn}-1)\Bigg]\\
&+H^{(1)}_4(k_0r^q_{mn})\left[\frac{1}{8}\sin^2\theta^q_{mn}(2\sin^2\theta^q_{mn}-1)\right]\Bigg\}
\end{aligned}
$$

$$
\begin{aligned}
\frac{\partial^2}{\partial x\,\partial y}V^q_{mn} &= k_0^2\sin\theta^q_{mn}\cos\theta^q_{mn}\\
&\cdot\Bigg\{H^{(1)}_0(k_0r^q_{mn})\Bigg[\frac{1}{4}\sin^2\theta^q_{mn}+\frac{1}{8}\\
&+\frac{4}{(k_0r^q_{mn})^2}(2\cos^2\theta^q_{mn}-1)\Bigg]\\
&+H^{(1)}_1(k_0r^q_{mn})\Bigg[\frac{1}{k_0r^q_{mn}}(2-5\sin^2\theta^q_{mn})\\
&+\frac{8}{(k_0r^q_{mn})^3}(2\sin^2\theta^q_{mn}-1)\Bigg]\\
&+H^{(1)}_2(k_0r^q_{mn})\Bigg[-\frac{1}{2}\sin^2\theta^q_{mn}\\
&+\frac{5}{(k_0r^q_{mn})^2}(2\sin^2\theta^q_{mn}-1)\Bigg]\\
&+H^{(1)}_4(k_0r^q_{mn})\left[\frac{1}{8}(2\sin^2\theta^q_{mn}-1)\right]\Bigg\}
\end{aligned}
$$

REFERENCES

[1] F. T. Ulaby, R. K. Moore, and A. K. Fung, *Microwave Remote Sensing: Active and Passive, Vol. II—Radar Remote Sensing and Surface Scattering and Emission Theory.* Norwood, MA: Artech House, 1986.

[2] K. Sarabandi, Y. Oh, F. T. Ulaby, "Polarimetric radar measurement of bare soil surfaces at microwave frequencies," in *Proc. IEEE Geosci. Remote Sensing Symp.*, Espoo, June 1991, pp. 387-390.

[3] J. A. Stratton, *Electromagnetic Theory.* New York: McGraw-Hill, 1941.

[4] Y. Rahmat-Samii, R. Mittra, and P. Parhami, "Evaluation of Sommerfeld integrals for lossy half-space problems," *Electromagn.*, vol. 1, no. 1, pp. 1-28, 1981.

[5] P. Parhami, Y. Rahmat-Samii, and R. Mittra, "An efficient approach for evaluating Sommerfeld integrals encountered in the problem of a current element radiating over lossy ground," *IEEE Trans. Antennas Propagat.*, vol. AP-28, pp. 100-104, 1980.

[6] J. S. Izadian, L. Peters, and J. H. Richmond, "Computation of scattering from penetrable cylinders with improved numerical efficiency," *IEEE Trans. Geosci. Remote Sensing*, vol. GE-22, pp. 52-61, 1984.

[7] J. R. Parry and S. H. Ward, "Electromagnetic scattering from cylinders of arbitrary cross section in a conducting half-space," *Geophys.*, vol. 36, no. 1, pp. 67-100, 1971.

[8] I. V. Lindell and E. Alanen, "Exact image theory for the Sommerfeld half-space problem, Part III: General formulation," *IEEE Trans. Antennas Propagat.*, vol. AP-32, pp. 1027-1032, 1984.

[9] I. V. Lindell, A. H. Sihvola, K. O. Muinonen, and P. W. Barber, "Scattering by a small object close to an interface, I: Exact image theory formulation," *JOSA*, no. A 8, pp. 472-476, 1991.

[10] I. V. Lindell, K. I. Nikoskinen, E. Alanen, A. T. Hujanen, "Scalar Green's function method for microstrip antenna analysis based on the exact image theory," *Ann. Telecommun.*, vol. 44, pp. 533-542, 1989.

[11] L. B. Felson and N. Marcuvitz, *Radiation and Scattering of Waves*. Englewood Cliffs, NJ: Prentice-Hall, 1973.

[12] G. Tyras, *Radiation and Propagation of Electromagnetic Waves*. New York: Academic, 1965.

[13] T. B. A. Senior, K. Sarabandi, and F. T. Ulaby, "Measuring and modeling the backscattering cross section of a leaf," *Radio Sci.*, vol. 22, pp. 1109-1116, 1987.

[14] J. H. Richmond, "Scattering by a dielectric cylinder of arbitrary cross section shape," *IEEE Trans. Antennas Propagat.*, vol. AP-13, pp. 334-341, May 1965.

[15] D. C. Handscomb, *Method of Numerical Approximations*. New York: Pergamon, 1966.

[16] K. Sarabandi, "Scattering from variable resistive and impedance sheets," *J. Electromagn. Waves Appl.*, vol. 4, no. 9, pp. 865-891, 1990.

Kamal Sarabandi, for a photograph and biography please see page 1110 of the July 1990 issue of this TRANSACTIONS.

AN IMPROVED NUMERICAL SIMULATION OF ELECTROMAGNETIC SCATTERING FROM PERFECTLY CONDUCTING RANDOM SURFACES

Yisok Oh* and Kamal Sarabandi**

* Department of Radio Science and Engineering
Hong-Ik University, Seoul, Korea
(He was in the University of Michigan, USA)

** Radiation Laboratory
Department of Electrical Engineering and Computer Science
The University of Michigan, Ann Arbor, MI 48109-2122

Abstract-

A Monte-Carlo simulation of electromagnetic scattering from one-dimensional perfectly conducting random surfaces is considered in this paper. Surface profiles of desired statistics are generated numerically using a standard procedure[1,2] and then the scattering solution for the surface samples of finite length is calculated using the method of moments. A new technique is used to reduce the effect of the edges of the finite surface samples. In this technique the conductivity of the surface near edges are controlled by adding an appropriate tapered resistive sheet. It is shown that the accuracy at large angles of incidence($\theta > 50^{o}$) and the computation efficiency are improved significantly using this method when compared to the standard tapered illumination method. Results based on this numerical approach are compared with those based on the small perturbation and physical optics approximations in their respective regions of validity.

1. Introduction

Numerical simulation of electromagnetic scattering from a one-dimensional perfectly conducting random surface is of interest [1-7], for its application as a benchmark in evaluating approximate theoretical models and a complementary solution to the theoretical models when they fail. Although numerical solutions for scattering problems are considered to be "exact", their accuracy becomes limited when applied to rough surfaces. Rough surfaces are targets of infinite extent, hence approximations to the geometry or the formulation of the problem must be considered to make the numerical solution tractable. The standard method to suppress the effect of the edges of a finite surface sample is the tapered illumination approximation. In this approach, the method of moments is applied to surface samples assuming that the incident wave has a Gaussian amplitude variation and the scattering coefficients are calculated from the second moments of the scattered field normalized by the illumination integral. The beamwidth of the tapered illumination should be narrow to suppress the edge contributions at large angles of incidence, which results in an inaccurate solution by excessive smoothing, specially for a relatively smooth random surface with a large correlation length. Therefore the beamwidth of the tapered illumination should be chosen carefully according to the incidence angle and the sample width. The tapered illumination approximation is numerically inefficient because the effective width of the sample surface contributing to the scattered field is much smaller than the width of the surface used in the numerical calculation.

In this paper, the contribution from the edges of the surface samples to the scattered field is minimized by controlling the conductivity of the surface near each edge by adding an appropriate tapered resistive sheet. It is shown that the addition of a short length of a tapered resistive sheet (1λ) at each end of surface sample can suppress the edge contribution significantly at even large angles of incidence. The validity of the numerical solution is examined using the energy conservation and reciprocity tests. Scattering simulations based on the new technique show a good agreement with the classical scattering models, the small perturbation method and the physical optics model, at their regions of validity. The backscattering coefficient predicted by the new technique is accurate for incidence angles as high as 80^0 while the angular validity range of the standard method is limited to lower incidence angles. This is particularly the case for relatively smooth surfaces with large correlation length ($ks<1.0$, $kl>6.0$ where k is wavenumber, s is the rms height, and l is the correlation length).

2. Formulation

The statistics of the scattered field from a one-dimensional conducting surface is obtained by a Monte Carlo simulation. Basically scattered fields from a large number of randomly generated sample surfaces are computed numerically, and are used to estimate the backscattering coefficient of the random surface. First, the surface current density $\mathbf{J}_e$ on each surface sample excited by a plane is determined using the method of moments (MoM). For a horizontally polarized wave the electric field integral equation (EFIE) and for a vertically polarized wave the magnetic field integral equation (HFIE) is used respectively which are given by

$$\mathbf{E}^i(\bar{\rho}) = \frac{k_0 Z_0}{4} \int_l \mathbf{J}_e(\bar{\rho})\ H_0^{(1)}(k_0|\bar{\rho}-\bar{\rho}'|)\, dl', \tag{1}$$

$$-\hat{n}\times \mathbf{H}^i(\bar{\rho}) = -\frac{1}{2}\mathbf{J}_e(\bar{\rho}) + \frac{i}{4} \int_l \hat{n}\times\{\mathbf{J}_e(\bar{\rho}')\times\ \nabla' H_0^{(1)}(k_0|\bar{\rho}-\bar{\rho}'|)\}\, dl'. \tag{2}$$

Here k_0 is the wave number, Z_0 is the intrinsic impedance of free space, $H_0^{(1)}$ is the zeroth-order Hankel function of the first kind, and ρ and ρ' are the position vectors of observation and source points, respectively. After a sample surface is discretized into sufficiently small cells, (1) and (2) are cast into matrix equations using pulse basis function and point matching technique.

The surface current induced by a horizontally polarized incidence wave exhibits the familiar singularity near the edges of the surface, which has a significant effect on the backscattered field away from normal incidence. However, this is not the case for the vertically polarized incidence wave for a one-dimensional perfectly conducting surface. To suppress the singular behavior of the current near the edges a tapered resistive sheet is added to each end of the surface sample as shown in Fig. 1. Using the following boundary conditions for resistive sheets[8],

$$[\hat{n}\times\mathbf{E}]_{-}^{+}=0, \qquad \hat{n}\times(\hat{n}\times\mathbf{E})=-R\,\mathbf{J}, \tag{3}$$

the integral equation for horizontal polarization becomes

$$\mathbf{E}^{i}(\bar{\rho}) = R(\bar{\rho})\,\mathbf{J}_{t}(\bar{\rho}) + \frac{k_0 Z_0}{4}\int_{l}\mathbf{J}_{t}(\bar{\rho})\,H_0^{(1)}(k_0|\bar{\rho}-\bar{\rho}'|)\,dl', \tag{4}$$

where R is the resistivity of the resistive sheet. Equation (4) is also cast into a matrix equation $[Z]\ [I] = [V]$ using point matching technique. The elements of the impedance matrix can be obtained from

$$z_{mn} \approx R(x_n,y_n)\,\delta_{mn} + \frac{k_0 Z_0}{4}\int_{\Delta x_n} H_0^{(1)}\left(k_0\sqrt{(x_m-x_n)^2+(z_m-z_n)^2}\right)\sqrt{1+\left(\frac{dz_n}{dx_n}\right)^2}\ dx_n \tag{5}$$

while the elements of the excitation vector $[V]$ are given by

$$v_m = \exp\left[i\,k_0\left(\sin\theta_i\,x_m-\cos\theta_i\,z_m\right)\right], \tag{6}$$

In (6) δ_{mn} is the Kronecker delta function.

The small argument expansion of the Hankel function is used in the evaluation of the diagonal elements of the impedance matrix, which is given by

$$z_{nn} \approx \frac{k_0 Z_0 \Delta d}{4}\left[1+\frac{i2}{\pi}\ln\left(\frac{k_0\gamma\Delta d}{4e}\right)-\frac{k_0^2(\Delta d)^2}{24}\left\{\frac{1-{}^{i2}\!/\!_{\pi}}{2}-\frac{i}{2}\ln\left(\frac{k_0\gamma\Delta d}{4\,e^{1/3}}\right)\right\}\right]+R(x_n,z_n) \tag{7}$$

where $\Delta d=\Delta x_n\sqrt{1+(dz_n/dx_n)^2}$, $e=2.718\cdots$, and $\gamma=0.5772\cdots$ is the Euler's constant. The non-diagonal elements, $z_{mn}(m\neq n)$, are obtained by evaluating the integral in (5) numerically using a four-point Gaussian-Quadrature integration technique.

The resistivity profile, *R(x)*, plays an important role in suppression of the edge current. The objective is to suppress the singular behavior of the current using a resistivity profile over the smallest possible width. Using trial and error the following resistivity profile was chosen:

$$R(x) = \begin{cases} 0, & |x|\le\dfrac{D}{2} \\ 0.005\,Z_0\left(\dfrac{D/2-|x|}{D_R}\right)^4, & \dfrac{D}{2}\le|x|\le\dfrac{D}{2}+D_R\,, \end{cases} \tag{8}$$

where D is the width of the sample surface and D_R is the width of the resistive section. In order to illustrate the effect of edge current on backscatter, scattering from a flat conducting surface with a width of 12λ is considered. The radar backscattering echo width (two-dimensional radar cross section) of the conducting strip is shown in Fig. 2a for both polarizations. The effect of edge current on echo width becomes important away from normal incidence for horizontal polarization. Figure 2b shows the backscattering echo width of the same conducting strip when resistive sheet segments are added to both edges of the conducting strip. In this case, the backscattering echo width for horizontal polarization decreases with incidence angle in a manner similar to the echo width for vertical polarization which clearly indicates the suppression of the edge currents.

Tapered resistive sheets were not used for the case of vertical polarization. For vertical polarization where the electric field is perpendicular to the edges of the surface samples, the surface current must go to zero near the edges. Therefore no significant backscatter can be attributed to the edges of the finite samples for vertical polarization. It is known that for flat strips a traveling wave is excited and its effect can be observed on the current distribution over the strip particularly near grazing angles. The traveling wave manifests itself in terms of repels superimposed on the physical optics current distribution. However, in the far-field region where the scattered field is proportional to the weighted average of the current distribution, the contribution from the repels are averaged out when the strip width is much larger than a wavelength. Besides, for rough surfaces, the roughness perturbs the phase coherency required for the excitation of traveling waves which would further suppress their effect in the far-field region.

3. Numerical Results From The New Technique

In order to demonstrate the validity of the numerical simulation, the sample surfaces with desired roughness statistics are generated using a standard approach[1,2]. First a random number string is generated for a Gaussian height distribution with zero-mean and standard deviation of 1. Then, the Gaussian distribution is correlated with a correlation function. In this paper a Gaussian correlation function having a correlation length l is correlated with the Gaussian distribution, N[0,1], and the desired standard deviation (rms height) s is multiplied by the surface height distribution to get desired roughness ks and kl where k is wavenumber. Figure 3 is a typical segment of a computer-generated random surface with ks=0.3 and kl=3.0. A surface of 1200 wavelength(λ) wide, generated with the input data of ks=0.300 and kl=3.000, gave the statistics of ks=0.301 and kl=3.007 which is very close to the input data.

Figure 4 shows the bistatic scattering coefficient for a Gaussian surface with ks=0.3 and kl=3.0 for both of VV- and HH-polarization at 30^{o} incidence angle. This figure also shows the effect of the length of the resistive sheet for the HH-polarization response. The solid and dotted line curves show the bistatic response when a resistive sheet of length 1λ and 3λ are used respectively. It is shown that the difference between the scattering patterns are negligible. In the computation of the bistatic response, the sample width D = 30λ and the number of independent samples N = 40 were used. The sample surfaces in the following examples are all loaded with a short tapered resistive sheet of width 1λ. When the sample surface width is 30λ, for example, a surface of total length 32λ including 1λ-resistive sheets at both ends is used for the computation of the surface current induced by the plane wave excitation. The currents induced over the resistive sheets are excluded from computation of the scattered field.

One way of testing the validity of the numerical results is the test of energy conservation. The incident energy is computed from the uniform plane wave excitation over finite length of a surface sample. The scattered energy is obtained by integrating the scattered power density over the surface of a cylinder enclosing the scatterer. Figure 5 shows the error in conservation of energy vs. incidence angle for a surface sample with ks=0.3 and kl=3.0 and the sample width D = 23λ. It is shown that the error is less than 1% and 2% for VV- and HH-polarizations, respectively, for incidence angles as high as 80°.

The small perturbation method (SPM) can be used to examine the validity of the numerical simulation for slightly rough surfaces. The surface with ks=0.3 and kl=3.0 was also used to generate incoherent bistatic scattering coefficients for VV- and HH-polarizations at 30° incidence in order to compare with the solution from the first-order small perturbation method (SPM). Figure 6 shows that the SPM solution agrees well with the numerical solution over the range of scattering angle $-80^{\circ} < \theta_s < 80^{\circ}$ for both polarizations. Since the practical interest in radar measurement is the backscattering direction, in the following examples the behavior of the backscattering coefficients will be studied.

The SPM is known to be valid when $ks \le 0.3$, $kl \le 3.0$, and $m \le 0.3$. Here m is the rms slope and is given by $m = \sqrt{2}\, s/l$ for a surface with a Gaussian correlation function. The backscattering coefficients from a surface with ks=0.15 and kl=2.0 are computed using the SPM and compared with the MoM solution as shown in Fig. 7. For the numerical computation of the backscattering coefficients, the sampling interval Δx = 0.1λ, the sample width D = 14λ and the number of independent samples N = 40 were used. Figure 7 shows that the SPM solution agrees very well with the MoM solution for incidence angles as high as 80°.

The physical optics approximation (PO) can be used to examine the validity of the numerical simulation at the other extreme roughness conditions. There are various PO solutions in the literature. For example, the PO model appeared in [9,11] is formulated by approximating the ensemble average within the diffraction integral by ignoring all local slope terms. Another familiar form of PO model is given in [12], which is formulated by including the first-order local slope term and ignoring "edge effect" contribution. Instead of using those models, an exactly formulated PO model is used in this paper to be compared with the MoM solution. The new PO model[13] is formulated by employing the spectral representation of the delta function and the characteristic function of a Gaussian random vector. The final form of the new PO model for a one-dimensional random surface is given in terms of a single integral which can be evaluated numerically. In this method

$$\left\langle \left|E^s_{vv}\right|^2 \right\rangle = \left\langle \left|E^s_{hh}\right|^2 \right\rangle = \frac{2|D_0|^2}{\pi s^2 \rho_0} \int_L^L du\,(L-|u|)\cdot \exp[ik_{dx}u]\cdot \exp\left[-s^2 k_{dz}^2 \{1-\rho(u)\}\right] \cdot \left\{ (\cos\theta - i\sin\theta\, s^2 k_{dz}\, \rho_u)^2 + \sin^2\theta\, s^2 \rho_0\, \rho_B \right\}, \tag{9}$$

where ρ(u) is the correlation function, $|D_0|^2 = k_0/(8\pi r_0)$, $\rho_u = \partial\rho(u)/\partial u$, $\rho_0 = -\rho_{uu}(0)$, $\rho_B = \rho_{uu}(u)/\rho_{uu}(0)$, $k_{dx} = 2k_0 \sin\theta$, and $k_{dz} = -2k_0\cos\theta$. Also, the coherent intensity for the conducting surface can be computed from

$$\left|\left\langle E^s_{vv}\right\rangle\right|^2 = \left|\left\langle E^s_{hh}\right\rangle\right|^2 = 4\,|D_0|^2 \exp\left[-s^2\, k_{dz}^2\right] \frac{\sin^2(k_{dz}\, L/2)}{(k_{dz}/2)^2} \tag{10}$$

which together with (9) are used to evaluate the desired incoherent backscattering coefficients

$$\sigma^{o}_{pp} = \lim_{r_0 \to \infty} \frac{2\pi r_0}{L} \cdot \frac{\left\langle \left| E^{s}_{pp} \right|^2 \right\rangle - \left| \left\langle E^{s}_{pp} \right\rangle \right|^2}{\left| E^{i}_{a} \right|^2}, \qquad pp = vv \quad or \quad hh. \tag{11}$$

The shadowing effect is also accounted for by incorporating the shadowing function given in [14]. Since the PO solution of the surface backscattering is proportional to the Fresnel reflectivity, the backscattering coefficients from a perfectly conducting surfaces computed by the PO model does not show a difference between VV- and HH-polarizations as shown by (9)-(11) and Fig. 8.

Figure 8 compares the backscattering coefficients as computed by the PO model and the new MoM for both polarizations. The roughness parameters of the surface are ks=1.0 and kl=8.0 which fall at margin of the validity region of PO model ($l \geq \lambda$, m<0.25 [9]). In this numerical simulation the following parameters were used: Δx=0.2λ, D=30λ and N=40. The PO solution agrees very well with the MoM solution over a wide range of incidence angles ($0^\circ < \theta < 70^\circ$).

Since the MoM with resistive sheets agrees very well with the SPM and the PO model at their validity region, it is reasonable to expect that the numerical simulation can accurately predict the statistics of the scattered field for surfaces with intermediate roughness conditions. It is known that the phase-difference statistics provides valuable information about the scattering mechanisms. This numerical technique is used to compute the co-polarized phase-difference statistics of the random surface of intermediate roughness, ks=0.62 and kl=4.6. The distribution of the co-polarized phase-difference ($\Phi_c = \Phi_{hh} - \Phi_{vv}$) statistics at 50° is shown in Fig. 9a. Figure 9b shows that the standard deviation of the Φ_c distribution versus incidence angle. The existing theoretical models cannot predict the phase difference statistics properly. The radar measurements of natural rough surfaces, however, show the phase-difference statistics similar to the numerical results shown in Figs. 9 a-b [16,17].

4. Comparison With Other Numerical Techniques

In order to demonstrate the efficiency of the new numerical method a comparison with existing numerical techniques is necessary. The most widely used numerical technique is based on the method of moments in conjunction with a tapered incident illumination [7]. The backscattering coefficients of the random surface with ks=1.0 and kl=6.13 are computed using the Gaussian-tapered illumination technique for comparing with the solution obtained by the new numerical technique. Figure 10 shows the comparison between the new PO model and the tapered illumination technique. In this comparison the taper function is given by [7]

$$E^{i}(\bar{\rho}) = \exp\left[i\bar{k}_i \cdot \bar{\rho}\left\{1 + w(\bar{\rho})\right\} - \frac{(x - z\tan\theta_i)^2}{g^2} \right], \qquad w(\bar{\rho}) = \frac{2(x - z\tan\theta_i)^2/g^2 - 1}{(k\,g\cos\theta_i)^2} \tag{12}$$

where $\bar{k}_i \cdot \bar{\rho} = k_0(\sin\theta_i\, x - \cos\theta_i\, z)$, θ_i is the incidence angle and g is a constant parameter controlling the tapering of the illumination. The resulting scattering coefficient is the ratio of scattering cross section normalized and the effective surface width L_{eff} given by [7]

$$L_{eff} = \sqrt{\pi/2}\, g \left[1 - \frac{0.5\left(1 + 2\tan^2 \theta_i\right)}{\left(k_0\, g \cos\theta_i\right)^2} \right]. \tag{13}$$

In this numerical computation, g is chosen to be $g=0.25D$ as recommended by [7], and D=30λ, Δx=0.2λ, and N=40. The backscattering coefficient computed by the Gaussian-tapered illumination method agrees well with the new PO model at small incidence angles ($0^0 < \theta_i < 50^0$), however, predict lower values for both polarizations at large incidence angles ($\theta_i > 50^0$) as shown in Fig. 10. Comparison of Figs. 8 and 10 clearly shows the new numerical method is more accurate than the standard method over a wide range of incidence angles.

Figure 10 shows that the backscattering coefficients are increasing over the angular range $75^0 < \theta_i < 90^0$. The reason for this is that the second term including $(k_i\, g \cos\theta_i)^2$ in (13) is not small enough to be neglected at large incidence angles. In addition, at large angles of incident the taper function could not eliminate the effect of the currents induced at the edges significantly and therefore the backscatter contribution from the edges are observable. Therefore, as the incidence angle increases, the sample surface width as well as the inverse of g ($1/g$) should be increased, which makes the numerical solution inefficient.

It should be noted that the effective surface width of the tapered illumination technique is much smaller than the physical width. For example, when $g=0.25D$ is used in (13), L_{eff} is about 31% of the physical width while the effective width of samples in the new simulation with 1λ resistive sheets is about 94% of the physical width when D=30λ. The scattered field is dominated by the contribution from the current induced over the effective width of a surface sample. Figure 11 shows the comparison of the normalized current distributions on a typical surface sample as computing by the new and the tapered illumination techniques.

Another drawback of the tapered illumination technique is the lack of a systematic approach to select g. Figure 12 shows the comparison of σ^0_{hh} between the new technique and the tapered illumination technique for various values of the parameter g for the surface with $ks=1.0$ and $kl=6.13$. The two numerical methods agree at low angles of incidence ($0^0 < \theta_i < 50^0$), however, the backscattering coefficients computed by the tapered illumination technique predicts conflicting results for $\theta_i > 50^0$ as the parameter g varies from $0.5D$ to $0.25D$.

Finally, the effect of the sample surface width on the backscattering coefficients (σ^0_{hh}) was tested for both numerical techniques at $\theta_i=40^0$ and 75^0 for the surface with $ks=1.0$ and $kl=6.13$. Figure 13a shows almost no sensitivity in σ^0_{hh} as computed by the new numerical method where the surface width varies from 5λ to 45λ for all incidence angles. Figure 13b shows the results computed by the tapered illumination technique where the backscattering coefficients changes drastically for $\theta_i=75^0$ when the surface width $D<27\lambda$.

Worse results were obtained, when other types of tapering functions were used. We examined the tapering function as suggested in [1]:

$$G\left(x - x_c\right) = \exp\left[- \frac{\left(x - x_c\right)^2}{g^2} \right] \qquad \text{with} \quad L_{eff} = \sqrt{\pi/2}\, g \tag{14}$$

where x_c is the coordinate of the illumination boresight on the surface. The tapering function used in [2] was also tested:

$$G(x-x_c) = \exp\left[-\frac{(x-x_c)^2}{g^2}\cos^2\theta_i\right] \qquad \text{with} \qquad L_{eff} = \frac{\sqrt{\pi/2}\,g}{\cos\theta_i} \tag{15}$$

where θ_i is the incidence angle.

5. Conclusions

A Monte Carlo simulation comprised of a random surface generator in conjunction with the method of moments is developed to obtain the scattering statistics of one-dimensional conducting random surfaces. A new approach is introduced which efficiently eliminates the effect of edge currents on the finite sample surfaces. By adding a resistive sheet to each end of the sample surface, the edge currents are suppressed. The numerical simulations using the resistive loaded surface samples agree very well with the existing theoretical models (SPM and PO) in their regions of validity. The new method offers two major advantages over the standard tapered illumination method: (1) it is numerically more efficient, that is, for a given accuracy the new method requires samples with smaller physical width, and (2) it has a wider angular range of validity which is independent of *ks*, *kl*, and any uncertain parameter like '*g*' employed in the tapered illumination technique. In addition to the magnitude, the phase-difference statistics was also computed by the new technique, and it was shown that the standard deviation of the phase-difference distribution increases with the incidence angle.

References

[1] Axline, R. M. and A. K. Fung, "Numerical computation of scattering from a perfectly conducting random surface," *IEEE Trans. Antennas Propagat.*, vol. AP-26, pp. 482-488, May 1978.

[2] Fung, A.K., and M. F. Chen, "Numerical Simulation of Scattering from Simple and Composite Random Surfaces", *J. Opt. Soc. Am.* A, vol. 2, no. 12, pp. 2274-2284, Dec. 1985.

[3] Lentz, R. R., "A numerical study of electromagnetic scattering from ocean-like surfaces," *Radio Science*, vol. 9, pp.1139-1146, December 1974.

[4] Nieto-Vesperinas, M. and J. M. Soto-Crespo, "Monte Carlo simulations for scattering of electromagnetic waves from perfectly conductive random rough surfaces", *Optics Lett.*, vol. 12, pp. 979-981, 1987.

[5] Durden,S. L. and J. F. Vesecky, "A numerical study of the separation wavenumber in the two-scale scattering approximation", *IEEE Trans. Geosci. Remote Sensing*, vol. 28, pp. 271-272, Mar. 1990.

[6] Rodriguez, E., Y. Kim, and S. L. Durden "A numerical assessment of rough surface scattering theories: I. Horizontal polarization, II. Vertical polarization," *Radio Science*, vol. 27, pp.497-527, July-Aug. 1992.

[7] Thorsos, E., "The validity of the Kirchhoff approximation for rough surface scattering using a Gaussian roughness spectrum", *J. Acoust. Soc. Am.* 83(1), pp. 78-92, January 1988.

[8] Senior, T.B.A., "Scattering by Resistive Strips," *Radio Sci.*, vol. 14, pp. 911-924, 1979.

[9] Ulaby, F.T., M.K. Moore, and A.K. Fung, "Microwave Remote Sensing, Active and Passive", vol 2, Artech House, Norwood, MA, 1982.

[10] Chen, M.F. and A.K. Fung, "Numerical study of validity of the Kirchhoff and Small-perturbation rough surface scattering models", *Radio Science*, vol.23, pp. 163-170, March 1988.

[11] Tsang, L., J.A. Kong, and R.T. Shin, "Theory of Microwave Remote Sensing", John Wiley and Sons, New York, 1985.

[12] Beckmann, P. and A. Spizzichino, "The Scattering of Electromagnetic Waves from Rough Surfaces", Pegamon Press, New York, 1979.

[13] Oh, Y., K. Sarabandi, F.T. Ulaby, "Re-examination of the Kirchhoff approximation for scattering from a rough surface", 1993 URSI Radio Science Meeting, Digest p.406, Ann Arbor, MI, June 28-July 2, 1993.

[14] Smith, B. G., "Geometrical shadowing of a random rough surface," *IEEE Trans. Antennas Propagat.*, vol. AP-15, pp. 668-671, Sep. 1967.

[15] Oh, Y., "Microwave Polarimetric Backscattering From Natural Rough Surfaces", Ph.D. Thesis, University of Michigan, December 1993.

[16] Sarabandi, k., Y. Oh, and F.T. Ulaby, "Polarimetric radar measurement of bare soil surfaces at microwave frequencies", in *Proc. IEEE International Geosci. Remote Sensing Symp.(IGARSS)*, pp.387-390, Espoo, Finland, June 1991.

[17] Oh, Y., Sarabandi, k., and F.T. Ulaby, "An empirical model for phase-difference statistics of rough surfaces", in *Proc. IEEE International Geosci. Remote Sensing Symp.(IGARSS)*, pp.1003-1005, Tokyo, Japan, August 1993.

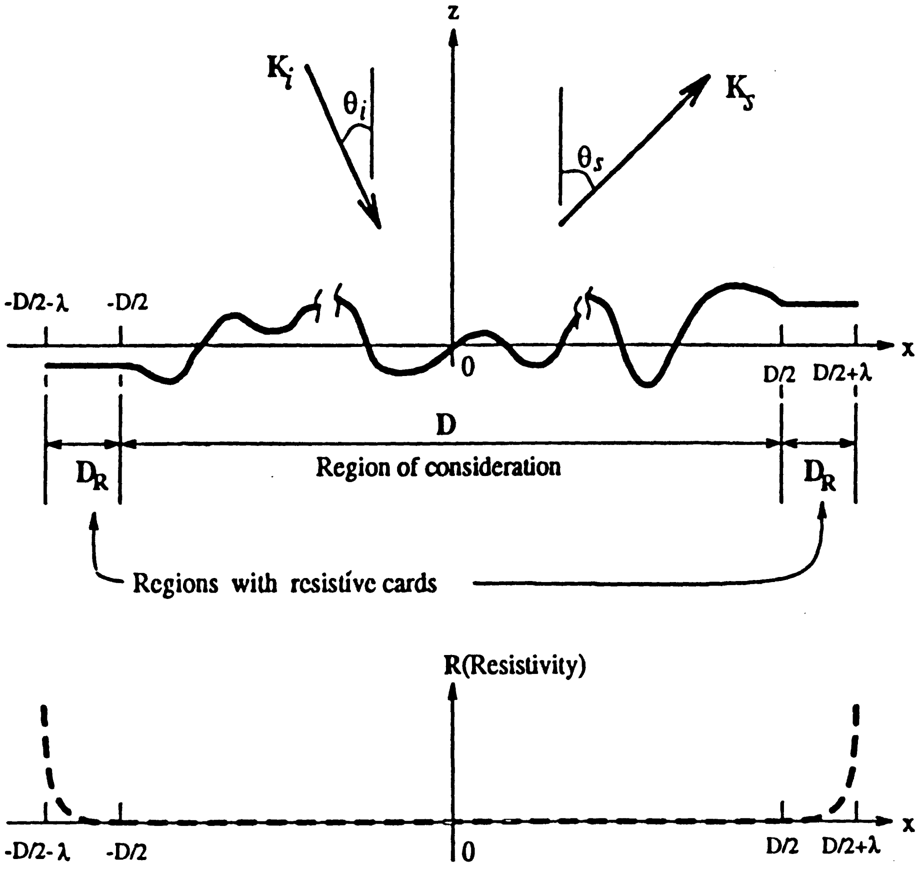

Figure 1: A sample surface loaded with resistive sheets and the resistivity function profile.

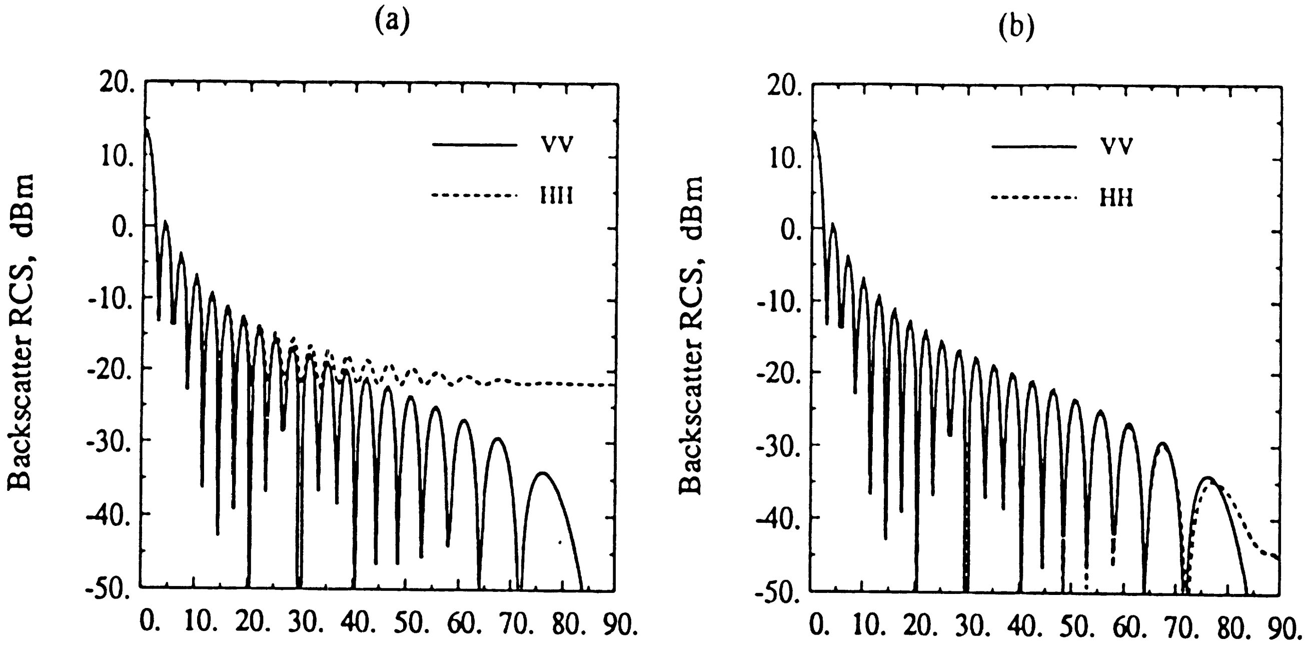

Figure 2: The backscattered echo width of a flat conducting strip (width=12λ) (a) without resistive sheets and (b) with resistive sheets.

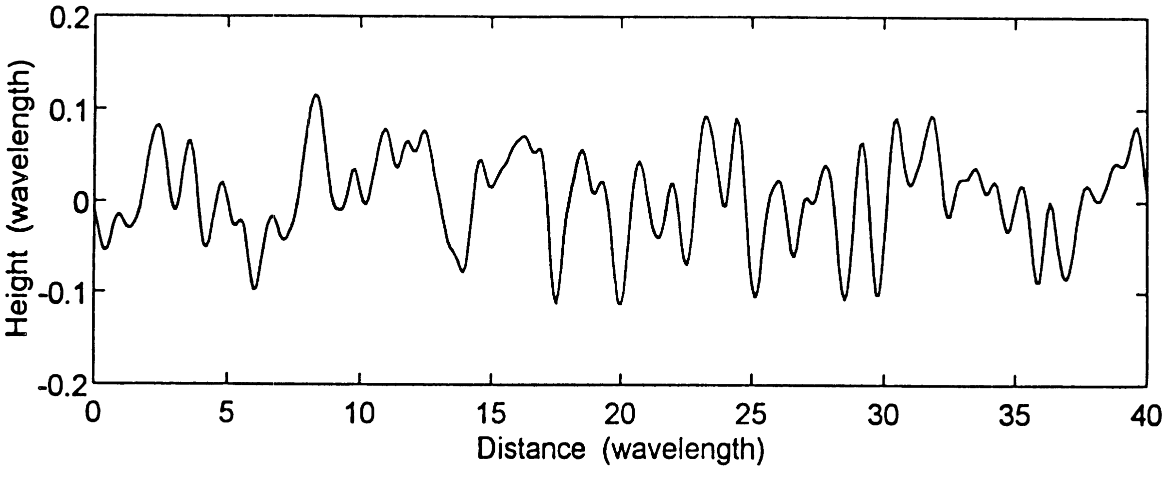

Figure 3: A typical sample surface with *ks*=0.3 and *kl*=3.0.

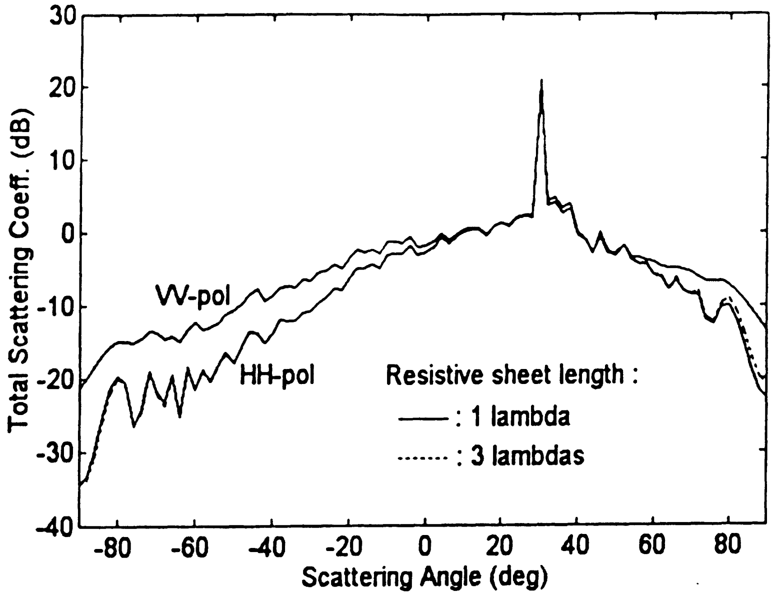

Figure 4: The total bistatic scattering coefficient (coherent+incoherent) for a surface with ks=0.3 and kl=3.0. Both polarizations are shown for incidence angle $\theta_i = 30^o$ and the effect of the width of tapered resistive sheet is also examined.

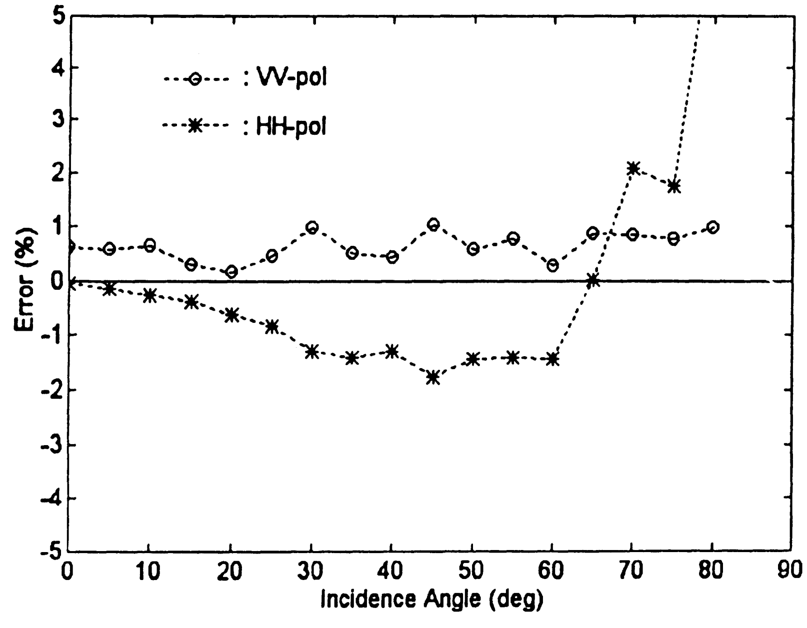

Figure 5: Error in the conservation of energy for a typical surface with ks=0.3 and kl=3.0 (D=23λ, Δx=0.1λ).

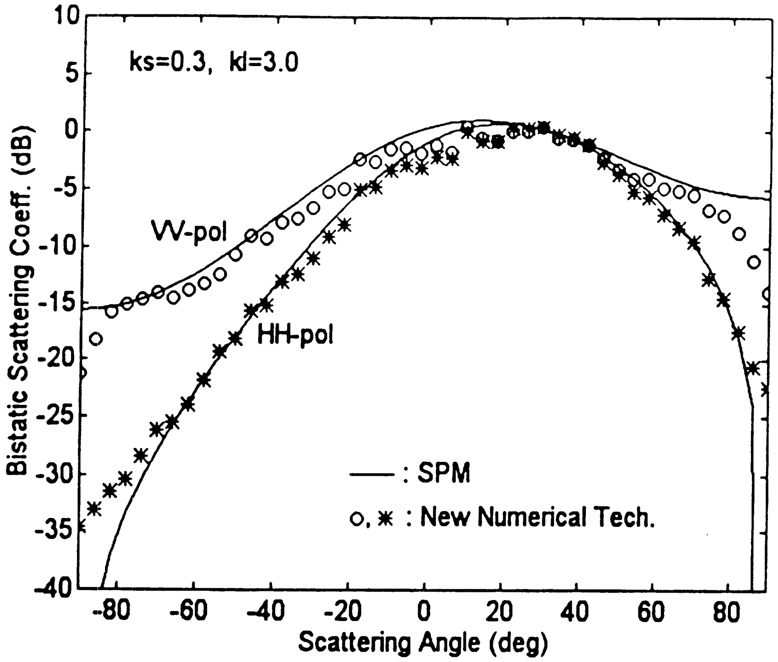

Figure 6: Incoherent bistatic scattering coefficient computed by the new numerical technique and the first-order small perturbation model for both polarizations. The following parameters were used in this computation: $\theta_i = 30°$, ks=0.3, kl=3.0, N=40, D=30λ, and Δx=0.2λ.

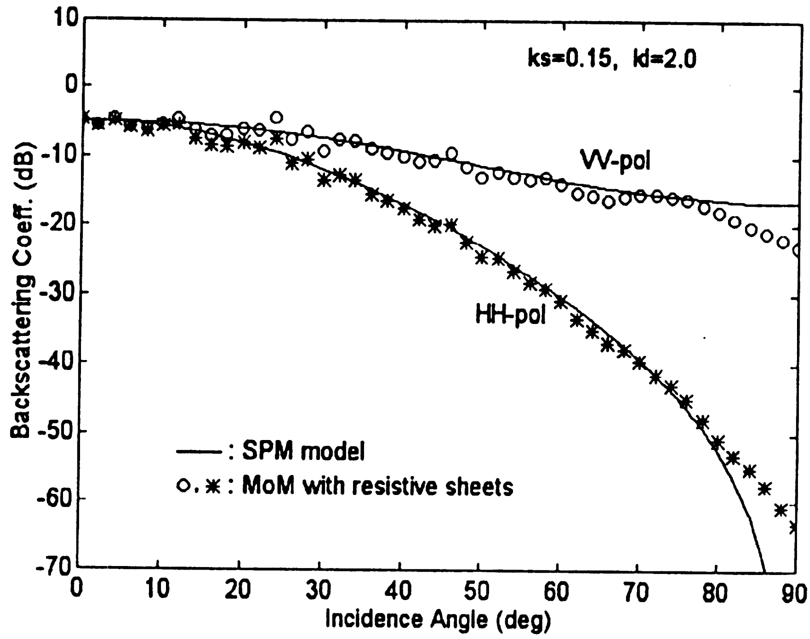

Figure 7: Comparison of backscattering coefficients (σ^0_{vv}, σ^0_{hh}) as computed by the new numerical method and the first-order small perturbation solution for a surface with ks=0.15 and kl=2.0 (N=40, D=14λ, Δx=0.1λ).

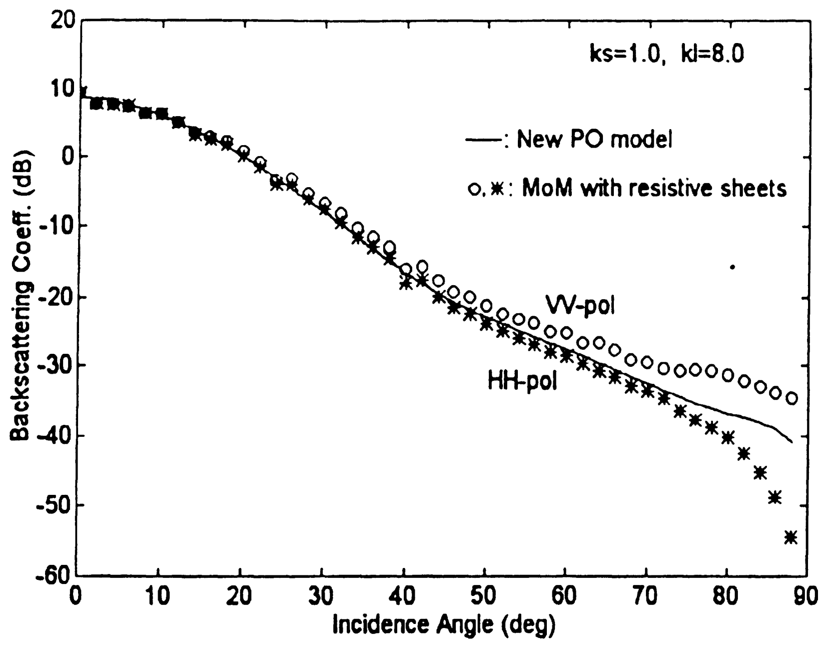

Figure 8: Comparison of backscattering coefficients (σ^0_{vv}, σ^0_{hh}) as computed by the new numerical method and the new formulation of Kirchhoff approximation for a surface with ks=1.0 and kl=6.13 (N=40, D=30λ and Δx=0.2λ).

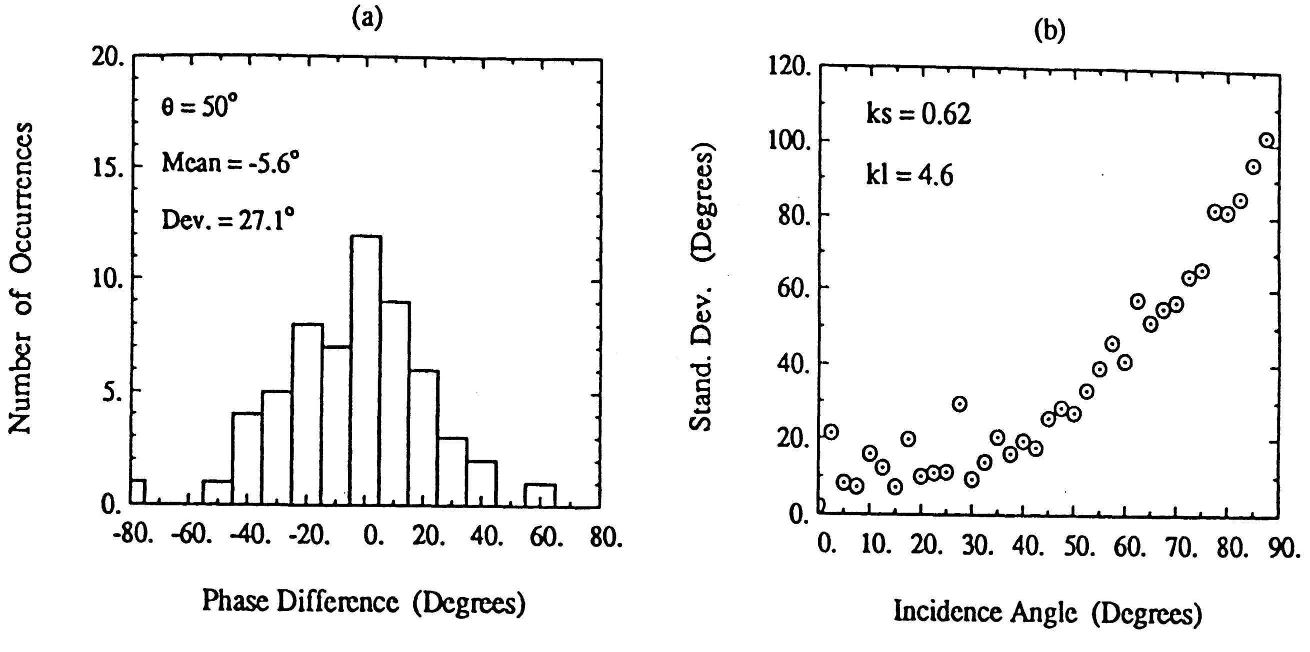

Figure 9: The distribution of the phase difference between the scattered fields of HH- and VV-polarization ($\Phi_c = \Phi_{hh} - \Phi_{vv}$) for a random surface with ks=0.62 and kl=4.6 at $\theta_i = 50°$(a) and the standard deviation of Φ_c distribution versus incidence angle (b).

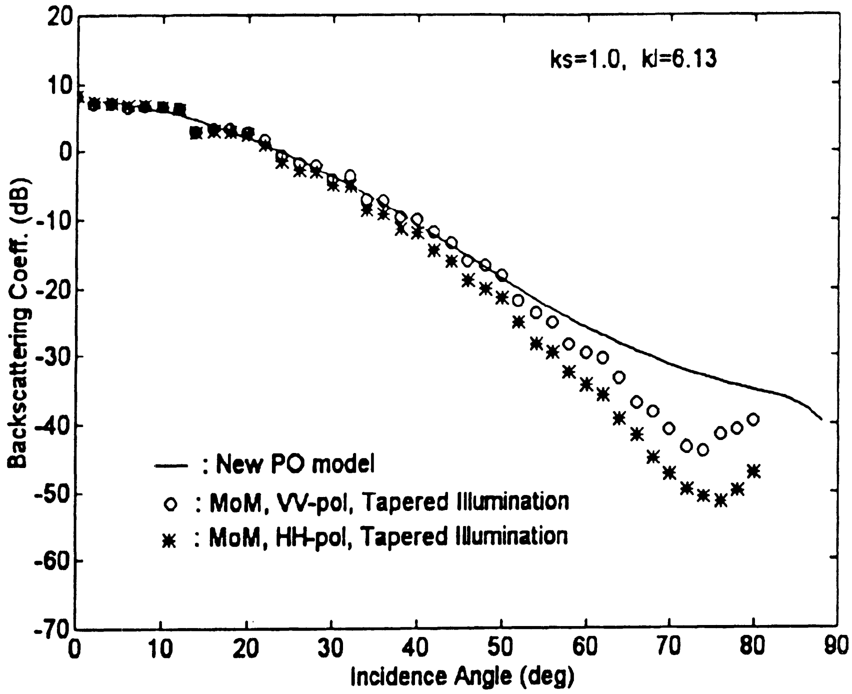

Figure 10: Backscattering coefficients (σ^0_{vv}, σ^0_{hh}) computed by the tapered illumination method and the new formulation of Kirchhoff approximation for a surface with ks=1.0 and kl=6.13 (N=40, D=30λ and Δx=0.2λ).

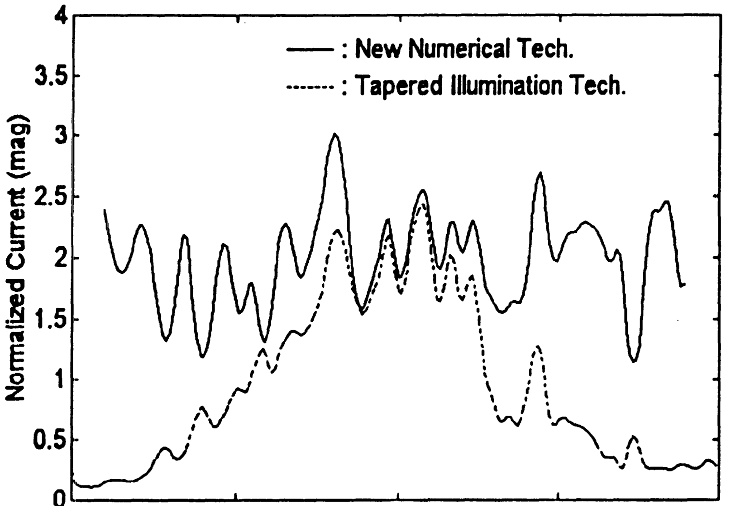

Figure 11: The comparison of the normalized current distributions computed by the new numerical technique and the tapered illumination technique on a surface sample with ks=0.3 and kl=3.0 (D=23λ and Δx=0.1λ).

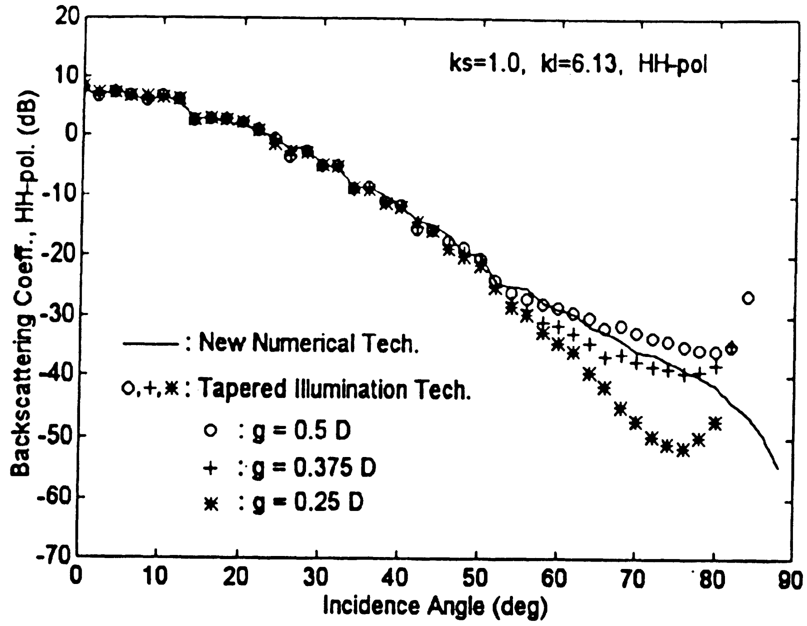

Figure 12: Backscattering coefficients (σ^0_{hh}) computed by the new numerical technique and the tapered illumination technique with various values of the tapering parameter g ($0.25D$, $0.375D$, and $0.5D$) for a surface with ks=1.0 and kl=6.13 (N=40, D=32λ and Δx=0.2λ).

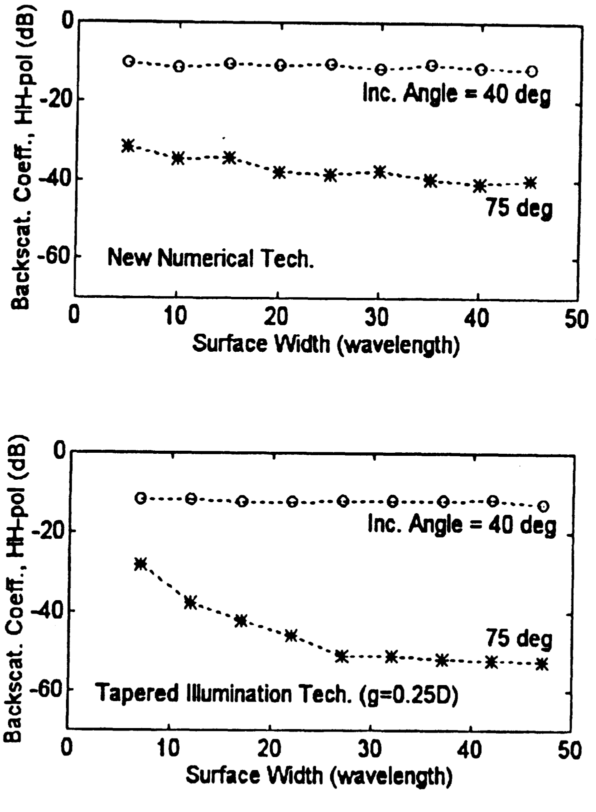

Figure 13: The effect of the sample surface width on backscattering coefficients (σ^0_{hh}) as computed by the new numerical technique (a) and the tapered illumination technique(g=0.25D case) (b) at 40°, and 75° incidence angles for a surface with ks=1.0 and kl=6.13 (N=40 and Δx=0.2λ).

Microwave Scattering Model for Grass Blade Structures

James M. Stiles, Kamal Sarabandi, *Senior Member, IEEE*, and Fawwaz T. Ulaby, *Fellow, IEEE*

***Abstract*—In this paper, the electromagnetic scattering solution for a grass blade with complex cross-section geometry is considered. It is assumed that the blade cross section is electrically small, but its length is large compared to the incident wavelength. In a recent study it has been shown that the scattering solution for such problems, in the form of a polarizability tensor, can be obtained using the low-frequency approximation in conjunction with the method of moments. In addition, the study shows that the relationship between the polarizability tensor of a dielectric cylinder and its dielectric constant can be approximated by a simple algebraic expression. The results of this study are used to show that this algebraic approximation is valid also for cylinders with cross sections the shape of grass blades, providing that proper values are selected for each of three constants appearing in the expression. These constants are dependent on cylinder shape, and if the relationship between the constants and the three parameters describing a grass blade shape can be determined, an algebraic approximation relating polarizability tensor to blade shape, as well as dielectric constant, can be formed. Since the elements of the polarizability tensor are dependent on only these parameters, this algebraic approximation can replace the cumbersome method of moments model. The moment method model is therefore used to generate a small but representative set of polarizability tensor data over the range of values commonly observed in nature. A conjugate gradient method is then implemented to correctly determine the three constants of the algebraic approximation for each blade shape. A third-order polynomial fit to the data is then determined for each constant, thus providing a complete analytic replacement to the numerical (moment method) scattering model. Comparisons of this approximation to the numerical model show an average error of less than 3%.**

I. INTRODUCTION

Scattering models of random media such as vegetation canopies require knowledge of scattering behavior of the individual vegetation constituents. To obtain efficient scattering formulations for the constituents such as branches, leaves, needles, or stems the structure of these particles are usually modeled by simple canonical geometries, such as circular cylinders or discs [12]. As a result, the particles can be characterized by a few specific geometric parameters, such as length, diameter, or thickness. In addition, scatterers with simple geometries often are amenable to analytic scattering solutions. Due to the random nature of vegetation canopies, scattering formulations for such media are quite complex, thus the two characteristics of simple geometric specification and analytical scattering formulations are highly desirable to provide a tractable vegetation scattering solution.

However, some structural characteristics not reflected in the simplified geometry can significantly affect the scattered response of a given vegetation constituent. That is, oversimplification can degrade the fidelity and accuracy of a canopy scattering model. To provide a greater degree of model accuracy, other physical aspects of these vegetation constituents may be considered, such as blade curvature, branch roughness, or dielectric inhomogeneity [6], [7]. For example, the constituents of a grass plant, such as stems and grass blades, can be modeled as long thin circular dielectric cylinders. The cross sections of grass blades, however, are far from circular. As will be shown, the scattering response of the actual shape is significantly different from that of an equivalent circular cylinder. In addition, a radiative transfer [9]–[11] canopy scattering model demonstrates the resulting discrepancies in backscattering coefficients predicted using the circular, rather than the actual grass blade geometries.

The scattering matrix of electrically thin cylinders with arbitrary cross sections can be determined only with numerical methods and can be expressed in terms of a polarizability tensor. Such is the case for grass blade elements, however, the numeric specification of grass blade shape, along with the numeric scattering solution, are contrary to the desired characteristics described earlier. Thus, the ideal solution would define the blade shape with a few geometric parameters, provide an analytic scattering solution which is a function of these parameters, yet also comprehend and account for the complex blade geometries which affect scattering response.

This is achieved by first approximating the general shape of a grass blade with a collection of geometric parameters, and then limiting the domain of these parameters to those found in nature. The polarizability tenors are obtained numerically for a representative collection of grass blade shapes located throughout this parameter domain, then an analytic function is determined which matches the numeric data and thus approximates the complex polarizability tensor values across the entire domain of shape parameters.

II. GRASS BLADE GEOMETRY

The fine geometry exhibited by most grass blades occurring in nature can be approximated by a set of five description parameters as shown in Fig. 1. These five parameters, thickness t, width w, blade angle θ, radius of curvature r, and blade length l can be combined to produce five new independent parameters, two of which describe the size of the blade while

---

Manuscript received September 1, 1992; revised May 3, 1993. This work was supported by NASA Contract NAGW-1101 and by the Jet Propulsion Laboratory under Contract JPL-958438.

The authors are with the Radiation Laboratory, Department of Electrical Engineering and Computer Science, University of Michigan, Ann Arbor, MI 48109-2122.

IEEE Log Number 9210716.

0196-2892/93$03.00 © 1993 IEEE

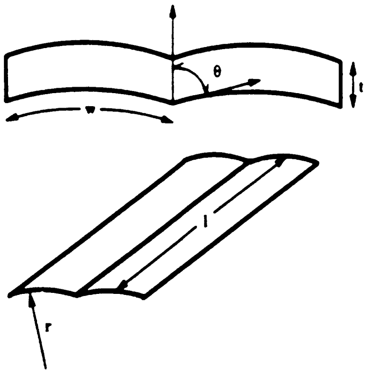

Fig. 1. Diagram of grass blade geometry including blade cross section (showing width w, thickness t, and blade angle θ) and overhead view (showing radius of curvature r and length l).

TABLE I
THE FIVE PARAMETERS DESCRIBING BLADE GEOMETRY, INCLUDING TWO PARAMETERS (LENGTH l, AND AREA A) WHICH SPECIFY BLADE SIZE, AND THREE DIMENSIONLESS PARAMETERS (ASPECT RATIO a, CURVATURE v, AND BLADE ANGLE θ) WHICH SPECIFY SHAPE

parameter	symbol	expression
Area	A	$\approx 2tw$
Length	l	l
Aspect Ratio	a	$t/(2w)$
Curvature	v	w/r
Blade Angle	θ	θ

the other three describe its shape. The first two of these parameters, as shown in Table I, are the cross-sectional area A and blade length l, which together specify the blade size. The three remaining parameters are dimensionless quantities, and thus specify only the blade shape. The first, aspect ratio a, is defined as the ratio of blade thickness to blade width. The second parameter, curvature v, is the arc angle in radians of the arc formed by the curvature of the blade on either side of the center rib. The final parameter, blade angle θ, is the angle formed by the vector normal to the grass blade surface at the center rib, and the vector tangent to the blade curvature at the center rib. In addition, for purposes of the scattering formulation, the grass blades are assumed to be both long and thin, such that $2w \ll \lambda$ and $l \gg w$.

III. SCATTERING FORMULATION

Given these blade parameters and assumptions, a formulation is required to accurately predict the electromagnetic scattering from grass blade structures, assuming an incident electric field of arbitrary direction and polarization. To solve this problem, the scattering formulation described by Sarabandi and Senior [5] shall be followed, a formulation which predicts the scattering from long, thin dielectric cylinders of arbitrary cross section.

Initially, the grass blade is assumed to be infinite in length, eliminating the z dependence of the scattered field and essentially reducing the scattering formulation to a two-dimensional problem involving only the grass blade cross section. If, in addition, the blade cross section is electrically small, the scattering formulation can be further reduced by employing the low frequency or Rayleigh approximation, wherein the higher order terms of the wave number k_0 are ignored [2], [8]. Thus, the Rayleigh approximation essentially reduces the scattering formulation to an electrostatics problem within the region of the blade cross section.

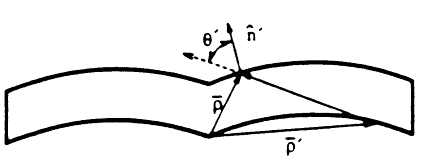

Fig. 2. Cross section of grass blade showing the source point $\bar{\rho}$, the observation point $\bar{\rho}'$, and angle $\theta' = \cos^{-1}[\hat{n}' \cdot (\bar{\rho} - \bar{\rho}')/|\bar{\rho} - \bar{\rho}'|]$.

The expression for the incident electric field after employing the Rayleigh approximation (zeroth order of k_0) is given as

$$E^i = \hat{a} = a_x\hat{x} + a_y\hat{y} + a_z\hat{z} \tag{1}$$

which can be written in terms of the electrostatic potential Φ as

$$E^i = -\nabla_t \Phi^i + a_z\hat{z} \tag{2}$$

where

$$\Phi^i = -a_x(x + c_1) - a_y(y + c_2). \tag{3}$$

Using superposition, the total (incident plus scattered) electrostatic potential can be written as

$$\Phi = a_x\Phi_1 + a_y\Phi_2 \tag{4}$$

where Φ_1 is the total electrostatic potential due to the fist term of (3), and similarly Φ_2 due to the second term.

As shown by Sarabandi and Senior [5], the integral equations specifying the two solutions, Φ_1 and Φ_2, about the outer surface of the blade are given as

$$\left(\frac{\epsilon_r + 1}{2}\right)\Phi_1(\bar{\rho}) - \left(\frac{\epsilon_r - 1}{2\pi}\right)\int_C \Phi_1(\bar{\rho}')\frac{\cos\theta'}{|\bar{\rho} - \bar{\rho}'|}dc' = -x - c_1 \tag{5}$$

and

$$\left(\frac{\epsilon_r + 1}{2}\right)\Phi_2(\bar{\rho}) - \left(\frac{\epsilon_r - 1}{2\pi}\right)\int_C \Phi_2(\bar{\rho}')\frac{\cos\theta'}{|\bar{\rho} - \bar{\rho}'|}dc' = -y - c_2 \tag{6}$$

where c_1 and c_2 are arbitrary constants and θ' is defined in Fig. 2.

These equations can be solved using the method of moments, thus determining the total electrostatic potential on the surface of the grass blade. However, this potential must now be related to the scattered electric field. As the scattered field from a nonmagnetic Rayleigh scatterer can be attributed to an electric dipole moment, the scattered field from an infinite Rayleigh cylinder can be attributed to electric dipoles along the infinite (z) axis, expressed as a dipole moment per unit length. The magnitude and direction of this dipole moment is related to the incident electric field vector as $\boldsymbol{p} = \epsilon_0 \boldsymbol{P} \cdot \hat{a}$, where $\boldsymbol{P}$ is the polarizability tensor [1], [2] . Because the assumed

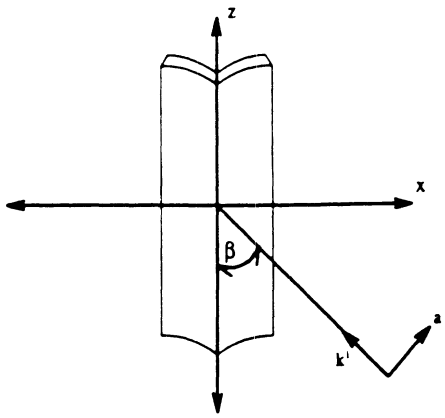

Fig. 3. Geometry of a finite grass blade including incident angle β.

grass blade cross section is symmetrical about the y-axis, the polarizability tensor is a diagonal matrix, and the three nonzero diagonal elements are given as [5]

$$P_{xx} = -(\epsilon - 1)\int_C \Phi_1 \hat{n}' \cdot \hat{x} \, dc' \tag{7}$$

$$P_{yy} = -(\epsilon - 1)\int_C \Phi_2 \hat{n}' \cdot \hat{y} \, dc' \tag{8}$$

$$P_{zz} = (\epsilon - 1)A. \tag{9}$$

It is important to note that these expressions specifying the polarizability tensor are dependent on only the dielectric constant and geometry of the grass blade. The direction and polarization of the incident electric field does not affect the values of the polarizability tensor, and enter into the scattering formulation only when computing the electric dipole moment ($\boldsymbol{p} = \epsilon_0 \boldsymbol{P} \cdot \hat{a}$).

As stated earlier, this solution was derived assuming an infinite length grass blade. Obviously this is a nonphysical assumption, and to determine the scattered field from a finite blade of length l, the physical optics approximation is employed [4], [8]. The fields on the blade surface calculated for the infinite case (constant with z) are likewise assumed to be valid for the long but finite blade. Integration of these truncated fields along the z axis leads to the familiar $(\sin x)/x$ scattering response in the elevation plane of the blade structure. The scattering intensities are thus given by the expressions [5]

$$\boldsymbol{S} = -\frac{k_0^2}{4\pi}\left\{\hat{k}^s \times \hat{k}^s \times [l\boldsymbol{P} \cdot \hat{a}]\right\}\frac{\sin U}{U} \tag{10}$$

where

$$U = \frac{k_0 l}{2}\left(\hat{k}^s \cdot \hat{z} - \cos\beta\right), \tag{11}$$

with $\boldsymbol{P}$ being the polarizability tensor given by (7)–(9), l the blade length, and β the incident angle in the elevation plane, as defined in Fig. 3. Fig. 4(a) displays a typical scattering pattern in the elevation plane, with the main lobe occurring at the forward scattering cone. Although this physical optics formulation is merely an approximation, it can predict the major scattering behavior for blades with electrical lengths as small as one λ, although accuracy generally increases with cylinder electrical length.

In the azimuth plane, the scattering response (Fig. 4(b)) is that of an electric dipole, as expected for electrically small (Rayleigh) cross sections. It should be noted, however, that except for the specific case of $P_{xx} = P_{yy}$, the radial electric dipole moment will not align with the incident electric field vector. Thus, the main forward and backscattering lobes will not be aligned with the radial direction of the incident field propagation vector.

To validate this scattering formulation, the backscattering coefficient is determined as a function ofelevation angle using an accurate three-dimensional numeric scattering model. If $\theta = 0$ and $v = 0$, the grass blade shape reduces to a flat dielectric strip. A flat, thin dielectric structure can be modeled as a resistive sheet [13], [14], and therefore the grass blade in this case is modeled as a resistive strip. Using a moment-method code which provides a scattering solution

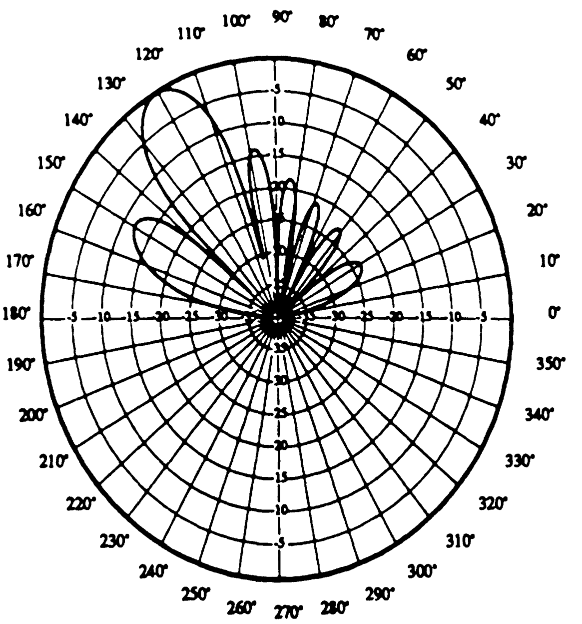

(a)

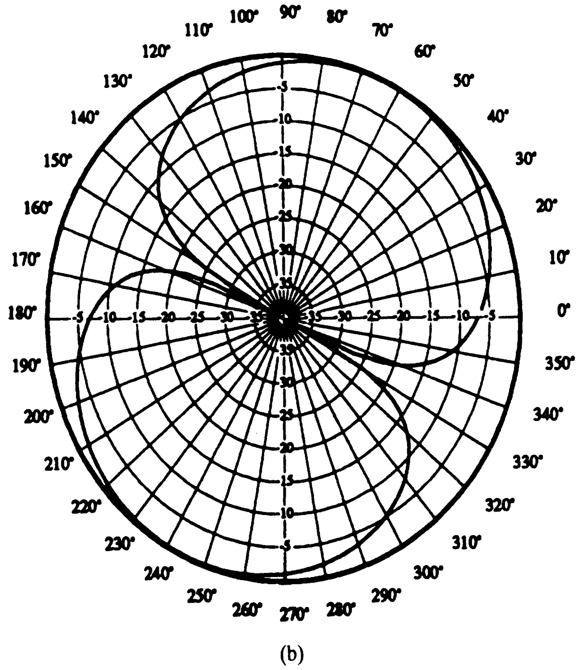

(b)

Fig. 4. Scattered intensity in the elevation (a) and azimuth (b) planes of a horizontally polarized wave incident on a finite dielectric cylinder ($\theta_i = 60°, \phi_i = 45°$, $l = 2\lambda, P_{xx} = 4.0, P_{yy} = 2.0$).

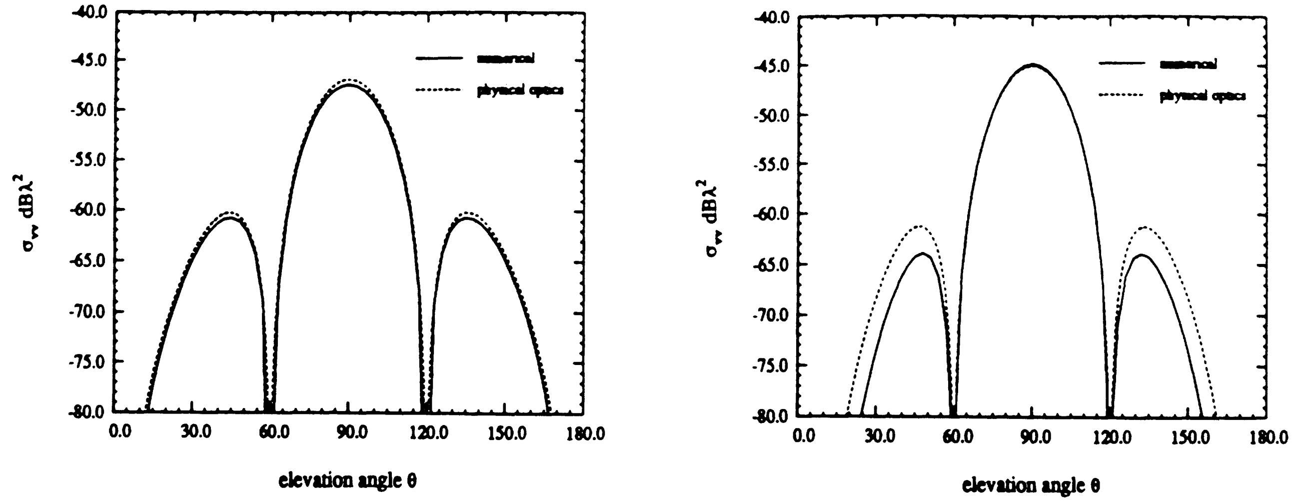

(a) (b)

Fig. 5. Normalized backscattering rcs σ_{hh} (a) and σ_{vv} (b) as determined by both a numeric scattering model and the scattering formulation of this paper. ($\phi = \pi/2$ $a = 0.05$ $\theta = v = 0, \epsilon = 5 - \imath 1, A = 1.25 \times 10^{-4}\lambda^2, l = \lambda$).

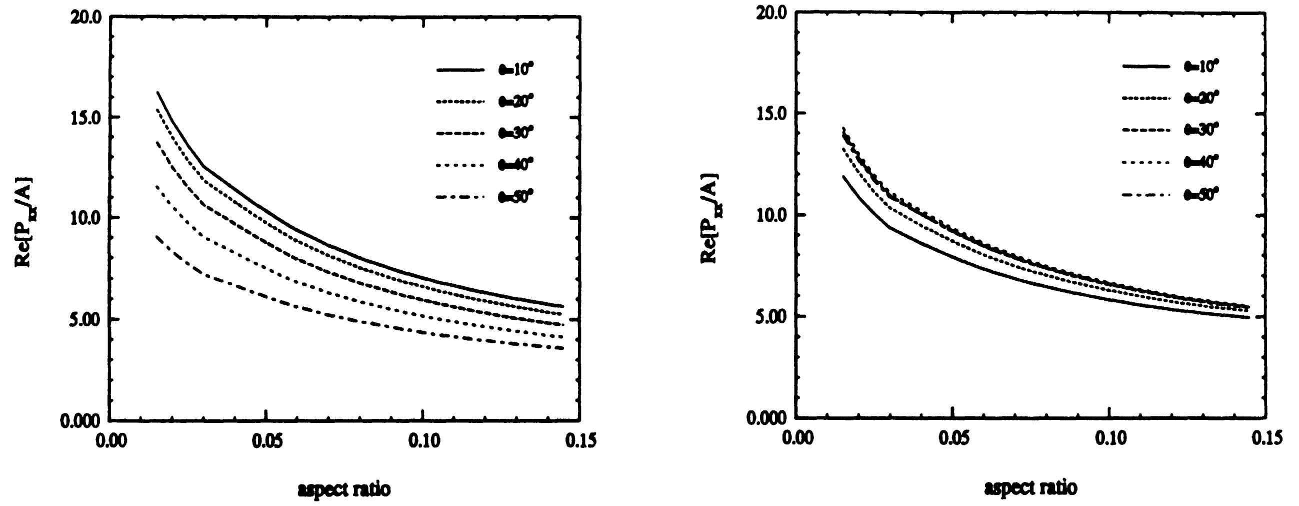

(a) (b)

Fig. 6. The real portion of the normalized polarizability tensor element P_{xx}/A as a function of aspect ratio a and blade angle θ for blade curvature v =(a) 0.2 and (b) 1.5 ($\epsilon = 30 + \jmath 9$).

for an arbitrary resistive sheet, the backscattering coefficient σ versus elevation angle was calculated and the results are given in Fig. 5, along with the data predicted by (10) using the polarizabity tensor. Good agreement between the two methods was found, with an error for σ_{hh} of less than 1 dB for all incidence angles. The error for σ_{vv} is similar when close to normal incidence, but becomes larger with increasing oblique incidence as traveling waves (not accounted for in the physical optics approximation) are induced. However, the cylinder of Fig. 5 is just one λ in length, and the error at large oblique angles diminishes as cylinder length increases.

IV. MODEL RESULTS

The effect of blade geometry on scattering from grass blades was evaluated using the scattering formulation outlined in the previous section. The parameter of interest in this case is the normalized polarizability tensor P/A. Each element of the polarizability tensor is directly proportional to the cross-section area A, thus the normalized polarizability tensor P/A is independent of A. Therefore, P/A is a function of only the dielectric constant and the shape, as described by the dimensionless shape parameters, curvature v, aspect ratio a, and blade angle θ. In general, the elements P_{xx} and P_{yy} are, respectively, proportional to the projected area of the blade shape onto the (x,z) and (y,z) planes. Thus, the parameter which most affects the normalized polarizability tensor elements is aspect ratio, followed by blade angle and then blade curvature. Fig. 6 demonstrates this dependence, showing the effect of aspect ratio and blade angle on the real part of P_{xx}/A for both a relatively flat and a relatively curved grass blade geometry.

Although these figures demonstrate the dependence of polarizability tensor, and hence scattering on blade geometry, the larger question of whether these shape parameters significantly affect scattering from an entire grassland target can not be inferred. Therefore, a radiative transfer scattering model [9]–[11] was implemented which modeled a layer of scatterers consisting of cylinders of a given length and cross-sectional

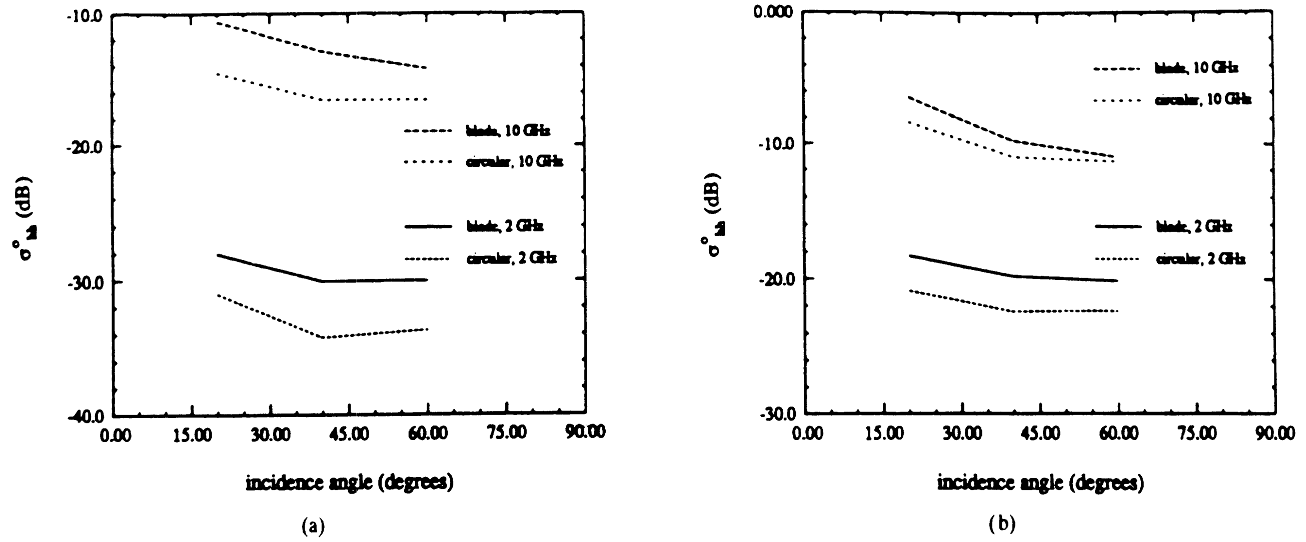

Fig. 7. σ°_{hh} for dry (a) and moist (b) vegetation as predicted by a radiative transfer based grassland model for blades of both grass blade and circular shaped cross sections ($a = 0.45$, $\theta = 0$, $v = 0.01$, $N = 2500/\text{m}^3$, $l = .5$ m, $A = .03$ cm^2, $M_g = 0.3$ (a) and 0.9 (b)).

area. Two cases were examined; in the first case, the cylinders were of circular cross section, while in the other a blade shaped cross section ($a = 0.045$, $\theta = 0$, $v = 0.01$) of identical area was implemented. Fig. 7 displays the results of this model at two frequencies for two dielectric constants and three incidence angles. The difference in the cross-section shape results in a difference of as much as 5 dB in the value of σ°_{hh}. This contrast is largest at lower frequencies and for drier grass blades. Although this data represents a limited test case, it does show that for electrically small cross sections, blade shape, in addition to blade size, *can* significantly affect the observed scattering from grassland targets.

V. ALGEBRAIC MODEL

For a cylinder of circular cross section, an exact analytic solution to the integral equations of (5) and (6) exists, thus leading to an exact solution of the normalized polarizability tensor elements as a function of the complex dielectric constant [5], [8]:

$$\frac{P_{xx}}{A} = \frac{P_{yy}}{A} = 2\frac{\epsilon - 1}{\epsilon + 1}. \tag{12}$$

As shown by Sarabandi and Senior [5], this equation can be modified to provide an approximate algebraic solution for cylinders of semi-circular, triangular, and square cross sections which, although not an exact solution to the integral equations, matches the numeric solution with exceptional accuracy. This modified expression is given as

$$\frac{P(\epsilon)}{A} = c_0\frac{\epsilon - 1}{\epsilon + 1}\cdot\frac{\epsilon + c_1}{\epsilon + c_2} \tag{13}$$

where the values of constants c_0, c_1, and c_2 are unique for each of the three cross sections. This expression is valid for both P_{xx}/A and P_{yy}/A, although the three constants are of course different for nonsymmetric cross sections (semicircular and triangular).

To determine if the validity of this expression extends to grass blade shapes, data was generated with the numerical model for a given blade geometry across a wide range of complex dielectric constants. Three constants c_1, c_2, and c_3 were then selected in an attempt to match (13) to the generated numerical data. As shown in Fig. 8, constants were found which provided a match with good accuracy between the approximation of (13) and the numerical data. Thus, (13) appears to be valid for not only simple geometrical cross sections, but for more general cross sections (grass blades) as well. The constants c_0, c_1, and c_2, denoted as vector $\mathbf{c}$, can therefore be selected to relate the dielectric constant to the polarizability tensor for a given blade geometry. Since these constants are dependent only on cross-section geometry, and since cross-section geometry for a grass blade has been defined by the three shape parameters v, a, and θ, a more general algebraic approximation relating grass blade geometry, in addition to the dielectric constant, can be hypothesized:

$$\frac{P_{xx}}{A} = c_0(\theta, a, v)\frac{\epsilon - 1}{\epsilon + 1}\cdot\frac{\epsilon + c_1(\theta, a, v)}{\epsilon + c_2(\theta, a, v)}. \tag{14}$$

The expressions relating $\mathbf{c}$ to the shape parameters v, a, and θ must therefore be determined.

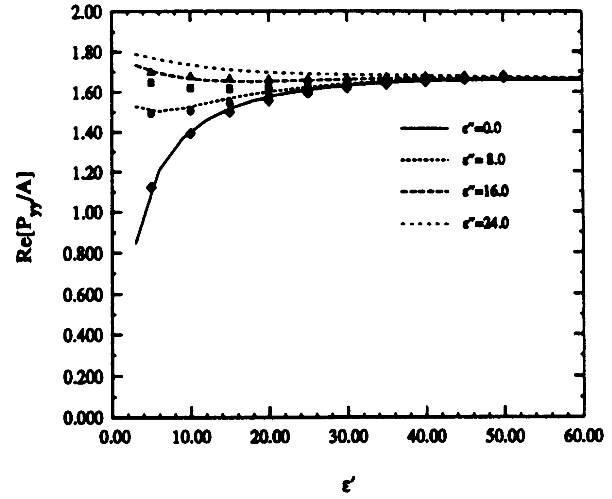

Fig. 8. Comparison of the predicted dependence of $\text{Re}[P_{yy}/A]$ on dielectric constant for both the numerical scattering model (lines) and the algebraic approximation (marks) of (13) ($a = 0.1$, $\theta = 28°$, $v = 0.01$, $c_0 = 1.753$, $c_1 = 9.703$, and $c_2 = 10.297$).

TABLE II
MODEL INPUT PARAMETER SPACE ESTIMATING THOSE VALUES GENERALLY OBSERVED IN NATURE

parameter	min.	max.
aspect ratio (a)	0.015	0.12
blade angle (θ)	0.0	50.0
curvature (v)	0.01	2.0
dielectric constant (ϵ')	5.0	45.0
dielectric constant (ϵ'')	2	25

VI. COEFFICIENT ESTIMATION

To determine these relationships, the numerical model was used to determine the normalized polarizability tensor P/A for various dielectrics for each of 512 separate blade geometries. These 512 geometries were uniformly selected from the parameter space shown in Table II, describing the limited domain of geometries and dielectrics which, in general, are observed for grass blades. For a given geometry, six constants c_n must be determined, three for each P_{xx}/A and P_{yy}/A. Using the results of the numerical model at three distinct dielectric constants, a non-linear system of three equations ($P(\epsilon_1)/A$, $P(\epsilon_2)/A$, $P(\epsilon_3)/A$) with three unknowns (c_1, c_2, c_3) is formed using (13). Thus, nonlinear inversion techniques can be used to determine the three elements of c [3, ch. 9]. However, because (13) is merely an approximation, and not an exact solution for P/A, inversion techniques may lead to erroneous results. Inversion techniques force a solution which produces zero error at each of the three data points $P(\epsilon_1)/A$, $P(\epsilon_2)/A$, and $P(\epsilon_3)/A$, however, in so doing may severely affect the accuracy of the approximation at other dielectric constant values.

As an alternative solution, the polarizability tensor elements were numerically computed at additional dielectric constants (six were found to be sufficient), and the three coefficients of c were then determined by locating those values which minimized the sum of the squared errors between (13) and the numerical data at these six dielectric values. Although the resulting algebraic approximation may exhibit nonzero error at all six dielectric values, the solution does match the numerical model results across the entire range of dielectric values. To determine an optimum selection of the vector c, the conjugate gradient technique [3, ch. 10] was implemented which iteratively converges to the values of c_1, c_2, and c_3 that minimize the total squared error equation:

$$\sum_{n=1}^{6}\left(P_{num}(\epsilon_n)/A - c_0\frac{\epsilon_n - 1}{\epsilon_n + 1}\cdot\frac{\epsilon_n + c_1}{\epsilon_n + c_2}\right)^2, \tag{15}$$

where $P_{num}(\epsilon_n)/A$ is the polarizability tensor element of a specified blade geometry with dielectric ϵ_n, as determined by the numerical model. Fig. 9 contrasts the difference in the solutions obtained by using both an inversion and a minimization technique on the same set of numerical data. The minimization (conjugate gradient) technique selects coefficients c which result in a model matching all the numeric data points, whereas the inversion (Newton–Raphson) method results in a range of dielectric constants where (13) produces erroneous values for P/A.

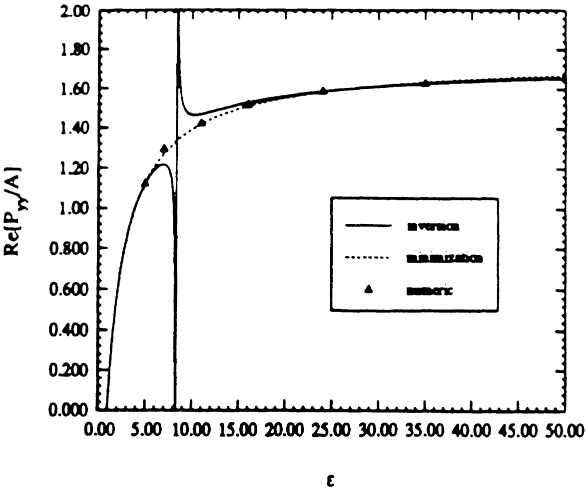

Fig. 9 . Re[P_{yy}/A] versus ϵ as predicted by (13) using coefficients c determined by both inversion and error minimization methods. The inversion method results in large errors for some values of ϵ.

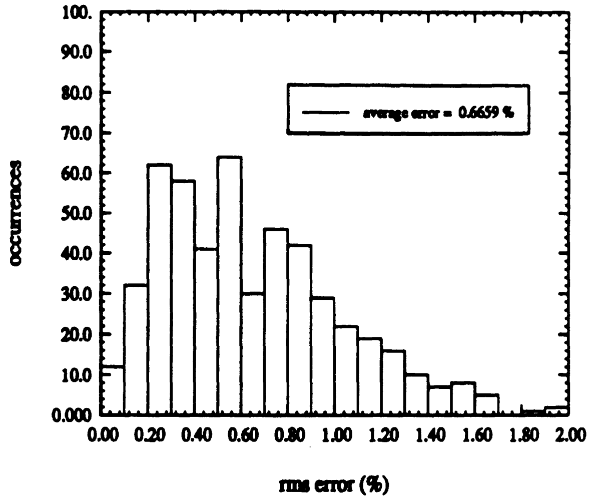

Fig. 10. Histogram showing the distribution of the average rms error resulting from the approximation of (13) determined at 512 test geometries. The coefficients c were selected using a conjugate gradient error minimization technique.

Therefore, the conjugate gradient method was implemented on the selected 512 geometries to provide two sets of vector c (one set for each P_{xx}/A and P_{yy}/A) for each of the 512 cases. Fig. 10 shows a histogram over the 512 geometries of the average rms error between the numerical model and the analytic approximation, using the coefficients as selected by the conjugate gradient technique. The average error for P_{xx}/A was 0.07%, whereas the average error for P_{yy}/A was determined to be approximately 0.7 %. For each of the 512 geometries, a set of constants was found which provided an accurate model of the relationship between the dielectric constant and the polarizability tensor.

The conjugate gradient method converges to a set of coefficients c which provide a model with a minimum total

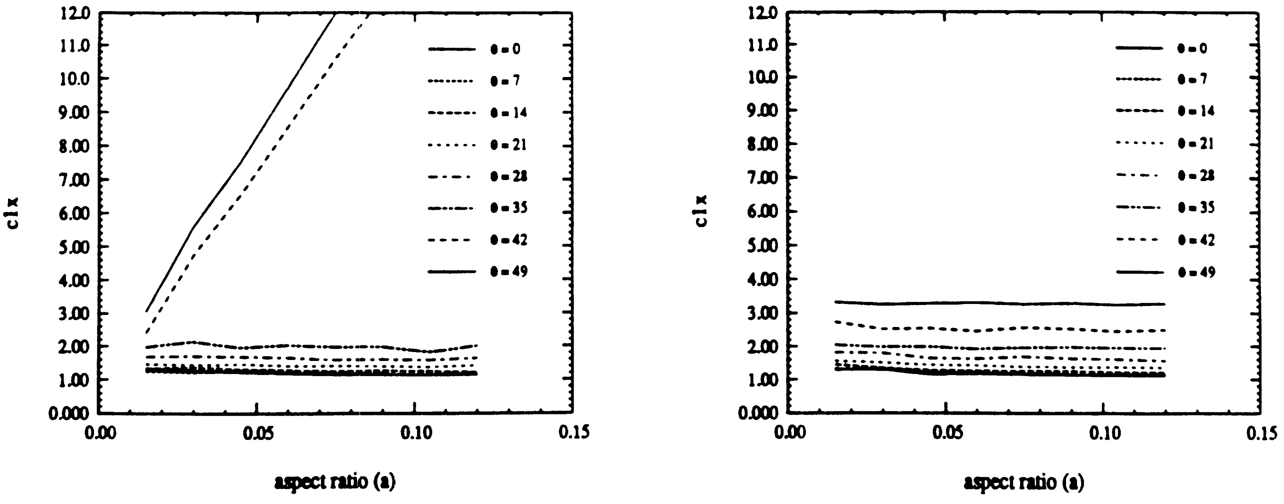

(a) (b)

Fig. 11. Two valid solutions for constant c_1 (of P_{xx}/A) versus aspect ratio and blade angle; a dual-mode solution (a) resulting in a discontinuous function of c_1 versus θ, and a single-mode solution (b) resulting in a continuous function of c_1.

squared error. However, this minimum may not be the global minimum, as the conjugate gradient may converge to any number of local minima, depending on the initial value of c used by the conjugate gradient routine. These minima can be thought of as different "modes," with each mode producing a slightly different curve for (13), each matching the six numerical data points $(P_{num}(\epsilon_n)/A)$ in a slightly different fashion. For instance, one mode may result in a model which slightly underestimates the first three data points $P(\epsilon)/A$ and slightly overestimates the last three, whereas for another mode the reverse may be true. Many of these modes may produce acceptable accuracy, but the desired solution is the mode associated with the smallest error (the global minimum). However, the mode associated with the global minimum at one geometry may not be the mode corresponding to the global minimum at another. Since we are ultimately seeking an expression relating c_1, c_2, and c_3 to the shape parameters v, a, and θ, a solution involving a single mode is required to avoid discontinuities in c across the domain of Table II. For example, Fig. 11(a) shows a solution for constant c_1 versus aspect ratio for various blade angle values. For blade angle values from $\theta = 0°$ to $\theta = 35°$, the minimum is associated with a single mode, however for $\theta = 42°$ and 49° the conjugate gradient algorithm converges to a different minimum, resulting in significantly different data and a large discontinuity in c_1 versus θ. Fig. 11(b) shows the single-mode solution, a solution which is well behaved and continuous across both aspect ratio and blade angle.

If, for various regions of the blade shape parameter space (Table II), the global minimum is associated with separate modes, then the selection of the "optimum" mode becomes a compromise between minimizing the average error across the parameter space and minimizing the maximum error occurring at any given point. In addition, forcing the conjugate gradient routine to converge to the same mode for all blade geometries may also prove to be difficult, as mode selection is determined only by the initial value of c of the conjugate gradient algorithm. This initial value must be "close" enough to the correct solution for the conjugate gradient method to converge to that minimum rather than to another. Since the correct solution is unknown, selection of the initial values of c for a given geometry is problematic. Often several trials were required to force the conjugate gradient to converge to the correct mode. However, as c was determined for a significant number of blade geometries, an approximate relationship between the elements of c and the shape parameters v, a, and θ was inferred, and then used to properly determine an initial value for a given geometry.

VII. POLYNOMIAL FIT

Once a single-mode solution for c for both P_{xx} and P_{yy} was determined for all 512 sample geometries, the mapping between c and the shape parameters v, a, and θ, could be replaced with a polynomial expression used to estimate the values of c across the domain of Table II. These polynomials can then be used in (14) to provide a complete algebraic approximation of the numerical scattering formulation of Section III.

To match a polynomial approximation to the data c, a solution is assumed which is a linear combination of M basis functions, each basis function being an expression involving the parameters v, a, and θ. The number of basis functions is a compromise between the complexity and accuracy of the polynomial approximation, and for this application a third-order expansion consisting of 20 basis functions was chosen. For the polynomials associated with the normalized polarizability tensor P_{xx}/A, the basis functions (as determined by trial and error) are expansions of the parameters v, $(1/a)$, and $\cos\theta$; the general polynomial approximations for c are therefore given as

$$c_n = \sum_{i=0}^{3}\sum_{j=0}^{3}\sum_{k=0}^{3} b_m \frac{\mathrm{v}^i \cos^j\theta}{\mathrm{a}^k}, \tag{16}$$

such that $i + j + k \leq 3$, $m = 1,20$, and $n = 1,3$. For the polynomials of P_{yy}/A, the chosen basis functions are an expansion of the parameters v, $(1/a)$, and $\sec\theta$, thus the

TABLE III
VALUES OF THE 20 COEFFICIENTS b_m FOR EACH OF THE SIX EXPANSIONS OF c_n AS GIVEN BY (17) AND (18)

		P_{xx}/A			P_{yy}/A		
i,j,k	b_m	c_0	c_1	c_2	c_0	c_1	c_2
0,0,0	b_1	-11.18	13.29	17.82	-12.94	28.02	-9.268
0,0,1	b_2	-0.8747	-3.469E-02	1.769	0.2781	9.4470E-03	-0.2167
0,0,2	b_3	-1.307E-02	-3.569E-05	-1.466E-02	-1.768E-03	2.574E-03	-4.961E-03
0,0,3	b_4	1.031E-04	-1.287E-06	1.108E-04	1.253E-05	-1.111E-05	5.296E-05
0,1,0	b_5	50.81	-24.15	-49.43	16.92	-16.94	21.39
0,1,1	b_6	3.444	9.537E-02	-1.197	-0.491	-5.920E-02	0.595
0,1,2	b_7	5.384E-04	1.068E-04	8.748E-04	4.137E-04	-1.204E-03	-1.098E-03
0,2,0	b_8	-85.25	15.15	44.45	-0.9688	-2.717	-4.099
0,2,1	b_9	-1.611	-5.654E-02	0.5463	0.2635	-2.507E-02	-0.1640
0,3,0	b_{10}	46.74	-3.199	-13.91	-2.435	3.558	-1.006
1,0,0	b_{11}	-10.16	-0.3726	-7.273	24.61	-38.03	38.43
1,0,1	b_{12}	0.5911	2.250E-02	-0.3542	0.1876	-0.2218	6.614E-02
1,0,2	b_{13}	6.520E-04	-4.893E-06	5.482E-04	-1.720E-04	7.368E-04	1.796E-04
1,1,0	b_{14}	42.69	-8.406	-1.913	-37.74	55.67	-54.33
1,1,1	b_{15}	-0.6183	-2.045E-02	0.2870	-0.1915	0.1518	-5.175E-02
1,2,0	b_{16}	-31.18	8.512	10.01	12.74	-16.36	15.16
2,0,0	b_{17}	-3.462	0.6613	6.350	-0.5466	1.895	-1.887
2,0,1	b_{18}	-6.594E-02	-3.032E-03	5.077E-02	3.487E-02	-1.413E-02	-2.532E-03
2,1,0	b_{19}	2.133	-5.807E-02	-4.617	1.855	-4.746	5.115
3,0,0	b_{20}	0.2449	4.645E-02	-0.5782	-0.3788	0.7839	-0.9007

polynomials are given as

$$c_n = \sum_{i=0}^{3}\sum_{j=0}^{3}\sum_{k=0}^{3} b_m \frac{\mathrm{v}^i \sec^j \theta}{\mathrm{a}^k}, \tag{17}$$

such that $i + j + k \leq 3$, $m = 1, 20$, and $n = 1, 3$.

Using orthogonality principles, the values of the coefficients b_m are determined by solving the linear estimation equation [3, ch. 141]

$$(X^T \cdot X) \cdot b = X^T \cdot C \tag{18}$$

where $\boldsymbol{b}$ is a 20 element vector containing the polynomial coefficients, $\boldsymbol{C}$ is a 512 element vector containing the conjugate gradient estimate of c_n at the 512 test geometries, and $\boldsymbol{X}$ is a 512 × 20 matrix containing rows of the 20 basis functions evaluated at the 512 test geometries. The coefficients $\boldsymbol{b}$ determined by this computation are given in Table III. Thus, (14), (16), and (17), along with the coefficients listed in Table III, provide a fast algebraic approximation to the slower numerical model of Section III.

VIII. RESULTS

To test the accuracy of this algebraic approximation, 3125 test points, covering the range of shape parameters and complex dielectric constants found in Table II, were selected and used to determine the complex elements of the polarizability tensor with both the numerical model and the algebraic approximation. The magnitude of the vector formed by P_{xx} and P_{yy}, defined as:

$$|P| = \sqrt{P_{xx}P_{xx}^* + P_{yy}P_{yy}^*}, \tag{19}$$

was calculated for both models, and this data was used to build the histogram of Fig. 12, showing the percent error of the algebraic approximation of $|P|$ as compared to the numerical model. As estimated from 3125 test cases, the algebraic approximation exhibited little bias, with a mean error of 0.2%, in addition to producing an acceptable rms error of 2.5%. Fig. 13 shows the accuracy typical of the approximation, displaying the predictions of both the numeric and algebraic models for $\mathrm{Re}[P_{xx}/A]$ versus aspect ratio at a number of blade angle values.

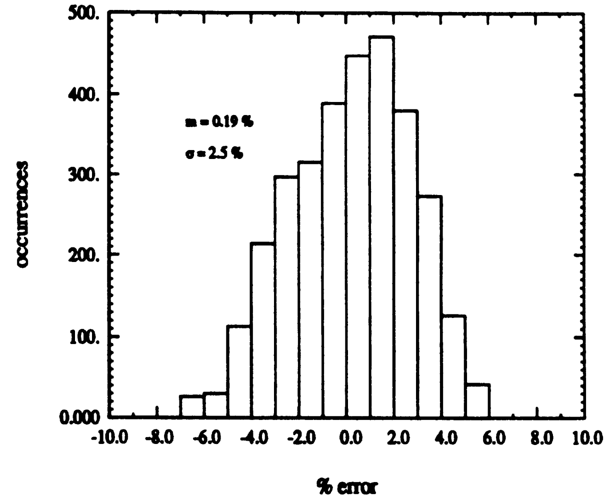

Fig. 12. Histogram showing the distribution of the error resulting from the approximation given by (14), as determined using 3125 test cases covering the range of parameters given in Table II.

IX. CONCLUSIONS

Using a numerical solution to solve the scattering problem of cylinders with arbitrary cross sections, it was determined that blade shape, in addition to blade size, can significantly affect the scattering solution for a long, thin grass blade structure. Likewise, a simple radiative-transfer model demonstrates

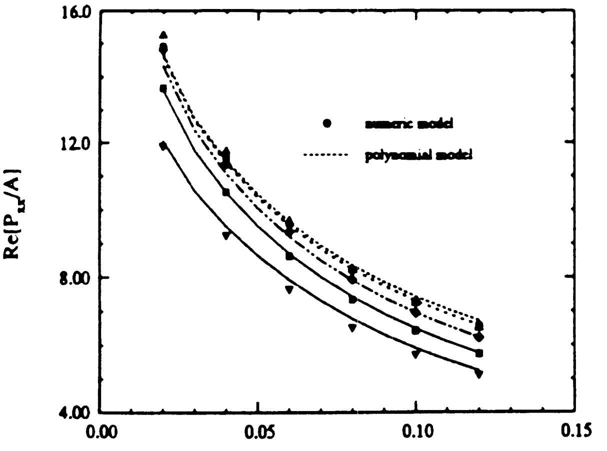

Fig. 13. Comparison of the polynomial approximation to the numerical model predictions for Re$[P_{xx}/A]$ versus aspect ratio at various blade angles.

that the calculated backscattering coefficients for grassland target can also be significantly affected. The numerical scattering model is required for characterizing scattering by complex grass blade shapes. However, direct implementation of this numerical model into a larger radiative-transfer solution for grassland targets can result in a model of unacceptable computation time and complexity, especially when the radiative-transfer model is used in an inversion algorithm.

Although the complexity of the numerical model is necessary to describe a cylinder of arbitrary cross section, the cross sections associated with grass blades are not arbitrary but are instead limited to those described by parameters a, v, and θ, and by the domain of Table II. These limits greatly reduce the information requirement of the numerical scattering model, thereby allowing for its replacement by a relatively simple analytical approximation. By combining the relationship of P/A with ϵ (13) and the relationship of c versus a, v, and θ inferred from a small but representative sample of numeric solutions (16), (17), an analytic approximation was developed that can predict the scattering response of blade shaped cylinders both rapidly and accurately.

REFERENCES

[1] J. B. Keller, R. E. Kleinman, and T. B. A. Senior, "Dipole moments in Rayleigh scattering," *J. Inst. Math. Appl.*, vol. 9, pp. 14–22, 1972.

[2] R. E. Kleinman and T.B.A. Senior, "Rayleigh scattering," in *Low and High Frequency Asymptotics*, V. K. Vardan and V. V. Vardan, Eds. Amsterdam: North-Holland, 1986, pp. 1–70.

[3] W. H. Press, *Numerical Recipes*. Cambridge: Cambridge University Press, 1989.

[4] G. T. Ruck, D. E. Barrick, W. D. Stuart, and C. K. Krichbaum, *Radar Cross Section Handbook*, vol. 1. New York: Plenum Press, 1970.

[5] K. Sarabandi and T. B. A Senior, "Low-frequency scattering from cylindrical structures at oblique incidence," *IEEE Trans. Geosci. Remote Sensing*, vol. 28, no. 5, pp. 879–885, 1990.

[6] K. Sarabandi, T. B. A. Senior, and F. T. Ulaby, "Effect of curvature on the backscattering from a leaf," *J. Electromag. Waves Appl.*, pp. 653–670, 1988.

[7] K. Sarabandi and F.T. Ulaby, "High frequency scattering from corrugated stratified cylinders',' *IEEE Trans. Antennas Propagat.*, vol. 39, pp. 512–520, Apr. 1991.

[8] T.B.A. Senior, and K. Sarabandi, "Scattering models for point targets," in *Radar Polarimetry for Geoscience Applications*, F.T. Ulaby and C. Elachi, Eds. Norwood, MA: Artech House, 1990.

[9] L. Tsang, J. A. Kong, and R. T. Shin, *Theory of Microwave Remote Sensing*. New York: Wiley, 1985, chapter 3.

[10] Y. Kuga, M. W. Whitt, K. C. McDonald, and F. T. Ulaby, "Scattering models for distributed targets," in *Radar Polarimetry for Geoscience Applications*, F.T. Ulaby and C. Elachi, Eds. Norwood, MA: Artech House, 1990.

[11] F. T. Ulaby, R. K. Moore, and A. K. Fung, *Microwave Remote Sensing: Active and Passive*. Norwood, MA: Artech House, 1981, chapter 13.

[12] F. T. Ulaby, K. Sarabandi, K. McDonald, M. Whitt, and M. C. Dobson, "Michigan microwave canopy scattering model," *Int. J. Remote Sensing*, vol. 11, no. 7, pp. 1223–1253, 1990.

[13] M. I. Herman and J. L. Volakis, "High-frequency scattering by a resistive strip and extensions to conductive and impedance strips," *Radio Sci.*, vol. 22, no. 3, pp. 335–349, 1987.

[14] R. F. Harrington and J. R. Mautz, "An impedance sheet approximation for thin dielectric shells," *IEEE Trans. Antennas Propag.*, vol. AP-25, pp. 531–534, 1975.

James M. Stiles was born in Kansas City, MO, in 1961. He received the B.S.E.E. degree from the University of Missouri in 1983, and the M.S.E.E. degree from Southern Methodist University in 1987. He is presently pursuing the Ph.D. degree in electrical engineering at the University of Michigan.

From 1983 to 1990 he was an RF Design Engineer for Texas Instruments Inc., Dallas, TX. His interest include electromagnetic scattering from vegetation and application of estimation theory to microwave remote sensing.

Kamal Sarabandi (S'87–M'90–SM'93) received the B.S. degree in electrical engineering from Sharif University of Technology, Tehran, Iran, in 1980, the M.S.E. degree in electrical engineering in 1986, and the M.S. degree in mathematics and the Ph.D. degree in electrical engineering in 1989, all three from the University of Michigan.

From 1980 to 1984 he worked as a Microwave Engineer in the Telecommunication Research Center in Iran. He is presently an Assistant Professor in the Department of Electrical Engineering and Computer Science at the University of Michigan. His research interests inlcude elctromagnetic scattering, microwave and milimeter wave remote sensing, and calibration of polarimetric SAR systems.

Dr. Sarabandi is a member of the Electromagnetics Academy and USNC/URSI Commission F.

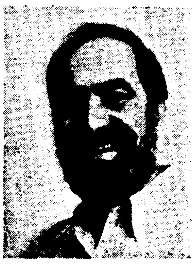

Fawwaz T. Ulaby (M'68–SM'74–F'80) received the B.S. degree in physics from the American University of Beirut, Lebanon, in 1964 and the M.S.E.E. and Ph.D. degrees in electrical engineering from the University of Texas, Austin, in 1966 and 1968, respectively.

He is currently Professor of Electrical Engineering and Computer Science at the University of Michigan, Ann Arbor, and Director of the NASA Center for Space Terahertz Technology. His current interests include microwave and millimeter wave remote sensing, radar systems, and radio wave propagation. He has authored several books and published over 400 papers and reports on these subjects.

Dr. Ulaby has received numerous awards, inluding the IEEE Geoscience and Remote Sensing Distinguished Achievement Award in 1983, the IEEE Centennial Medal in 1984, and the Kuwait Prize in Applied Science in 1986.

A Scattering Model for Thin Dielectric Cylinders of Arbitrary Cross Section and Electrical Length

James M. Stiles, *Member, IEEE*, and Kamal Sarabandi, *Senior Member, IEEE*

***Abstract*—A scattering solution for long, thin, dielectric cylinders of arbitrary cross section and electrical length is presented. The infinite-cylinder scattering formulation is shown to be an asymptotic solution for the finite-cylinder case, regardless of cylinder electrical length or cross section. The generalized Rayleigh–Gans (GRG) approximation for circular cylinders is shown to be a specific case of this general formulation, and therefore, the assertions of GRG are explicitly proven. A moment-method (MM) solution for thin circular cylinders is likewise presented and is used to examine and quantify the asymptotic errors associated with this solution.**

I. INTRODUCTION

IN activities such as radar remote sensing, accurate scattering models of elemental constituents are essential in constructing robust scattering models of random media such as vegetation. This challenge is often compounded by the arbitrary and complex nature of these constituent elements. For example, a type of element often encountered are long, thin dielectric cylinders of arbitrary cross section, including grasses and needle structures. In the microwave region, the radius of these cylinders are usually very small compared to the incident wavelength, whereas the electrical length may take any value. This generality in structure precludes the implementation of specific scattering solutions. The arbitrary value of electrical length $k\ell$ eliminates asymptotic solutions such as Rayleigh ($k\ell \ll 1$) or physical optics ($k\ell \gg 1$), and the generally noncanonical cross sections leave inapplicable solutions for circular and elliptical structures. Thus, a scattering solution is required which accurately comprehends these arbitrary particles.

One relevant analysis is that of Sarabandi and Senior [1], who explicitly derived the scattering solution of an electrically thin, but infinitely long, dielectric cylinder of arbitrary cross section. This work provides a general solution for the internal electric fields and demonstrates that the far-field scattering can be expressed in terms of a dipole moment per unit length. Using the high-frequency approximation, the scattering from a finite, but electrically long, ($k\ell \gg 1$) cylinder can be approximated by truncating the solution of the equivalent infinite length case. Although this solution is correct for arbitrary cross sections, its validity can apparently be justified only for cylinders of large electrical length $k\ell$.

A solution which is often employed to model circular cylinders of smaller $k\ell$ is the generalized Rayleigh–Gans approximation (GRG) introduced by Schiffer and Thielheim [2]. In this approximation, terms of the Borne (or Rayleigh–Gans) approximation are modified by the Rayleigh solution of a long, thin, spheroidal particle. The GRG approximation is said to be valid for electrically small, circular dielectric cylinders, provided that their normalized length ℓ/a is very large. No constraint is explicitly placed on electrical length $k\ell$. The GRG approximation was presented by first hypothesizing the solution and then successfully comparing the results to the asymptotic solutions known for both the long ($k\ell \ll 1$) and short ($k\ell \gg 1$) wavelength cases. On this basis, it was inferred that GRG validity is independent of electrical length. Whereas this presentation provides evidence as to the accuracy of the GRG approximation, it does not prove its general validity; the scattering from objects with dimensions on the order of a wavelength is often quite different from either the short or long wavelength cases. In addition, the analysis does not address the issue of cylinder cross section, only circular cylinders were considered.

In this paper, a scattering solution for the general case of an electrically-thin dielectric cylinder of arbitrary cross section and electrical length will be presented. The solution will be explicitly shown to be the unique asymptotic solution to the scattering problem as the electrical radius ka converges to zero. A moment-method (MM) solution will likewise be implemented to quantify the convergence of this asymptotic solution.

II. AN ANALYSIS OF THIN CYLINDER SCATTERING

Consider an infinite length dielectric cylinder lying along the z-axis. This cylinder is illuminated by a uniform plane wave $\boldsymbol{E}^i(\overline{r}) = \hat{e}\, e^{ik_0\hat{k}^i\cdot\overline{r}}$ where $\hat{e}\cdot\hat{k}^i = 0, \hat{e} = e^i_x\hat{x} + e^i_y\hat{y} + e^i_z\hat{z}$, and $\hat{k}^i$ is the propagation direction vector, $\hat{k}^i = \sin\beta\cos\phi\ \hat{x} + \sin\beta\sin\phi\ \hat{y} + \cos\beta\ \hat{z}$. As the electrical radius of the cylinder approaches zero ($ka \to 0$), the total electric field in the interior of the cylinder is given by Sarabandi and Senior [1] as

$$\boldsymbol{E}(\overline{r}) = (-e^i_x\ \nabla\Phi_1(\overline{\rho}) - e^i_y\ \nabla\Phi_2(\overline{\rho}) + e^i_z\ \hat{z})e^{ik_0\cos\beta z} \quad (1)$$

Manuscript received January 27, 1995; revised September 18, 1995.

The authors are with the Radiation Laboratory, Department of Electrical Engineering and Computer Science, University of Michigan, Ann Arbor, MI 48109 USA.

Publisher Item Identifier S 0018-926X(96)01211-2.

0018-926X/96$05.00 © 1996 IEEE

where $\Phi_1(\overline{\rho})$ and $\Phi_2(\overline{\rho})$ are electrostatic potentials specified as the solution to the following integral equations [1]

$$\begin{aligned}\Phi_1(\overline{\rho}) + x + b_1 &= \frac{(\epsilon_r - 1)}{2\pi} \int_A \nabla_t' \Phi_1(\overline{\rho}') \cdot \nabla_t' \ln |\overline{\rho} - \overline{\rho}'| \, d_A' \\ \Phi_2(\overline{\rho}) + y + b_2 &= \frac{(\epsilon_r - 1)}{2\pi} \int_A \nabla_t' \Phi_2(\overline{\rho}') \cdot \nabla_t' \ln |\overline{\rho} - \overline{\rho}'| \, d_A'.\end{aligned} \tag{2}$$

The constants b_1 and b_2 are arbitrary, and A defines the area of the cylinder cross section. Using the physical optics approximation, this solution can likewise be applied to finite cylinders, provided its electrical length $k\ell$ is sufficiently large. From this formulation, the scattering solution for a thin cylinder of circular cross section can be determined

$$E(\overline{r}) = \left(\frac{2e_x^i}{\epsilon_r + 1} \hat{x} + \frac{2e_y^i}{\epsilon_r + 1} \hat{y} + e_z^i \hat{z} \right) e^{\imath k_0 \cos\beta z}. \tag{3}$$

This solution, derived from the infinite cylinder formulation, is identical to that provided by the GRG approximation. Thus, for a circular cylinder the two solutions resulting from each formulation are in agreement. However, their general validity regions are in conflict. The GRG approximation claims that the above expression is valid for all electrical lengths $k\ell$, whereas the infinite cylinder approximation has only a high-frequency justification of $k\ell \gg 1$. The requirement for the normalized cylinder length ($\ell/a \gg 1$) is implied in the infinite cylinder approximation (since $ka \ll 1$, then $k\ell/ka \gg 1$), and explicitly required by GRG.

If the assertions of the GRG approximation are correct, it suggests that the validity limits placed on the truncated infinite cylinder solution are too restrictive. That is, in addition to the high-frequency limit ($k\ell \gg 1$), the infinite-cylinder solution could likewise be applied to finite cylinders with electrical lengths in the resonance ($kl \approx 1$) and Rayleigh ($kl \ll 1$) regions. However, given the heuristic nature of the GRG approximation, this is strictly conjecture, particularly with regard to noncircular cross sections. Thus, we seek to determine under what conditions (1) and (2) define a valid scattering solution for thin, finite dielectric cylinders. Are they valid only for electrically-long cylinders, or does the validity extend to cylinders of other $k\ell$? If so, is this true only for circular cylinders, or is the solution generally valid for all cross sections?

If a formulation $E(\overline{r})$ is a valid electromagnetic solution, then it will uniquely satisfy the integral equation which describes the scattering problem, $E(\overline{r}) = E^i(\overline{r}) + E^s(\overline{r})$, where the scattered field $E^s(\overline{r})$ is given as

$$E^s(\overline{r}) = [k_0^2 + \nabla\nabla\cdot] \int_V (\epsilon_r - 1) E(\overline{r}') g_0(|\overline{r} - \overline{r}'|) \, dv' \tag{4}$$

and $g_0(|\overline{r} - \overline{r}'|)$ is the free space Green's function. For a given type of scatterer (e.g., thin cylinders), a function $E(\overline{r})$ may in general satisfy the integral equation, or perhaps satisfy only under specific conditions, such as a circular cross section or infinite electrical length. Therefore, to determine the validity of the truncated infinite-cylinder solution, (1) and (2) will be inserted into the integral equation for a thin finite cylinder and evaluated. The conditions under which the integral equation is satisfied will then be determined, thus defining the validity regions of this solution.

A. Transverse Components

Since (1) is a superposition of three terms, each proportional to a single component of the incident electric field vector (e_x^i, e_y^i, e_z^i), each term must individually satisfy the integral equation in order for the total solution to be valid. We first examine the transverse term proportional to e_x^i, given as

$$E(\overline{r}) = -e_x^i \nabla \Phi_1(\overline{\rho}) e^{\imath k_0 \cos\beta z}. \tag{5}$$

Inserting (1) into (4), evaluating the integrals and making the substitution $\overline{kr} = k_0 \overline{r}$, the scattered field $E^s(\overline{r})$ is given as

$$\begin{aligned} E^s(\overline{kr}/k_0) = &-e_x^i \frac{(\epsilon_r - 1)}{4\pi} \int_{k^2 A} \nabla_{kt} \Phi_1(\overline{k\rho}'/k_0) \\ &\cdot \int_{k\ell} \frac{e^{\imath kz' \cos\beta} e^{\imath |\overline{kr} - \overline{kr}'|}}{|\overline{kr} - \overline{kr}'|} \, dkz' \, dk_A^{2'} \\ &+ e_x^i \frac{\imath(\epsilon_r - 1)}{4\pi} \int_{kC} \hat{n}' \cdot \nabla_{kt} \Phi_1(\overline{k\rho}'/k_0) \\ &\cdot \int_{k\ell} \frac{e^{\imath kz' \cos\beta} e^{\imath |\overline{kr} - \overline{kr}'|}}{|\overline{kr} - \overline{kr}'|^2} (\overline{kr} - \overline{kr}') \, dkz' \, dkc' \\ &- e_x^i \frac{(\epsilon_r - 1)}{4\pi} \int_{kC} \hat{n}' \cdot \nabla_{kt} \Phi_1(\overline{k\rho}'/k_0) \\ &\cdot \int_{k\ell} \frac{e^{\imath kz' \cos\beta} e^{\imath |\overline{kr} - \overline{kr}'|}}{|\overline{kr} - \overline{kr}'|^3} (\overline{kr} - \overline{kr}') \, dkz' \, dkc'. \end{aligned} \tag{6}$$

The electrical length $k\ell$ is finite but otherwise arbitrary, kc defines the outer contour of the arbitrary cylinder cross section, and $k^2 A$ similarly defines cross section area. However, since the inserted solution (1) is valid in the limit as electrical radius ka approaches zero, this constraint must likewise be placed on the above equation. Therefore, we seek to evaluate the above integral in the limit as ka approaches zero ($\lim_{ka \to 0} E^s(\overline{kr}/k_0)$).

Each of the three terms in (6) contain an explicit integral of kz', but none can be directly evaluated. However, since the integration is over a finite region $k\ell$, the exponential term can be approximated in the region $-k\ell/2 < kz < k\ell/2$ as its Taylor series expansion

$$e^{\imath |\overline{kr} - \overline{kr}'| + \imath kz' \cos\beta} \approx \sum_{n=0}^{N} \frac{(\imath |\overline{kr} - \overline{kr}'| + \imath kz' \cos\beta)^n}{n!} \tag{7}$$

where N is arbitrarily large. Inserting this series into the kz' integrals, the order of integration and summation can be interchanged, since both N and $k\ell$ are finite. The integration of each term can now be directly evaluated, resulting in a series whose coefficients are in terms of $|\overline{k\rho} - \overline{k\rho}'|$. For example, the

kz' integral from the first term of (6) can be approximated as

$$\begin{aligned}\int_{k\ell} &\frac{e^{\imath|\overline{kr}-\overline{kr}'|-\imath kz'\cos\beta}}{|\overline{kr}-\overline{kr}'|}\,dkz'\\ &=\sum_{n=0}^{N}\int_{k\ell}\frac{(\imath|\overline{kr}-\overline{kr}'|-\imath kz'\cos\beta)^n\,dkz'}{n!|\overline{kr}-\overline{kr}'|}\\ &\approx e^{\imath kz\cos\beta}(\mathrm{Ei}[\imath c_1(kl/2-kz)]\\ &\quad+\mathrm{Ei}[\imath c_2(kl/2+kz)]-2(\gamma+\imath\pi/2)\\ &\quad-2\ln[\sin\beta|\overline{k\rho}-\overline{k\rho}'|/2])+O(|\overline{k\rho}-\overline{k\rho}'|)\end{aligned}\tag{8}$$

where γ is Euler's constant, $c_1=1+\cos\beta.\,c_2=1-\cos\beta$ and $\mathrm{Ei}[x]$ is the exponential integral function defined as $\mathrm{Ei}[x]=-\int_{-x}^{\infty}(e^{-}t/t)\;dt$. Discarding the higher order elements of $O(|\overline{k\rho}-\overline{k\rho}'|)$, (8) provides an accurate approximation to the integral, providing $1\gg ka>|\overline{k\rho}-\overline{k\rho}'|$. Fig. 1 graphically displays this, showing both the approximation and a numerical solution to a representative integral.

Similar approximations can be determined for the remaining two kz' integrals. Inserting these into (6), the scattered field expression can now be evaluated in the limit as electrical radius ka approaches zero. The first two terms of (6) vanish, but the third terms remains nonzero, and the scattered field reduces to

$$\begin{aligned}\lim_{ka\to 0}&\boldsymbol{E}^s(\overline{kr}/k_0)\\ &=-e_x^i\frac{(\epsilon_r-1)}{4\pi}e^{\imath kz\cos\beta}\int_{kc}\hat{n}'\\ &\quad\cdot\nabla'_{kt}\Phi_1(\overline{k\rho}'/k_0)\frac{2(\overline{k\rho}-\overline{k\rho}')}{|\overline{k\rho}-\overline{k\rho}'|^2}\,dkc'\\ &=-e_x^i\frac{(\epsilon_r-1)}{2\pi}e^{\imath k_0z\cos\beta}\nabla_t\int_A\nabla'_t\Phi_1(\overline{\rho}')\\ &\quad\cdot\nabla'_t\ln|\overline{\rho}-\overline{\rho}'|\,d'_A.\end{aligned}\tag{9}$$

The task remaining is to therefore evaluate the integral over dA. Recall that the potential $\Phi_1(\overline{\rho})$ is not arbitrary, but is the unique solution to the integral (2). Notice the integral appearing in both (2) and (9) are identical, and from (2) is given as

$$\int_A\nabla'_t\Phi_1(\overline{\rho}')\cdot\nabla'_t\ln|\overline{\rho}-\overline{\rho}'|\,d'_A=\frac{2\pi}{(\epsilon_r-1)}(\Phi_1(\overline{\rho})+x+b_1).\tag{10}$$

This condition is now enforced by replacing the integral in (9) with equation (10). The scattered field reduces to

$$\begin{aligned}\boldsymbol{E}^s(\overline{r})&=-e_x^i\nabla_t(\Phi_1(\overline{\rho})+x+b_1)e^{\imath k_0z\cos\beta}\\ &=-e_x^i(\nabla_t\Phi_1(\overline{\rho})+\hat{x})e^{\imath k_0z\cos\beta}\end{aligned}\tag{11}$$

and the original integral equation is therefore

$$\begin{aligned}\boldsymbol{E}(\overline{r})&=\boldsymbol{E}^i(\overline{r})+\boldsymbol{E}^s(\overline{r})\\ &=e_x^ie^{\imath k_0z\cos\beta}\hat{x}-e_x^i(\nabla_t\Phi_1(\overline{\rho})+\hat{x})e^{\imath k_0z\cos\beta}\\ &=-e_x^i\nabla_t\Phi_1(\overline{\rho})=\boldsymbol{E}(\overline{r}).\end{aligned}\tag{12}$$

Insertion of the second transverse term $-e_y^i\nabla\Phi_2(\overline{\rho})$ leads to an identical evaluation and result. Thus, the transverse terms of (1) and (2) asymptotically satisfy the integral equation as ka approaches zero.

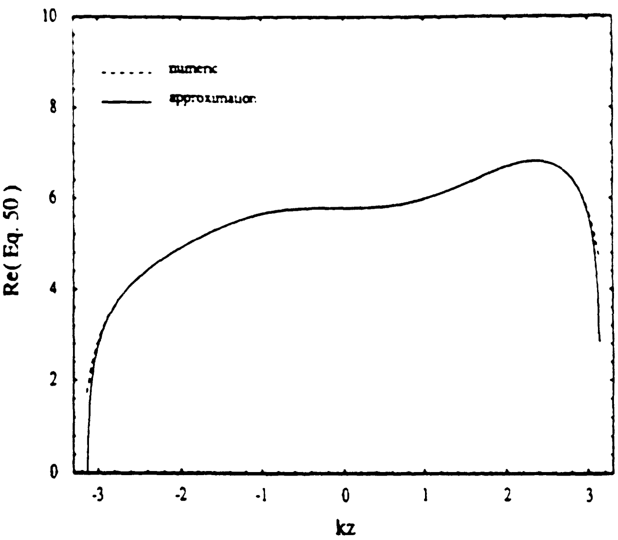

Fig. 1. The real part of (8), both the exact numerical evaluation and the analytic approximation ($ka=0.1, k\ell=2\pi, \epsilon_r=10$).

B. Axial Solution

The remaining component of (1) is the axial, z-directed term given as

$$\boldsymbol{E}(\overline{r})=\hat{z}e_z^ie^{\imath k_0\cos\beta z}.\tag{13}$$

Again, inserting this equation into (4), the scattered electric field can be expressed as

$$\begin{aligned}&\boldsymbol{E}^s(\overline{kr}/k_0)=\\ &\quad e_z^i\frac{(\epsilon_r-1)}{4\pi}\int_{k^2A}\int_{k\ell}\frac{e^{\imath kz'\cos\beta}e^{\imath|\overline{kr}-\overline{kr}'|}}{|\overline{kr}-\overline{kr}'|}\,dkz'\,dk_A^{2'}\\ &\quad-e_z^i\frac{\imath(\epsilon_r-1)}{4\pi}\int_{k^2A}\bigg|_{-k\ell/2}^{k\ell/2}\frac{e^{\imath kz'\cos\beta}e^{\imath|\overline{kr}-\overline{kr}'|}}{|\overline{kr}-\overline{kr}'|^2}\\ &\quad\cdot(\overline{kr}-\overline{kr}')\,dk_A^{2'}\\ &\quad+e_z^i\frac{(\epsilon_r-1)}{4\pi}\int_{k^2A}\bigg|_{-k\ell/2}^{k\ell/2}\frac{e^{\imath kz'\cos\beta}e^{\imath|\overline{kr}-\overline{kr}'|}}{|\overline{kr}-\overline{kr}'|^3}\\ &\quad\cdot(\overline{kr}-\overline{kr}')\,dk_A^{2'}\\ &\quad-e_z^i\frac{\cos\beta(\epsilon_r-1)}{4\pi}\int_{k^2A}\int_{-k\ell/2}^{k\ell/2}\frac{e^{\imath kz'\cos\beta}e^{\imath|\overline{kr}-\overline{kr}'|}}{|\overline{kr}-\overline{kr}'|^2}\\ &\quad\cdot(\overline{kr}-\overline{kr}')\,dkz'\,dk_A^{2'}\\ &\quad-e_z^i\frac{\imath\cos\beta(\epsilon_r-1)}{4\pi}\int_{k^2A}\int_{-k\ell/2}^{k\ell/2}\frac{e^{\imath kz'\cos\beta}e^{\imath|\overline{kr}-\overline{kr}'|}}{|\overline{kr}-\overline{kr}'|^3}\\ &\quad\cdot(\overline{kr}-\overline{kr}')\,dkz'\,dk_A^{2'}.\end{aligned}\tag{14}$$

The integrals involving kz' are the same as those encountered for the transverse case, therefore, their approximations can again be implemented in (14). As in the previous section, the limit for each term of (14) is determined as $ka\to 0$. However, we find that for the axial case, every term vanishes, not a single nonzero term remains. The scattered field is, therefore, approximately zero, and the integral equation reduces to $E(\bar{r}) = E^i(\bar{r})$. Since both $E(\bar{r})$ and $E^i(\bar{r})$ are equal to $e_z^i e^{ik_0 \cos\beta z}\hat{z}$, this equation is satisfied.

Thus, it has been explicitly demonstrated that the formulation of (1) and (2) obtained from the infinite cylinder solution, asymptotically satisfy the scattering-integral equation for a finite-dielectric cylinder as $ka \to 0$. It should be noted that nowhere in the preceding analysis was any specific condition or constraint required to satisfy the integral equation. No restriction or assumption was placed on cross section or electrical length. Thus, the infinite cylinder formulation is a valid scattering solution for electrically thin, finite-dielectric cylinders of all cross sections and electrical lengths. However, the solution is only asymptotically valid as the electrical radius approaches zero. Since kl is a fixed constant, as $ka \to 0$, the ratio $ka/kl = a/l$ likewise approaches zero. Therefore, ka must not only be numerically small ($ka \ll 1$), but small compared to the electrical length, as well $ka \ll k\ell$. To satisfy this last constraint, the normalized length ℓ/a is required to be large.

Finally, since this formulation is independent of $k\ell$, it is valid for Rayleigh cylinders where $k\ell \ll 1$. Thus, the electrostatic solutions $\Phi(\bar{\rho})$, derived for infinite cylinders, are likewise the asymptotic solutions for a Rayleigh cylinder as $\ell/a \to \infty$. The GRG approximation which considers circular cylinders is, therefore, a specific case of the more general approximation defined by (1) and (2). As such, the validity regions of the GRG approximation, being identical to the requirements stated above ($ka \ll 1, ka \ll k\ell$ for all $k\ell$), have been explicitly proven by the analysis of this section.

III. ASYMPTOTIC ERROR EVALUATION

As this solution is asymptotic, it will exhibit a finite error which becomes diminishingly small as $ka \to 0$. To evaluate the asymptotic error of (1) and (2), a moment-method (MM) solution was constructed to evaluate the scattering from a thin, circular, dielectric cylinder. It was assumed that the electric field in the cylinder is dependent on axial position z only; that is, the fields are constant with respect to the transverse dimension ρ. The interior field is therefore described as

$$E(\bar{r}) = e_x \frac{2\, f_x(z)}{(\epsilon_r + 1)}\hat{x} + e_y \frac{2\, f_y(z)}{(\epsilon_r + 1)}\hat{y} + f_z(z)\hat{z} \tag{15}$$

where the expressions $f_x(z), f_y(z)$, and $f_z(z)$ are unknown complex scalar functions. Comparing the above equation with (3), the values of $f_w(z) (w \in \{x, y, z\})$ predicted by the asymptotic scattering solution are $f_w(z) = e^{ik_0 \cos\beta z}$, so that $|f_w(z)| = 1.0$ for all k_0, β, and z.

The ability of the MM solution to accurately reflect the exact scattering solution depends on the general validity of (15). To test this accuracy, the moment method code was applied to a circular Rayleigh cylinder ($k\ell \gg 1$) at a variety of dielectrics and normalized lengths ℓ/a. The results were used to determine the polarizability tensor elements for each cylinder, and were then compared to the known values for circular cylinders [5]. These results are presented in Fig. 2. The MM solution matches the Rayleigh values well over all dielectrics and normalized lengths ℓ/a, thus providing evidence as to the accuracy of (15).

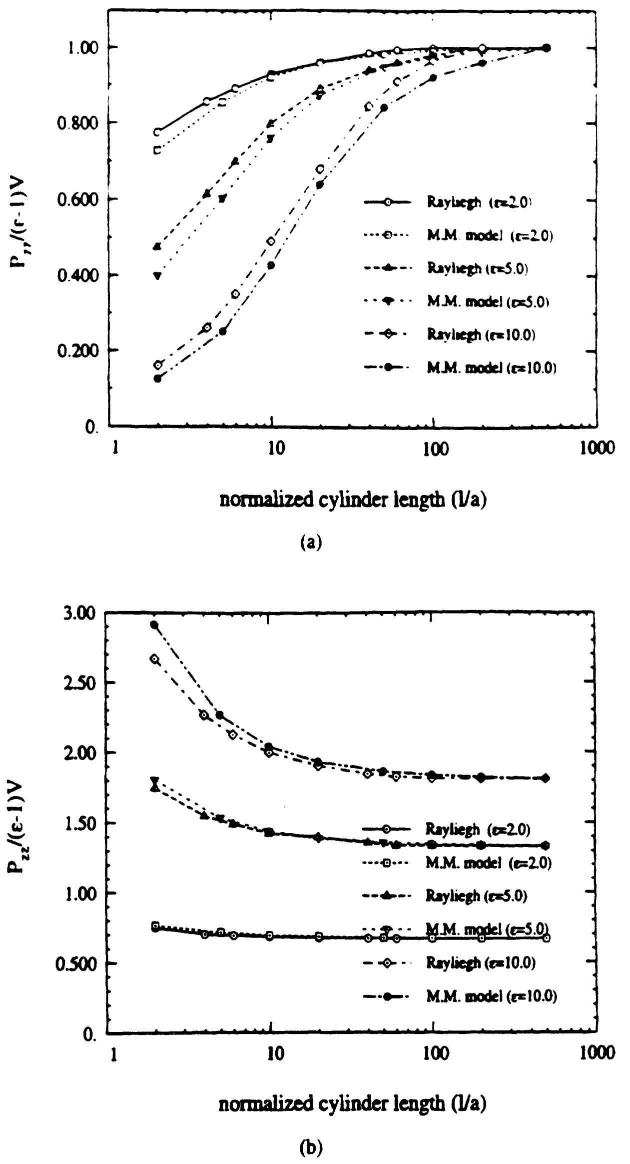

Fig. 2. (a) The axial and (b) transverse polarizability tensor elements of a circular cylinder, both the exact values and those determined using the MM model.

The MM solution was first used to evaluate the scattering from a thin cylinder with a large normalized length $\ell/a = 200$. The magnitude of $f(z)$ was determined at each point z along the cylinder for various electrical lengths. The results are given by Fig. 3, and show that the asymptotic solution ($|f_w(z)| = 1.0$) is valid at all points along the cylinder except for small regions near the cylinder ends. As expected, this is true regardless of electrical length $k\ell$. The error at the cylinder ends is likewise independent of $k\ell$, but is more pronounced for the axial component $f_z(z)$.

The analysis was then reversed, fixing the electrical length $k\ell = \pi/2$ and evaluating the MM solution at various normalized lengths ℓ/a. In contrast to $k\ell$, the scattering solution exhibits a strong dependence as a function of ℓ/a (Fig. 4). The result is a confirmation of the requirement that the

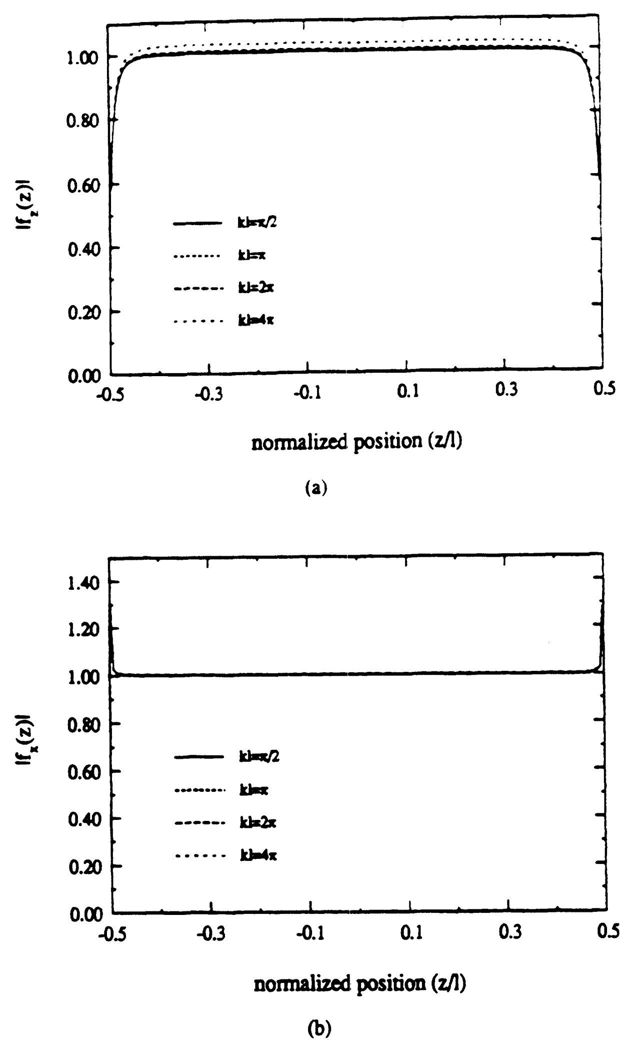

(a)

(b)

Fig. 3. (a) The axial and (b) transverse magnitude of the internal electric field in a thin circular cylinder for various electrical lengths $(\ell/a = 200, \epsilon_r = 5.0, \beta = \pi/2)$.

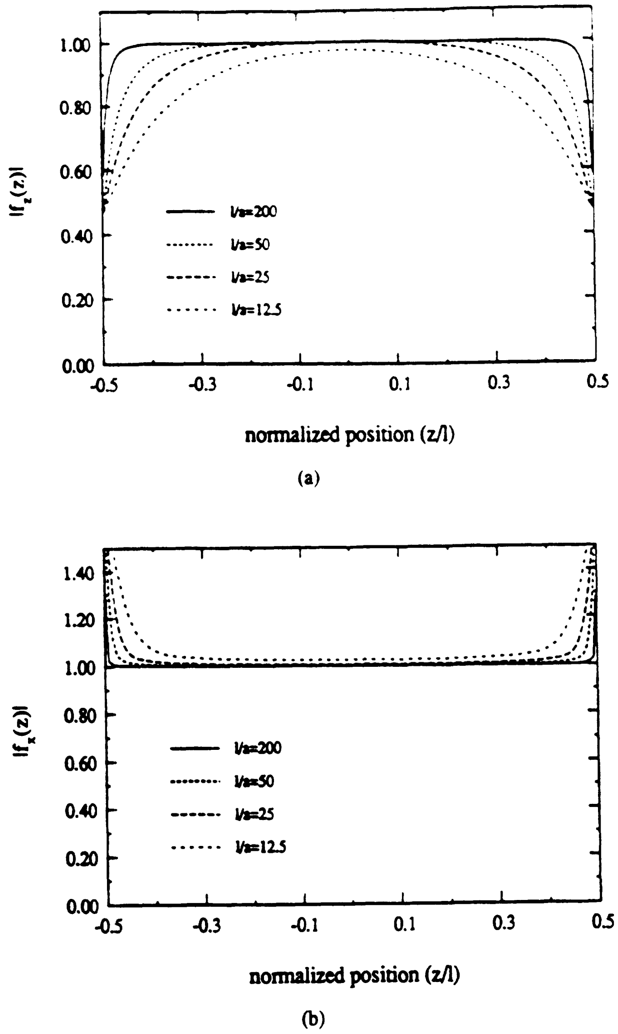

(a)

(b)

Fig. 4. (a) The axial and (b) transverse magnitude of the internal electric field in a thin circular cylinder for various normalized lengths $(k\ell = \pi/2, \epsilon_r = 5.0, \beta = \pi/2)$.

normalized length ℓ/a be large (i.e., $ka \ll kl$) to ensure a valid approximation. As the normalized length becomes smaller, the MM solution greatly diverges from the asymptotic approximation of $|f(z)| = 1$. The error at the cylinder end expands as ℓ/a is reduced, occupying an increasingly greater portion of total cylinder length. Eventually, the formulation of (1) and (2) no longer provide an accurate approximation to the actual electric field $E(\bar{r})$. Conversely, as ℓ/a increases, the error region will become diminishingly small.

To further examine its performance, the accuracy of the solution is examined as a function of both incidence angle and dielectric constant. Fig. 5 displays the MM solution calculated for an oblique incidence angle ($\beta = \pi/8$). Although the solution $f(z)$ is dependent on incidence angle β, almost no sensitivity to this parameter was detected in regard to approximation accuracy; the error regions at the ends of the cylinder remain constant regardless of incidence angle. Conversely, accuracy is greatly influenced by dielectric constant ϵ_r. Fig. 6 displays the MM solution for various dielectric constants. It is quite evident that as the value of ϵ_r is increased, so too does the region of significant error. This sensitivity to dielectric constant is observed almost entirely for the axial component $f_z(z)$; the transverse components display only minor sensitivity to ϵ_r.

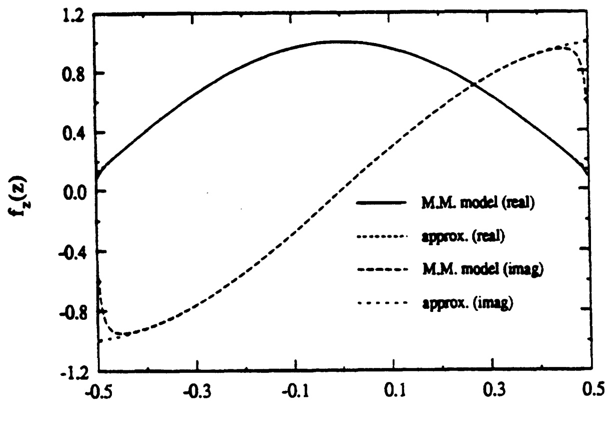

Fig. 5. The axial magnitude of the internal electric field in a thin circular cylinder for an oblique incidence angle ($\beta = 22.5$). Both the MM model and the infinite cylinder approximation are plotted $(k\ell = \pi . \ell/a = 200, \epsilon_r = 5.0)$.

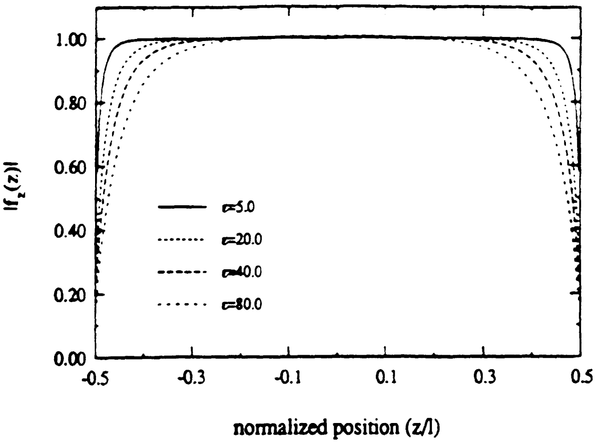

Fig. 6. The axial magnitude of the internal electric field in a thin circular cylinder for various dielectric values ($k\ell = \pi/2, \ell/a = 200, \beta = \pi/2$).

Using the MM solution as a standard, the validity limits of the asymptotic solution can be inferred. From the numerical results, we conclude that the accuracy of (1) and (2) are dependent mainly on normalized length ℓ/a and dielectric ϵ_r. The MM solution likewise demonstrates that for all conditions the axial component $\hat{z}$ exhibits significantly greater error than the transverse component. Therefore, the axial solution will be used to define limits on ℓ/a and ϵ_r.

The far-field scattering is a function of the internal field $E(\bar{r})$ and the free-space Green's function integrated over the cylinder length. Therefore, the metric selected to define accuracy is proportional to the average magnitude of the internal electric field, defined by integrating $|f_z(z)|$ over cylinder length ℓ

$$m = \frac{1}{\ell}\int_{-\ell/2}^{\ell/2} |f_z(z)|\, dz \propto \frac{1}{\ell}\int_{-\ell/2}^{\ell/2} |E_z(z)|\, dz. \qquad (16)$$

The asymptotic solution yields a value of $m = 1.0$ for all cases. As the solution breaks down, the actual value of m (as determined from the MM code) will decrease from this value. Placing an arbitrary error limit of 5% ($m > 0.95$), we determine from the numeric solution the following criteria for the validity of (1) and (2).

$$\ell/a > 20\sqrt{|\epsilon_r|}. \qquad (17)$$

In addition to the above requirement, the electrical radius ka must likewise be small. The upper bound on ka is determined by the error of the Rayleigh approximation, a topic which has been addressed previously and, therefore, will not be examined here [4, pp. 92–101].

IV. Far-Field Scattering from Thin Cylinders

The far-field scattering from a long, thin, dielectric cylinder can be determined by using the familiar far-field scattering equation [4, p. 55]

$$E^s = -k_0^2\hat{k}^s \times \hat{k}^s \times \Pi^e(\bar{r}) \qquad (18)$$

where the Hertz potential $\Pi^e(\bar{r})$ in the far field is given as

$$\Pi^e(\bar{r}) = -\frac{e^{ik_0 r}}{r}\frac{(\epsilon_r - 1)}{4\pi}\int_V E(\bar{r}')e^{-ik_0\hat{k}^s\cdot\bar{r}'}\, dv'. \qquad (19)$$

Since the cylinder is electrically thin, the phase kernel $\exp(ik_0\hat{k}^s \cdot \bar{r}')$ is approximated as $\exp(ik_z^s z')$. Inserting (1) and integrating over the cross section A, the electric Hertz potential can be succinctly written as

$$\Pi(\bar{r}) = \frac{e^{ik_0 r}}{4\pi r}\int_\ell P \cdot \hat{a}e^{-ik_0(\hat{k}^s\cdot\hat{z} - \cos\beta)z'}\, dz' \qquad (20)$$

where P is defined as the polarizability tensor per unit length, whose elements can be determined from $\Phi(\bar{\rho})$ using the formulation of Sarabandi and Senior [1].

Finally, integrating over the cylinder length ℓ, the electric Hertz vector potential is given as

$$\Pi(\bar{r}) = \frac{e^{ik_0 r}}{4\pi r}\ell P \cdot \hat{a}\frac{\sin U}{U} \quad \text{where}$$
$$U = \frac{k_0\ell}{2}(\hat{k}^s \cdot \hat{z} - \cos\beta). \qquad (21)$$

Therefore, the far-field scattering for a long, thin, dielectric cylinder of arbitrary cross section and electrical length is expressed as

$$E^s = -\frac{e^{ik_0 r}}{4\pi r}k_0^2\{\hat{k}^s \times \hat{k}^s \times [\ell P \cdot \hat{a}]\}\frac{\sin U}{U}. \qquad (22)$$

V. Conclusion

This paper has addressed the scattering from long, electrically-thin dielectric cylinders of arbitrary electrical length and cross section. As such, it provides a solution which eliminates the additional constraints required by methods which might otherwise be used on these thin cylinder structures. For example, the Rayleigh approximation is limited to small $k\ell$ [5], physical optics to large $k\ell$ [1], the Borne approximation to small ϵ_r [3], and generalized Rayleigh–Gans to circular cross sections [2].

Equations (1) and (2) are the scattering solution for an infinite cylinder ($kl = \infty$) as $ka \to 0$. Yet, this paper has demonstrated that they also satisfy the integral equation defining the scattering from a finite-length cylinder with arbitrary $k\ell$, again as ka approaches zero. By definition, (1) and (2) are therefore the asymptotic solution to this scattering problem as $ka \to 0$. The MM solution was constructed merely to evaluate the asymptotic error associated with nonzero ka. Section II alone provides the general proof of this paper's hypothesis.

References

[1] K. Sarabandi and T. B. A Senior, "Low-frequency scattering from cylindrical structures at oblique incidence," *IEEE Trans. Geosci. Remote Sensing*, vol. 28, no. 5, pp. 879–885, 1990.

[2] R. Schiffer and K.O. Thielheim, "Light scattering by dielectric needles and disks," *J. Appl. Phys.*, vol. 50, no. 4, pp. 2476–2483, Apr. 1979.

[3] H. C. van de Hulst, *Light Scattering by Small Particles*. New York: Wiley, 1957.

[4] T. B. A. Senior, and K. Sarabandi, "Scattering models for point targets," in *Radar Polarimetry for Geoscience Applications*. Norwood, MA: Artech House, F. T. Ulaby and C. Elachi, Eds., 1990.

[5] D. F. Herrick and T. B. A. Senior, "Low-frequency scattering by rectangular dielectric particles," *Appl. Phys.*, vol. 13, pp. 175–183, 1977.

James M. Stiles (S'91–M'95) was born in Kansas City, MO, in 1961. He received the B.S.E.E. degree from the University of Missouri, Columbia, in 1983, and the M.S.E.E. degree from Southern Methodist University, Dallas, TX, in 1987. He is presently working toward the Ph.D. degree in electrical engineering at the University of Michigan, Ann Arbor, MI.

From 1983–1990, he was an RF design engineer for Texas Instruments Inc., Dallas, TX. His interests include electromagnetic scattering from vegetation, and application of estimation theory to microwave remote sensing.

Kamal Sarabandi (S'87–M'90–SM'93) received the B.S. degree in electrical engineering from Sharif University of Technology, Tehran, Iran, in 1980. He entered the graduate program at the University of Michigan, Ann Arbor, in 1984, and received the M.S.E. degree in electrical engineering, in 1986, and the M.S. and Ph.D. degrees in mathematics and electrical engineering, respectively, in 1989.

From 1980–1984, he worked as a microwave engineer in the Telecommunication Research Center in Iran. He is presently an Assistant Professor in the Department of Electrical Engineering and Computer Science at the University of Michigan. He has 15 years of experience with microwave sensors and radar systems.

Dr. Sarabandi has served as Principal Investigator and Co-Investigator on many projects sponsored by NASA, JPL, ARO, DARPA, etc., in the past six years, all related in some way to the radar remote sensing of environment. He has published four book chapters and more than 50 papers in refereed journals on electromagnetic scattering, random media modeling, microwave measurement techniques, radar calibration, application of neural networks in inverse scattering problems, and microwave sensors. He has also had more than 80 papers and presentations in national and international conferences and symposia on similar subjects. He is listed in *Who's Who in Electromagnetics*, and is the Chairman of the Geoscience and Remote Sensing Society—Southeastern Michigan chapter.